



**HAL**  
open science

# Wheel-Vehicle Aerodynamic Interactions: Consequences for Drag

Di Bao

► **To cite this version:**

Di Bao. Wheel-Vehicle Aerodynamic Interactions: Consequences for Drag. Other. ISAE-ENSMA Ecole Nationale Supérieure de Mécanique et d'Aérotechnique - Poitiers, 2023. English. NNT: 2023ESMA0004 . tel-04206475

**HAL Id: tel-04206475**

**<https://theses.hal.science/tel-04206475>**

Submitted on 13 Sep 2023

**HAL** is a multi-disciplinary open access archive for the deposit and dissemination of scientific research documents, whether they are published or not. The documents may come from teaching and research institutions in France or abroad, or from public or private research centers.

L'archive ouverte pluridisciplinaire **HAL**, est destinée au dépôt et à la diffusion de documents scientifiques de niveau recherche, publiés ou non, émanant des établissements d'enseignement et de recherche français ou étrangers, des laboratoires publics ou privés.

# THÈSE

Pour l'obtention du grade de

## DOCTEUR DE L'ÉCOLE NATIONALE SUPÉRIEURE DE MÉCANIQUE ET D'AÉROTECHNIQUE

(Diplôme National - Arrêté du 25 Mai 2016)

*École Doctorale* : MIMME - Mathématiques, Informatique,  
Matériaux, Mécanique, Energétique

Secteur de Recherche : MÉCANIQUE DES MILIEUX FLUIDES

Présentée par

**Di BAO**

---

---

### Wheel-vehicle aerodynamic interactions: consequences for drag

---

Directeur de thèse : **M. Jacques BORÉE**

Co-encadrant : **M. Christophe SICOT**

Soutenue le 15 Juin 2023 devant la Commission d'Examen

#### JURY

---

S. KRAJNOVIĆ	Professor, Chalmers University of Technology, Gothenburg (SE)	Rapporteur
C.N. NAYERI	Associate Professor, Technische Universität Berlin, Berlin (DE)	Rapporteur
O. CADOT	Professor, University of Liverpool, Liverpool (UK)	Président
T. CASTELAIN	Maître de conférences, Université Lyon 1, Lyon	
S. SEBEN	Professor, Chalmers University of Technology, Gothenburg (SE)	
J. BORÉE	Professeur, Institut PPRIME, Poitiers	
C. SICOT	Maître de conférences, Institut PPRIME, Poitiers	



C.Roebroek, Engineer, Supervised this PhD for Michelin

欲穷千里目，更上一层楼。

— 唐·王之涣《登鹳雀楼》

**Desire for a grander sight by going up a higher floor.**

— Tang dynasty · *Zhihuan Wang*



# Acknowledgements

One year before the start of my PhD study, I was reading the manuscripts and articles by previous PhDs of Jacques. At that moment, I was already sure that this research group, in a small town in France, is consisted of intelligent and diligent people. Therefore, I decided to come here and sent the first email to Jacques (my main PhD supervisor). Jacques replied to me very quickly and we had a meeting together with Ruiying and Christophe (also my PhD supervisor). After conquered unprecedented difficulties, Jacques finally made this PhD possible. I will always remember this, as well as all his kind moves, the discussions till late evening, the pizza we made at his place, and the encounter when I was cycling.

The first day I arrived at ENSMA, Jacques welcomed me and introduced me to all my colleagues. Armando (so tall), Gabriel (I thought he was a professor), Muhittin, Yann (very cold at the beginning), and Catherine (first bisous in my whole life). We then had a meeting to work on the car model with François, Mathieu, and Jean-Marc. To be honest, I was really really sleepy, but Christophe was able to notice this and at a good time, translate the talk into English for me. From this moment till the end of my PhD, Christophe's help was always there for my study and for my life.

We are deeply indebted for the support from MFP Michelin, the CPER Feder programme Transport and China Scholarship Council (CSC No. 201806260262). With this collaboration with Michelin, I was able to meet a very kind engineer Côme. I would like to thank Côme for his help during my whole PhD and for his introduction to vintage cars and some very cool mangas.

There is an old saying in China that I believe exists everywhere: never trust the first impression. I do admit that this sentence is true but sometimes we got seduced by our instincts. This happened many times during my PhD, the most remarkable ones were with Ksenia and Yann. Ksenia proposed the “vodka=dog” paradox and till now most of us don't agree. I was a little bit offended by this paradox at the beginning but in the end, we became very close friends. Moreover, as I mentioned before, Yann was absolutely cold when I first meet him. This lasted for more than one month, Yann only talked once to me: “When are you moving to our office”. But it turned out that Yann is one of the nicest and coolest people among us. “oh what you really don't know this?” “OK I help you.” “This is really nice result, let's discuss it”. “I will read the draft Saturday night”.

It is well known that fluid mechanics is one of the hardest research topics. From my side, I understood this when I sat inside the wind tunnel. Everyone needs to be extremely careful because even a tiny small mistake can make all your results collected for one month go wrong. This has been prevented numerous times during my PhD, by Jean-Marc, François, Romain, Patrick, Mathieu and Bastien. I would like to thank them for all the help for manufacturing the model, for installing the PIV system, and for the preparation of the experiments.

Thanks to Gabriel, I read a lot of memes. Some of them are very stupid but some are very thought-provoking. If you consider your life as a line, you meet a friend at some points and then depart from each other. As a PhD student, every year students graduate and also come. This means that you say good bye to old friends and welcome new friends. There were some nice moments that I still have the image memory in my brain. According to Yann's professional lesson from Youtube, we made nice dumpling dinner with Armando, Yann, Ksenia, Gabriel, Justine and Arun. The nice bike rides with Ksenia at Cognac, with Armando around Poitiers. The hot pot party with Agostino, Mickael, Marco, Lucas, and Antoine. The lunches with all the people mentioned before as well as Yassine, Augustin, Momo, and Miguel.

To be honest, I am very very bad at dealing with stress. I had a remarkable record for cannot fall asleep for 3 or 4 days during exams. It was really surprising that the stress suddenly became

not that strong during my PhD. For example in my defense, I was very relaxed when doing the presentation and answering the questions. I would credit this to my nice jury members: Sinisa, Navid, Olivier, Thomas, and Simone. Their kindness in taking care of young folks in this field and their insightful questions really helped me.

These four years really changed me and made me a better person. I would like to thank all the people I met, and I hope we can have the chance to cross in the future. Finally, I would like to thank my family, my parents and my sister, also my cousin Boqi, for all the love and support.

Di  
22/06/2023 at Poitiers

# Contents

<b>1</b>	<b>Introduction</b>	<b>1</b>
1.1	Industrial context . . . . .	2
1.2	General features of bluff body wakes . . . . .	3
1.3	Flow around simplified car models . . . . .	5
1.3.1	Flow separation and wake dynamics . . . . .	6
1.3.2	Sensitivity of the wakes . . . . .	8
1.4	Objectives and outline of the thesis . . . . .	11
<b>2</b>	<b>Experimental methods</b>	<b>13</b>
2.1	Model geometry . . . . .	14
2.2	Experiments setup . . . . .	15
2.2.1	Wind-tunnel facility . . . . .	15
2.2.2	Model setup in the test section . . . . .	16
2.2.3	Wheel setup . . . . .	18
2.3	Measurement techniques . . . . .	20
2.3.1	Pressure measurements . . . . .	20
2.3.2	Aerodynamic force measurements . . . . .	23
2.3.3	Velocity measurements: particle image velocimetry . . . . .	23
<b>3</b>	<b>Baseline flow</b>	<b>27</b>
3.1	Mean flow around the square-back Windsor body . . . . .	28
3.1.1	Mean pressure field . . . . .	28
3.1.2	Boundary conditions at rear separation . . . . .	29
3.1.3	Mean wake flow . . . . .	30
3.1.4	Variations with Reynolds number and model length . . . . .	32
3.2	Wake reversal and mean asymmetries . . . . .	35
<b>4</b>	<b>Simplified modeling for wheels</b>	<b>39</b>
4.1	Need for model configurations of wheels . . . . .	40
4.2	Experimental setup . . . . .	40
4.3	Global effects of perturbations . . . . .	42
4.3.1	Base drag sensitivity . . . . .	42
4.3.2	Pressure fields . . . . .	44
4.4	Global and local wake modifications . . . . .	49
4.4.1	Evolution of the near wake of the body . . . . .	50
4.4.2	Obstacle wake characteristics in different regimes . . . . .	53
4.5	Further discussions and concluding remarks . . . . .	56
4.5.1	A momentum exchange model to evaluate the mass exchange effects . . . . .	56
4.5.2	Concluding remarks . . . . .	59
<b>5</b>	<b>Salient features of wheel-vehicle interactions</b>	<b>61</b>
5.1	Introduction . . . . .	62
5.2	Experimental setup . . . . .	63
5.3	Salient features of wheel-vehicle interactions . . . . .	64
5.3.1	Drag sensitivity to wheel-to-base distance . . . . .	64

5.3.2	Global forcing of vehicle wake by the wheels . . . . .	65
5.3.3	Near wake interactions for small wheel-to-base distance . . . . .	67
5.4	Influence of initial asymmetry of the baseline wake . . . . .	73
5.5	Discussions and concluding remarks . . . . .	75
5.5.1	Evaluating the effect of mass exchange on the base drag . . . . .	75
5.5.2	Effects of wheel state: rotating or stationary . . . . .	76
5.5.3	Influence of tire width on base drag . . . . .	77
5.5.4	Concluding remarks . . . . .	77
<b>6</b>	<b>Influence of wheel geometry</b>	<b>79</b>
6.1	Wheel geometry and drag . . . . .	80
6.2	Experimental setup . . . . .	81
6.3	Preliminary parametric survey . . . . .	82
6.4	Detailed investigation of the effects of front wheels . . . . .	84
6.4.1	Impact of front-wheel bluntness on drag . . . . .	84
6.4.2	Global effects of front wheels . . . . .	87
6.4.3	Influence on near-wake interactions . . . . .	91
6.4.4	Scaling of drag changes in the drag-sensitive regime . . . . .	96
6.5	Discussions and concluding remarks . . . . .	97
6.5.1	Model . . . . .	97
6.5.2	On the drag sources from near-wake interactions . . . . .	100
6.5.3	Concluding remarks . . . . .	101
<b>7</b>	<b>Extension to a different vehicle back shape</b>	<b>103</b>
7.1	Dependency of wheel-vehicle interactions on vehicle shape . . . . .	104
7.2	Experimental setup . . . . .	105
7.3	Baseline flow . . . . .	107
7.4	Effects of underflow perturbations . . . . .	109
7.5	Effects of wheels . . . . .	114
7.6	Concluding remarks . . . . .	118
<b>8</b>	<b>General synthesis and perspectives</b>	<b>119</b>
8.1	General synthesis . . . . .	119
8.1.1	Mean mass transfer: sensitivity, origin, and consequences . . . . .	119
8.1.2	Variation in vehicle wake balance . . . . .	121
8.2	Perspectives . . . . .	121
8.2.1	Interactions of multi-scale separation regions . . . . .	121
8.2.2	A road towards industrial applications . . . . .	122
8.2.3	Drag-reduction strategies . . . . .	123
<b>A</b>	<b>Numerical simulations for the square-back Windsor body</b>	<b>125</b>
A.1	Methodology . . . . .	126
A.1.1	Model geometry and numerical setup . . . . .	126
A.1.2	Underflow perturbations . . . . .	128
A.2	Comparison between numerical and experimental results . . . . .	128
A.3	Further insights of near-wake interactions . . . . .	130
A.3.1	Global pressure distributions . . . . .	131
A.3.2	Origin of the mean mass exchange . . . . .	132
A.3.3	Effect of mean mass exchange on base pressure . . . . .	133
	<b>Résumé étendu</b>	<b>147</b>

# Chapter 1

## Introduction

---

Understanding the complex separation regions and their interactions is of crucial importance for the drag reduction of road vehicles. The interactions between the wheels and the main vehicle body are considered in the present thesis. In this introductory chapter, we start by briefly reviewing the general features of bluff body wakes. Then, we discuss the wake of simplified car models and its sensitivity to various parameters and perturbations. Special attention is paid to the influence of the wheels, which are considered as underflow perturbations. Finally, the specific problems tackled by the present manuscript are highlighted leading to a presentation of the thesis outline.

*'Things we lose have a way of coming back to us in the end'*  
- Recirculating bubble (originally by J.K. Rowling)



## Contents

1.1	Industrial context . . . . .	2
1.2	General features of bluff body wakes . . . . .	3
1.3	Flow around simplified car models . . . . .	5
1.3.1	Flow separation and wake dynamics . . . . .	6
1.3.2	Sensitivity of the wakes . . . . .	8
1.4	Objectives and outline of the thesis . . . . .	11

## 1.1 Industrial context

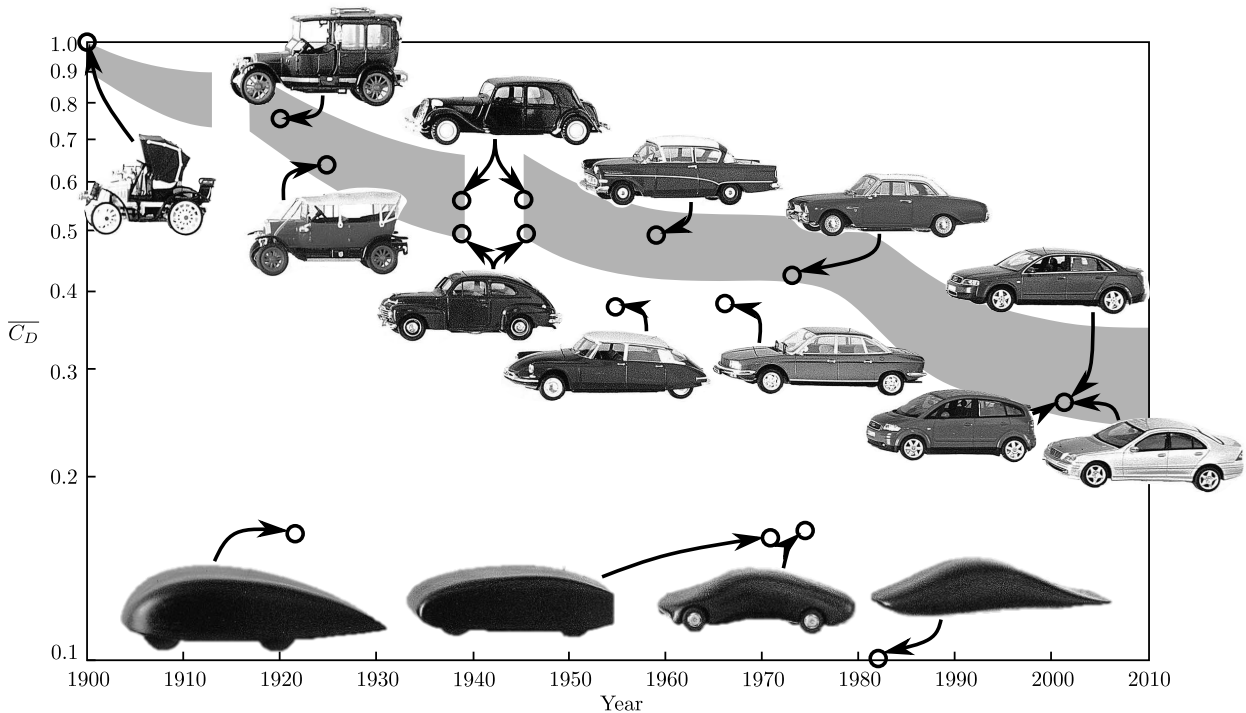


Figure 1.1: History of the drag coefficient  $\overline{C_D}$  of road vehicles (top) and car-like bodies (bottom) adapted from Schuetz (2016).

Since the invention of the assembly line by Henry Ford in 1913, the increased affordability combined with population growth and urbanization has led to a surge in automobile sales. The number of registered vehicles has reached over one billion by around 2010 and is expected to be doubled in the next decades (Davis & Boundy, 2021). This astonishing number of vehicles has led to high levels of air pollution and greenhouse gas emissions, which cause climate change and have harmful effects on human health and the environment. In particular, the European Union (EU) has established regulations for the automotive industry, such as the *EU CO<sub>2</sub> Regulation 2019/631*, which aims to reduce average emissions from the manufacturer's fleet to 95 gCO<sub>2</sub> km<sup>-1</sup> by 2021 and to 37.5 gCO<sub>2</sub> km<sup>-1</sup> by 2030.

In order to diminish the environmental impacts, several key factors are considered by automotive manufacturers such as the optimization of the propulsion system, the application of lightweight materials, and the reduction of drag force. When a road vehicle is moving on a road without inclination and acceleration, the total drag force is comprised of two elements: the rolling resistance exerted by the road on the tires and the aerodynamic drag exerted by air on the vehicle body. With increasing speed, the rolling resistance is approximately constant while the energy dissipation induced by the aerodynamic drag increases as the cube of vehicle speed. At high speeds (typically above 60 km h<sup>-1</sup>), the aerodynamic drag exceeds the rolling resistance and becomes the major

contributor to the total drag (Schuetz, 2016). Therefore, reducing the aerodynamic drag is considered by automotive manufacturers as a promising way to regulate the emission of greenhouse gases.

The pursuit of aerodynamic drag reduction can be dated back to the 1900s. In figure 1.1 the history of the aerodynamic drag of road vehicles is presented. In this figure, the aerodynamic drag is quantified by a dimensionless coefficient  $\overline{C_D}$ , allowing comparisons between vehicles of different sizes and shapes. A gradual decrease of  $\overline{C_D}$  from the 1900s to the 1970s is noted and is followed by a quite remarkable drop in the 1980s. The latter one is driven by the energy crisis and the usage of wind tunnels. However, in the last few decades, the aerodynamic drag coefficient  $\overline{C_D}$  has apparently hit a cap of about 0.3.

Several constraints impede further reduction of the aerodynamic drag. First of all, for a given vehicle size, customers always demand the highest possible carrying capacity. This limits the application of more streamlined shapes for example the black models shown in figure 1.1 which provide a  $\overline{C_D}$  of  $\sim 0.1$ . Furthermore, there are trade-offs between aerodynamic efficiency and other design considerations, such as stability, maneuverability, and safety. Finally, implementing advanced aerodynamic technologies often entails cost and practical challenges. Given these limitations, only minor changes are allowed to be made by aerodynamic optimizations. Therefore, alternative strategies with more design freedom should be developed. This can only be achieved through a deep understanding of the drag generation mechanisms.

For modern road vehicles, the common blunt shape leads to massive flow separations. The separation regions and the interactions between them are direct or indirect sources of aerodynamic drag. Considering the scale of the separation regions, the wheel wakes and the vehicle wake are the dominant ones. Indirect effects of the wheel wakes on the near wake of the main body leading to a decrease in the base pressure have a very detrimental effect on the aerodynamic efficiency of a vehicle. To give some figures, the wheels themselves and their interactions with the main body are responsible for more than 25% of the aerodynamic drag (Wickern *et al.*, 1997).

In this industrial context, the present work aims at improving the physical understanding of the wheel-vehicle aerodynamic interactions and their consequences for drag. The goal is to improve the aerodynamic drag reduction process taking into account the interaction mechanisms. In the following, an introduction from an academic point-of-view is started by picturing the wakes of simple bluff bodies which is followed by reviewing the sensitivity of their wakes to various kinds of parameters and perturbations including the wheels.

## 1.2 General features of bluff body wakes

A *bluff body* is a term used to describe a solid object placed in a fluid flow that generates separations of flow and a wake behind it. It exists widely in nature and in industrial applications. Based on the complexity of the geometry, we may categorize bluff bodies into three groups in figure 1.2(a). As the simplest category, two-dimensional (2-D) geometries have been extensively investigated dating back to the 1930s (Williamson, 1996). The understanding of the flow of these geometries has helped to identify the essential features linking the wake dynamics with the forces acting on the geometry. With increasing geometry complexity, the family of axisymmetric bluff bodies contains several celebrities: the sphere and the bullet-shaped geometry. The famous designs of the golf ball and rifling are rooted in the dynamics of the wakes (Bearman & Harvey, 1976; Jiménez-González *et al.*, 2014). When the number of symmetry planes is reduced, three-dimensional (3-D) geometries with a greater geometry complexity are achieved. This category includes simple parallelepiped bodies for example the rectangular flat plate and cube. When the leading edges of the cube are rounded, the reference geometries for automotive industries, the Ahmed body (Ahmed *et al.*, 1984) and the Windsor body (Le Good & Garry, 2004), are formed. With added details, most importantly the wheels, the ground vehicles including trucks, lorries and passenger cars are also inside this category. In these highly complex situations, the near wake of these ground vehicles still represents 30 to 50 % of the aerodynamic drag (Schuetz, 2016).

For all these geometries, the wake is the key ingredient of the flow. It features complex dynamics resulting from the interactions between flow structures having a rich variety of length and time

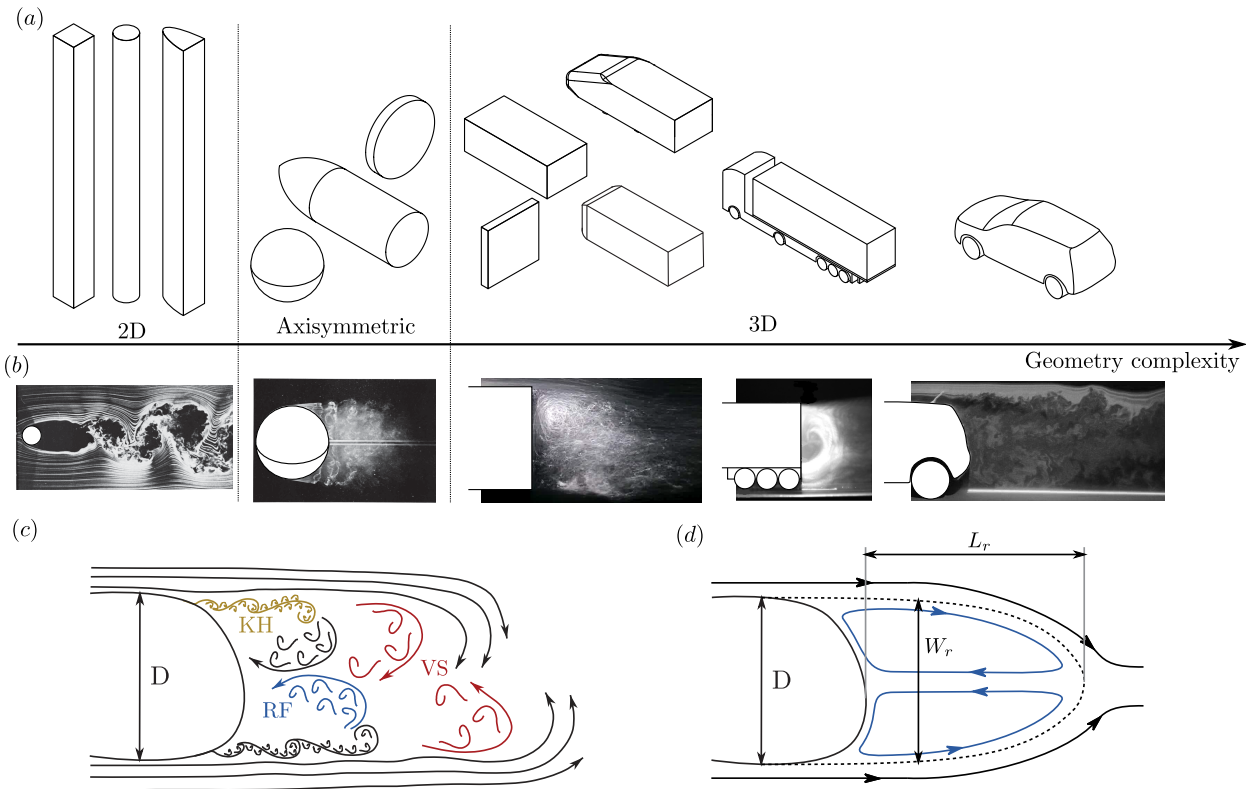


Figure 1.2: Bluff body flows. (a) Different bluff bodies ranging from two-dimensional (2-D) cylinders to three-dimensional (3-D) geometries. (b) Representative flow visualizations for different bluff bodies, from left to right: Circular cylinder at  $Re = 10^4$ , Sphere at  $Re = 1.5 \times 10^4$  (Van Dyke, 1982), Ahmed body at  $Re = 2.16 \times 10^5$  (Cadot *et al.*, 2015), heavy truck at  $6 \times 10^5$  (Lo & Kontis, 2017), and passenger car (Grandemange, 2013). (c) General features of the wake flow of bluff bodies (adapted from Barros (2015); Haffner (2020)). (d) Time-averaged sketch of (c) (adapted from Grandemange (2013); Haffner (2020)).

scales. We picture the wakes of these geometries in figure 1.2(b)<sup>1</sup>. Despite the striking differences in geometry and usage of these bluff bodies, their wakes still share several common features as summarized in the sketch in figure 1.2(c). For a bluff body having a characteristic length of  $D$ , the boundary layer on its surface detaches at the rear end, either due to sharp trailing edges or an adverse pressure gradient caused by curved surfaces. This leads to the formation of free shear layers dividing the high-momentum free stream from the low-momentum wake region. As these shear layers move downstream, they become susceptible to the Kelvin-Helmholtz instability (represented by KH in Figure 1.2c and can be noticed in several configurations in figure 1.2b), which amplifies small- and large-scale vortical structures. The presence of these vortices and the shear layer development lead to further interactions between shear layers of opposite vorticity, resulting in the shedding of large-scale vortices in a periodic manner, known as the Von Kármán vortex shedding (represented by VS in Figure 1.2c and can be clearly seen for the 2-D configuration in figure 1.2b).

The presence of vortical structures such as K-H and Von Kármán vortices along the shear layers facilitates the exchange of mass and momentum between the high-momentum external flow and the low-momentum wake region. These structures play a crucial role in feeding the high-momentum flow into the wake (see RF in figure 1.2c) and draining the low-momentum flow out of it (Philip & Marusic, 2012; Stella *et al.*, 2017; Trip & Fransson, 2017). According to the model proposed by Gerrard (1966), the equilibrium between these inflows and outflows results in the formation of the recirculation region. As a result, the length of the recirculation region ( $L_r$ ), as seen in the time-averaged sense in figure 1.2(d), can be linked directly to the dynamics of the Von Kármán vortices and the dynamics of the shear layer.

With a brief understanding of the general features of wake dynamics, we now discuss the

<sup>1</sup>Under incompressible flow at a Reynolds number typically above  $10^4$ .

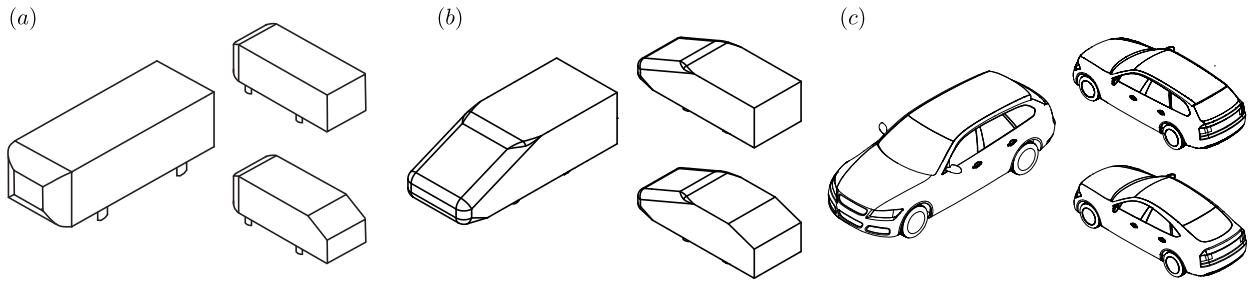


Figure 1.3: Simplified vehicle models: (a) Ahmed body. (b) Windsor body. (c) DrivAer model. Both square-back and fast-back versions are shown.

relationship between the wake and the aerodynamic drag of a bluff body. The aerodynamic drag is generated as a result of the momentum loss in the flow caused by the turbulence within a wake<sup>2</sup>. Nevertheless, it has been almost infeasible to practically calculate this process<sup>3</sup>, particularly in experimental situations where measurement data is limited. Therefore, many previous works were focused on providing simple descriptions linking a wake and the drag it induced. The first attempt was made by Kirchhoff (1869) and later by Brillouin (1911) using the free-streamline theory. Their model was based on a 2-D wake having an infinite length ( $L_r = \infty$ ) and a pressure the same as the free-stream pressure  $p_0$ . Under current knowledge, this model is impractical for two reasons. For the first reason, an infinite wake length is only possible when the Reynolds number approaches infinite ( $Re \rightarrow \infty$ ) as proposed by Sychev *et al.* (1998). The second reason is that the real pressure inside a wake is always smaller than the free-stream pressure  $p_0$ . Batchelor (1956) then proposed that this model can be made more realistic by considering a wake of finite length. This led to the development of several improved models (Roshko, 1954, 1955; Parkinson & Jandali, 1970). Later on, Sychev (1982) and Roshko (1993) proposed a different approach by considering the momentum balance along the closed separating streamline around a 2-D wake, which links the length  $L_r$  and width  $W_r$  of the recirculation region with the pressure on the base. A detailed examination of this idea was provided by Balachandar *et al.* (1997) based on several 2-D wake configurations.

Specifically, the concept of the wake bluntness introduced by Roshko (1955) defined as  $W_r/D$  as shown in figure 1.2(d) has an important link with the base pressure. This is exemplified by the drag crisis of 2-D circular cylinders. When the Reynolds number reaches a threshold<sup>4</sup>, the separation points move downstream. This results in a decrease of  $W_r/D$  and a drag decrease of  $\sim 70\%$  (Zdravkovich, 1997). In some situations when the wake bluntness  $W_r/D$  is fixed, such as the D-shaped cylinder with  $W_r/D = 1$ , the recirculation length  $L_r$  is another decisive factor for the drag. A longer  $L_r$  corresponds to a lower drag (Bearman, 1967). In a more general perspective, these two parameters  $W_r$  and  $L_r$  can be united by looking at the ratio  $L_r/W_r$  as proposed in Sychev *et al.* (1998). For complex situations such as 3-D bluff bodies, the relation between the size of the wake ( $L_r$  and  $W_r$ ) and the drag is still reliable for example as shown in Grandemange *et al.* (2013c); Barros *et al.* (2016a); Lorite-Díez *et al.* (2020b); Haffner *et al.* (2020b).

### 1.3 Flow around simplified car models

Simplified models of road vehicles have become prevalent in road vehicle aerodynamics research over the past few decades. This is because they offer a suitable compromise between capturing the key aspects of the flow fields of real road vehicles and making experiments and computations manageable. The Ahmed body (Ahmed *et al.*, 1984) and the Windsor body (Le Good & Garry, 2004) as shown in figure 1.3 are perhaps the most well-known models. They feature a rectangular cross-section and a streamlined front part. Recently, models with more intricate geometries have emerged, such as the ASMO model (Aljure *et al.*, 2014) and the DrivAer model (Heft *et al.*, 2012), which is based on the average of several road vehicles and is depicted in figure 1.3(c). The most significant distinction, when comparing these more realistic models with the Ahmed and Windsor

<sup>2</sup>A detailed review can be found in Oxlade (2013).

<sup>3</sup>Recently, Bonnavion *et al.* (2022) used numerical simulations to relate this process with the drag.

<sup>4</sup>Around  $10^5$  but depends on the inflow conditions and the surface roughness of the cylinder.

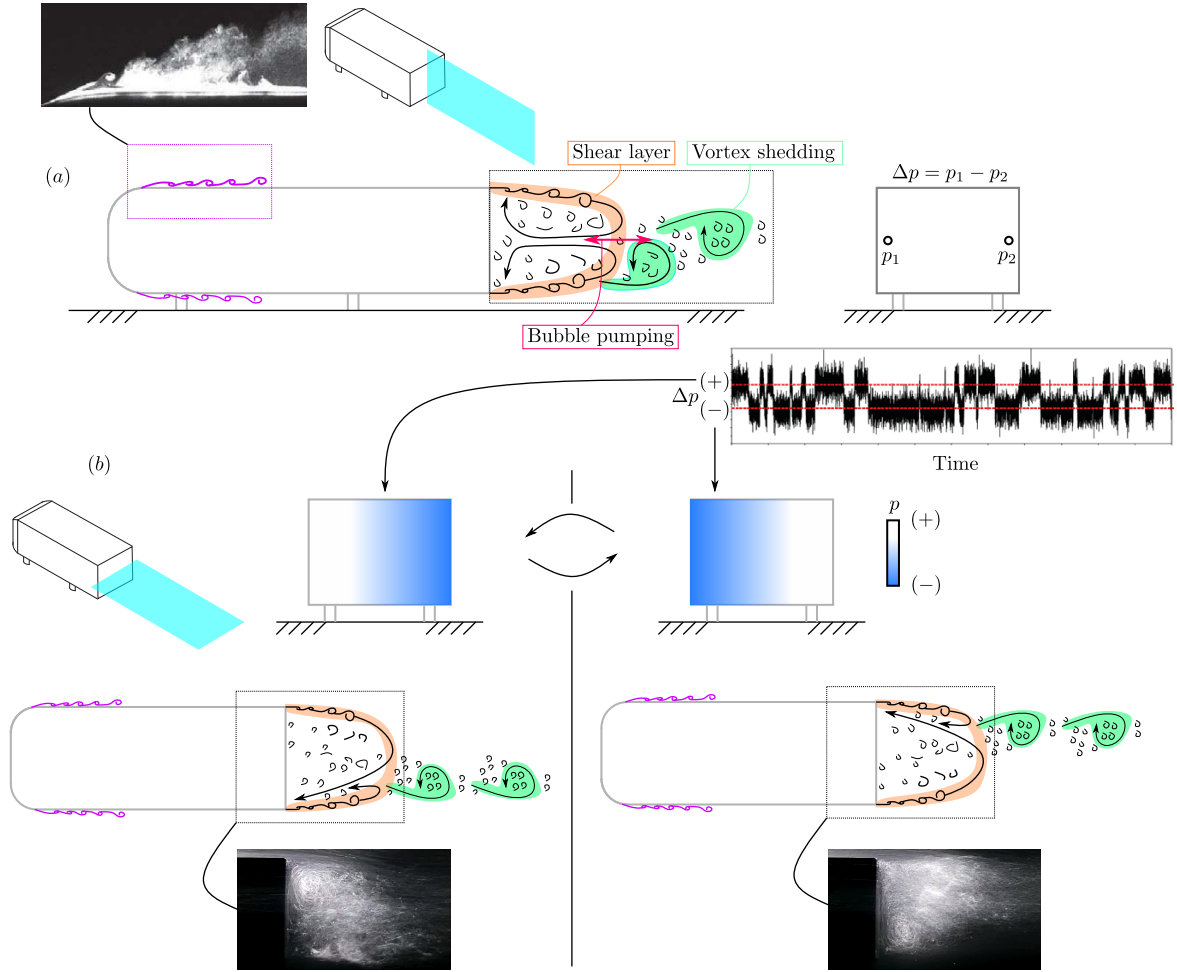


Figure 1.4: (a) A sketch of the flow separation and wake dynamics of the original square-back Ahmed body, flow visualization from Grandemange (2013) shows the separation at the front. (b) A simplified description of the horizontal wake bi-stability. The time evolution of the pressure difference  $\Delta p$  between two locations on the base  $p_1$  and  $p_2$  shows two wake states having large-scale horizontal asymmetry. The two states are shown in sketches and in flow visualizations from Cadot *et al.* (2015).

bodies, is that wheels are not considered for the Ahmed and Windsor bodies. Recently, on the basis of the rich knowledge gained using the Ahmed and Windsor bodies, the design of a new Windsor body with wheels by Pavia & Passmore (2017) enables us to examine the influence of wheels on the wake and drag, which is the main focus of the present study. This section begins by examining the flow around the Ahmed body with a square back, then explores how their wakes are affected by the variations of different parameters and perturbations. In particular, the impacts of the wheels are discussed in the second part.

### 1.3.1 Flow separation and wake dynamics

We start here by describing the flow around the square-back Ahmed body. It is noted that the Windsor body used for the present manuscript has very similar flow features as the Ahmed body. Unless otherwise stated, all the descriptions are based on the investigations at a Reynolds number above the order  $10^5$  corresponding to the typical speed of road vehicles.

For the original square-back Ahmed body designed by Ahmed *et al.* (1984) with a ratio between the height  $H$  and the width  $W$  smaller than 1 ( $H/W < 1$ ), we show in figure 1.4(a) a sketch of the flow in the symmetry plane of the model. At the front of the model, flow separation and reattachment just after the curved front leading edges were reported in some studies (Spohn & Gilliéron, 2002; Grandemange *et al.*, 2013b; Zhang *et al.*, 2015). In figure 1.4(a) the flow visualization from Grandemange (2013) in the front separation region is shown. The periodic dynamics measured around the separation bubble corresponds to a Strouhal number of  $St_H \sim 0.2$

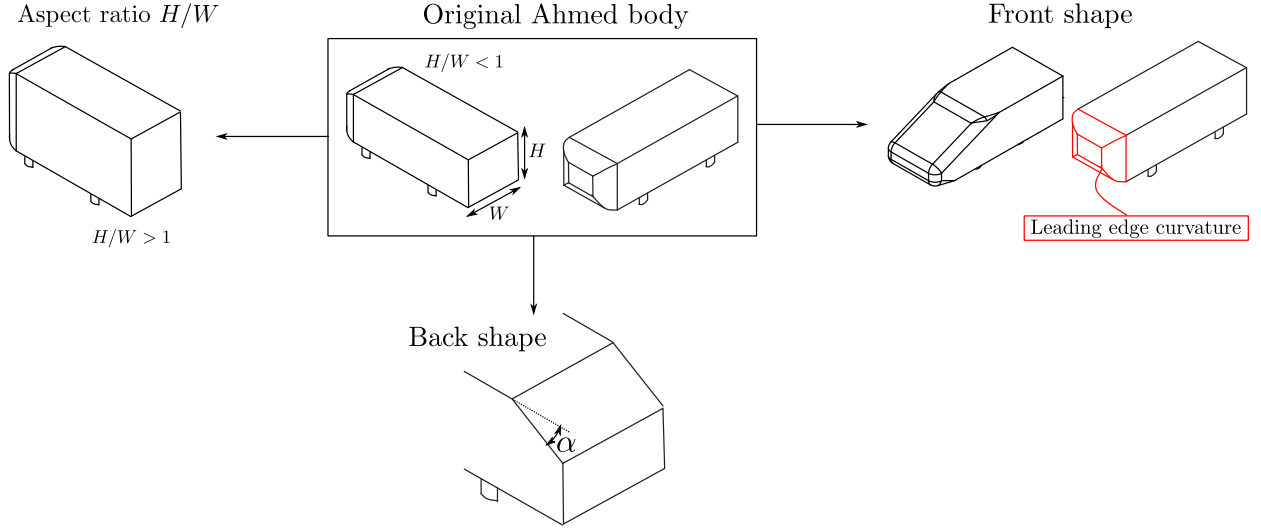


Figure 1.5: Illustrations of several geometrical modifications of the original Ahmed body.

( $St_H = fH/U_0$ , where  $H$  is the characteristic length of the model: the height, and  $U_0$  is the free-stream velocity). For simple parallelepiped bodies such as the cube (Klotz *et al.*, 2014; Hearst *et al.*, 2016) with sharp leading edges and a small length-to-width ratio, massive flow separation exists at the leading edges and is strongly coupled with the wake dynamics. These features are expected to be attenuated for the Ahmed and Windsor bodies because of the flow reattachment along the body. However, they can still importantly influence the boundary layer characteristics at the rear separation (Mariotti *et al.*, 2015), the development of the shear layers, and consequently the wake dynamics.

Further downstream, the blunt trailing edges impose massive flow separations behind the model which leads to the formation of a 3-D wake. The dynamics of the wake are similar to the discussion in §1.2 in a general context. Here the special features of this kind of wakes are examined. First of all, the interaction of the opposite shear layers leads to vortex shedding in the vertical and horizontal directions. The oscillation frequency of these dynamics is at  $St \sim 0.2$  (the characteristic length is the model dimension in the direction of the vortex shedding) as measured in several studies downstream of the recirculation region (Grandemange *et al.*, 2013b; Lahaye *et al.*, 2014; Volpe *et al.*, 2015; Barros *et al.*, 2016a,b; Lorite-Díez *et al.*, 2020b). When the wake is asymmetric, this oscillating mode is organized in a one-side shedding manner as discussed in Grandemange *et al.* (2013b) and visualized in Dalla Longa *et al.* (2019). In addition, in some studies (Duell & George, 1999; Khalighi *et al.*, 2001; Lahaye *et al.*, 2014; Volpe *et al.*, 2015; Dalla Longa *et al.*, 2019; Haffner *et al.*, 2020a), a low-frequency peak at around  $St_H \sim 0.08$  is detected by examining the base pressure and/or the velocity fluctuation in the recirculation region. This peak was associated with the phenomenon of wake bubble pumping observed in Berger *et al.* (1990) behind a disk.

In the horizontal direction of the wake, Grandemange *et al.* (2013b) revealed a random switching of wake orientation between two states leading to statistical symmetry. This is depicted by the sketch and flow visualizations from Cadot *et al.* (2015) in figure 1.4(b). The base pressure gradient imposed by the wake as shown in figure 1.4(a) was also used by the authors to show the time evolution of this random dynamics. A long timescale of the order of  $O(10^3 H/U_0)$  is normally needed between the shifting events (Grandemange *et al.*, 2013b) therefore this bi-stable mode is usually referred to as the static mode. At low Reynolds numbers, the first symmetry-breaking bifurcation of the wake leads to steady wake asymmetry as shown experimentally by Grandemange *et al.* (2012) and numerically by Evstafyeva *et al.* (2017). In the turbulent regime, the reason for the wake switching is recently investigated by several studies (Dalla Longa *et al.*, 2019; Haffner *et al.*, 2020a; Pavia *et al.*, 2020; Podvin *et al.*, 2021) but is still an open question.

### 1.3.2 Sensitivity of the wakes: from global parameters to wheels

From a stability point-of-view, the shear layers of a wake act as a noise amplifier due to convective instability, while the periodic shedding of vortices is a result of absolute instability and behaves like a resonator (Huerre & Monkewitz, 1990). This makes wakes highly susceptible to even very small perturbations. In this section, the sensitivity of 3-D wakes to different kinds of parameters and perturbations is discussed.

One of the most significant factors that affect the wake topology and dynamics is the shape of the bluff body. In figure 1.5, several geometrical modifications are schematically shown. First of all, modifying the base aspect ratio  $H/W$  from  $H/W < 1$  for the original Ahmed body to  $H/W > 1$  rotates the direction of the random wake switching to the vertical direction as shown experimentally in Grandemange *et al.* (2013a) and assessed numerically in Dalla Longa *et al.* (2019). It is important to note here that a sufficient ground clearance  $G$  and a moderate aspect ratio  $H/W$  are needed<sup>5</sup>. Moreover, the front shape may play an important role in the wake due to the interaction between the ground and the front separation bubble as examined in Easanesan *et al.* (2020) for a 2-D D-shaped cylinder. However, these features have never been systematically studied for 3-D bluff bodies. When comparing the original Ahmed body and the Windsor body (Pavia, 2019; Varney *et al.*, 2020), this front shape effects are not observed since these two bodies produce very similar wakes. Nevertheless, the effects of front shape can be seen when comparing the wakes of two modified Ahmed bodies used respectively in Barros (2015) and in Haffner (2020). Both of these works were conducted in the same wind tunnel with similar setups. In Barros (2015), the wake is dominated by a top recirculating flow with a strong vertical asymmetry and no horizontal bi-stability. On the contrary, a mean vertical symmetric wake with horizontal bi-stability was observed by Haffner (2020). A major difference between the two modified Ahmed bodies is that the rounding of the front leading edges in Haffner (2020) is specially designed with a continuous evolution of curvature from the front surface to the side surfaces. This design was aimed at preventing local flow separation. On the other hand, a fixed curvature was considered in Barros (2015). If front separation exists in the situation of Barros (2015), we suggest that the floor is able to cause differences in the sizes of the top and bottom front separation bubbles that influence the vertical wake asymmetry as shown in Easanesan *et al.* (2020). Finally, some of the geometrical modifications are located at the back. The most well-known one is the angle of the slant back  $\alpha$ , varying this angle modifies a wide range of flow structures and dynamics. This will be discussed in §7.1 in chapter 7 when a fast-back Windsor body is investigated.

In addition to these geometrical modifications, the 3-D wake produced by the square-back bluff bodies was found to be very sensitive to various kinds of perturbations. These perturbations range from global ones such as the background turbulence to very local ones such as the presence of wheels as sketched in figure 1.6. We may categorize them according to whether they respect the symmetries of the bluff bodies or not. When the perturbations respect these symmetries, the mean wake equilibrium is not varied in most cases. However, the dynamics in the wakes, such as the shear layer instabilities and the global modes, were found to be fundamentally changed. The effects of background turbulence on the wake bi-stability were evaluated recently in Cadot *et al.* (2020) and in Burton *et al.* (2021). It was revealed in Burton *et al.* (2021) that the switching rate of the bi-stability increases monotonically with the free-stream turbulence intensity. When the perturbations are located more locally, the wakes can still be greatly influenced. This is already the case when applying suction (Barros, 2015; Ahmed & Morgan, 2022) or boundary layer tripping (Fan & Cadot, 2023) at the front surface of the model. The changes in the flow structures and boundary layer characteristics were believed to affect the shear layers and the wake dynamics, especially the bi-modal dynamics.

At the trailing edges, a large variety of perturbations from passive devices such as cavity and flaps to active fluidic forcing were developed for drag reduction. Drag reduction by reducing the bluntness of the wake was achieved using boat-tailing (Lorite-Díez *et al.*, 2017; Bonnavion & Cadot, 2018, 2019), inwards-oriented flaps (Grandemange *et al.*, 2013c; de la Cruz *et al.*, 2017a; Urquhart

---

<sup>5</sup>These two parameters affect the wake asymmetry in a coupled manner as detailed in Grandemange *et al.* (2013a). Generally, the ground clearance  $G$  imposes vertical asymmetry to the wake leading to the disappearance of bi-stability. A very large or small  $H/W$  leads to a 2-D wake and therefore the disappearance of the bi-stability.

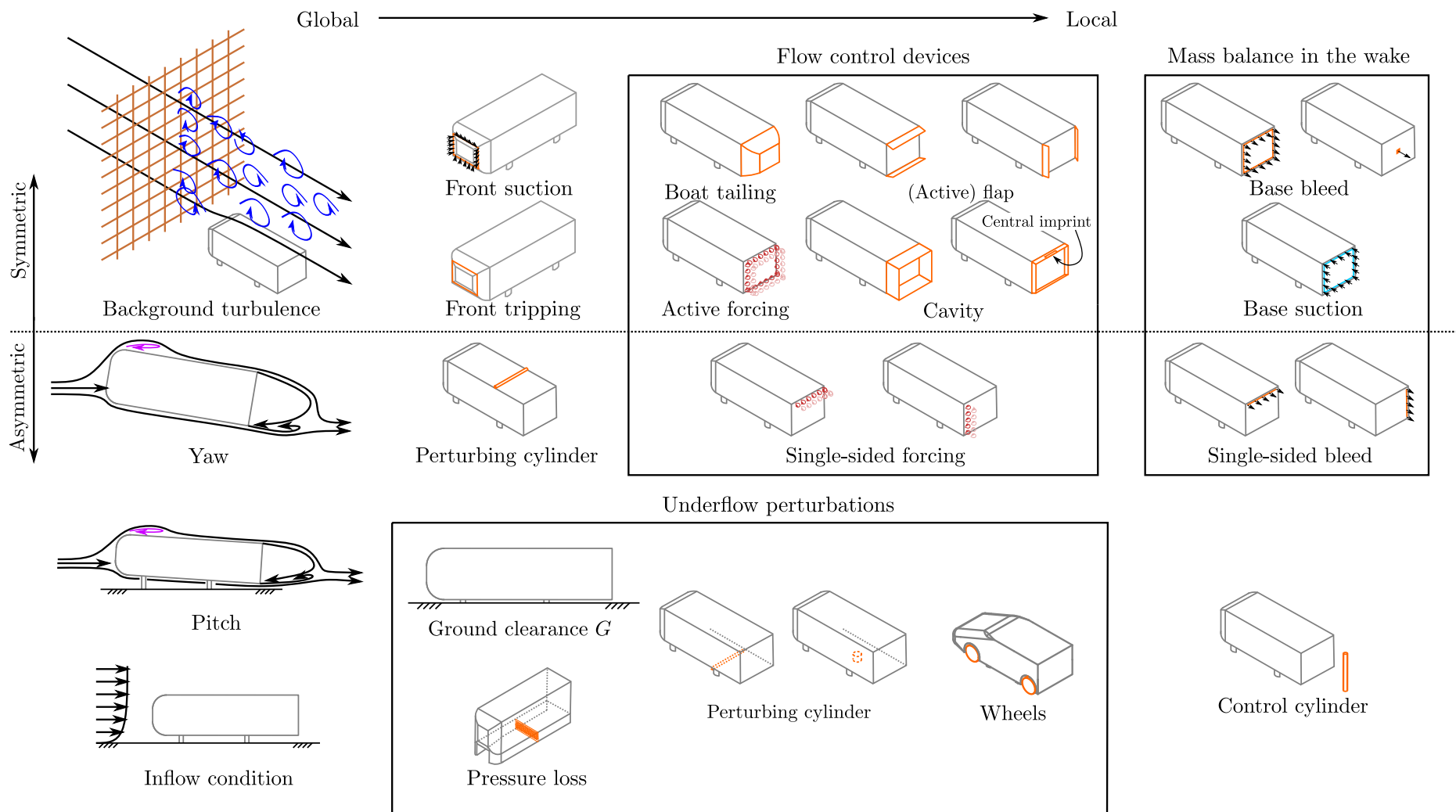


Figure 1.6: Illustrations of flow perturbations leading to strong drag changes and/or wake modifications. Some of the figures are adapted from Barros (2015) and Haffner (2020).

*et al.*, 2018), side taping (Varney *et al.*, 2020; Perry *et al.*, 2016), and fluidic forcing (Barros *et al.*, 2016a; Pfeiffer & King, 2018; Li *et al.*, 2019; Plumejeau *et al.*, 2019; Haffner *et al.*, 2020b). Elongation of the recirculation region by using cavity (Evrard *et al.*, 2016; Lucas *et al.*, 2017; Bonnavion, 2018; Fan *et al.*, 2022) was found able to reduce the drag and suppress the bi-modal dynamics when the cavity is long enough (around  $0.3H$ ). Particularly, the recent work of Darabasz *et al.* (2023) showed that the use of a shorter cavity (around  $0.17H$ ) consisting of a central imprint and a bottom inclined spoiler is able to reduce the drag and stabilize the horizontal bi-modal dynamics. This was attributed to the formation of a streamwise vortex pair at the imprint edges.

In 2-D situations, a continuous injection or extraction of mass flux from the recirculating bubble was found in Wood (1964) and Bearman (1967) to have a fundamental influence on the vortex formation length<sup>6</sup> and the drag. On the basis of these studies, Lorite-Díez *et al.* (2020b,a); Khan *et al.* (2022) and Hsu *et al.* (2021) tested the effects of base bleed/suction on the wake dynamics and drag. In Lorite-Díez *et al.* (2020b), the continuous base bleed was applied through four slits along the trailing edges. With increasing bleed strength, two successive flow regimes were identified and were named as the mass regime and the momentum regime. In the mass regime with a small base bleed, a drag reduction and a suppression of the bi-modal dynamics were observed. This is accompanied by an increase in the recirculation length and was interpreted using the mass balance concept introduced by Gerrard (1966). On the other hand in the momentum regime with a strong base blowing, the shear layer dynamics are enhanced leading to a reduction in the recirculation length and a drag increase. These effects of base bleed were strengthened by moving its location to the center of the base as shown in Khan *et al.* (2022). A complete suppression of the bi-modal dynamics and a higher level of drag reduction were achieved. On the other hand, when extracting mass flux from the recirculating bubble as tested in Hsu *et al.* (2021), a continuous increase in drag and a gradual suppression of the bi-modal dynamics were found with increasing base suction flow rate. This is accompanied by a deflection of the recirculating bubble. All these studies clearly show the importance of mass balance in the recirculating bubble. By breaking the original mass balance of fluxes filling and emptying the recirculating bubble using base blowing/suction, the wake is modified and forms a new mass balance leading to variations in the drag and wake dynamics. In this process, the mass and momentum exchanges between the wake and the surrounding flow are varied as evidenced by the adjustment of the recirculating length.

There are also important consequences in the natural wake equilibrium if the upstream perturbations are asymmetric about the bluff body as shown in the bottom part of figure 1.6. When the pitch or yaw angle is varied, the asymmetry is first observed at the front of the model with an imbalance in the separation bubbles as measured in Fan *et al.* (2022) (schematically shown in figure 1.6). Moreover, the asymmetry in the inflow due to pitch or yaw also influences the wake. In the horizontal direction, with a very slight change in yaw of about  $0.5^\circ$ , the wake selects one of the two wake states and presents large-scale horizontal mean asymmetry (Bonnnavion & Cadot, 2018; Haffner *et al.*, 2020a). This was also observed by applying at the side trailing edges pulsed-jet forcing (Barros *et al.*, 2016a) or base bleed (Lorite-Díez *et al.*, 2020b). In the vertical direction, increasing or decreasing the pitch angle gradually enhances the vertical asymmetry in the wake and suppresses the horizontal bi-stability (Bonnnavion & Cadot, 2018). This is similar to the observation of Kang *et al.* (2021) by varying the inflow condition. The relation of vertical wake asymmetry and horizontal bi-stability was also systematically measured by Barros *et al.* (2017); Haffner *et al.* (2020a) using different kinds of obstacles located at the top/bottom surfaces of the model and by Lorite-Díez *et al.* (2020b) using single-sided base bleed at the top/bottom trailing edges. This means that the wake always presents asymmetry in the form of either horizontal bi-modal asymmetry or permanent vertical asymmetry. These asymmetries are an important source of drag ( $\sim 5\%$  of the total drag) as suggested by Grandemange *et al.* (2013b) based on the induced drag theory and by Haffner *et al.* (2020a) based on the interaction mechanism between opposite shear layers. These observations have promoted several studies aimed at symmetrizing the wake using passive or active flow control devices near the trailing edge (Li *et al.*, 2019, 2016; Brackston *et al.*, 2016; Urquhart *et al.*, 2018; Varney *et al.*, 2020; de la Cruz *et al.*, 2017b; Haffner *et al.*, 2022, 2021). In addition, Grandemange *et al.* (2014) perturbed the wake using a control cylinder located horizontally and vertically (see right-hand side of figure 1.6). When the cylinder is posi-

<sup>6</sup>Streamwise distance from the base to the location having the maximum flow fluctuation.

tioned asymmetrically about the model, the wake either locks in one of the horizontal wake states or presents vertical permanent asymmetry. When the cylinder is symmetric about the model, suppression of the bi-modal dynamics and reduction of the drag were observed in some locations.

An important subset of asymmetric perturbations is located between the underside of the bluff body and the ground (see the bottom part of figure 1.6). The importance of this subset lies in their frequent encounters under real road conditions. The underflow momentum is manipulated in some studies by reducing the ground clearance ([Grandemange et al., 2013a](#)), by using a pressure loss system ([Castelain et al., 2018](#)), or by introducing underbody roughness ([Perry & Passmore, 2013](#)). On the other hand, turbulence and flow blockage are introduced in the underflow by using different kinds of obstacles such as a horizontal or vertical perturbing cylinder ([Barros et al., 2017](#); [Haffner et al., 2020a](#)). In general, these perturbations have the ability to modify the natural wake equilibrium in the vertical direction and in some cases promote the appearance of bi-modal dynamics. Therefore, their consequences for the drag depend on the initial wake equilibrium. This is exemplified in [Haffner et al. \(2021\)](#) by applying pulsed jets at the bottom trailing edge on three different initial wake asymmetries.

These underflow perturbations, especially the vertical perturbing cylinder used in [Barros et al. \(2017\)](#), have already put our understanding of basic bluff bodies a step further toward real road vehicles. Indeed, very similar observations of the wake equilibrium were found when including rotating/stationary wheels on a Windsor body in [Pavia & Passmore \(2017\)](#); [Pavia et al. \(2020\)](#) and in [Su et al. \(2023\)](#). Starting from a wake having vertical vanishing asymmetry with horizontal bi-stable asymmetry, these three works showed that the wheels increase the vertical symmetry and suppress the horizontal bi-stable asymmetry. Recently, [Wang et al. \(2020\)](#) investigated the effects of wheels on the wake of a square-back ASMO model, rotating/stationary wheels having representative deformable tires were found to influence the vertical asymmetry of the wake. Moreover, there exists a mean merging between the rear wheel wakes and the model wake which was identified as a key enabler for local interactions giving rise to a strong drag penalty. This was extended further in [Wang \(2019\)](#) by perturbing the model wake using a pair of 2-D circular or D-shaped obstacles in the underflow. The drag was found to be very sensitive to the distance between the obstacles and the base. However, the underlying interaction mechanisms remain to be analyzed in more detail.

## 1.4 Objectives and outline of the thesis

This brief literature review was focused on bluff body wakes and their sensitivity to various kinds of parameters and perturbations. In each subsequent chapter, the literature review is expanded to address various specific concerns from an industrial perspective. Based on these previous studies, several key features of wheel-vehicle interactions and their consequences for drag are focused on in the manuscript.

- For a road vehicle, flow separations occur all around the vehicle and are of a multi-scale nature. The separation regions and the interactions between them are direct or indirect sources of aerodynamic drag. This is particularly the case when considering the interactions between the wakes of the wheels and the wake of the vehicle as demonstrated by [Wang \(2019\)](#). Locally at the scale of the wheels, the merging of the rear wheel wakes with the vehicle wake was found to drive a local interaction and give rise to a strong drag penalty. However, the flow mechanism leading to this drag penalty still remains to be revealed. A further investigation of the mechanism would allow better optimization of the aerodynamic efficiency and promote the design of new drag-reduction devices.
- An important property of the 3-D wake behind square-back bluff bodies is the presence of large-scale asymmetries which is very sensitive to small changes in flow perturbations or geometrical parameters. The presence of the wheels and their characteristics<sup>7</sup> have been found able to influence greatly these asymmetries ([Pavia & Passmore, 2017](#); [Pavia et al., 2020](#); [Wang et al., 2020](#); [Su et al., 2023](#)). However, a detailed investigation is still needed for

---

<sup>7</sup>The shape and the state of the wheels (rotating or stationary).

further consideration of this feature in the aerodynamic development of road vehicles. This means that the consequences of this feature for the drag require further investigation.

- Road vehicles are designed to fulfill different needs. This means that the shapes of the main vehicle body and wheels can be varied greatly. Therefore, the model dependency (both main body shape and wheel shape) of wheel-vehicle interactions is another decisive factor to be considered.

The manuscript is organized as follows to offer a refined grasp of wheel-vehicle interactions and their impact on drag.

Following the literature review in this chapter, Chapter 2 outlines the experimental methods utilized in the subsequent investigations of the manuscript. The chapter covers the model geometry, the mounting of the model in the wind tunnel, and the measurement techniques employed. Additionally, it includes a description of how the wheels are integrated into the model.

Chapter 3 introduces briefly the features of the natural flow around the square-back Windsor body without wheels. In particular, the wake dynamics and its time-averaged statistics are investigated. This flow serves as the baseline for the forthcoming chapters where the wake is greatly modified by the presence of wheels.

Chapter 4 is dedicated to investigating the wheel-vehicle interactions in a model situation, taking inspiration from Wang (2019). We perturb the wake of the square-back body by placing, in the underflow, a pair of streamlined “D-shaped” obstacles. The obstacle width and the relative distance from the obstacles to the base of the body are systematically varied to perform a sensitivity study and to provide scaling laws for the drag. In addition, extensive measurements of pressure and velocity fields are taken to elucidate the drag generation mechanism at the obstacle scale and to provide a physical model connecting this mechanism with drag changes.

In Chapter 5, rotating wheels are introduced to the square-back body to uncover the salient features of wheel-vehicle interactions and their consequences for drag. A systematic variation of the initial wake asymmetries allows a detailed assessment of the global effects of the wheels on the wake equilibrium and the drag. The length of the model is further varied in order to provide different local interaction strengths between the rear wheels and the body wake. This approach reveals the same drag generation mechanism observed in Chapter 4 using modeled obstacles.

Chapters 6 and 7 are structured in order to provide more general ideas. The influence of wheel geometry on the wake and drag of the square-back body is investigated in Chapter 6. The wheel shoulder radii at the front and rear axles are considered separately or together. The systematic variation of the radii and several additional parameters (distance between the rear wheels and the base  $l$ , mean vertical asymmetry of the vehicle wake) reveals complex interactions between three players: the front wheels, rear wheels, and the vehicle wake. The understanding of these interactions provides a scaling law linking the front wheel properties to the drag changes and a physical model describing the phenomenon. In Chapter 7, the dependency of wheel-vehicle interactions on vehicle shape is investigated. Based on a  $20^\circ$  fast-back Windsor body, additional measurements repeating the investigations in previous chapters using a square-back geometry are carried out. By comparing the results from the two different vehicle shapes, the aim of this chapter is to show the similarities and differences in wheel-vehicle interactions: which feature can be generalized and which feature needs to be considered specifically.

In Chapter 8, we conclude by summarizing the main findings and offering a glimpse into future work that could enhance and broaden the present work.

## Chapter 2

# Experimental methods

---

A description of the experimental setup is given in this chapter. We first outline the simplified vehicle model and the wind tunnel used. Subsequently, the mounting of the model in the test section of the wind tunnel is presented. This part also includes a description of how the wheels are integrated into the model. Finally, the measurement techniques, including pressure, force and velocity measurements, are given in detail.



## Contents

<b>2.1</b>	<b>Model geometry</b>	<b>14</b>
<b>2.2</b>	<b>Experiments setup</b>	<b>15</b>
2.2.1	Wind-tunnel facility	15
2.2.2	Model setup in the test section	16
2.2.3	Wheel setup	18
<b>2.3</b>	<b>Measurement techniques</b>	<b>20</b>
2.3.1	Pressure measurements	20
2.3.2	Aerodynamic force measurements	23
2.3.3	Velocity measurements: particle image velocimetry	23

## 2.1 Model geometry

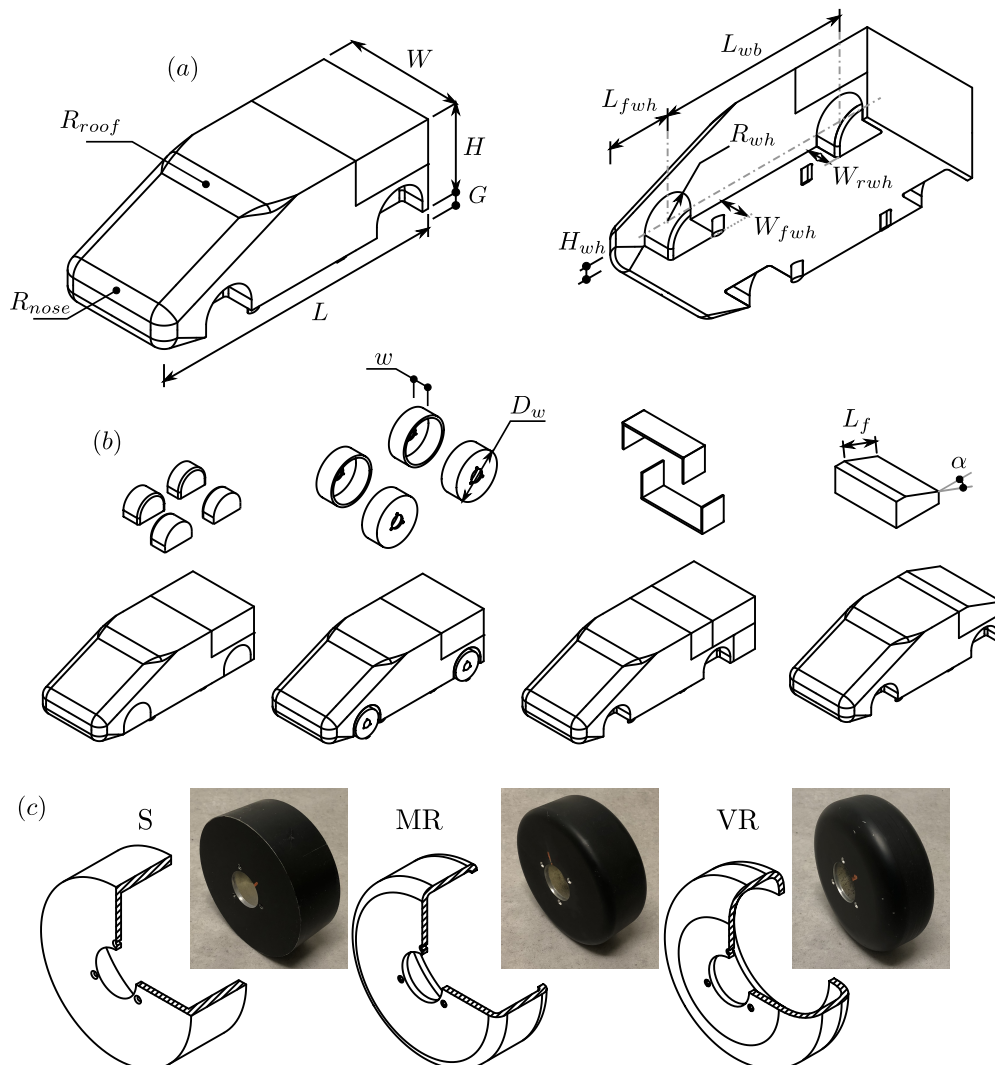


Figure 2.1: Model geometry. (a) Isometric views of the model and the geometrical dimensions. (b) Accessories for adapting the model to different experimental setups. (c) Isometric views of three sets of wheels. S, MR and VR denote, respectively, sharp-edged, medium-rounded, and very-rounded shoulder wheels.

The bluff body studied in the present work is based on the Windsor model (Le Good & Garry, 2004), which features a rectangular cross-section, a slanted front-end with the leading edges

Parameter	Symbol	Value [mm]
Height	$H$	289
Width	$W$	389
Length	$L$	986 - 1146.8
Nose radius	$R_{nose}$	50
Roof radius	$R_{roof}$	200
Ground clearance	$G$	50
Wheelhouse height	$H_{wh}$	35
Front wheelhouse depth	$W_{fwh}$	96
Rear wheelhouse depth	$W_{rwh}$	76
Front wheelhouse location	$L_{fwh}$	242
Wheelbase	$L_{wb}$	637
Wheelhouse radius	$R_{wh}$	85
Wheel diameter	$D_w$	150
Wheel width	$w$	55
fast-back length	$L_f$	222
fast-back angle	$\alpha$	20°

Table 2.1: Main characteristics of the blunt body used in this study. All the geometric parameters are explicated in figure 2.1.

rounded to prevent massive separation. Our investigations on the effects of wheels are enabled by the proposition of Pavia & Passmore (2017), who introduced four wheelhouses to the original Windsor model<sup>1</sup>. Figure 2.1(a) depicts the geometry of the model. This simplified geometry, especially the parallelepiped rear section, greatly reduces the complexity of the flow field. This allows us to focus on the interactions between the wheels and the main body.

Different sets of accessories (see figure 2.1b) are designed to adapt the model to different experimental setups. First of all, the treatment of the wheelhouses constitutes two crucial test groups in this study. By plugging the wheelhouses, the standard Windsor body, which serves as the baseline case for this study, is obtained. On the other hand, with reference to the baseline cases, the effects of the wheels are investigated by installing four wheels in the four wheelhouses, respectively. A detailed description of how the wheels are placed is given later in §2.2.3. On top of these two test groups, the length of the body  $L$  is varied to give different interaction strengths between the wheels and the wake of the body (the range of the body length is given in table 2.1). This is achieved by using several sets of metal plates. Finally, the rear section of the body can be modified, our choice is a  $\alpha = 20^\circ$  fast-back with the aim to check the model dependency of the main conclusions. Table 2.1 summarizes the dimensional characteristics of the model and its accessories.

To examine the effects of wheel geometry, we design three types of wheels that vary in their shoulder radius. These wheels, denoted as S, MR, and VR, correspond to sharp-edged, medium-rounded, and very-rounded shoulder wheels, respectively. They are machined from solid aluminum and have a hollow shape to reduce inertia. The shoulder radii are set at 0,  $0.15w$ , and  $0.3w$ , where  $w$  denotes the width of the wheels. These values were chosen to reflect different types of tires, including sporty or standard options. For example, The radius of  $0.3w$  is designed based on the average of several standard tire shoulder radii found in the market (e.g. 205/55R16 and 235/55R19).

## 2.2 Experiments setup

### 2.2.1 Wind-tunnel facility

The experiments are performed inside the test section of a subsonic wind tunnel (*Soufflerie béton S620*, ENSMA, Poitiers, France). A global view of the facility is given in figure 2.2. Along the

<sup>1</sup>The model and all the accessories were manufactured at Pprime institute. We are deeply indebted to Prof. M. Passmore and Dr. G. Pavia for providing the CAD files of the original Windsor geometry with and without wheels.

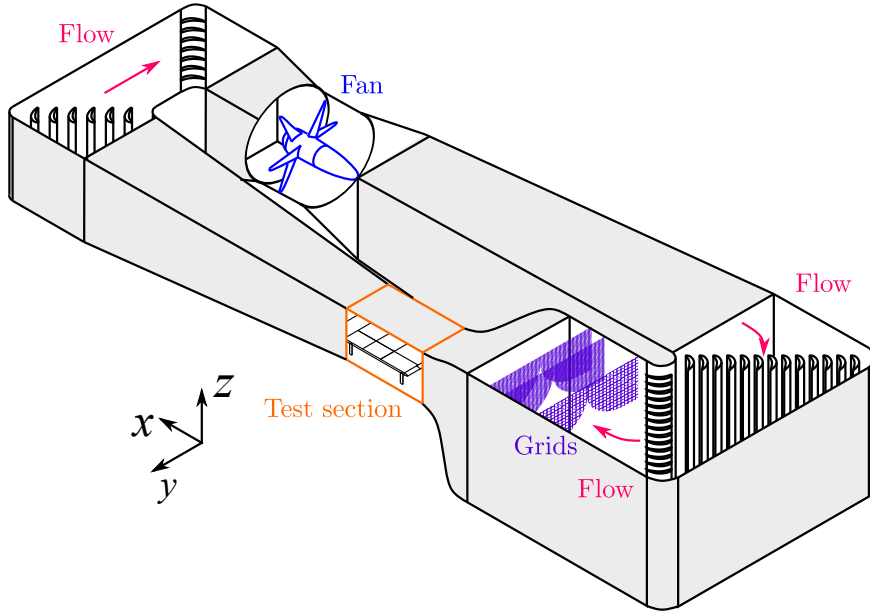


Figure 2.2: Schematic of the wind tunnel facility used for the experiments. The locations of the fan system, the flow conditioning grids and the test section are denoted by different colors. The arrows highlight the flow direction when the wind tunnel operates.

direction of the flow indicated by arrows, the fan system, the flow conditioning grids and the test section are highlighted. The grids are made of one layer of flow straighteners with a grid size of  $50 \text{ mm}^2$  and two layers of wire meshes with grid sizes respectively of  $6 \text{ mm}^2$  and  $4 \text{ mm}^2$ . The rectangular test section has an area of  $6.2 \text{ m}^2$  ( $2.4 \text{ m}$  (width)  $\times$   $2.6 \text{ m}$  (height)). The maximum operating velocity in the test section is  $60 \text{ m s}^{-1}$  with flow stability ensured for velocities greater than  $5 \text{ m s}^{-1}$ . Upstream of the test section, a convergence of 7:1 and the flow conditioning grids give the flow turbulence intensity of the order of 0.5% at most operating conditions, with satisfactory flow homogeneity.

### 2.2.2 Model setup in the test section

A detailed view of the arrangement in the test section is given schematically in figure 2.3. Downstream of the convergence, a raised floor spanning the whole width of the test section is used in order to control the boundary layer characteristics upstream the model. The floor is composed of an elliptical leading edge, a flat plate and a downstream flap. An aerodynamic balance connected to a turntable (*Newport RV350-BPE*) is integrated within of floor. The exposed part of these devices to the flow under the floor is carefully covered with several fairings. The model is connected to the balance through four profiled supports. Their hollow shape allows cables from inside the model to pass through. These cables are carefully fixed on the turntable in order to avoid any interference with force measurements and are extended to the bottom of the test section through the fairings.

Before the installation of the model, attention was paid to the system composed of the raised floor and the fairings. The imbalance between the overflow and the underflow has the ability to influence the location of flow stagnation point at the leading edge and the static pressure gradient above the floor. The latter one is of particular importance for the present work since different lengths of the model are considered. To quantify this, a Pitot probe is traversed along a streamwise line located at  $235 \text{ mm}$  ( $0.81H$ ) above the floor and  $400 \text{ mm}$  ( $1.38H$ ) offset from the symmetry plane of the test-section (without the presence of the model). When the angle of the flap  $\gamma$  is regulated to  $2^\circ$  (see figure 2.3), the whole setup is found to give a relatively low pressure gradient ( $d\overline{C_p}/dx = 0.004\text{m}^{-1}$ ) in the region where the near wake of the model is located. For the model wake located at different streamwise locations due to the variation in the model length  $L$ , this pressure gradient can maximally result in a base pressure variation of  $\Delta\overline{C_{pb}} = 6 \times 10^{-4}$  (Based on the method proposed in [Mercker et al. \(2005\)](#)). This slight change does not seem to

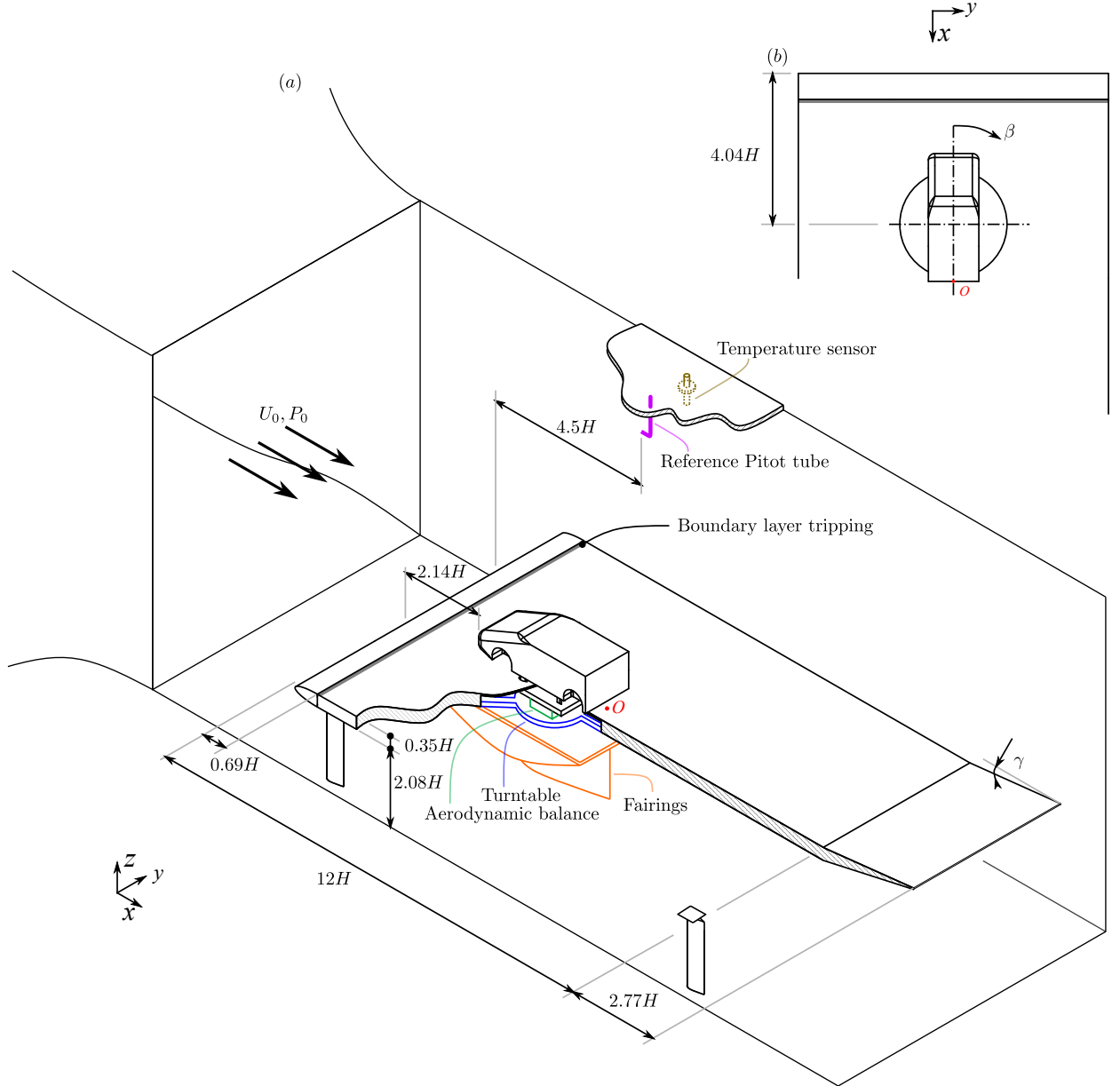


Figure 2.3: Detailed setup in the test-section of the wind tunnel. (a) Isometric view of the model mounting on a raised floor. (b) Top view of the model detailing the rotating center of yaw.

influence the results gathered in the present work because it is far below the uncertainty of the system for surface pressure measurement on the model. Moreover, the blockage ratio of the model's cross-section with respect to the test section area above the floor is 2.4 %. Due to this low value, no blockage corrections are performed (West & Apelt, 1982).

The velocity  $U_0$  and static pressure  $p_0$  of the free stream are measured by a Pitot tube installed at the ceiling of the test section (see figure 2.3). Additionally, the temperature  $T_0$  in the test section is measured by a temperature sensor located near the Pitot tube. Together with the atmospheric pressure, the air density  $\rho$  is calculated. The measurement uncertainties for the free-stream velocity  $U_0$  and for the air density  $\rho$  are, respectively,  $\pm 0.1 \text{ m s}^{-1}$  and  $\pm 0.001 \text{ kg m}^{-3}$ . In the present work, the free-stream velocities considered are  $U_0 = \{15, 20, 25, 30, 35\} \text{ m s}^{-1}$ , corresponding to Reynolds numbers  $Re_H = U_0 H / \nu = \{2.87, 3.82, 4.78, 5.74, 6.70\} \times 10^5$ . Here  $\nu$  represents the kinematic viscosity of air at operating temperature.

The origin of the coordinate system  $O$  (shown in figure 2.3 behind the model) is always located at the intersection point of the floor surface, the rear surface, and the symmetry plane of the model. The axes of the system are defined as streamwise ( $x$ ), spanwise ( $y$ ) and floor-normal ( $z$ )

Configuration	$\delta_{99}$ [mm]	$\delta^*$ [mm]	$\theta$ [mm]	$\delta^*/\theta$	$\delta_{99}/G$
Without model	6.7	1.34	0.81	1.65	0.13
With model	7.9	1.08	0.70	1.54	0.16

Table 2.2: Ground boundary layer characteristics at  $0.86H$  upstream of the model nose (370 mm downstream of the leading edge of the floor) for  $U_0 = 25 \text{ m s}^{-1}$ .

directions. Under this system, the velocity vector is decomposed into  $\mathbf{U} = (U_x, U_y, U_z)$ . Unless otherwise stated, all physical quantities are normalized by any appropriate combination of the model height  $H$ , the free-stream velocity  $U_0$  and the air density  $\rho$  during the measurements. For convenience, the normalized velocity vector is denoted by lowercase letters, i.e.  $\mathbf{u} = (u_x, u_y, u_z) = (U_x/U_0, U_y/U_0, U_z/U_0)$ . The Reynolds decomposition is employed to decompose a quantity  $\mathcal{X}$  into  $\mathcal{X} = \overline{\mathcal{X}} + \mathcal{X}'$ , where  $\overline{\mathcal{X}}$  and  $\mathcal{X}'$ , respectively, denote its time-averaged and fluctuation components.

At 200 mm after the leading edge of the floor (right at the end of the elliptical shape), the boundary layer is tripped with a 15-mm wide belt of  $250\mu\text{m}$ -grain-sized carborundum in order to fix the transition point ensuring the robustness of the experiments. Slightly upstream the model, the boundary layer is quantified by a flattened Pitot tube measuring the mean streamwise velocity. The boundary layer thickness based on 99% of the outer velocity  $\delta_{99}$ , the displacement thickness  $\delta^*$  and the momentum thickness  $\theta$  are gathered in table 2.2 for two different configurations. The thicknesses of the boundary layers  $\delta_{99}$  at this location are about 15% of the ground clearance ( $G = 50 \text{ mm}$ ) which is fixed throughout the experiments. The shape factor of the boundary layer  $\delta^*/\theta$  varies around 1.6, therefore the boundary layer is considered as turbulent.

In appendix A, numerical simulations are conducted to model the experimental setup. The cross-section of the computational domain is the same as that of the region above the raised floor. In addition, the boundary condition is specially treated so that the ground boundary layer in front of the vehicle model has the same thickness as in the experiments.

### 2.2.3 Wheel setup

In this section, we detail the integration of the wheels into the experimental setup presented before. The setup is schematically shown in figure 2.4. Before the installation of each wheel is completed (see figure 2.4a), the location of the wheel is carefully regulated to make it flush to the side of the model, tangent to the floor and longitudinally in the center of the corresponding wheelhouse. This final look can be achieved using two different methods as shown respectively in figure 2.4(b) and (c). The first method involves connecting each wheel directly to the model as shown in figure 2.4(b). This design was originally used in Varney (2020). With this setup, the wheel assembly can be quickly removed and the model can be easily changed, for example to the standard Windsor model. On the other hand, the second method uses the same design as in Pavia (2019) allowing the rotation of the wheels. For this method, the model is not in contact with the wheel assembly as depicted in figure 2.4(c). Inside each wheelhouse, a *Maxon EC 45* brushless motor with an external diameter of 42.8 mm is fixed on the floor through a profiled support. The wheel is then connected to the rotor using a wheel hub.

Under each wheel, a 3 mm recess as shown in figure 2.4(b) is designed for both wheel setups to prevent direct contact between the wheels and the floor. This is particularly important for protecting the motors in the setup involving wheel rotation. A further regulation of this recess is promoted by preliminary pressure measurements using stationary wheels as shown in figure 2.5. The pressure in the wakes of the front and rear wheels is measured by the pressure taps on the underside of the model. When the recesses are sealed either by high-density foams or kraft papers, the pressure in the wakes of the wheels is lower than when the recesses are open. The flow passing through the recesses has a strong influence on the wakes of the wheels, which may consequently influence the interactions between the wheels and the model. Therefore, sealing the recesses using foams or papers is preferable as they better represent real on-road conditions. In addition, although the difference between these two options is minimal in terms of the pressure in the wakes of the wheels, using papers may be problematic because they can deform or wear out

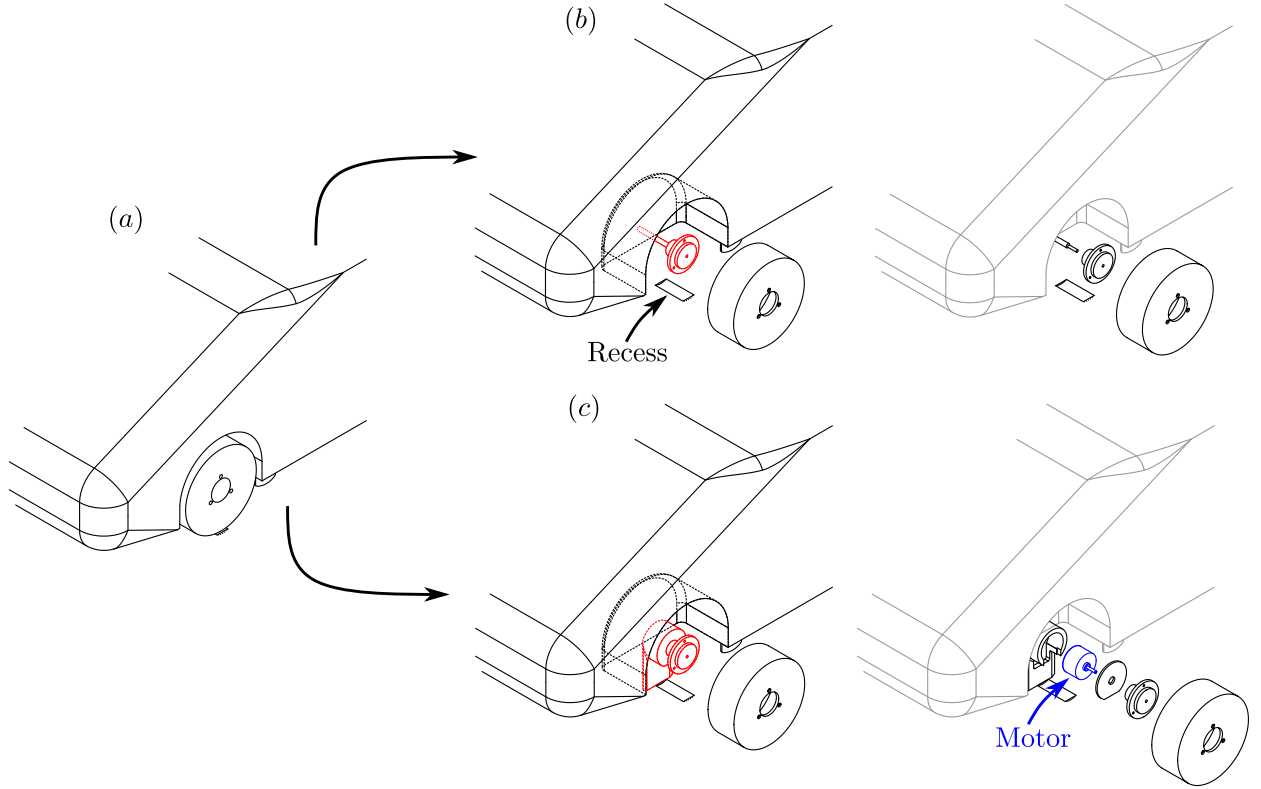


Figure 2.4: Setup for the wheels. (a) A schematic of the final installation, two different methods are designed with (b) and without (c) contact between the model and wheels.

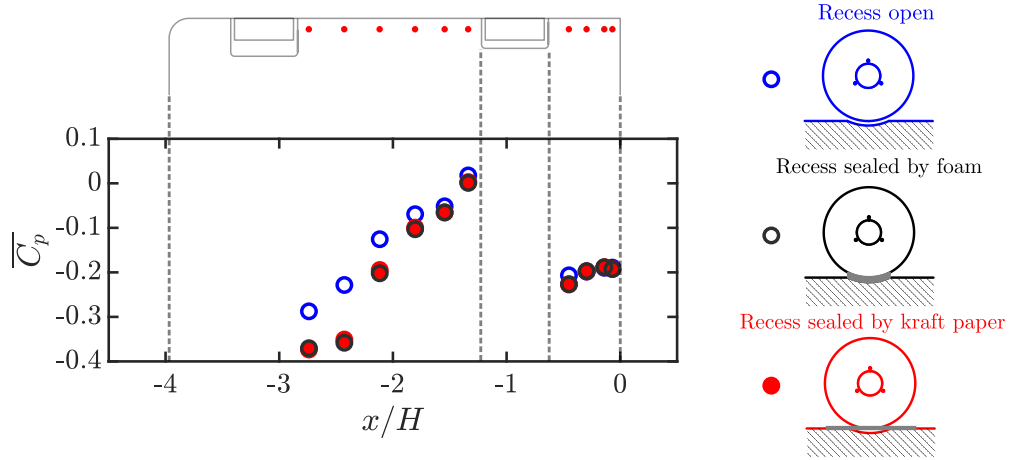


Figure 2.5: Different contact treatment choices for the wheels and their effects on the pressure in the wakes of the front and rear wheels.

quickly due to wheel rotation.

Different contact treatment options are then selected for different wheel setups. For the first wheel installation method when the wheels are connected directly to the model, the option with a foam filling the recess is applied with an additional aluminum tape covering the top of the recess to maintain floor integrity. The tapes are shaped to give always a physical contact between the wheels and the tapes. For the second method involving wheel rotation, the option with a kraft paper is used. This is because the paper provides the minimum friction force for the wheels allowing the motor to work functionally. Moreover, this method is used with special attention to maintaining its effectiveness over time. Indeed, prior to each measurement group, which typically involves no more than one hour of continuous wheel rotation, the paper is replaced to avoid excessive wear. Upon completion of each measurement group, a stationary wheel case is measured. Then, for the measurement of another case, the kraft papers are removed and the recesses are filled using the

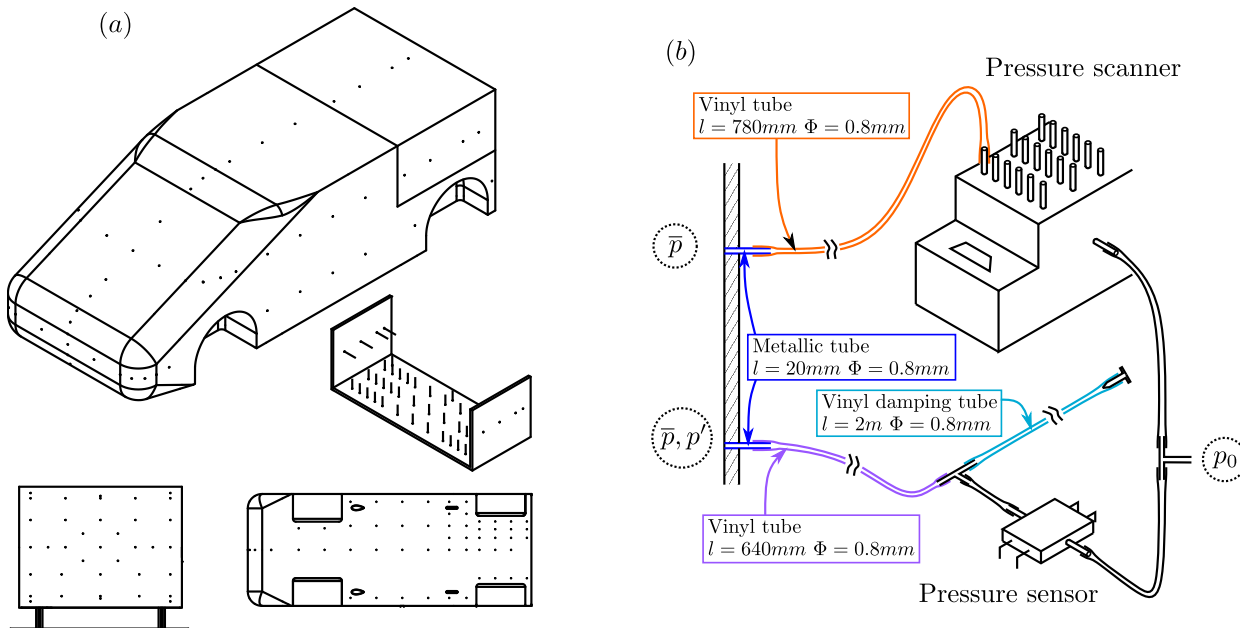


Figure 2.6: Pressure measurement technique. (a) Pressure tap locations on the model and on the metal plates (for longer models). (b) Sketch of the connection between the pressure taps and the two different systems: pressure scanners for mean and long-timescale measurements and pressure sensors for time-resolved measurements.

foams. By comparing these two cases, the degree of wear on the kraft papers is quantified. The mean base pressure is found to vary maximally by  $\sim 0.8\%$  between the cases.

Several factors of the present wheel setup that may influence the results are now discussed. First of all, the floor is fixed and the ground boundary layer reduces the flow momentum under the vehicle compared to moving floor condition (Krajnović & Davidson, 2005; Strachan *et al.*, 2007). Two different vehicles with stationary wheels, namely a sedan and a square-back, were tested by Elofsson & Bannister (2002) to investigate the effect of moving floor (a central belt). It was found to have a very slight effect on the aerodynamic drag. In the present situation where the ground boundary layer is taken care of by the raised floor, we expect a slight change in the wake equilibrium of the vehicle. In addition, the contact patches between the wheels and the floor are not considered due to the non-deformable shape of the model wheels. In Mlinarić & Sebben (2008), the influence of contact patch size on a passenger car was investigated. It was concluded that tire deflection has a limited effect on the drag of the car and that the flow field is only changed locally near the contact patches of the wheels. A similar observation was made in Yu *et al.* (2020). One important hypothesis of this research is that, at first order, the wheel wake development is responsible for the local near-wake interactions between the rear wheels and the main wake. The results presented in the thesis support this hypothesis. While an accurate representation of the contact patch - very difficult at a reduced scale (Wäschle, 2007; Wittmeier *et al.*, 2014) - is needed to obtain quantitative results on a specific car configuration, the use of rigid wheels is justified to focus on the main physical contributions, which is the goal of the present work.

## 2.3 Measurement techniques

### 2.3.1 Pressure measurements

To perform surface pressure measurements, more than 200 pressure taps are designed on the surface of the model and on the prolonged plates as shown in figure 2.6(a). A large portion of these taps is located on the bottom and base surfaces with the rest situated in the model symmetry plane and horizontal planes crossing the nose and A-pillars. A detailed picture of the tapping is depicted in figure 2.6(b). The drilling on the model surface is plugged by a metallic tube having a length of 20 mm with an internal diameter of  $\Phi = 0.8$  mm. Depending on the region of interest, different

	System 1: Pressure scanners		System 2: Differential pressure sensors
Range /Pa	$\pm 1000$	$\pm 2500$	$\pm 250$
Measurement location	Base and near rear wheelhouses	The rest	Base and near rear wheelhouses
Accuracy /Pa	$\pm 1.5$	$\pm 3.75$	$\pm 0.7$
” $\sqrt{C_p} \times 10^{-2}$	$\pm 0.41$	$\pm 1.02$	$\pm 0.19$
” $\%C_B$ (Mean base drag)	$\pm 2$	N/A	$\pm 1$
Frequency response correction		No	Yes, a posteriori
Bandwidth /Hz		$\sim 50$	200
Acquisition frequency /Hz		100	2000
Acquisition length /s		300	300
” $/(H/U_0)$		$2.6 \times 10^4$	$2.6 \times 10^4$

Table 2.3: Summary of the specifications of the pressure measurement systems. The free-stream velocity  $U_0 = 25 \text{ m s}^{-1}$  is taken for the estimations.

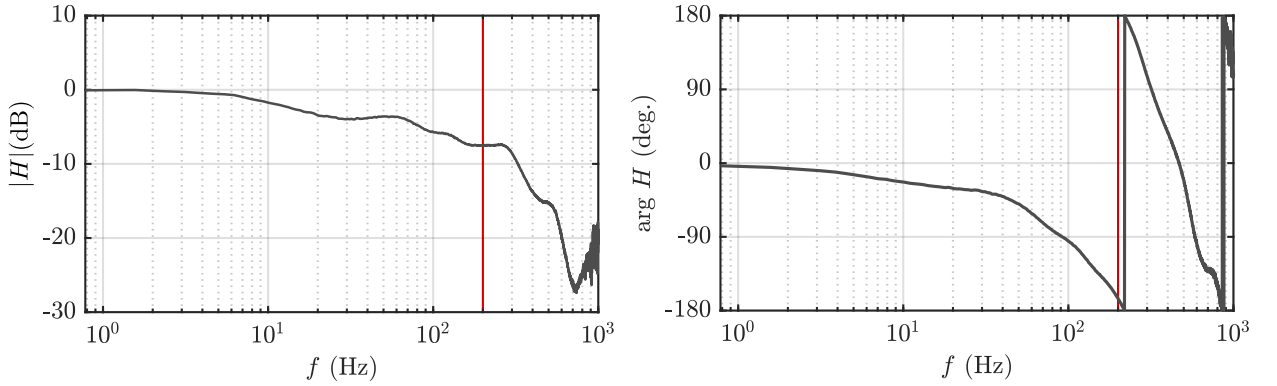


Figure 2.7: Modulus  $|H|$  and phase  $\arg H$  of the frequency response function for the system consisted of the differential pressure sensor and the tubing. Red lines indicate the threshold of 200 Hz, below which frequency response calibration is applied.

sets of pressure taps are used in different chapters. The taps which are not used are closed using a combination of a short Vinyl tube and an end plug to prevent the flow from entering or exiting the inside of the model.

The pressure taps are connected to two pressure measurement systems located inside the model as schematically shown in figure 2.6(b). The specifications for these two measurement systems are gathered in table 2.3. For mean and long-timescale measurements, the pressure taps are connected to two 64-channel *Pressure Systems ESP-DTC-64HD* scanners through 780 mm long vinyl tubes. These two scanners have ranges of  $\pm 1$  and  $\pm 2.5$  kPa. For the pressure taps near the rear wheelhouses and on the base, the small range scanner is used in order to achieve better accuracy. The tubing for this system leads to a cut-off frequency of around 50 Hz. The second system for time-resolved measurements is used for several positions at the region downstream of the rear wheelhouses and on the base. This system consists of 12 *SensorTechnics HCLA 02X5DB* differential pressure sensors connected to a special tubing pipeline. The pipeline consists of a 640 mm vinyl tube from the tap to the pressure sensor, and an additional bifurcation before the sensor towards a 2 m long vinyl tube closed in the end by a plug. This tubing system has been used successfully in previous works for damping the pressure oscillations inside the tubes (Ruiz *et al.*, 2009; Barros, 2015; Li, 2017; Haffner, 2020). The frequency response function of the system consisting of the sensor and the tubing is measured using a dedicated test bench and is shown in figure 2.7. The reference of the bench is the same sensor but with minimized tube length giving a cut-off frequency of 2000 Hz as stated by the manufacturer. Using the frequency response function, the measurements are a posteriori calibrated and corrected in the frequency or time domain to compensate for the pressure distortions induced by the tubings so that the frequency response of the system is flat on the whole frequency range (0-200 Hz) considered in the present study.

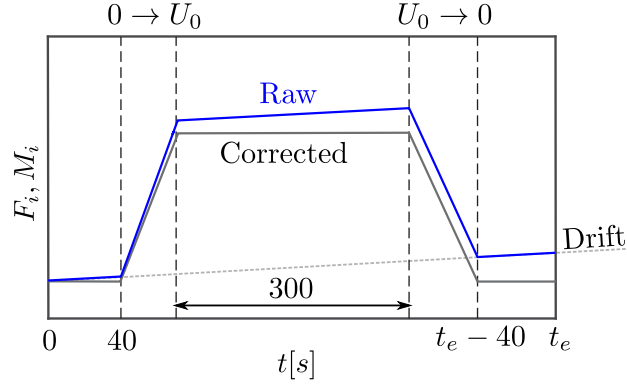


Figure 2.8: Procedure used for performing force measurements and for correcting the drift of the piezoelectric sensors of the balance.

The measurement uncertainties for the two systems are gathered in table 2.3. For the pressure measurements on the base, they are below 2 % or 1 % of the mean base drag  $\overline{C_B}$  (the opposite of the mean base pressure). For all the cases gathered, the duration of the pressure measurements is 300 s. For the baseline case presenting lateral bimodal behavior on a long-timescale of the order of  $O(10^3 H/U_0)$  (Grandemange *et al.*, 2013b), this measurement duration is not sufficient to obtain complete statistical convergence. Nevertheless, this time window is chosen as a compromise between a reasonable duration of the experimental campaigns and a satisfactory convergence of the mean base pressure. For a baseline case having a horizontal bi-stable wake, the standard deviation of mean base pressure values obtained from repeated measurements spanning weeks is found to be less than 2% of the averaged value in chapter 4 and less than 1 % in chapter 5. In order to further reduce the error due to daily variation of the pressure measurement systems, the obtained base pressure values are always expressed relative to the value of the corresponding baseline case (will be introduced in chapter 3) of the same measurement day.

All the pressure measurements are expressed as the pressure coefficient  $C_p$ , which is defined as:

$$C_p = \frac{p - p_0}{0.5\rho U_0^2} \quad (2.1)$$

The reference pressure  $p_0$  is obtained by connecting the reference pressure from the Pitot tube at the ceiling of the test section to the pressure measurement systems as schematically shown in figure 2.6(b).

For detailed investigation of the pressure measurements, we define  $\langle C_p \rangle$  as the spatial-averaged pressure coefficient from the left-hand  $L$  and right-hand  $R$  side of the body in order to reduce the influence of any residual asymmetry of the main wake:

$$\langle C_p \rangle = \frac{1}{2}(C_p(y_i, z_i, t) + C_p(-y_i, z_i, t)). \quad (2.2)$$

In order to quantify the asymmetry of the model wake, the two components of the base center-of-pressure (CoP)  $y_b$  and  $z_b$  relative to the center of the base of coordinates  $(y_c, z_c)$  are defined as:

$$y_b = \frac{\int_{base} (y - y_c) C_p ds}{\int_{base} C_p ds}, z_b = \frac{\int_{base} (z - z_c) C_p ds}{\int_{base} C_p ds}. \quad (2.3)$$

In the same fashion as Varney (2020), the mean horizontal component of the base CoP  $\overline{y_b}$  is used to achieve the zero yaw condition based on a pressure measurement of 10 minutes (i.e.  $5 \times 10^4$  convective time units  $H/U_0$ ). The turntable as shown in figure 2.3(a) is used to yaw the unperturbed body with an increment of  $0.1^\circ$ . The mechanical yaw angle with the minimum  $|\overline{y_b}|$  is found to be  $0.1^\circ$  and is chosen as the zero yaw condition.

### 2.3.2 Aerodynamic force measurements

The aerodynamic force acting on the model is measured by a 6-component balance composed of *Kistler 9129AA* piezoelectric sensors and a *Kistler 5080A* charge amplifier. Prior to the experiments, the balance has been in-house calibrated<sup>2</sup> using known weights and a pulley system. Pure forces, moments, or a combination of both are applied on the balance. The expected forces and moments of the model are covered in the calibration. In our setup (see figure 2.3), the balance is fixed on a 50-mm steel base at the top of the turntable. Above the balance, a 20-mm metal plate is connected by 20 bolts with the tightening torque regulated to the level specified by the balance manufacturer. Then, the model is fixed on the metal plate by four profiled struts. The stiffness of the whole system is ensured with the streamwise deformation during the experiment of approximately 0.075 mm (Haffner *et al.*, 2020b).

The data from the charge amplifier is acquired by a 16-channel *Data Translation DT9857E* data acquisition module at a sampling rate of 200 Hz. A low-pass filter at 10 Hz is applied directly to the charge amplifier to limit high-frequency noise. Giving different models and free-stream velocities, different ranges of the balance are set according to the expected aerodynamic forces. The measurement uncertainty for the balance depends on the range and is smaller than 0.6% of the full range. This represents 1% of the mean drag force  $\overline{F_x}$  for example.

The piezoelectric sensors are prone to drift, which is corrected through a procedure shown in figure 2.8. At the quiescent wind-tunnel condition, forces are recorded for 40 seconds before the fan is started. Once the free-stream velocity stabilizes, pressure measurement begins. After pressure measurement, the fan engine is stopped until the quiescent wind-tunnel condition is reached again, and an additional 40-second force measurement is conducted. The first and last 40 seconds of each force measurement are used to estimate the linear drift of the sensors and to correct the whole measurement. Once this procedure is complete, the forces measured during the time interval of the corresponding pressure measurement are used for time-averaging. This leads to the same conclusion regarding statistical convergence as the pressure measurement.

All the force measurements are expressed in the form of force coefficient, defined as:

$$C_i = \frac{F_i}{0.5\rho U_0^2 HW}, \quad i \in \{x, y, z\}. \quad (2.4)$$

### 2.3.3 Velocity measurements: particle image velocimetry

Particle image velocimetry is performed behind the model ( $x/H > 0$ ) to analyze the near-wake and to understand how it interacts with the wakes of the rear wheels. The system consists of a *Quantel Evergreen 2 × 200 mJ* laser and two *LaVision Imager LX 16 Mpx* cameras. Five different setups are mounted and used independently. Their fields of view (FOVs) are shown in figure 2.9.

The first two big FOVs are located respectively in the symmetry plane ( $y/H = 0$ , figure 2.9a) and in a horizontal plane at the half height of the model ( $z/H = 0.67$ , figure 2.9b). These two FOVs are of two-dimensional two-component (2D2C) setup, capturing the in-plane velocity components. They are planned to understand the global modifications of the model wake.

The other three FOVs are planned to understand the interactions between the wakes of the rear wheels and the model wake. They are located in the symmetry plane of the left wheels ( $y/H = -0.58$ , figure 2.9c), in a plane at half the height of the ground clearance ( $z/H = 0.09$ , figure 2.9d) and in a cross-flow plane 10 mm downstream of the model base ( $x/H = 0.03$ , figure 2.9e). The first one is of 2D2C setup while the rests are of two-dimensional three-component (2D3C, stereoscopic) setup, obtaining three velocity components. For the 2D3C setup, two *LaVision version 3* Scheimpflug mounts are installed between the objectives and the cameras to compensate for the angle between the camera CMOS and the measurement plane, which is around 45°. For all five FOVs, the geometrical ranges and details of the instruments (e.g. objectives.) are documented in table 2.4.

During the measurement of each FOV, The seeding of the flow is introduced downstream of the raised floor using an *Antari X-515* fog generator and recirculates through the tunnel closed

<sup>2</sup>See Li (2017) for a full description.

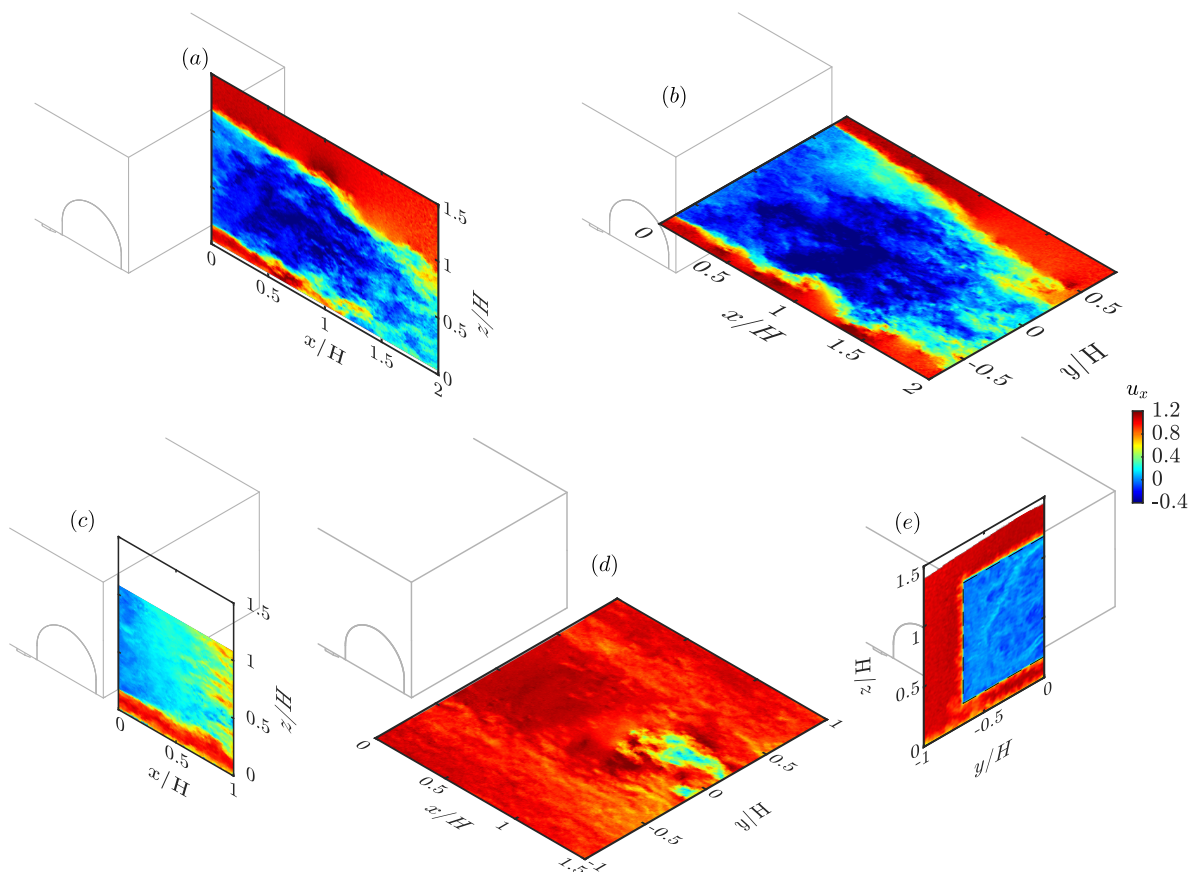


Figure 2.9: Fields of view (FOVs) for PIV measurements in the symmetry plane of the model  $y/H = 0$  (a), in a horizontal plane at the half height of the model  $z/H = 0.67$  (b), in the symmetry plane of the left wheels  $y/H = -0.58$  (c), in the horizontal plane at half the ground clearance height  $z/H = 0.09$  (d), and in a cross-flow plane near the model base  $x/H = 0.03$  (e).

circuit. Particles with diameter of  $1 \mu\text{m}$  are generated by atomization of *Contest Hd* liquid. Special attention is paid to prevent laser light reflection on the surface of the model or the floor. A fine layer of linseed oil ( $\sim 10 \mu\text{m}$ ) is coated on the model and on the floor where the reflection happens. For each measurement no matter the FOVs, 1200 pairs of images are captured at a sample rate of 4 Hz, during the same time interval as the pressure and force measurements. This number of image pairs is satisfactory for statistical convergence of first- and second-order statistics. The *Davis 10.1* software is utilized for processing the image pairs. For all cases, a time-series filter is first employed to eliminate the background from the images. A multi-pass approach is then employed to process the images, using either a final interrogation window of  $16 \times 16$  pixels or  $32 \times 32$  pixels with a 50% overlap, depending on the field-of-views and the quality of the original images. The resulting vectors are subjected to post-processing using a nonlinear filter that eliminates any vectors with outliers greater than twice the standard deviation of their neighboring vectors. Vectors with outliers less than three times the standard deviation are iteratively replaced using a smoothing pass filter of  $7 \times 7$ . The resulting vector spacing and all other details are presented in table 2.4.

	Model symmetry plane	Model half-height plane	Wheel symmetry plane	Half ground clearance plane	Cross-flow plane
Location	$y/H = 0$	$z/H = 0.67$	$y/H = -0.58$	$z/H = 0.09$	$x/H = 0.03$
Setup	2D2C	2D2C	2D2C	2D3C	2D3C
$x/H$ range <sup>3</sup>	[0, 2.7]	[0, 2.5]	[0, 1.0]	[0, 1.8]	-
$y/H$ range	-	[-0.9, 0.9]	-	[-1.1, 1.1]	[-1.6, 1.6]
$z/H$ range	[0, 1.8]	-	[0, 1.1]	-	[0, 1.4]
Laser	<i>Quantel Evergreen 2</i> × 200 mJ				
Camera (s)	<i>LaVision Imager LX</i> 16 Mpx				
Objective(s)	<i>Zeiss</i> <i>Makro-Planar</i> <i>ZF 50 mm</i>	<i>Zeiss</i> <i>Makro-Planar</i> <i>ZF 50 mm</i>	<i>Nikon AF</i> <i>Micro-Nikkor</i> 105 mm	<i>Sigma DG</i> <i>Macro 105 mm</i>	<i>Sigma DG</i> <i>Macro 105 mm</i>
Scheimpflug mounts	-	-	-	<i>LaVision</i> <i>version 3</i>	<i>LaVision</i> <i>version 3</i>
Camera resolution /px <sup>2</sup>	4900 × 3300				
Pixel size /μm	7.4				
$U_0$ /m s <sup>-1</sup>	15,20,25,30,35	25	25	25	25
$\Delta t$ /μs	70,60,50,40,30	50	30	40	40
IW /px	16 × 16 or 32 × 32	16 × 16	16 × 16	16 × 16	16 × 16 or 32 × 32
Overlap /%	50				
Vector spacing / $H$	4.5 or $9.0 \times 10^{-3}$	$4.3 \times 10^{-3}$	$2.3 \times 10^{-3}$	$3.7 \times 10^{-3}$	3.4 or $6.8 \times 10^{-3}$
Sampling rates /Hz	4				
Maximum uncertainty <sup>4</sup> / $U_0$	0.013	0.012	0.011	0.012	0.013
Number of samples	1200				
Measurement time /s	300				

Table 2.4: Details of the fields of view (FOVs) of the PIV measurements, the locations of the FOVs are shown in figure 2.9.

<sup>3</sup>Slight variations present between different measurement campaigns.<sup>4</sup>Based on a maximal uncertainty of 0.1 px in the correlation peak localization.

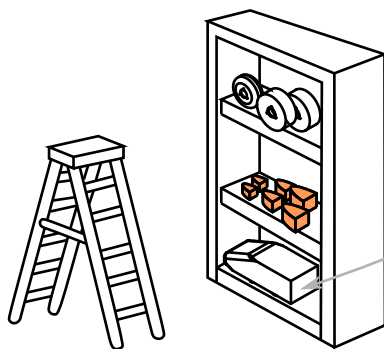


# Chapter 3

## Baseline flow

---

This chapter introduces briefly the features of the natural flow around the standard square-back Windsor body without wheels. In particular, the wake dynamics and its time-averaged statistics are investigated. This flow serves as the baseline for the forthcoming chapters where the wakes are greatly modified by the presence of wheels.



This Chapter

*\*Special thanks to Prof. Passmore and Dr. Pavia for providing the CAD model*

## Contents

<b>3.1 Mean flow around the square-back Windsor body . . . . .</b>	<b>28</b>
3.1.1 Mean pressure field . . . . .	28
3.1.2 Boundary conditions at rear separation . . . . .	29
3.1.3 Mean wake flow . . . . .	30
3.1.4 Variations with Reynolds number and model length . . . . .	32
<b>3.2 Wake reversal and mean asymmetries . . . . .</b>	<b>35</b>

## 3.1 Mean flow around the square-back Windsor body

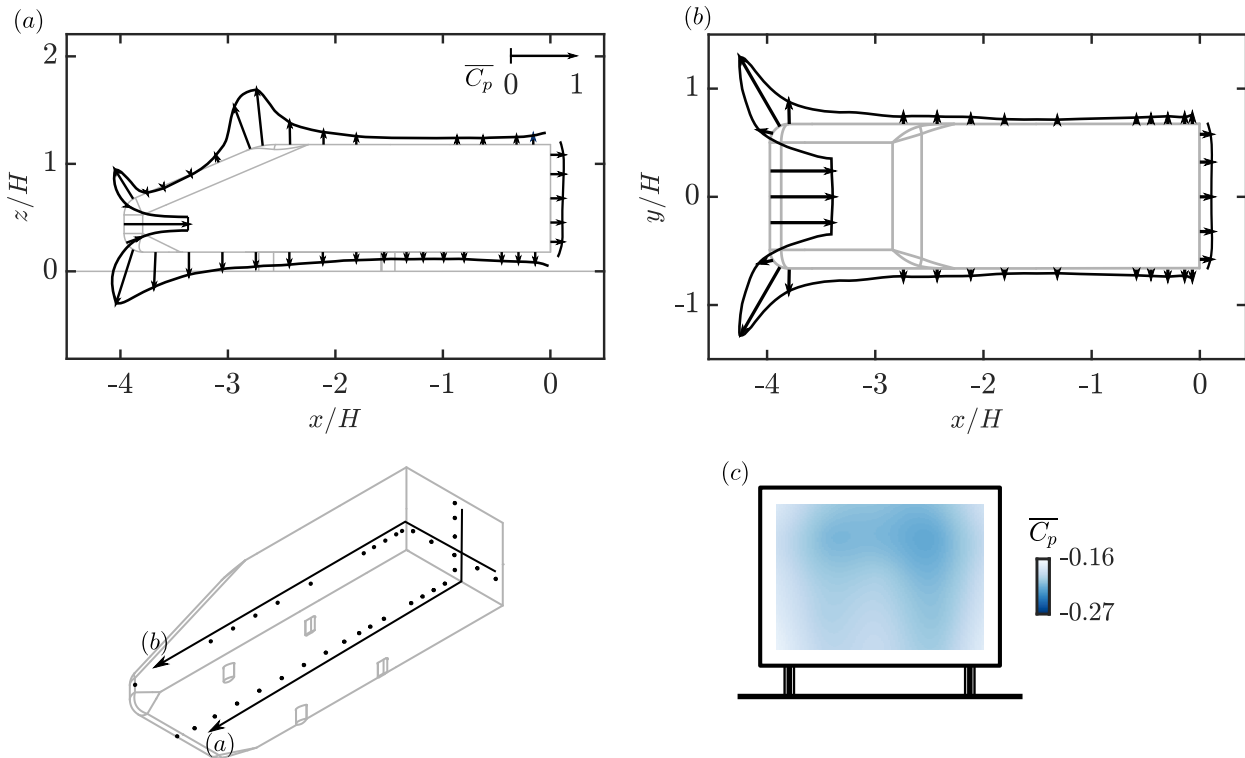


Figure 3.1: For the square-back Windsor body having the longest length  $L/H = 3.97$ : Mean pressure in the symmetry plane  $y/H = 0$  (a), in a horizontal plane at  $z/H = 0.43$  (b) and on the base (c). The free-stream velocity is  $U_0 = 25 \text{ m s}^{-1}$  ( $Re_H = 4.8 \times 10^5$ ). Positive  $\overline{C}_p$  is indicated with arrows pointing inwards.

## 3.1.1 Mean pressure field

The general flow features of the square-back Windsor body are described first based on the body having the longest length  $L/H = 3.97$ . A global idea of the mean flow around the body is given in figure 3.1 by the mean pressure field. At the front of the body, flow stagnation is measured at the front surface having a  $\overline{C}_p \approx 1$ . Slightly downstream of the nose, the curvature at the leading edges and at the roof leads to a sharp drop of pressure and local flow acceleration in the potential flow. This can be seen in both the horizontal plane and the vertical plane. After the pressure drop, adverse pressure gradients are spotted which have the ability to induce flow separation and to form recirculation bubbles (Spohn & Gilliéron, 2002). This kind of recirculation bubble was measured by Grandemange *et al.* (2013b) and Fan *et al.* (2020) based on an Ahmed body and is characterized by a low-pressure plateau inside the bubble. In our case, a continuous pressure recovery is measured after the sharp pressure drop, therefore separation bubbles having a size exceeding the distance between consecutive pressure taps are not expected to exist. After the

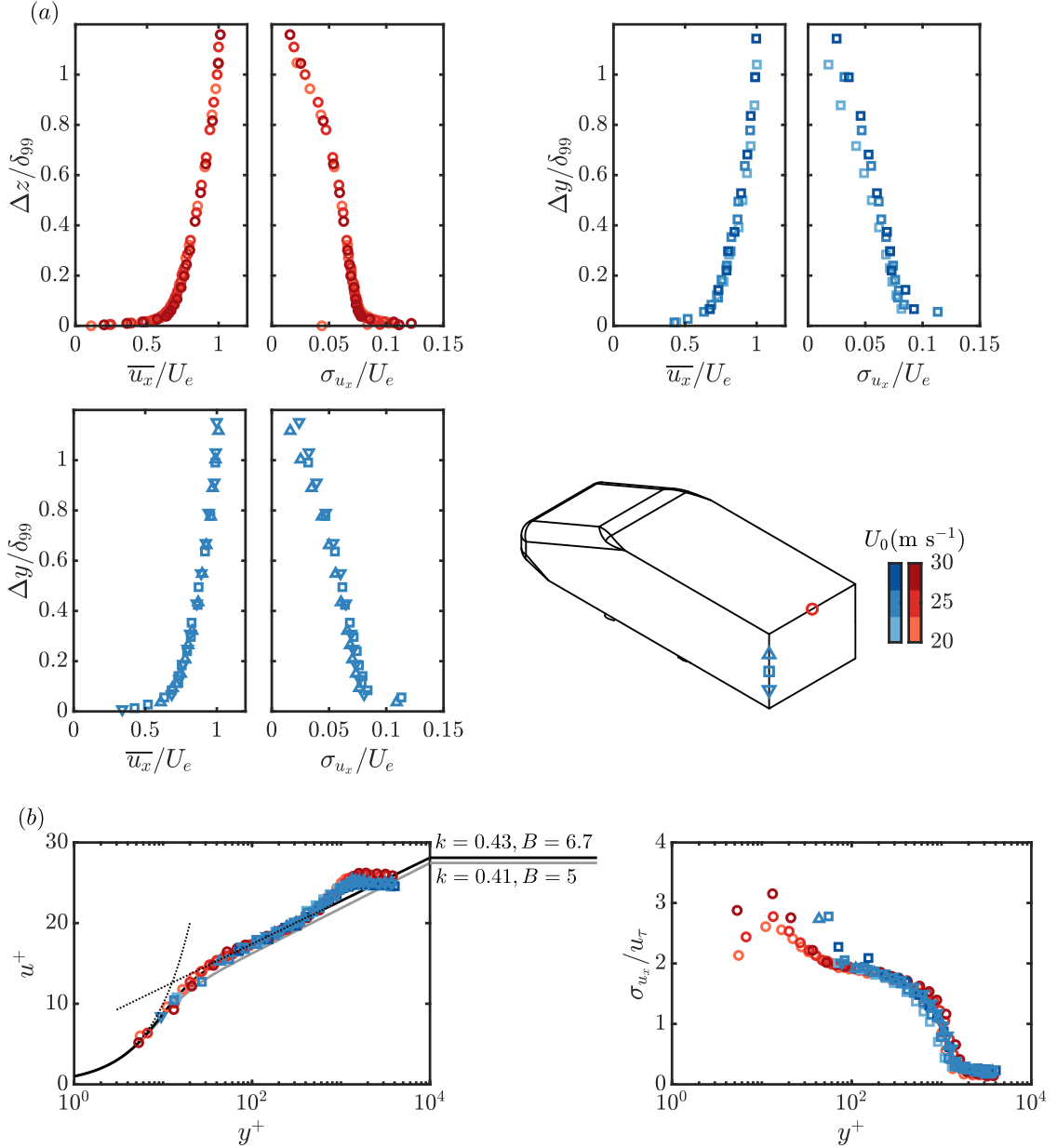


Figure 3.2: For the square-back Windsor body having the longest length  $L/H = 3.97$ : Mean  $\overline{u_x}$  and standard deviation  $\sigma_{u_x}$  of the velocity profiles for the boundary layers at separation. The profiles are scaled in (a) with outer variables (boundary layer thickness  $\delta_{99}$  and external velocity  $U_e$ ) and in (b) with inner variable (friction velocity  $u_\tau$ ). In (b), dotted lines indicate Spalding profile (Spalding, 1961) and solid lines represent Musker profiles (Musker, 1979).

pressure recovery, the pressure maintains a relatively constant value until the approaching of the trailing edges, where the pressure decreases slightly. All these features described here, measured upstream of the base, are crucial in providing the separation conditions at the trailing edges and then in forming the near wake. In addition, the pressure footprint of the wake on the base is presented in figure 3.1(c), it exhibits horizontal symmetry and slight vertical asymmetry.

### 3.1.2 Boundary conditions at rear separation

The boundary layer characteristics at the rear trailing edges of the model are quantified by hot-wire anemometry (HWA) at  $0.5 \text{ mm}$  ( $\sim 0.25\theta$ ) downstream of the model base. Several different free-stream velocities  $U_0$  are considered, with Reynolds number  $Re_H$  ranging from  $3.8 \times 10^5$  to  $5.7 \times 10^5$ . In figure 3.2, velocity measurements characterizing the top and the side boundary layers are respectively colored in red and in blue. They are measured at  $y/H = 0$  for the top boundary layer

Location	$U_0$ [m s <sup>-1</sup> ]	$\delta_{99}$ [mm]	$\delta^*$ [mm]	$\theta$ [mm]	H	$u_\tau$ [m s <sup>-1</sup> ]
T (○)	20	19.3	3.19	2.34	1.36	0.83
T (○)	25	18.2	2.92	2.14	1.36	1.01
T (○)	30	17.5	2.49	1.79	1.39	1.19
S (□)	20	18.5	2.43	1.70	1.43	0.85
S (□)	25	14.1	1.87	1.29	1.45	1.06
S (□)	30	13.0	1.89	1.13	1.67	1.24
ST (△)	25	17.6	2.68	1.87	1.43	1.02
SB (▽)	25	16.6	2.43	1.71	1.42	1.03

Table 3.1: For the square-back Windsor body having the longest length  $L/H = 3.97$ : Characteristics of the boundary layers at separation. T, S, ST and SB represent different measurement locations respectively at top ( $y/H = 0$ ), side middle ( $z/H = 0.67$ ), side top ( $z/H = 0.92$ ), and side bottom ( $z/H = 0.42$ ).

and at several locations  $z/H = [0.42, 0.67, 0.92]$  for the side boundary layer. The characteristic quantities of the boundary layers are gathered in table 3.1.

In figure 3.2(a), the time averaging  $\overline{u_x}$  and the standard deviation  $\sigma_{u_x}$  of the streamwise velocity are plotted against the distance from the top ( $\Delta z$ ) or side ( $\Delta y$ ) surfaces of the model. There are normalized respectively by the external velocity  $U_e$  and by the classic boundary layer thickness  $\delta_{99}$ . All the measured profiles depict fully turbulent boundary layers, as also confirmed by the shape factor calculated by  $H = \delta^*/\theta$  that varies between 1.3 and 1.6. Compared to the top boundary layer, a slight Reynolds number dependency is noticed for the side boundary layer. This is probably due to the different upstream developments. For the top boundary layer, there exists a slow transition from the vertical front surface to the horizontal top surface. For the side boundary layer, a sharp transition from the vertical front surface to the side surface is possibly accompanied by a roll-up of A-pillar vortices. Additionally, the vertical asymmetry of the fore-body has a slight influence on the boundary layer characteristics at the trailing edge. This is remarked by the side boundary layer thickness at different  $z/H$  locations (see table 3.1).

The friction velocity  $u_\tau$  is estimated using the method proposed in [Kendall & Koochesfahani \(2008\)](#). The method is based on calculating the value of  $u_\tau$  that best fits the experimental measurement to the Musker boundary layer profile ([Musker, 1979](#)). In the logarithmic region, the Musker profile features the form of the classical log-law:

$$u^+ = \frac{1}{k} \ln y^+ + B, \quad (3.1)$$

where  $u^+ = \overline{u_x}/u_\tau$  and  $y^+ = yu_\tau/\nu$ .  $k$  and  $B$  are respectively  $k = 0.41$  and  $5$  for zero pressure gradient boundary layers. In our situation, the boundary layer experiences a favorable pressure gradient just before the trailing edges (see figure 3.1). Therefore, for the two constants, we refer to the boundary layer measurement by [Morris & Foss \(2003\)](#) slightly downstream of a backward-facing step with  $k = 0.43$  and  $B = 6.7$ . With these two constants, the Musker profile is calculated and then the friction velocity  $u_\tau$  is derived. For all the measured profiles, the profiles with inner variable scaling are then shown in figure 3.2(b). The friction velocity is gathered in table 3.1.

### 3.1.3 Mean wake flow

The wake flow of the model is shown by the time-averaged velocity measurements in the symmetry plane of the body ( $y/H = 0$ ) and in a horizontal plane at the half height of the body ( $z/H = 0.67$ ) in figure 3.3. Downstream of the base, massive flow separation happens at the blunt trailing edges of the body where shear layers are formed. Following the shear layers in the streamwise direction, flow instabilities begin to grow which are crucial in the flow entrainment from the free stream to the wake and the formation of the recirculation region ( $\overline{u_x} < 0$ , denoted by blue region in the figure). At the end of the recirculation region ( $x/H = 1.65$ ), mean streamlines shown in both planes highlight an important flow curvature. A global look at the wake shows perfect symmetry in the horizontal plane thanks to the symmetry of the setup. However, a slight wake asymmetry presents in the vertical plane, probably due to the asymmetry of the fore-body in the vertical

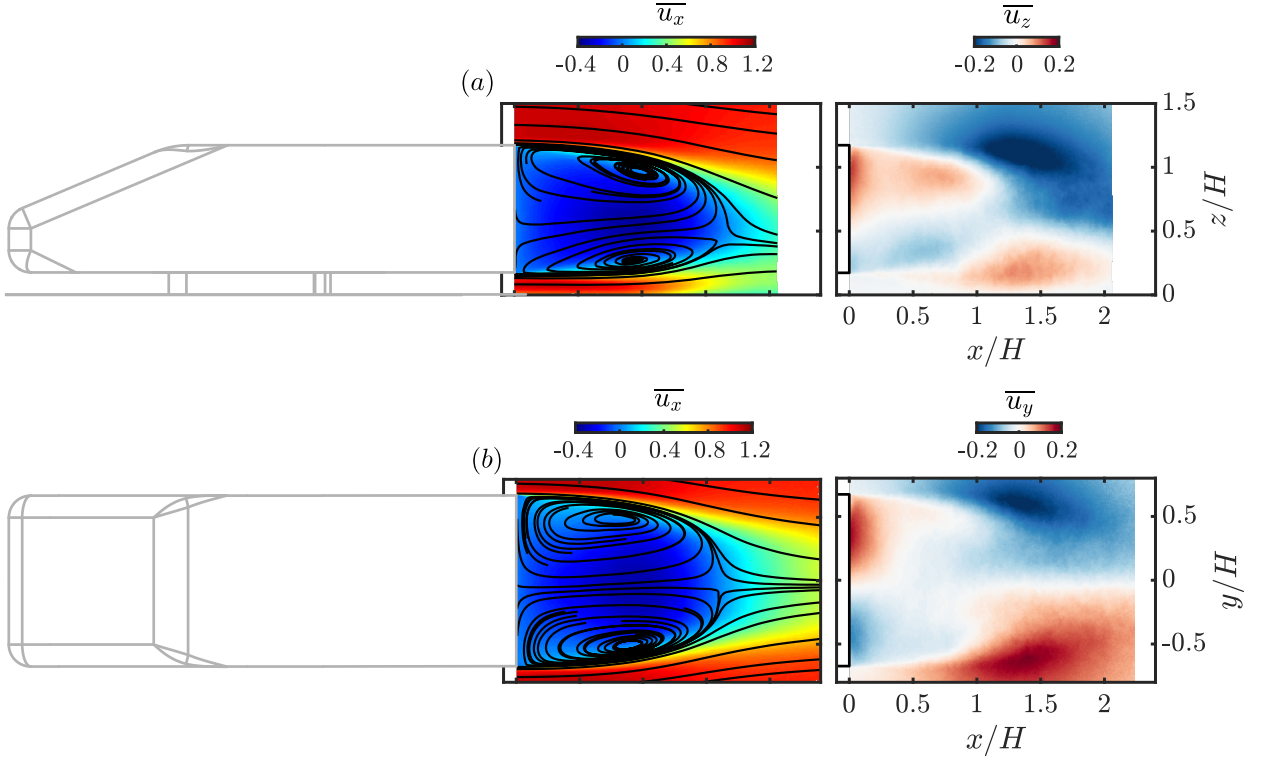


Figure 3.3: For the square-back Windsor body having the longest length  $L/H = 3.97$ : Distributions of mean streamwise velocity  $\overline{u_x}$  (superimposed with mean streamlines) and mean vertical velocity  $\overline{u_z}$  in the symmetry plane  $y/H = 0$  (a) and in the horizontal plane at half height of the model  $z/H = 0.67$  (b).

direction and the presence of the ground. Indeed, even for a model having vertical symmetry, for example the Ahmed body (Ahmed *et al.*, 1984), a slight vertical asymmetry of the wake was observed in various studies (Grandemange *et al.*, 2013b; Bonnavion & Cadot, 2018; Dalla Longa *et al.*, 2019; Fan *et al.*, 2020). In some cases, the wake is of strong vertical asymmetry (Krajnovic & Davidson, 2003; Barros *et al.*, 2016a).

The dynamics in the wake are statistically characterized by the distributions of Reynolds stresses in figure 3.4. The same planes as in figure 3.3 are shown. In the symmetry plane of the model ( $y/H = 0$ , figure 3.4a), the highest values of the stresses are measured along the shear layers, with an important vertical flow fluctuation (denoted by the  $\overline{u'_z u'_z}$ ) at the end of the recirculation region. This points out the important role of the associated flow dynamics in the mean wake closure. On the other hand, in the horizontal plane at  $z/H = 0.67$  (figure 3.4b), apart from the same feature along the shear layers, we observe a stronger flow fluctuation inside the recirculation region. This is particularly clear for the distribution of the normal stress  $\overline{u'_y u'_y}$ , where a high value is measured near the base of the body. In Grandemange *et al.* (2013b), the same observation was made which is the signature of the bi-stable wake dynamics. A detailed description will be given later in 3.2.

A global look at these Reynolds stress distributions confirms the wake asymmetries measured in the mean fields. In the vertical direction, higher stresses are measured in the bottom shear layer. In the horizontal direction, the mean wake symmetry is respected with a symmetric distribution for all the components. These stresses play an important role in the pressure drag at the base as interpreted through the streamwise momentum balance written in Balachandar *et al.* (1997) for 2-D wakes. This momentum balance was also used in 3-D situations, for example in Grandemange *et al.* (2013a) and Liu *et al.* (2021), to emphasize the importance of the mean transport of the fluctuating momentum by turbulent velocity fluctuations.

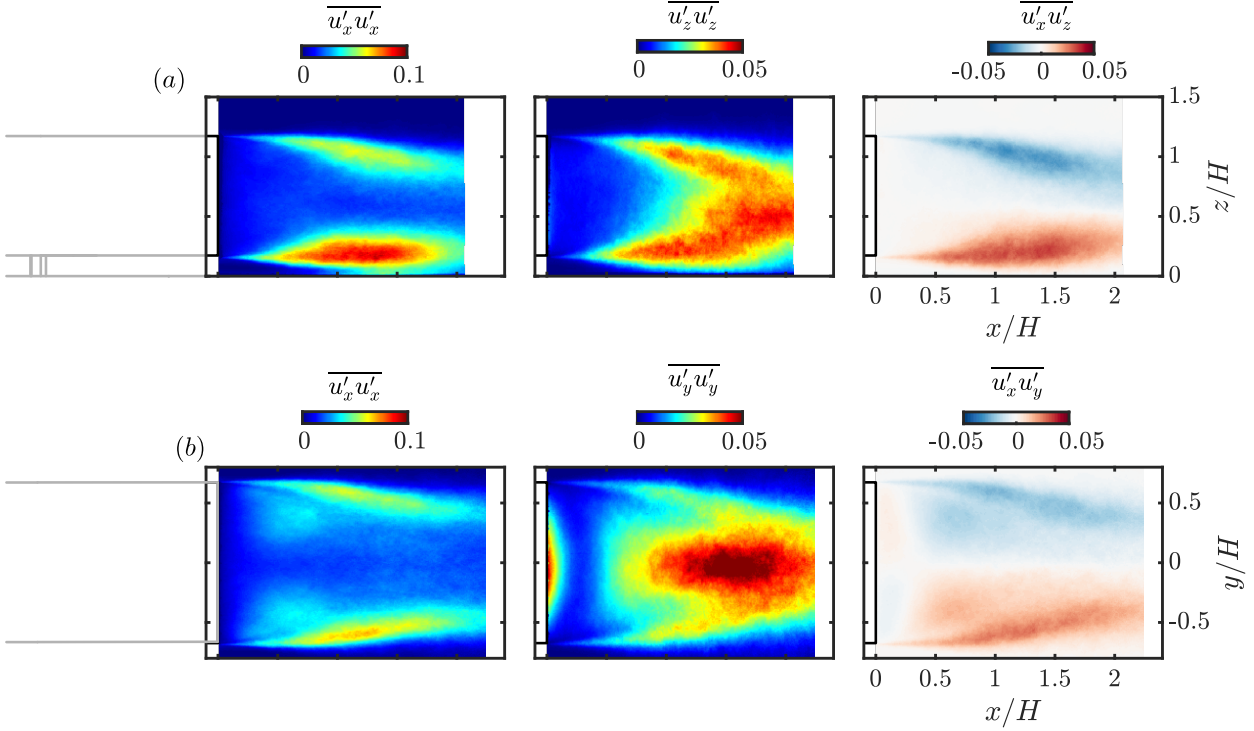


Figure 3.4: For the square-back Windsor body having the longest length  $L/H = 3.97$ : Distributions of Reynolds stresses in the symmetry plane  $y/H = 0$  (a) and in the horizontal plane at half height of the model  $z/H = 0.67$  (b).

$U_0$ [m s <sup>-1</sup> ]	15	20	25	30	35
$Re_H$ ( $\times 10^5$ )	2.9	3.8	4.8	5.7	6.7
$\overline{C_{B0}}$	0.190	0.191	0.193	0.195	0.196
$\overline{C_{D0}}$	0.245	0.235	0.225	0.221	0.219
$\overline{C_{L0}}$	-0.123	-0.126	-0.128	-0.126	-0.126

Table 3.2: Evolution of the mean aerodynamic coefficients with the free-stream velocity  $U_0$  for the model having the longest length  $L/H = 3.97$ .

### 3.1.4 Variations with Reynolds number and model length

We now discuss the variations of the mean wake properties with the Reynolds number and the model length. For the model having the longest length  $L/H = 3.97$ , there is a slight variation of the base pressure with the free-stream velocity  $U_0$  as summarized in table 3.2. The base pressure is denoted by the base drag coefficient  $\overline{C_{B0}}$  (opposite of the mean space-averaged pressure coefficient on the base). Other global forces, the total drag coefficient  $\overline{C_{D0}}$  and the lift coefficient  $\overline{C_{L0}}$  are also shown. We note a slight increase of  $\overline{C_{B0}}$  with increasing  $U_0$ . On the contrary,  $\overline{C_{D0}}$  decreases rapidly from 15 to 25 m s<sup>-1</sup>, which is followed by a slight decrease from 25 to 35 m s<sup>-1</sup>. The difference evolution of  $\overline{C_{B0}}$  and  $\overline{C_{D0}}$  indicates the change of pressure at the fore-body. The lift coefficient  $\overline{C_{L0}}$  denotes a downforce with no systematic variation with  $U_0$ . These coefficients measured here are in good accordance with previous studies of different bluff bodies. The drag and lift coefficients are in good accordance with the measurements by [Howell & Le Good \(2005\)](#) using a Windsor geometry at  $Re_H = 5.2 \times 10^5$  with the same ground clearance, who obtained  $\overline{C_D} = 0.232$  and  $\overline{C_L} = -0.122$ . The slight difference could be attributed to the differences in the support method. [Favre & Efraimsson \(2011\)](#) also obtained a series of  $\overline{C_D}$  using detached-eddy simulations, which ranged from 0.222 to 0.229. The base drag coefficient  $\overline{C_B}$  is also consistent with a large amount of data available from the recent literature using either the Windsor body or the Ahmed body.

The changes of the aerodynamic coefficients with the length of the body  $L/H$  are documented in table 3.3. With decreasing  $L/H$ ,  $\overline{C_{D0}}$  shows no obvious change. However, there is a continuous

$L$ [mm]	986	1009	1037	1064	1092	1119	1147
$L/H$	3.41	3.49	3.59	3.68	3.78	3.87	3.97
$\overline{C_{B0}}$	0.202	0.200	0.199	0.197	0.196	0.195	0.193
$\overline{C_{D0}}$	0.225	0.226	0.226	0.226	0.226	0.225	0.225
$\overline{C_{L0}}$	-0.123	-0.117	-0.124	-0.122	-0.120	-0.128	-0.128
$L_r/H$	1.66	1.66	1.66	1.66	1.65	1.64	1.65

Table 3.3: Evolution of the mean aerodynamic characteristics with the model length  $L$  at  $U_0 = 25 \text{ m s}^{-1}$  ( $Re_H = 4.8 \times 10^5$ ).

increase of  $\overline{C_{B0}}$  by  $\sim 5\%$  from the longest case to the shortest case as plotted in figure 3.5(a). Giving the friction velocity  $u_\tau$  calculated in table 3.2 and simplifying the four side surfaces of the model as flat plates, the skin friction force reduction with the model length variation is calculated and is found to be of the same order of magnitude as the base drag increase. This explains the constant value for  $\overline{C_{D0}}$ .

On the other hand, an examination of the wake shows that the mean wake characteristics remain the same for all the lengths. First of all, the mean recirculation length  $L_r/H$  as shown in table 3.3, defined as:

$$L_r = \max(x)_{\overline{u_x} \leq 0}, \quad (3.2)$$

is used to indicate the flow curvature around the separating streamlines, which is only varied by maximally  $\sim 1\%$ . In addition, it may be argued that the boundary layer thickness at separation is reduced with decreasing  $L/H$ . Thinner boundary layers are found in Rowe *et al.* (2001) and Mariotti *et al.* (2015) having the ability to give stronger flow fluctuations in the wake and therefore a lower base pressure. However, this is not the case in our situation when examining the Reynolds stresses in the wake. Indeed, the distributions of Reynolds stresses are almost not varied with  $L/H$ .

In order to study with another perspective the reason for the base drag changes with model length, a series of Reynolds-Averaged Navier-Stokes (RANS) computations is conducted. Several body lengths under the same boundary conditions as the experiments are selected. A detailed description of the numerical setup can be found in Appendix A. In figure 3.5(a), we notice that the simulations yield smaller base drag  $\overline{C_{B0}}$  than the experiments. This is a major deficiency for RANS simulation in modeling the complex dynamics of 3-D wakes. However, the trend of  $\overline{C_{B0}}$  increase with decreasing  $L/H$  is well captured. This is better depicted in figure 3.5(a) by defining a base drag variant  $\overline{C_{B0}^*} = \overline{C_{B0}} - \overline{C_{B0}}(\max(L/H))$ .

Based on the numerical simulation of the longest model, the mean streamlines in the symmetry plane of the model ( $y/H = 0$ ) are shown in figure 3.5(b). After the flow stagnation at the front surface of the body, we notice a reduction of distance between the nearby streamlines indicating flow acceleration outside the boundary layer in the potential flow region. This is more clearly observed by showing the velocity magnitude  $\overline{u} = \sqrt{\overline{u_x^2} + \overline{u_y^2} + \overline{u_z^2}}$  in figure 3.5(b). In the potential flow region, velocity increases are observed near the roof and around the wake (also around the leading edges but not shown here for brevity).

When the length of the body  $L/H$  is decreased, no obvious change in the wake is noticed in figure 3.5(c). The recirculation length  $L_r$ , for example, is not modified with the length of the body. This observation is in accordance with the experimental measurements. On the other hand, the mean velocity magnitude  $\overline{u}$  presented in figure 3.5(d) shows that the flow acceleration region at the roof is situated closer to the base of the body when the body length decreases. Accordingly, it is expected to have a stronger influence on the wake. We further depict the streamwise evolution of the maximum  $\overline{u}$  in figure 3.5(e) for the  $\min(L/H)$  case and the  $\max(L/H)$  case. It is clear that the velocity acceleration regions located at the front part of the vehicle move towards to base with decreasing  $L/H$ . This is accompanied by a slight velocity increase in the potential flow region surrounding the wake (see also the zoom figure in figure 3.5e). Making use of the Bernoulli relationship in the potential flow region, a larger velocity magnitude implies a lower static pressure.

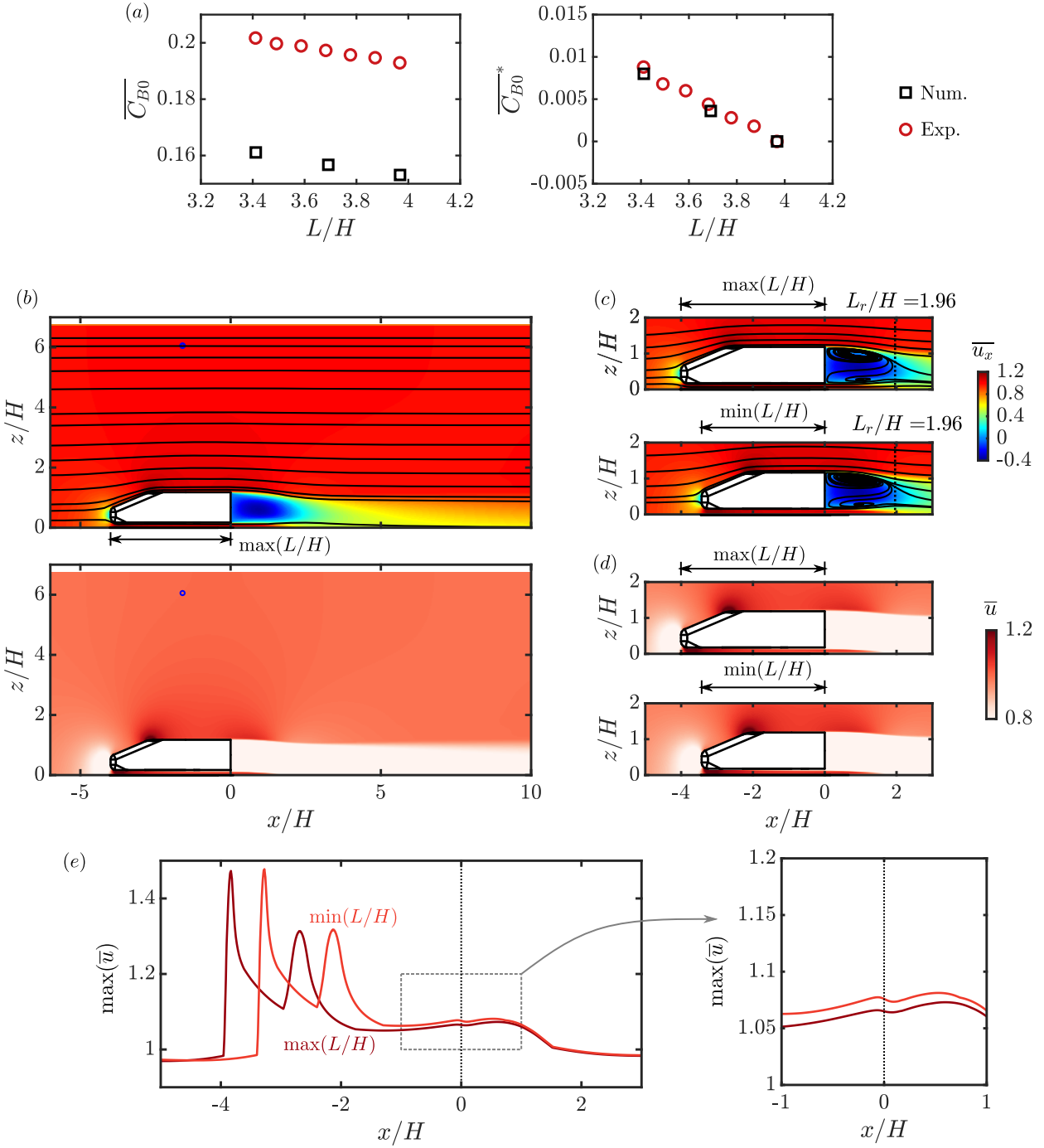


Figure 3.5: Reynolds-Averaged Navier-Stokes (RANS) simulations for the Windsor body with variation in length. (a) Base drag  $\overline{C_B}$  and base drag variant  $\overline{C_{B0}^*} = \overline{C_{B0}} - \overline{C_{B0}}(\max(L/H))$  evolution with model length. (b) Distributions of mean streamwise velocity  $\overline{u_x}$  (superimposed with mean streamlines) and mean velocity magnitude  $\overline{u}$  in the symmetry plane  $y/H = 0$ , the length of the model is the longest model  $L/H = 3.97$ . (c – d) Effects of model length decrease on the  $\overline{u_x}$  and  $\overline{u}$  distributions. (e) Streamwise evolution of the maximum  $\overline{u}$  for the cases in (d).

In the normal direction of the separating streamlines surrounding the wake, the momentum balance (Bradshaw, 1973) is written as:

$$\frac{\partial \overline{C_p}}{\partial n} = 2\overline{C_{u_s}^2} - 2\frac{\partial \overline{u_n' u_n'}}{\partial n}, \quad (3.3)$$

where  $\overline{u_s}$  and  $\overline{u_n' u_n'}$  are respectively the tangential velocity and Reynolds stress of the normal velocity.  $C$  is the local curvature of the separatrix. This balance guarantees that if the wake

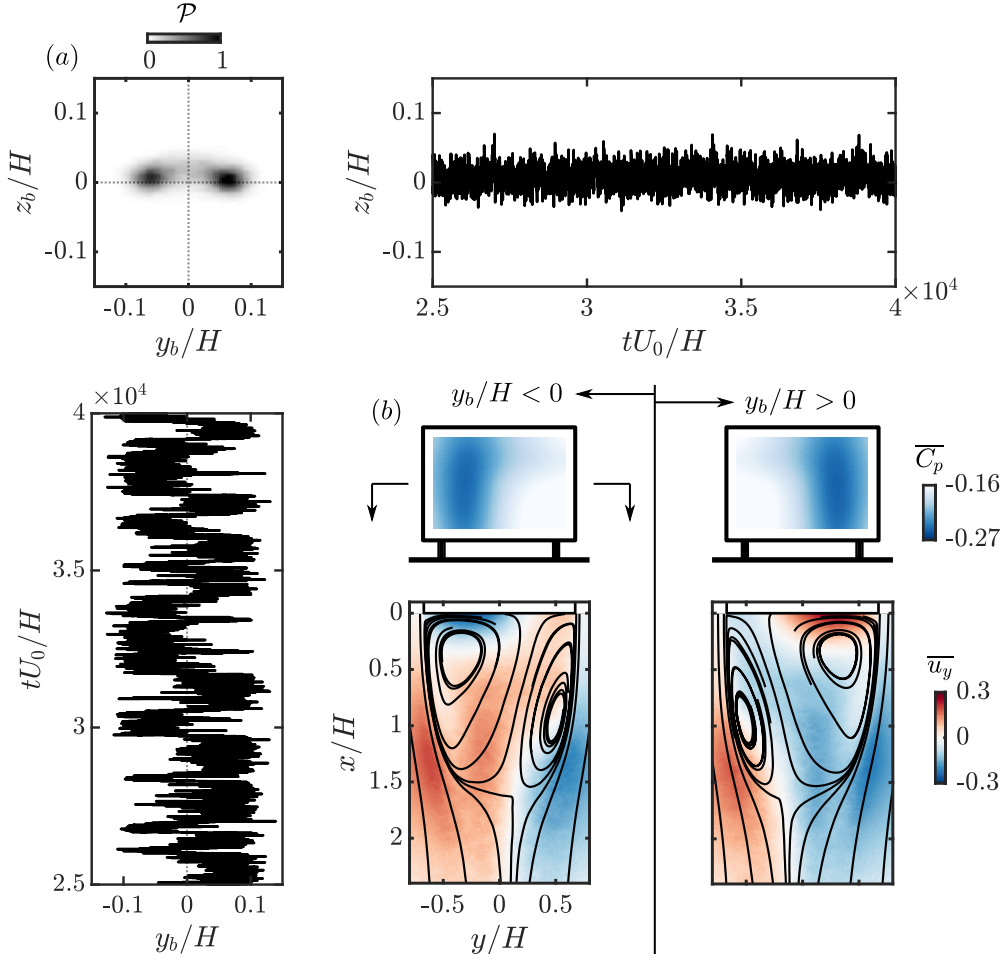


Figure 3.6: For the square-back Windsor body having the longest length  $L/H = 3.97$ : (a) Joint probability density function (p.d.f.) and time evolution of the two components of the base center-of-pressure (CoP)  $y_b/H$  and  $z_b/H$  showing large-scale wake switching dynamics, the two wake states are conditional-averaged based on the sign of  $y_b/H$  in (b) using pressure measurement at the base and velocity measurement at half height of the model.

properties are preserved (right-hand side of the formula), a pressure decrease surrounding the wake induces the same level of pressure decrease inside the recirculation region. Therefore, we believe that this potential flow effect is the main base drag increase mechanism when the length of the body is decreased. In chapter 5 and 6, when the wheels are installed on different baseline models having different lengths, the base drag is always expressed relative to the corresponding baseline case with the same length in order to focus on the role of the wheels.

### 3.2 Wake reversal and mean asymmetries

A common feature for square-back bluff bodies having vanishing vertical wake asymmetry is also observed for the present model. In fact, the mean wake symmetry in the horizontal direction is composed of two equiprobable states presenting strong asymmetry in the horizontal direction. In figure 3.6(a), we show the joint probability density function (p.d.f.) of the two components of the base center-of-pressure (CoP)  $y_b$  and  $z_b$  relative to the center of the base of coordinates  $(y_c, z_c) = (0, G + H/2)$ . The time evolution for the two components is shown in the same figure. At most of the time instants, each wake state is asymmetric in the horizontal direction (denoted by  $y_b/H$ ) imposing a horizontal pressure gradient on the base. The interval between two switching events takes a long time period of  $\sim 10^3$  convection time scale  $H/U_0$ . On the other hand, in the vertical direction,  $z_b/H$  maintains a slight variation relative to the small mean value. This bi-stable behavior was measured for the same Windsor body in Pavia *et al.* (2018) and for the

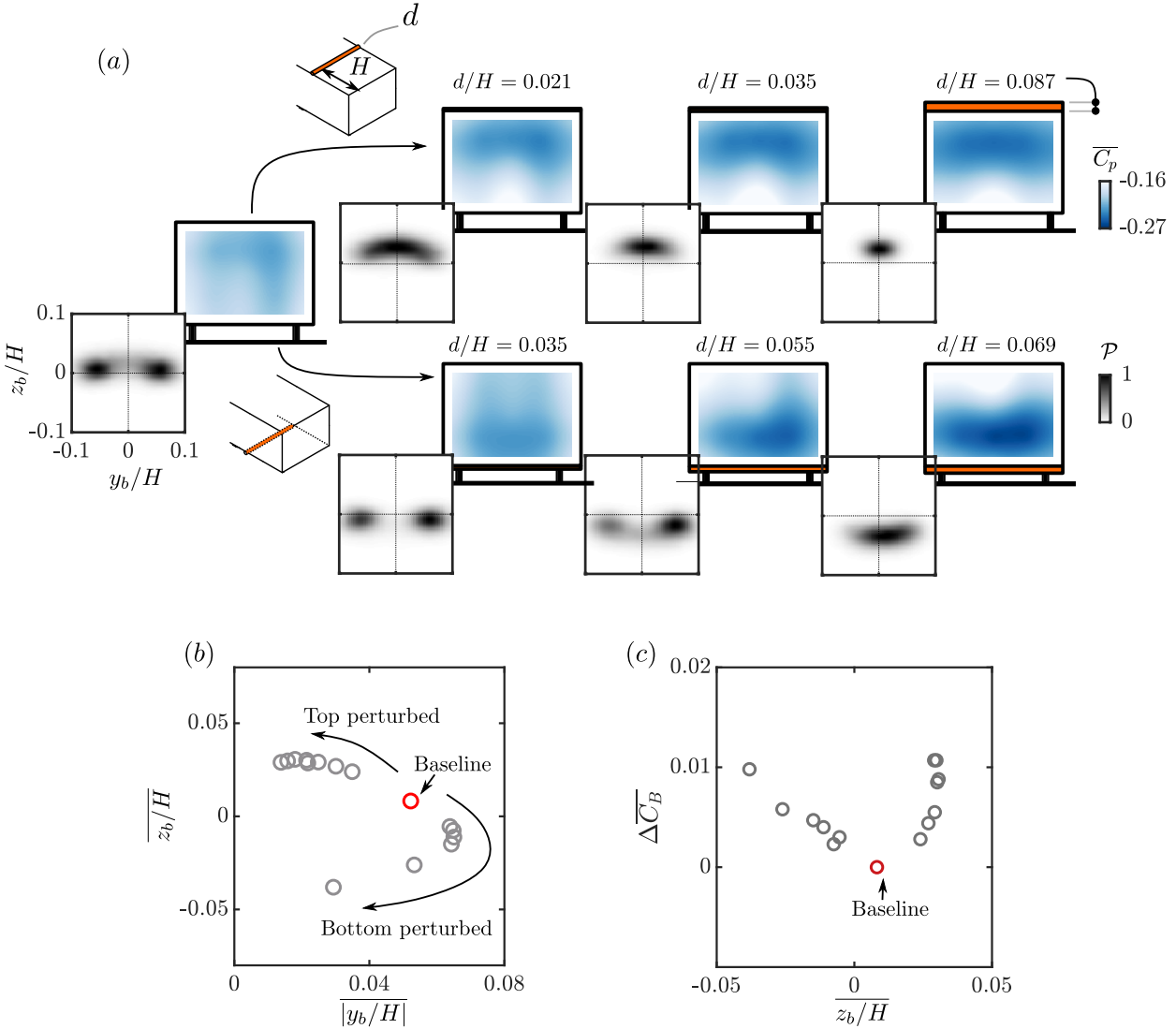


Figure 3.7: For the square-back Windsor body having the longest length  $L/H = 3.97$ : (a) Evolution of the mean base pressure distribution and the joint p.d.f. of the base center-of-pressure with the size of the perturbing cylinder located either at the top or bottom surface of the model. (b) Relationship between  $\overline{z_b/H}$  and  $|y_b/H|$  for the baseline model perturbed with the cylinder. (c) Base drag  $\Delta \overline{C_B}$  relative to the baseline case versus  $\overline{z_b/H}$  for the same cases in (c).

Ahmed body in Grandemange *et al.* (2013b). The associate symmetry-breaking instability originates from the pitchfork bifurcation in the laminar regime and then persists in the turbulent regime (Grandemange *et al.*, 2012). The conditional averaging of the wake states based on the sign of  $y_b/H$  is given in figure 3.6(b). It is shown that the two states are dominated by a large recirculating flow located at the left-hand and right-hand sides of the wake, respectively.

As discussed in chapter 1, the equilibrium of the wake can be manipulated by the changes in upstream condition (Kang *et al.*, 2021), in yaw/pitch variation (Bonnaivon & Cadot, 2018; Fan *et al.*, 2022), and in underflow conditions (Grandemange *et al.*, 2013a; Barros *et al.*, 2017; Castelain *et al.*, 2018). This is especially the case when the wheels are installed. By installing rotating wheels on a Windsor model, Pavia & Passmore (2017) have shown that the vehicle wake is modified from a well-balanced one to an asymmetric one dominated by a bottom recirculating flow.

Barros *et al.* (2017) have shown that a systematic variation of the wake equilibrium can be induced by placing different kinds of perturbations in the underflow. The same evolution is also observed in Bonnaivon & Cadot (2018) by varying the pitch angle. In order to obtain a large span of wake orientations for the reference body, our choice is then to use the same strategy as Barros *et al.* (2017) – see also Haffner *et al.* (2020a, 2022); Legeai & Cadot (2020) – by placing a circular

cylinder of varying diameter  $d$  (from  $d/H = 0$  to  $0.087$ ) spanning the whole width of the baseline vehicle at  $x/H = -1$  on either the top or bottom surface. A large number of cases are selected in order to have a good description of the effect of global equilibrium modification on the reference body.

As shown in figure 3.7(a), the cylinder is of varying diameter and is located at  $x/H = -1$  upstream of the base. From the baseline case described before, placing the cylinder at the top/bottom surface is able to reorganize the recirculation region, imposing a negative/positive pressure gradient in the vertical direction of the base. At the same time, the bi-stable dynamics is suppressed gradually with increasing cylinder size. This bifurcation scenario with a competition between the vertical static asymmetry and the horizontal bi-modal asymmetry is further shown in figure 3.7(b) by the relationship between  $\overline{z_b/H}$  and  $|\overline{y_b/H}|$ . This relationship follows approximately an elliptic shape, as pointed out by the elliptic model proposed by [Bonnaïon & Cadot \(2018\)](#) and used in [Lorite-Díez \*et al.\* \(2020b\)](#).

Finally, this change in wake equilibrium has consequences on the base pressure as depicted in figure 3.7(c) by showing the evolution of the mean base drag  $\Delta\overline{C_B} = \overline{C_B} - \overline{C_{B0}}$  with the mean vertical wake asymmetry  $\overline{z_b/H}$ . The evolution matches with the measurements in [Haffner \*et al.\* \(2020a\)](#) by perturbing an Ahmed body with the same technique. The evolution shows that the baseline case with small  $|\overline{z_b/H}|$  presenting horizontal bi-modal dynamics has the least mean base drag. The reasons for the base drag increase with increasing  $|\overline{z_b/H}|$  were proposed in [Grandemange \*et al.\* \(2013b\)](#) in the framework of induced drag and in [Haffner \*et al.\* \(2020a\)](#) as the interaction between the recirculating flow and the opposite shear layer. [Pavia \*et al.\* \(2018\)](#) suggested that the interaction between the core of the recirculating structures and the base of the model is important in this drag variation.

This database describes the effects of global equilibrium modification on the standard Windsor body. It will be used in the subsequent chapters as a reference to show how the wheels change the equilibrium of the body wake.



## Chapter 4

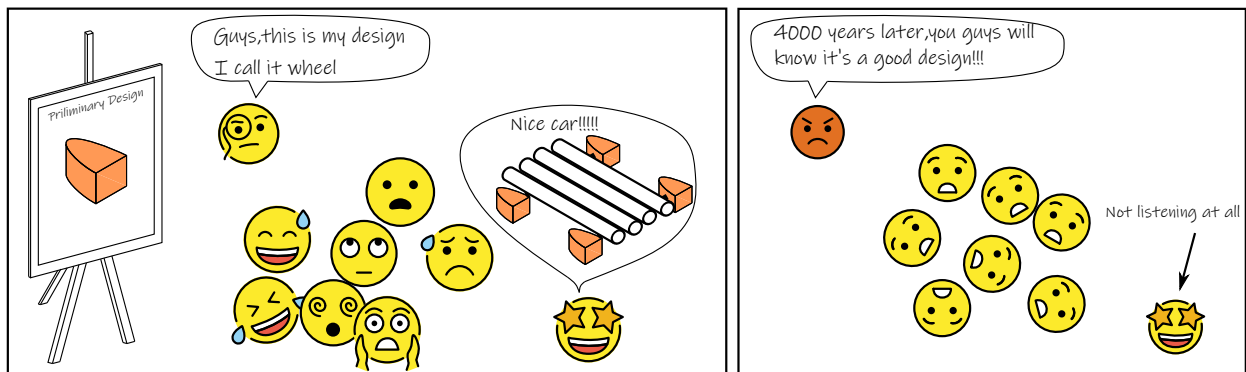
# Simplified modeling for wheels: passive underflow perturbations

A model experiment is conducted in this chapter in order to allow a rigorous parametric study of the modifications in the wake of a car geometry by reference underflow perturbations mimicking the effects of wheels. The three-dimensional near wake of the square-back Windsor body in ground proximity is perturbed by placing a pair of D-shaped obstacles under the body. Five obstacle widths  $d$ , from 12 % to 26 % of the height of the body<sup>1</sup>, are used to perform a sensitivity study of the body's pressure drag by varying the relative distance  $l$  between the obstacle pair and the base. Two successive drag-sensitive regimes are identified for obstacle-to-base distances  $l/d < 2.5$ , where the pressure drag of the body is increased up to 22 %. In different regimes, the flow dynamics measured downstream of the obstacles are found to be very different. When the obstacles are the closest to the base,  $l/d < 1.5$ , the pressure drag changes of the main body are driven by mean merging between the wakes of the obstacles and of the main body, and scale with  $d$ . Contrarily, when the obstacles are located farther from the base  $1.5 < l/d < 2.5$ , the wakes of the obstacles are isolated from the main body wake. Here the dynamics of the obstacle wake drive the pressure drag changes of the main body, which scale with  $d^2$ . In both regimes, we measure a mean mass transfer from the wake of the main body to the wakes of the obstacles. This is the main mechanism responsible for the pressure drag changes. Using our results and reference studies describing the effects of base suction on the pressure drag of bluff bodies, a physical model is proposed to explain the contrasting scalings of the pressure drag increase in the different regimes observed in this chapter.

Most of these results are published in [Bao \*et al.\* \(2022\)](#) in the *Journal of Fluid Mechanics*.

~4000 years ago, ancient Egypt in a different universe

Still need to build the



<sup>1</sup>This gives an underbody blockage ratio of  $2d/W = 0.18$  to  $0.39$ , where  $W$  is the width of the body.

---

**Contents**

<b>4.1</b>	<b>Need for model configurations of wheels</b>	<b>40</b>
<b>4.2</b>	<b>Experimental setup</b>	<b>40</b>
<b>4.3</b>	<b>Global effects of perturbations</b>	<b>42</b>
4.3.1	Base drag sensitivity	42
4.3.2	Pressure fields	44
<b>4.4</b>	<b>Global and local wake modifications</b>	<b>49</b>
4.4.1	Evolution of the near wake of the body	50
4.4.2	Obstacle wake characteristics in different regimes	53
<b>4.5</b>	<b>Further discussions and concluding remarks</b>	<b>56</b>
4.5.1	A momentum exchange model to evaluate the mass exchange effects	56
4.5.2	Concluding remarks	59

---

## 4.1 Need for model configurations of wheels

Even in very simplified reduced-scale model studies using reference academic geometries, it is very difficult to achieve a systematic and rigorous survey of the flow mechanisms driving wheel-wake interactions. For example, for obvious mechanical reasons, it is very difficult to change the width of the wheels and their location relative to the base for the same car geometry. Therefore, there is a need for intermediate model configurations that allow a rigorous parametric study of the modifications in the wake of the body and its base drag by reference underflow perturbations.

The nature of wheel-vehicle aerodynamic interaction was studied in Wang (2019) with a basic question: what are the salient features of the flow perturbations induced by wheels that drive this interaction? Starting from rotating/stationary wheels having representative deformable tires (Wang *et al.*, 2020), it was shown that the momentum deficit created in the underflow by the wheels, in particular the rear wheels, is an important enabler to this interaction. At first order, it is therefore believed that wheels can be seen as underbody perturbations and that the key aerodynamic features are the underflow blockage, the wheel-wake development in the underflow and its interaction with the near wake of the vehicle. It was then proposed in Wang (2019) that wheels can be seen as underbody geometric perturbations. Model obstacles were then introduced in the underflow to mimic the key aerodynamic features, namely the underflow blockage, the development of the wakes of the wheels and their interactions with the near wake of the model. It was observed that the obstacles globally have qualitatively similar effects to the rear stationary/rotating wheels. However, the underlying interaction mechanisms remain to be analyzed in more detail.

In the present chapter, a model situation allowing a precise and systematic study of several critical parameters is designed. The wake of a simplified square-back geometry is perturbed by placing, in the underflow, a pair of streamlined “D-shaped” obstacles of varying width. The two obstacles are mounted at varying relative distance from the base of the body. Our goal is first to analyze how the wake of the body (hereafter named as the main wake) is modified by the wakes of these obstacles, of much smaller size, developing along the underflow. The final goal is to understand how the drag of the body is modified due to the presence of the obstacles. The experimental apparatus used for this chapter are detailed in §4.2. By varying the distance from the obstacles to the base, the modifications in the base drag and pressure fields are presented in §4.3. Then, in §4.4, the velocity fields are further investigated to reveal the interaction mechanisms leading to base drag increase. Finally, in §4.5, discussions based on our quantitative data and previous studies are provided, which are followed by concluding remarks.

## 4.2 Experimental setup

The square-back Windsor body shown in figure 4.1 with the longest length  $L/H = 3.97$  is selected for the sensitivity study in this chapter. In order to perturb the main body wake as well as its drag,

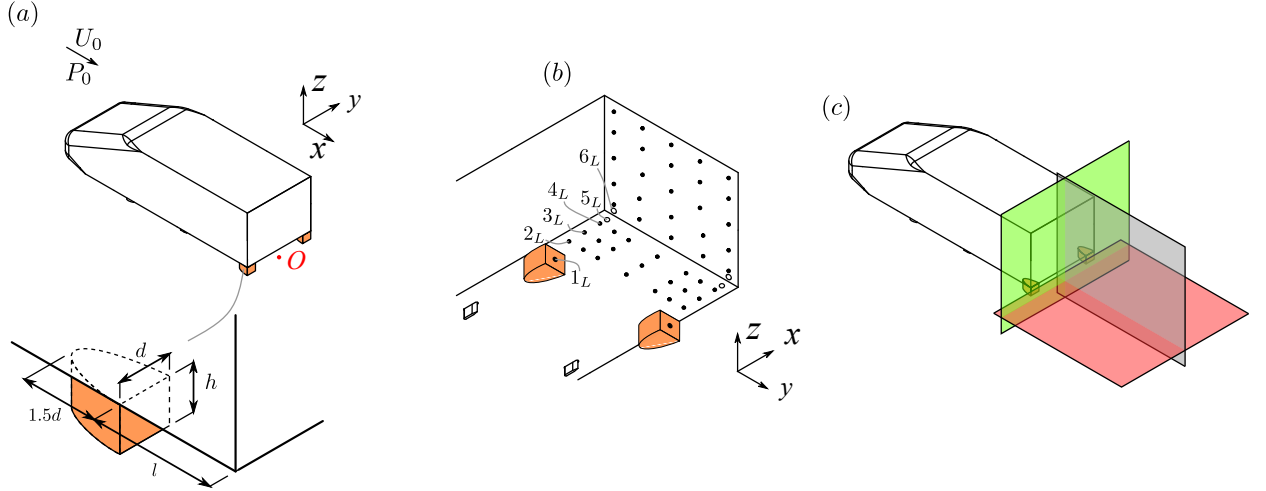


Figure 4.1: Experimental setup. (a) Arrangement of the model and the underflow perturbing obstacle pair. (b) Locations of pressure taps on the base, underside and behind the obstacles. Points indicate locations of mean pressure measurements and circles indicate locations of time-resolved pressure measurements. (c) Particle image velocimetry (PIV) fields of view (FOVs) in the symmetry plane ( $y/H = 0$ , colored in gray), cross-flow plane ( $x/H = 0.03$ , colored in green) and half-ground-clearance plane ( $z/H = 0.09$ , colored in red).

a similar approach to Wang (2019) is used with a pair of obstacles placed upstream of the base of the body, between the underside of the body and the floor (see figure 4.1a). The two-dimensional (2-D) obstacles have a half-elliptical cross-section, whose length is 1.5 times the width  $d$ . This shape is chosen to minimize the influence of unwanted changes in the separation point on the interactions between the obstacles and the main wake. Several obstacle shapes were tested during preliminary measurements using a different square-back bluff body. It was shown that the drag of the body perturbed by obstacles with inertial separation is insensitive to the Reynolds number.

The widths of the obstacles are  $d/H = \{0.12, 0.16, 0.19, 0.22, 0.26\}$  and the height is  $h/H = 0.17$ . The median width  $d/H = 0.19$  is the same as the width of the wheels used in the subsequent chapters. Therefore, the configuration using the  $d/H = 0.19$  obstacle pair is taken as the reference configuration and is subjected to substantial measurements. Between each obstacle and the body, a gap of 1.5 mm exists and is carefully filled with high-density foam to reduce the complexity of the flow and to focus on the interactions between the obstacles and the main wake. This disables the measurements of the aerodynamic force acting on the model. However, the main focus of the present chapter is the modifications in the main wake and therefore the base pressure is sufficient for quantifying the main effects of the obstacles.

The obstacle pair is always placed symmetrically to the symmetry plane of the model, with its rear surface parallel to the base of the body and its left-hand/right-hand side tangents to the left-hand/right-hand side of the body. The degree of freedom of the pair in the streamwise direction is fixed by the obstacle-to-base distance  $l$ , which is defined as the streamwise distance from the base of the obstacles to the base of the body. The parameter  $l$  for all the  $d/H$  configurations ranges from  $0 d$  (flush-mounted to the base) to  $5 d$ .

Unless otherwise stated, all the results presented are collected under a free-stream velocity  $U_0 = 25 \text{ m s}^{-1}$ , corresponding to a height-based Reynolds number  $Re_H = U_0 H / \nu = 4.8 \times 10^5$ , where  $\nu$  is the kinematic viscosity of the air at operating temperature. For some representative test cases,  $U_0 = 20$  and  $30 \text{ m s}^{-1}$  ( $Re_H = 3.8$  and  $5.8 \times 10^5$ ) are also utilized to check the Reynolds number sensitivity.

Two different pressure measurement systems are used to perform surface pressure measurements. The first one for time-averaged and long-timescale measurements uses the pressure scanners. 25 taps on the base and 21 taps on the underside (see figure 4.1b) are used in the present chapter. The taps on the base and on the underside are connected, respectively, to the two scanners with ranges of  $\pm 1$  and  $\pm 2.5$  kPa. For the reference configuration  $d_{ref}/H = 0.19$  with specific obstacle-to-base distances  $l/d = \{0, 1.45, 2.73, 4.91\}$ , two 5.4 m-long tubes are arranged along the

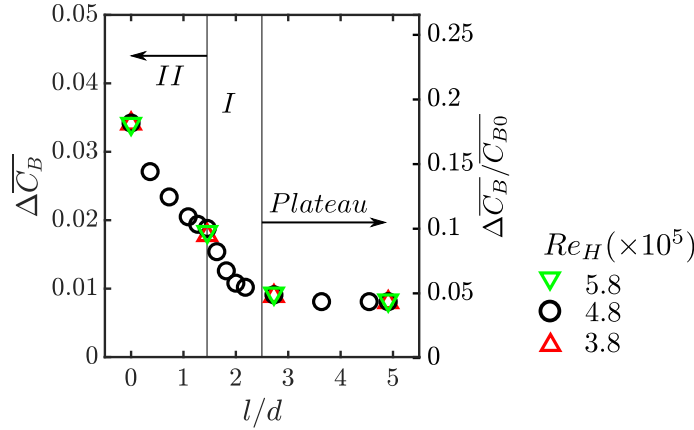


Figure 4.2: Base drag of the body  $\Delta \overline{C}_B = \overline{C}_B - \overline{C}_{B0}$  as a function of the obstacle-to-base distance  $l/d$  for the reference configuration  $d_{ref}/H = 0.19$ .

floor in order to obtain the mean base pressure of the obstacles. The pressure taps for this measurement are located at the center of the base of the obstacles (see figure 4.1b) and the tubes are connected to two differential pressure sensors located outside the test section (*NovaSensor NPH802.50H*). The sensors have a range of  $\pm 2.5$  kPa and an accuracy of  $\pm 5$  Pa. On the other hand, the second system dedicated to time-resolved measurements uses the differential pressure sensors connected to the four pressure taps located on the base and the underside. The pressure taps used extensively in the investigation are numbered as  $n \in [1 - 6]_{L,R}$  as shown in figure 4.1(b).

The velocity fields in the near wake are measured by the particle image velocimetry (PIV) system. Three two-dimensional fields of view (FOVs) are considered as depicted in figure 4.1(c). The first one located in the symmetry plane of the body ( $y/H = 0$ ) is of 2-D two-component (2D2C) setup, obtaining the streamwise  $u_x$  and vertical  $u_z$  velocity components. The other two FOVs are respectively located in a cross-flow plane in proximity to the base of the body ( $x/H = 0.03$ ) and a plane at half the height of the ground clearance ( $z/H = 0.09$ ). These two FOVs are of stereoscopic (2-D three-component (2D3C)) setup, capturing three velocity components.

In order to provide further ideas of the interactions between the obstacles and the main body wake, supplementary Reynolds-averaged Navier–Stokes (RANS) simulations are conducted in appendix A. The present experimental setup is reproduced numerically with the dimensions of the model and the test section respected. Under a free-stream velocity of  $U_0 = 25$  m s $^{-1}$  (the same as  $U_0$  for the main results in this chapter), the reference obstacle pair  $d_{ref}/H = 0.19$  is placed under the body to perturb the main body wake.

## 4.3 Global effects of perturbations: base drag sensitivity and modifications in the pressure field

### 4.3.1 Base drag sensitivity

We present first the base drag variation  $\Delta \overline{C}_B = \overline{C}_B - \overline{C}_{B0}$  with varying obstacle-to-base distance  $l/d$  for the reference configuration  $d_{ref}/H = 0.19$  in figure 4.2. The subscript 0 indicates the unperturbed baseline case. Moving the obstacle pair from the most upstream position  $\max(l)/d$  towards the base, the configuration presents first a plateau with a slight increase in base drag, followed by a drag-sensitive regime with a rapid base drag increase until the flush-mounted position is reached. In the drag-sensitive regime, the maximum base drag increase is  $\Delta \overline{C}_B / \overline{C}_{B0} \approx 18\%$ . This important drag increase indicates a great sensitivity of drag to the obstacle-to-base distance. Therefore the present chapter aims at educing the interaction mechanisms between the wakes of the obstacles and the main wake in the drag-sensitive regime. We also notice that the slope of the monotonous base drag increase experiences a sudden change at  $l/d \approx 1.5$ . A criterion based on the mean and fluctuating properties in the wake of the obstacles, detailed later in §4.3.2, will show that we observe two regimes that are characterized by different interaction mechanisms between

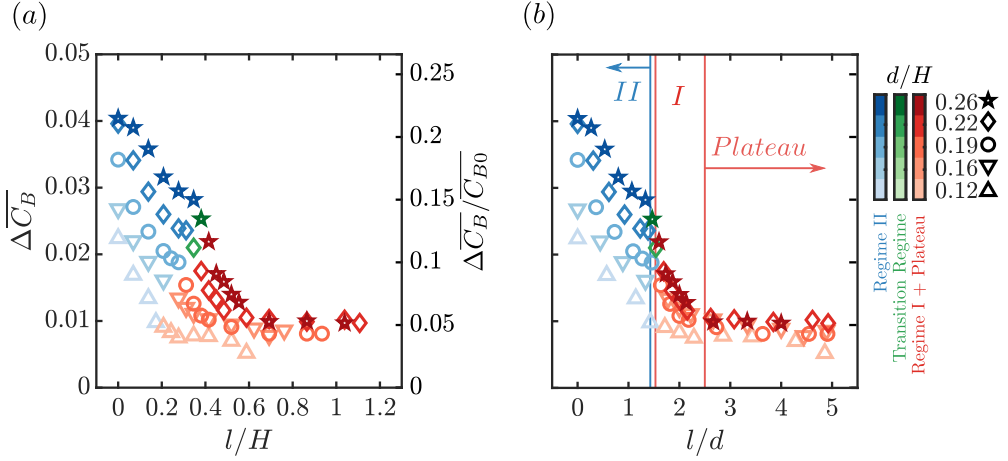


Figure 4.3: Impact of the position  $l$  and width  $d$  of the obstacles on the base drag of the body, darker color indicates wider obstacle. The base drag is scaled by  $l/H$  ( $H$  is the height of the model) in (a) and  $l/d$  in (b). See §4.3.2 for the meaning of the colors.

the wakes of the obstacles and the main body. We name these two regimes as regime I and II. The Reynolds number sensitivity is also checked for some cases as shown by different colors, we observe no obvious dependence of  $\Delta \overline{C}_B$  on the free-stream velocity (Below 0.5 % of  $\overline{C}_{B0}$ ).

Before analyzing detailed local measurements, integral measurements can be very helpful in exploring scaling properties. Figure 4.3(a) and (b) show the evolution of  $\Delta \overline{C}_B$  for all the  $d/H$  configurations. Using the same criterion as the reference configuration which will be shown later in §4.3.2, regime I and the plateau are colored in red and regime II is colored in blue. Few cases present transition between the two regimes as indicated by the green color and are detailed also in §4.3.2. In these two figures, the obstacle-to-base distance  $l$  is scaled, respectively, with the height of the body  $H$  and the width of the obstacles  $d$ . It is clearly shown that  $l/d$  is the correct scaling as the distance to the base is concerned. For all the available cases, the  $l/d$  ranges for the plateau, regime I and regime II are  $l/d > 2.5$ ,  $2.5 > l/d \geq 1.56$  and  $1.45 \geq l/d \geq 0$ , respectively.

Moreover, the sensitivity of  $\Delta \overline{C}_B$  to  $l/d$  also depends on the obstacle width  $d/H$  as shown in figure 4.3(b). Concentrating first on regime I, with decreasing  $l/d$ , the base drag increases from the end of the plateau. Along the plateau the obstacles are expected to induce perturbations of the underflow that may alter the near-wake balance as shown by Barros *et al.* (2017) and used by Haffner *et al.* (2021). In our situation, a base drag increase of  $\sim 5\%$  is observed in the plateau for all the configurations from the baseline case. In order to focus only on the base drag sensitivity in regime I and remove the drag increase of  $\sim 5\%$ , we define a variant of the base drag variation  $\Delta \overline{C}_B^I = \overline{C}_B(l/d) - \overline{C}_B(l/d = 2.5)$ . More precisely, the base drag values of the cases with  $l/d$  values closest to  $l/d = 2.5$  are approximately used as  $\overline{C}_B(l/d = 2.5)$ . Figure 4.4(a) then shows a clear scaling property of the base pressure variation in regime I:

$$\Delta \overline{C}_B^I = (d/d_{ref})^2 \Delta \overline{C}_{Bref}^I, \quad (4.1)$$

where  $\overline{C}_{Bref}^I$  denotes the base drag evolution of the reference configuration. Using quadratic fitting, the base drag evolution in regime I can be approximated for all the  $d/H$  configurations:  $\Delta \overline{C}_B^I = 0.2(d/H)^2(2.5 - l/d)^2$ . On the other hand in regime II (figure 4.4b), the main trend observed is a linear shift of  $\Delta \overline{C}_B$  proportional to the width of the obstacles  $d$ , *i.e.*:

$$\Delta \overline{C}_B = (d/d_{ref}) \Delta \overline{C}_{Bref}. \quad (4.2)$$

Similarly to regime I, a quadratic fitting gives  $\Delta \overline{C}_B = 0.03(d/H)((l/d)^2 - 3.3l/d + 6.5)$ . The physical arguments for these specific scaling properties will be detailed in §4.5 in order to help building a physical model of the phenomenon.

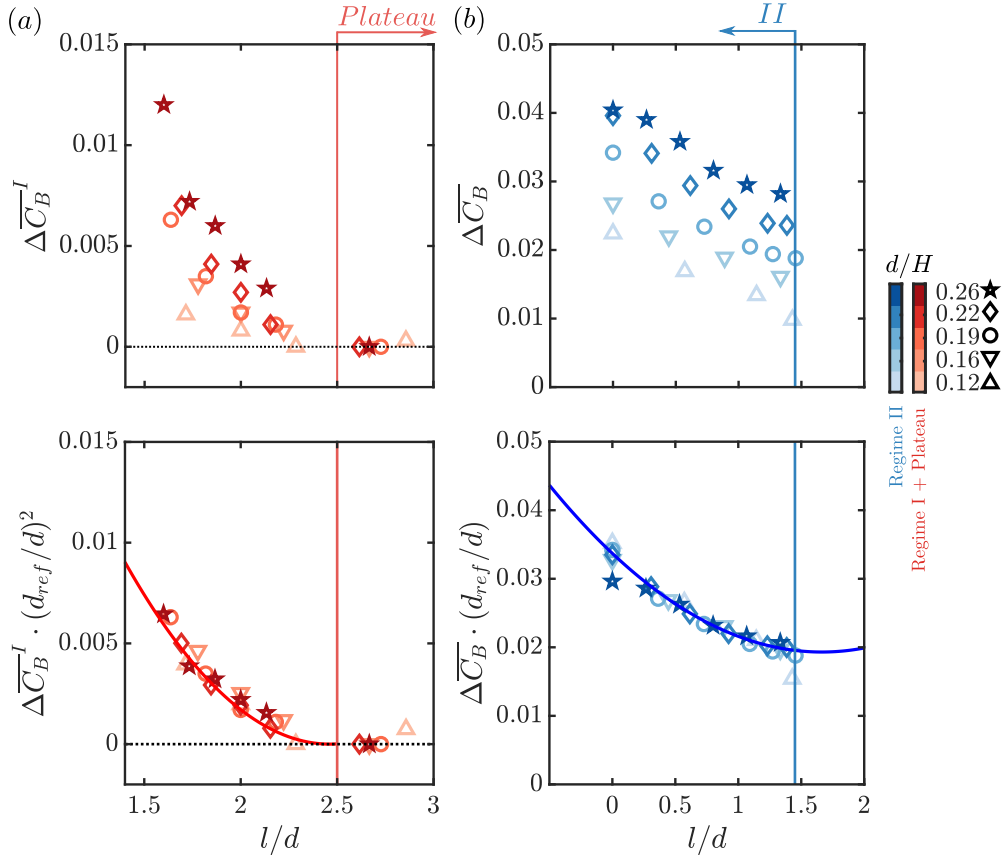


Figure 4.4: Scalings of the base drag evolution in regime I (a) and in regime II (b).

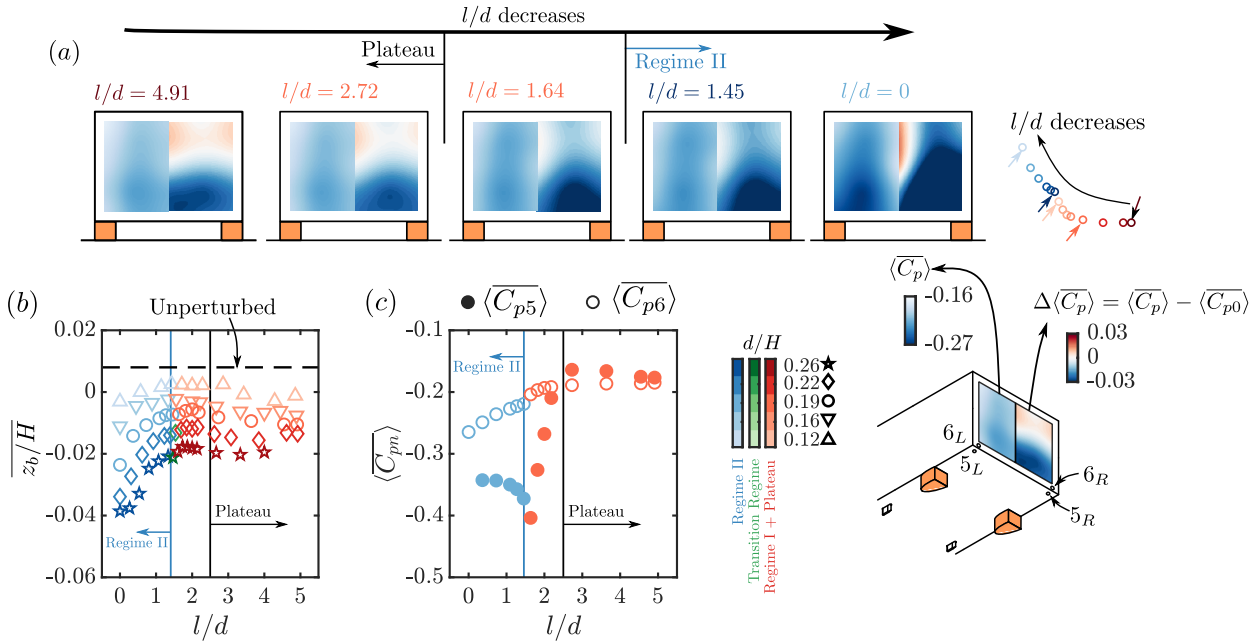


Figure 4.5: (a) Evolution of the base pressure distribution with the obstacle-to-base distance  $l/d$  for the reference configuration  $d_{ref}/H = 0.19$ , the mean values and the differences with respect to the baseline case are, respectively, presented at the left-hand and right-hand sides of the base. (b) Evolution of the mean vertical position of the base CoP  $\overline{z}_b/H$  with  $l/d$ . (c) Comparison between the evolution of  $\langle C_{p5} \rangle$  and  $\langle C_{p6} \rangle$  for the reference configuration  $d_{ref}/H = 0.19$ .

### 4.3.2 Pressure fields

In order to better understand the base drag increase under the perturbation of the obstacles, we now analyze the mean pressure fields over the body and in the wake of the obstacles, starting by the

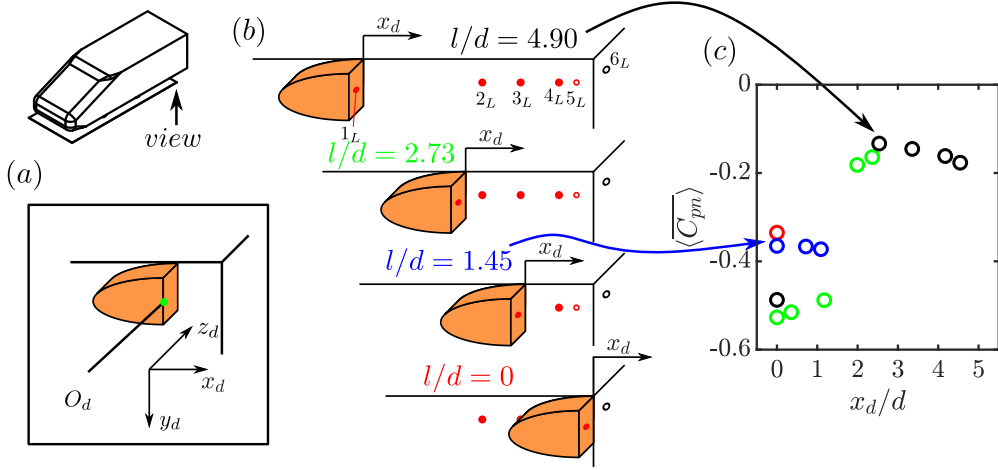


Figure 4.6: (a) Definition of an obstacle-fixed coordinate system. (b) The relative position of the obstacle and the pressure taps for cases  $l/d = 4.90, 2.73, 1.45$  and  $0$  of the reference configuration  $d_{ref}/H = 0.19$ . (c) Evolution of the time- and space-averaged pressure coefficients  $\langle C_{pn} \rangle$  obtained from the pressure taps used ( $n \in [1, 2, 3, 4, 5]$ ) as a function of the streamwise distance from the base of the obstacles  $x_d$ , only the cases in (b) are shown with colors related to the  $l/d$  values.

mean base pressure distribution of the reference configuration in figure 4.5(a). On the right-hand side of the base, the distribution of pressure difference  $\Delta \langle \overline{C_p} \rangle$  with respect to the baseline case is also presented for comparison. From case  $l/d = 4.91$  to  $l/d = 1.64$ , the transition from the plateau to regime I is described. On the other hand, from  $l/d = 1.45$  to  $l/d = 0$ , regime II is visualized. In the plateau, the base pressure decrease of  $\sim 5\%$  from the baseline case is located at the bottom half of the base with a slight pressure recovery at the top half. This observation of top/bottom symmetry breaking was also captured by Barros *et al.* (2017) using similar underflow perturbations located far from the base ( $l/d > 4$ ). In regime I, we observe a further pressure decrease at the bottom half of the base with now also a slight decrease at the top half. The pressure decrease is not homogeneous laterally but rather located near the obstacles.

In regime II, the base pressure is importantly modified and the modification is mainly located at the bottom half of the base and horizontally near the obstacle pair. This observation indicates that in regime II the interactions between the main wake and the wakes of the obstacles greatly modify the structure of the main wake. This is better illustrated in figure 4.5(b) by the mean vertical position of the base center-of-pressure (CoP)  $\overline{z_b}/H$ . In the plateau and regime I no obvious modification in  $\overline{z_b}/H$  is witnessed. However, in regime II,  $\overline{z_b}/H$  decreases continuously with decreasing  $l/d$ .

We now consider the pressure distribution in the vicinity of the obstacles. In figure 4.5(c) a comparison is presented between the evolution of  $\langle \overline{C_{p5}} \rangle$  and  $\langle \overline{C_{p6}} \rangle$  for the reference configuration. As shown in the sketch in figure 4.5, sensors  $5_L$  and  $6_L$  ( $5_R$  and  $6_R$ ) are located in the symmetry plane of the left-hand (right-hand) reference obstacle. They are positioned on both sides of the bottom trailing edge of the body, which are the key locations for the problem considered here. In the plateau,  $\langle \overline{C_{p5}} \rangle$  is slightly higher than  $\langle \overline{C_{p6}} \rangle$ . This is expected for a mean curved streamline after separation, inducing a lower pressure inside the recirculating bubble due to centrifugal effect (Bradshaw, 1973). However, in both regime I and II,  $\langle \overline{C_{p5}} \rangle$  is lower than  $\langle \overline{C_{p6}} \rangle$ . With decreasing  $l/d$ , the pressure difference  $\langle \overline{C_{p6}} \rangle - \langle \overline{C_{p5}} \rangle$  increases strongly in regime I. On the contrary, in regime II,  $\langle \overline{C_{p6}} \rangle - \langle \overline{C_{p5}} \rangle$  decreases with decreasing  $l/d$ , which gives a possible explanation for the sudden change in the slope of the base drag evolution between regime I and II.

The influence of the obstacles on the main wake as presented using  $\langle \overline{C_{p5}} \rangle$  changes rapidly in the drag-sensitive regimes. Therefore, we turn to the perspective of the obstacles to understand the evolution of  $\langle \overline{C_{p5}} \rangle$ . To this aim, an obstacle-fixed reference frame is defined and is shown in figure 4.6(a). The origin  $O_d$  lies at the intersection point of the floor, the base of the left-hand obstacle and the symmetry plane of the left-hand obstacle. In this way, as shown in figure 4.6(b), the pressure taps indicated by red symbols act like a streamwise pressure rake. We choose four  $l/d$  cases of the reference configuration as an example in figure 4.6(b). At each  $l/d$  location, the

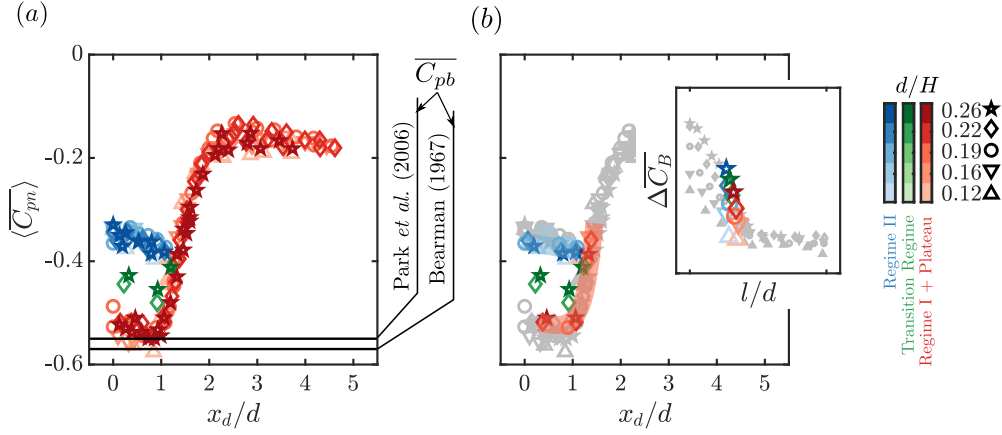


Figure 4.7: Pressure evolution in the wake of the obstacles: evolution of  $\langle C_{pn} \rangle$  ( $n \in [1, 2, 3, 4, 5]$ ) as a function of  $x_d$  for all the cases (a) and for the cases around the boundary of regimes (b), different colors indicate different flow regimes.

streamwise pressure development in the wake of the obstacles can be at best characterized by five pressure taps except that for small  $l/d$ , some of the taps with  $x_d/d < 0$  are covered by the obstacles. The  $\langle C_{pn} \rangle$  values obtained from the available pressure taps, therefore, can be gathered onto a single plot in figure 4.6(c). This allows a comparison of the streamwise pressure development behind the obstacles between different  $l/d$  cases. We proceed further in figure 4.7(a) by presenting the evolution of  $\langle C_{pn} \rangle$  with  $x_d/d$  for all the  $d/H$  configurations. Typical base pressure coefficients  $\overline{C_{pb}}$  from previous studies are also presented for comparison.

In regime I and the plateau, the streamwise pressure developments in the wake of the obstacles superimpose on a same curve (colored red). Near the obstacle base, the pressure  $\langle C_{pn} \rangle \sim -0.5$  is of the same level as the base pressure values measured by Bearman (1967) and Park *et al.* (2006) using 2-D bluff bodies with similar cross-section shapes as the obstacle. Downstream of the obstacle base, the strong longitudinal pressure gradient along  $1 < x_d/d < 2.5$  towards  $\langle C_{pn} \rangle \sim -0.2$  indicates closure of the obstacle wake bubble. For a reference 2-D mean wake, the increase in mean static pressure can be understood by writing the streamwise momentum balance along the centerline:

$$-\frac{1}{2} \frac{\partial \overline{C_p}}{\partial x^*} = \overline{u_x} \frac{\partial \overline{u_x}}{\partial x^*} + \frac{\partial \overline{u'_x u'_x}}{\partial x^*} + \frac{\partial \overline{u'_x u'_y}}{\partial y^*}, \quad (4.3)$$

where  $x^*$  and  $y^*$  are normalized dimensions using the characteristic length of the 2-D bluff bodies. In our case, they are normalized by the width of the obstacles  $d$ . An additional investigation based on the detailed PIV measurements in the wake of a 2-D circular cylinder at  $Re = 2150$  acquired from Konstantinidis *et al.* (2005) is shown in figure 4.8. Note that similar orders of magnitudes were found with the study of Parkin *et al.* (2014) at a higher Reynolds number. Figure 4.8 shows respectively the evolution of the mean streamwise velocity  $\overline{u_x}$  and the different terms of the mean longitudinal momentum balance (equation 4.3) along the centerline of the near wake. Near the end of the mean recirculation region ( $x/d = 2$ ), we observe a peak of pressure gradient  $\frac{\partial \overline{C_p}}{\partial x^*}$ , which is driven mostly by the term  $\frac{\partial \overline{u'_x u'_y}}{\partial y^*}$ . In this region, the transport of fluctuating longitudinal velocity by the transverse fluctuating velocity  $\overline{u'_x u'_y}$  is mainly the signature of the Kármán vortex shedding. This suggests that the strong longitudinal pressure gradient in our case (shown in figure 4.7a along  $1 < x_d/d < 2.5$ ) is the result of the Kármán vortex shedding behind the obstacles.

At a specific  $l/d$  position, the pressure value at the bottom trailing edge of the body downstream of the obstacles is equal to the  $\langle C_{pn} \rangle$  value at  $x_d/d = l/d$ . In regime I ( $1.56 \leq l/d < 2.5$ ), the trailing edge experiences a sharp pressure decrease with decreasing  $l/d$ . This was shown before in figure 4.5(c) by the evolution of  $\langle C_{p5} \rangle$  with  $l/d$ . The transition from regime I to regime II is pictured in figure 4.7(b) by presenting only the cases near the boundary of the regimes. It is clear that despite the small  $l/d$  change, the pressure in the obstacle wake is completely altered.

Regime II (colored blue in figure 4.7a) presents a higher pressure near the obstacle base ( $x_d/d < 1$ ). A strong coupling between the main wake and the wakes of the obstacles is expected in this

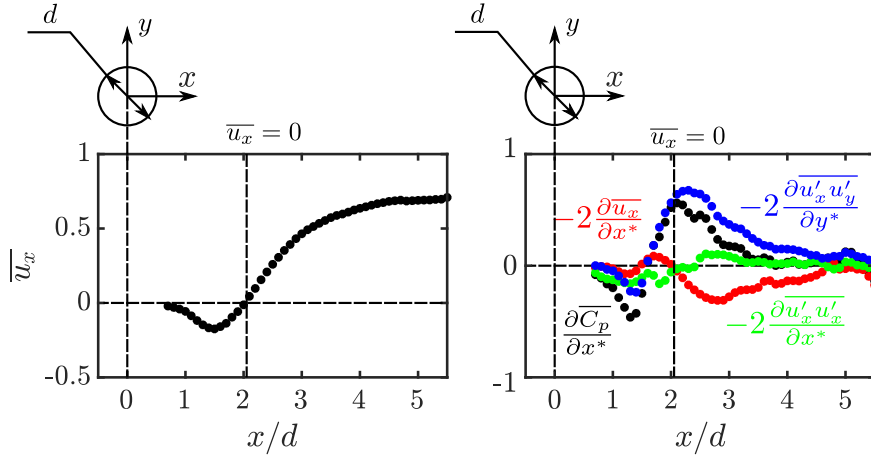


Figure 4.8: Left: Evolution of mean streamwise velocity  $\bar{u}_x$  along the centerline of a circular cylinder at  $Re_d = 2150$ . Right: Contributions of different terms in equation 4.3 to the streamwise pressure gradient along the centerline. The data is acquired from the database of Konstantinidis *et al.* (2005).

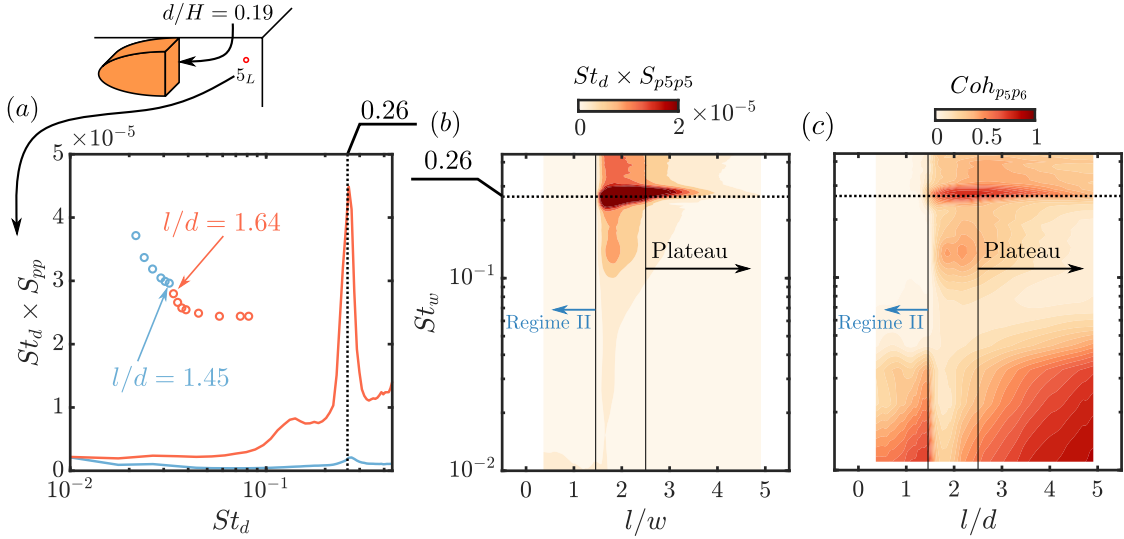


Figure 4.9: For the reference configuration  $d_{ref}/H = 0.19$ : (a) premultiplied spectra of the pressure data obtained from taps  $n = 5$  for cases  $l/d = 1.45$  and  $l/d = 1.64$ . (b) Evolution of the premultiplied spectrum of the pressure signal  $C_{p5}$  with  $l/d$ . (c) Spectral coherence between pressure signals  $C_{p5}$  and  $C_{p6}$ .

regime. The pressure recovery near the obstacle base from regime I to regime II is approximately 34%. It is interesting to note that a similar trend of pressure recovery is obtained in the wakes of 2-D bluff bodies when flow control techniques are applied, with the natural Kármán vortex shedding in these wakes attenuated by 3-D perturbations using tab devices (Park *et al.*, 2006) or by splitter plate (Bearman, 1965).

The different streamwise pressure developments in different regimes efficiently distinguish the cases belonging to regime I and II. At different  $l/d$  positions in the same regime, the wakes of the obstacles keep their mean properties. Hence, the obstacles are decisive for the global evolution of the flow. Apart from the two regimes, some cases present intermediate pressure levels near the base of the obstacles which lie between the two regimes and are colored green. It is important to note here that the cases are carefully checked and no obvious difference is found in the pressure between taps located on two sides. This prevents the situation that the two obstacles are subjected, respectively, to different regimes.

We now investigate the pressure dynamics in the wake of the obstacles. The focus is put on the Kármán vortex shedding observed in 2-D wakes. The existence of the vortex shedding in such a scenario is captured by Zhang *et al.* (2015) and Wang *et al.* (2013). In their works two different  $St_d$ , respectively behind the front and rear cylindrical struts used for model supporting, are reported and are interpreted as the signatures of the vortex shedding ( $d$  denotes the diameter

of the struts). By carefully examining the spectral content of the unsteady pressure sensors, the coherent dynamics of the obstacle wake are captured by taps  $5_L$  and  $5_R$  located downstream of the obstacle pair. The premultiplied spectra obtained from  $5_L$  and  $5_R$  are averaged and the result is shown in figure 4.9(a). Only the two cases near the dividing point,  $l/d = 1.45$  (regime II) and 1.64 (regime I), are pictured. A clear distinction is noticed between the cases, where an important peak is noticed for the case  $l/d = 1.64$  (regime I). This peak occurs at  $St_d = 0.26$  which is in good agreement with the studies based on D-shaped cylinders (Bearman, 1965; Park *et al.*, 2006; Bearman, 1967). In these studies, the authors interpret the peak frequency as the vortex shedding frequency. On the other hand in regime II, the pressure fluctuation is much weaker and the peak at  $St_d = 0.26$  is barely discernible, implying suppression of the periodic motion.

For the reference configuration, the evolution with  $l/d$  of the premultiplied spectrum of the pressure signals from the taps numbered 5 is presented in figure 4.9(b). In regime I, the continuous decrease in  $\langle \overline{C_{p5}} \rangle$  with decreasing  $l/d$  is accompanied by an increase in the energy of the peak at  $St_d = 0.26$  thus the coherent dynamics have growing effects on the main wake. On the other hand in regime II, although the peak at  $St_d = 0.26$  is not observable, relatively lower energy is found at very low frequency. This suggests that through the expected wake coupling as envisioned before, the wakes of the obstacles are influenced by the low-frequency dynamics of the main wake.

We present further the spectral coherence  $Coh_{p_5p_6}$  of the unsteady pressure sensors named by  $5_{L,R}$  and  $6_{L,R}$  as depicted in figure 4.6, which is calculated via:

$$Coh_{p_5p_6} = 0.5 \sum_{i=L,R}^i \left( \frac{|S_{p_5i p_6i}|^2}{S_{p_5i p_5i} S_{p_6i p_6i}} \right), \quad (4.4)$$

where  $S_{p_5i p_5i}$  and  $S_{p_6i p_6i}$  are the power spectral densities of the pressure coefficients  $C_{p_5i}$  and  $C_{p_6i}$ , respectively, and  $S_{p_5i p_6i}$  is the cross power spectral density of the pressure coefficients  $C_{p_5i}$  and  $C_{p_6i}$  ( $i$  denotes L or R). The evolution of  $Coh_{p_5p_6}$  with  $l/d$  is presented in figure 4.9(c). It is shown that in regime I the base pressure is strongly coupled with the coherent dynamics at  $St_d = 0.26$ . We also observe a strong coherence at low frequency in the plateau and regime II. Apart from the bistable dynamics, this frequency range of  $0.05 < St_H < 0.21$  (based on the height of the body) also contains several coherent dynamics of the main wake, for example the low-frequency pumping motion of the recirculation region observed by Volpe *et al.* (2015) and Dalla Longa *et al.* (2019). The lack of coherence in the low-frequency range in regime I suggests that the wake dynamics of the obstacles dominate the interactions between the obstacles and the main wake.

The coupling between the dynamics of the main wake and the wakes of the obstacles promotes an investigation on the low-frequency dynamics of the main wake, which could be helpful to better understand the interaction mechanisms. The sensitivity map of the CoP position  $y_b/H$  and  $z_b/H$  to  $l/d$  is presented in figure 4.10(a). For all the configurations ( $d/H = 0.16$  and  $0.22$  are not shown for clarity), the horizontal bistable dynamics is observed during the entire regime I and the plateau. In regime II, a gradual suppression of asymmetry in the horizontal direction with decreasing  $l/d$  is observed. This suppression is accompanied by an increase in asymmetry in the vertical direction. For the  $d/H = 0.19$  and  $0.26$  configurations with decreasing  $l/d$ , the vertical symmetry breaking in regime II rotates the two bistable states to a locked state with a permanent asymmetry in the vertical direction.

The low-frequency content in the plateau and regime II as discussed in figure 4.9(b) is further investigated by checking the time evolution of the pressure signal from tap  $5_L$ . It is found in figure 4.10(c) that in the plateau and regime II, the time evolution of the pressure presents two preferred values. However in regime I, we observe only one peak in the p.d.f. of  $C_{p_5L}$ , which is consistent with the investigation using the spectral coherence in figure 4.9(c).

Finally, the gradual rotation of the wake asymmetry direction is better quantified in figure 4.10(c) by the relation between  $\overline{z_b/H}$  and  $|\overline{y_b/H}|$ . First of all, the relationship between mean vertical  $\overline{z_b/H}$  and horizontal  $|\overline{y_b/H}|$  asymmetries of the baseline case perturbed by top/bottom spanwise cylinder from figure 3.7(b) is presented by gray squares. The elliptic shape they formed gives all the possible wake asymmetries that can be selected by passive perturbations when they are located far from the base (no variation of the ellipse shape with the distance from the perturbations to the base). A similar method was used in Lorite-Díez *et al.* (2020b) to quantify the effect of

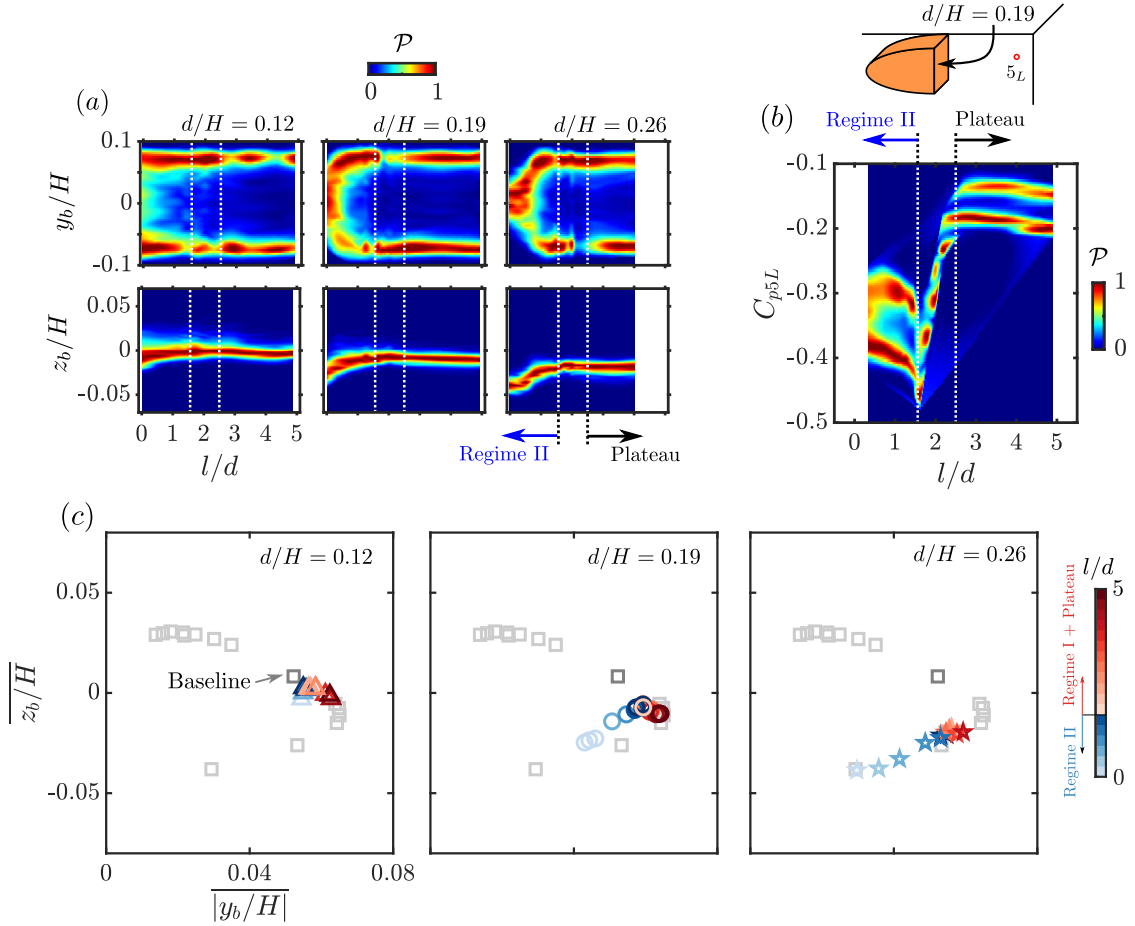


Figure 4.10: (a) Sensitivity maps of the horizontal and vertical CoP position  $y_b/H$  and  $z_b/H$  to  $l/d$  for the configurations  $d/H = [0.12, 0.19, 0.26]$ , the p.d.f. of each  $l/d$  case is normalized by its most probable value. (b) Sensitivity maps of the pressure signal  $C_{p5L}$  to  $l/d$  for the reference configuration  $d_{ref}/H = 0.19$ , the p.d.f. of each  $l/d$  case is normalized by its most probable value. (c) Evolution of the mean wake asymmetry with  $l/d$  portrayed by the relation between  $\overline{z_b/H}$  and  $\overline{|y_b/H|}$ , the cases perturbed by top/bottom perturbing cylinder from figure 3.7(b) are used to show all the possible wake asymmetries that can be selected by passive perturbations when they are considered to be far from the base (colored in gray).

steady base blowing on the wake asymmetry strength. The ellipse was provided by the model proposed by [Bonnaïon & Cadot \(2018\)](#). When the base CoP of a case is located inside the ellipse, the wake asymmetry strength is considered to be reduced. In our situation, for the three selected configurations, when the obstacle pair is located at  $l/d \approx 5$ , the wake asymmetry strength is not modified compared to the ellipse. With decreasing  $l/d$ , there is a continuous reduction of mean asymmetry strength as can be seen for the  $d/H = 0.19$  and  $0.26$  configurations in regime I. This is followed by a gradual increase of vertical asymmetry and a reduction of horizontal asymmetry in regime II. With a combination of these two trends, it is measured for some cases in regime II of the  $d/H = 0.19$  configuration that a moderate reduction of mean asymmetry strength is reached. It is interesting to note here that the overall evolution for the configuration  $d/H = 0.19$  is quite similar to the measurements in [Lorite-Díez \*et al.\* \(2020b\)](#) when the steady base blowing is only located at the bottom trailing edge of the base.

## 4.4 Global and local wake modifications

The flow mechanisms resulting in the base drag sensitivity in different regimes are investigated in this section. A global description of the main wake is presented first, which is followed by a detailed analysis of the wake of the obstacles. Most of the investigations in this section are based on the reference configuration since other configurations provide the same conclusions.

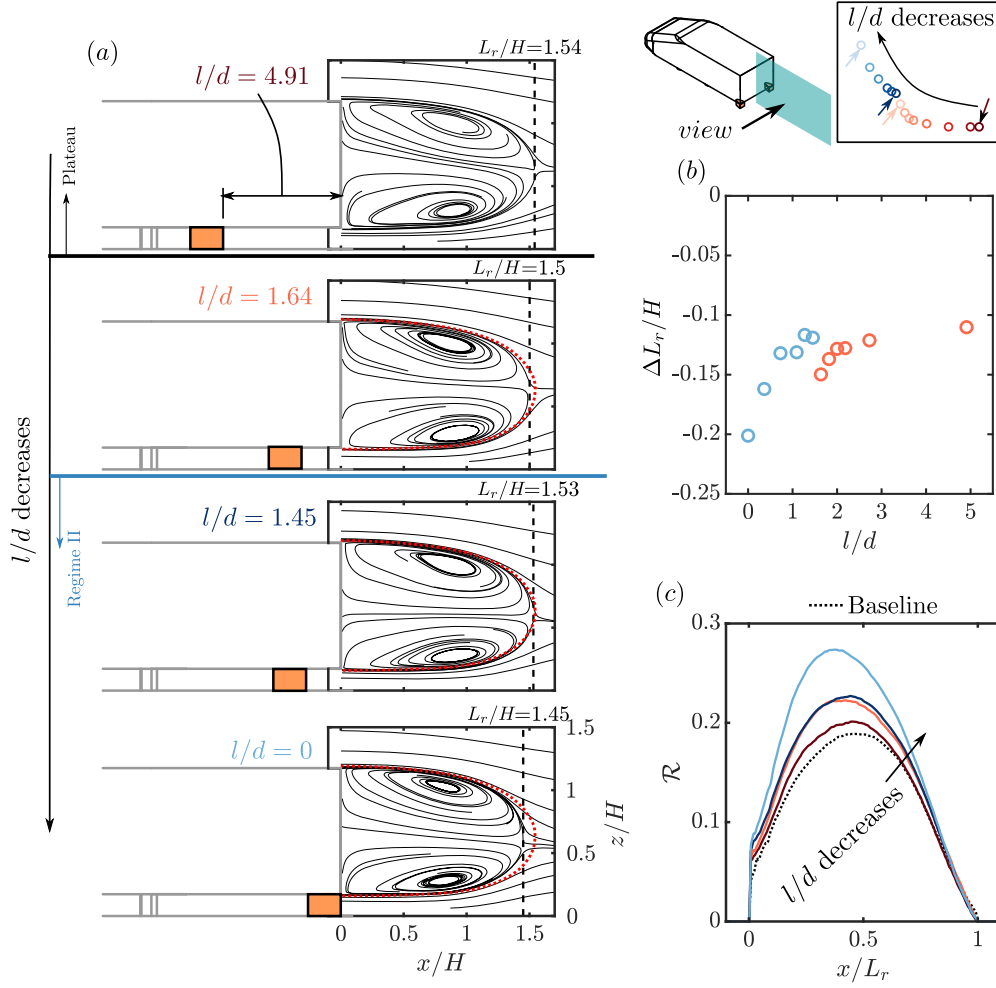


Figure 4.11: Evolution of the main wake topology with  $l/d$  for the reference configuration  $d_{ref}/H = 0.19$ . (a) Streamlines in the symmetry plane ( $y/H = 0$ ) for cases of the plateau ( $l/d = 4.91$ ), regime I ( $l/d = 1.64$ ) and regime II ( $l/d = 1.45$  and  $0$ ). The dashed curve represents the separatrix of the  $l/d = 4.91$  case. (b) Evolution of the recirculation length  $L_r$  with  $l/d$ . (c) Comparison of the recirculation strength  $\mathcal{R}$  for the cases presented in (a).

#### 4.4.1 Evolution of the near wake of the body

We now describe the time-averaged main wake for the reference configuration in figure 4.11(a), which is the origin of the low-pressure footprint over the base. From the plateau to regime I, the recirculating bubble is shortened by 2.5 %, and the base drag increases by 3.7 %. In regime II, the base drag increase is also accompanied by the decrease in bubble length. We observe a sudden increase in  $L_r/H$  of 2 % from  $l/d = 1.64$  to  $l/d = 1.45$ . The whole evolution of the recirculation length  $\Delta L_r/H = L_r/H - L_{r0}/H$  with  $l/d$  is further shown in figure 4.11(b) and the sudden increase in  $L_r$  is again confirmed. This indicates that the interactions between the main wake and the wakes of the obstacles in the two regimes are totally different.

Apart from the mean velocity fields discussed, where the flow curvature importantly influences the base drag, the Reynolds stresses also play an important role in the base drag as interpreted through the streamwise momentum balance proposed by Balachandar *et al.* (1997) for 2-D wakes. This momentum balance was also used in 3-D situations, for example in Grandemange *et al.* (2013a) and Liu *et al.* (2021), to emphasize the importance of the mean transport of the fluctuating momentum by turbulent velocity fluctuations. One of the consequences of the Reynolds stresses in the mean velocity fields is the changes in the intensity of the recirculating flow, since they represent the small-scale entrainment and large-scale engulfment inside the recirculation region. The intensity of the recirculating flow is measured by a quantity  $\mathcal{R}$ , which is defined as:

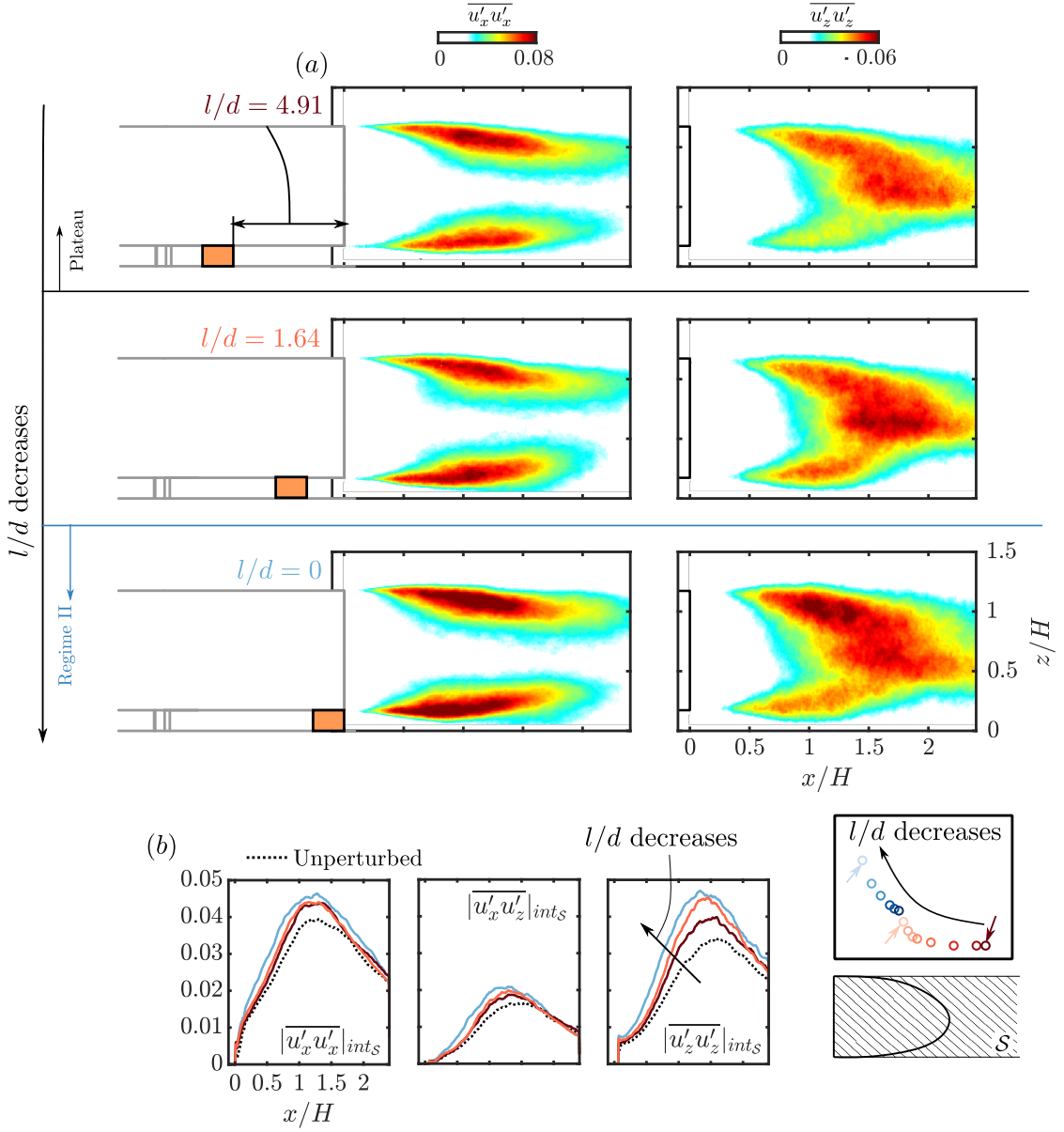


Figure 4.12: Reynolds stresses in the symmetry plane  $y/H = 0$  for the cases of the plateau ( $l/d = 4.91$ ), regime I ( $l/d = 1.64$ ) and regime II ( $l/d = 0$ ). The width of the obstacles is  $d_{ref}/H = 0.19$ . (a) Normal stress  $\overline{u'_x u'_x}$  and  $\overline{u'_z u'_z}$ . (b) Streamwise profiles of the integrals of Reynolds stresses over region  $\mathcal{S}$ .

$$\mathcal{R}(x) = \int_{\overline{u_x} \leq 0} \sqrt{\overline{u_x^2} + \overline{u_z^2}} d(z/H). \quad (4.5)$$

This quantity is displayed in figure 4.11(c). It is shown that the obstacle pair leads to an overall enhancement of the recirculating motion from the baseline case. For the case with the highest drag increase ( $l/d = 0$ ), the maximum of the recirculation strength  $\mathcal{R}$  increases substantially by  $\sim 50\%$  from the baseline case. With decreasing  $l/d$ , we observe that the drag and the recirculation strength increase continuously. This is not the case for the recirculation length as observed in figure 4.11. The recirculation length should therefore be used with particular caution when analyzing complex wakes.

A detailed examination of the Reynolds stresses in the symmetry plane is presented in figure 4.12. Comparing these three selected cases, no obvious difference is noticed in the  $\overline{u'_x u'_x}$  and  $\overline{u'_x u'_z}$  (not shown here for brevity) components. The  $\overline{u'_z u'_z}$  component, on the other hand, shows more evident changes. From the plateau ( $l/d = 4.91$ ) to regime I ( $l/d = 1.64$ ),  $\overline{u'_z u'_z}$  increases locally in the bottom shear layer and in the end of the mean wake bubble. However, from regime I ( $l/d = 1.64$ ) to regime II ( $l/d = 0$ ), the predominant increase is localized in the top shear layer.

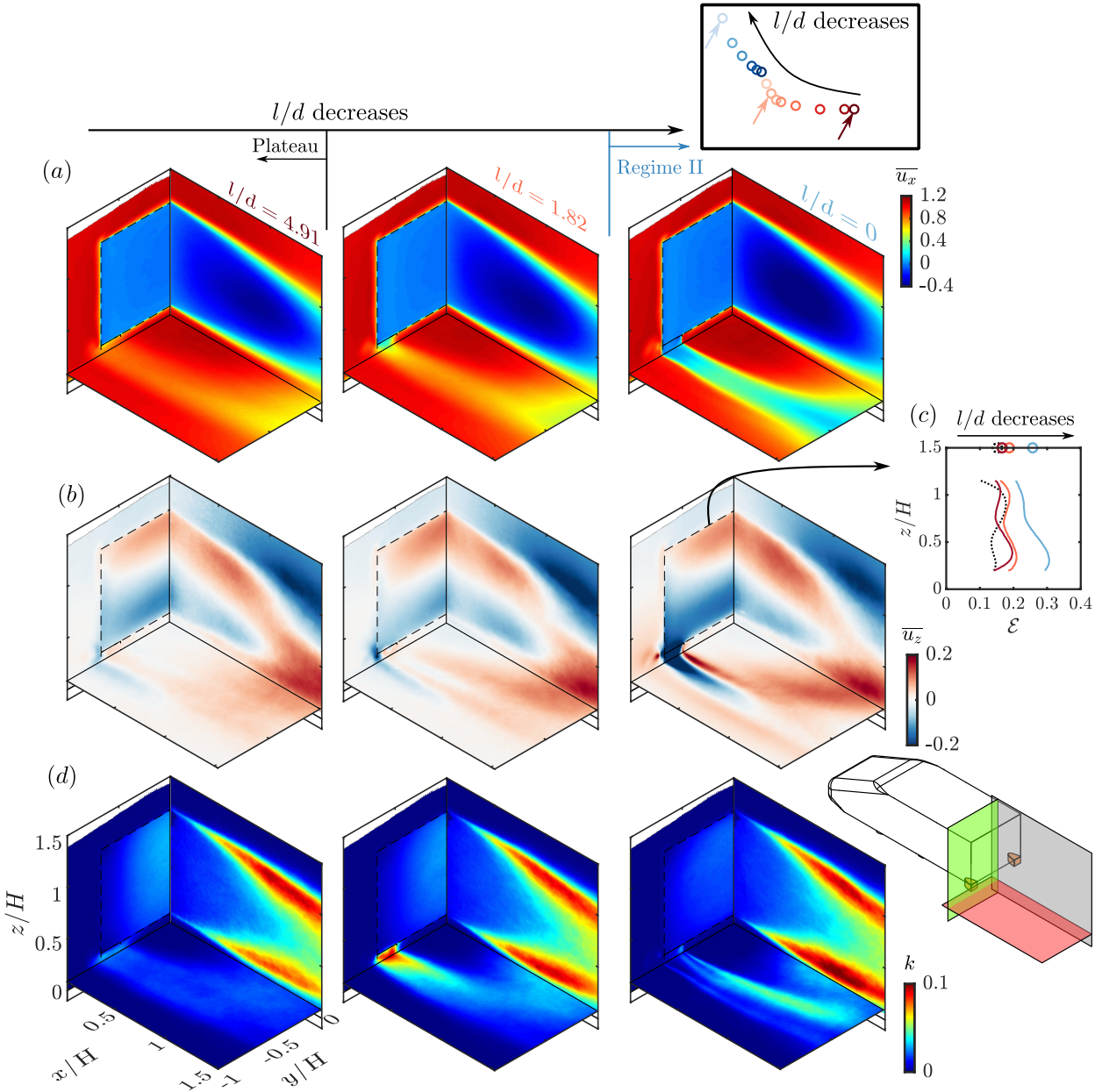


Figure 4.13: Mean velocity components (a)  $\overline{u_x}$  and (b)  $\overline{u_z}$  in the three PIV planes for the cases of the plateau ( $l/d = 4.91$ ), regime I ( $l/d = 1.82$ ) and regime II ( $l/d = 0$ ). The width of the obstacles is  $d_{ref}/H = 0.19$ . (c) Comparison of the cross-flow strength  $\mathcal{E}$ , the space-averaged values are shown over the top axis. (d) Turbulent kinetic energy  $k$  distributions in the three PIV planes for the same cases as (a) and (b).

A quantitative comparison is achieved by integrating the absolute value of the stresses inside a rectangular region  $\mathcal{S}$  limited by the body height as shown in figure 4.12(b). The reference case is also shown for comparison. It is clear that the obstacle pair globally enhances the turbulent fluctuations in the wake compared with the reference case, proved by the substantial increases in all components. For the perturbed cases,  $|u'_x u'_x|_{int\mathcal{S}}$  and  $|u'_x u'_z|_{int\mathcal{S}}$  have the same evolution, with no obvious change from the plateau to regime I and a slight increase from regime I to regime II. On the other hand,  $|u'_z u'_z|_{int\mathcal{S}}$  increases substantially from case  $l/d = 4.91$  to  $l/d = 1.64$  followed by a slight increase from case  $l/d = 1.64$  to  $l/d = 0$ .

We present now a 3-D description of the main wake by gathering the velocity measurements in the three PIV planes. The velocity distributions are shown in figure 4.13 for three cases of the reference configuration in the plateau ( $l/d = 4.91$ ), regime I ( $l/d = 1.82$ ) and regime II ( $l/d = 0$ ). Focusing first on the streamwise velocity  $\overline{u_x}$  distributions (figure 4.13a), no obvious difference between the cases is noticed in the main wake. However, as also observed by Wang (2019), the

different sensitivities in different regimes are marked by the momentum deficit behind the obstacles, where in regime II ( $l/d = 0$ ) the same velocity level as in the recirculation region of the main wake is observed in the cross-flow plane. This indicates that in regime II the wakes are merged. For these three cases, the velocity at the exit of the underbody in the center region in-between the obstacles (see measurements in plane  $x/H = 0.03$ ) does not evolve from the baseline flow. More generally, only very minor modifications of this longitudinal underflow momentum between the obstacles are observed for varying  $l/d$  and  $d/H$ . In addition to the wake merging, regime II also presents a strong downwash flux from the main wake to the wakes of the obstacles as depicted using the vertical velocity  $\overline{u_z}$  in figure 4.13(b). Concomitantly, the downward motion in the bottom half of the main wake is enhanced. This downward flux is possibly the main reason for the enhancement of the recirculation strength and the modification in the vertical balance of the main wake. We show the strength of the cross-flow near the base of the body by defining a quantity  $\mathcal{E}$ , such that:

$$\mathcal{E}(z/H) = \int_{-W/2H}^{W/2H} \sqrt{\overline{u_y}^2 + \overline{u_z}^2} d(y/H), \quad (4.6)$$

The evolution of  $\mathcal{E}$  with  $z/H$  from  $z/H = G/H$  to  $z/H = G/H + 1$  (the projection of the top and bottom edges of the base to the present plane) is displayed in figure 4.13(c). Both the selected cases and the baseline case are shown. With the underflow perturbed at the most upstream position, the bottom part of the recirculating flow is enhanced. Entering into regime I,  $\mathcal{E}$  is globally higher than in the plateau but is more balanced vertically. Arriving at the flush-mounted position,  $\mathcal{E}$  increases and a stronger bottom recirculating flow is observed. All the observations are in accordance with the investigation based on the base pressure.

By looking at the fluctuating velocity fields, we also observe a profound difference of the case in regime I, which is presented in figure 4.13(d) by the distributions of the mean turbulent kinetic energy  $k$ . A strong unsteady motion is detected in the wakes of the obstacles in regime I but not in regime II. This trend from the plateau to regime II is in accordance with the spectral information shown before in figure 4.9. From these velocity measurements, we note that the local flow fields near the obstacles are greatly modified by the interactions between the obstacles and the main wake. Therefore, in the following section, we focus on the detailed velocity fields around the obstacles.

#### 4.4.2 Obstacle wake characteristics in different regimes

In this section, we focus on the wake dynamics of the obstacles in different regimes following the obstacle-fixed coordinate system defined in figure 4.6. This helps us to understand the differences between different flow regimes observed in figure 4.13 near the obstacles. Unless otherwise stated, the obstacle considered in this section is the obstacle located at the left-hand side ( $y/H < 0$ ) because the right-hand obstacle is only a mirror symmetry of the left-hand one in a time-averaged point of view.

Figure 4.14 presents the distributions of the mean streamwise velocity  $\overline{u_x}$  at  $z/H = 0.09$  (plane XY) and  $x/H = 0.03$  (plane YZ) downstream the obstacle. Meanwhile, under the obstacle-fixed reference frame, plane YZ moves downstream with  $l/d$ . The relative positions of plane YZ to plane XY are marked by the traverse dotted lines in figure 4.14(a) and (b). Starting from a case in the plateau, the left-hand two columns, case  $l/d = 2.72$  and  $1.82$  characterize the evolution from the plateau to regime I. On the other hand,  $l/d = 1.45$ ,  $0.73$  and  $0$  describe the development of regime II.

We focus first on the cases near the dividing point, case  $l/d = 1.82$  and  $l/d = 1.45$ . As already seen in figure 4.13, a major difference between regime I and II is that for the case  $l/d = 1.45$ , the mean recirculating flow downstream of the obstacle extends downstream of the base of the body, as shown in figure 4.14(a). Moreover, no shear flow is noticed between the wake of the obstacle and the main wake in figure 4.14(b) (case  $l/d = 1.45$ ) at the streamwise position of plane YZ. This indicates that the wakes of the obstacles and the main wake are merged, which is further illustrated in figure 4.14(c) by plotting  $\overline{u_x}$  distribution along  $y_d/d = 0$  in plane YZ for all the available  $l/d$  cases. Regime II on one hand presents no obvious velocity gradient between wakes. On the other hand in regime I and the plateau, the shear is evidenced with a gradual recovery

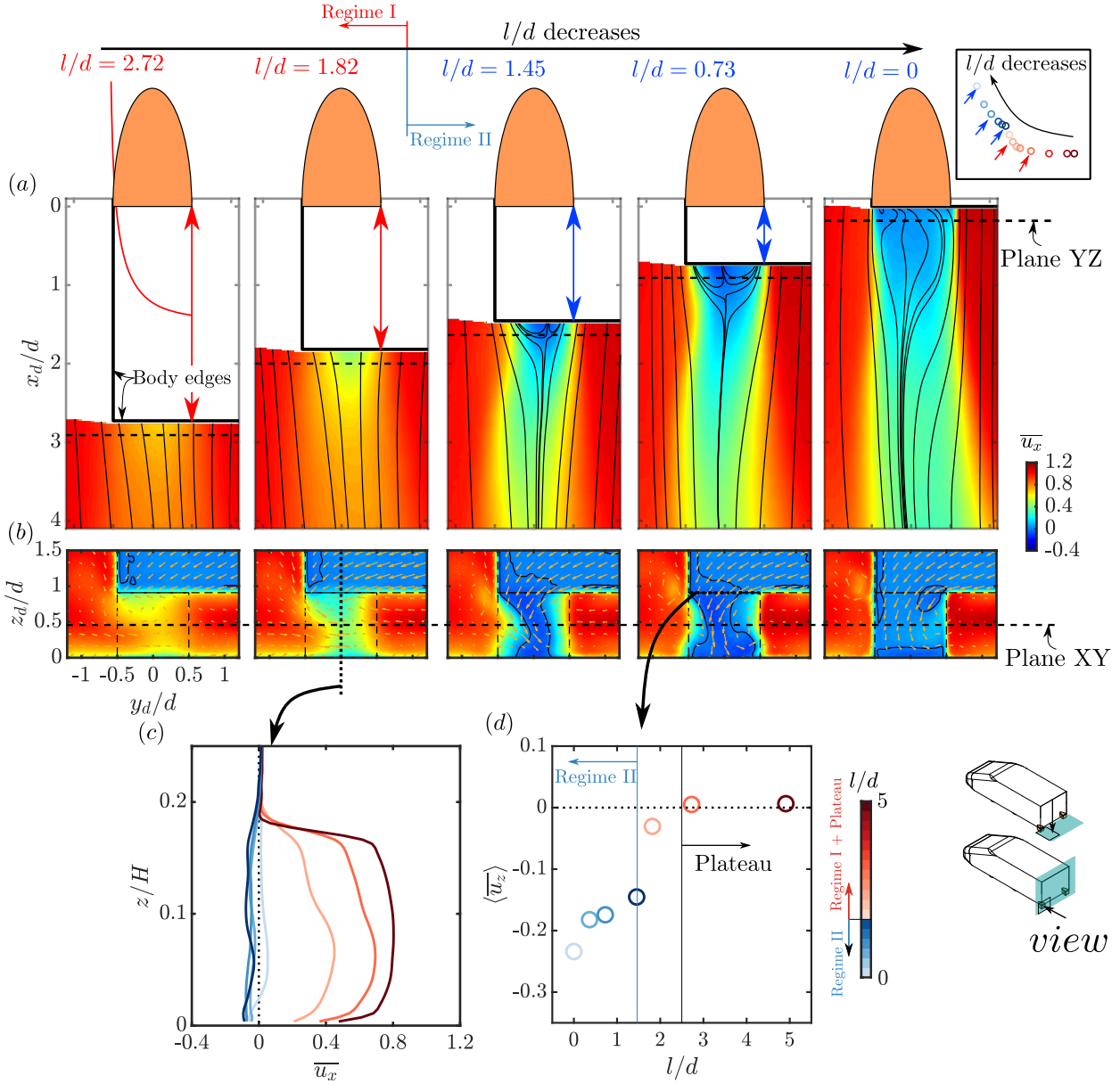


Figure 4.14: Evolution of the mean streamwise velocity  $\bar{u}_x$  with the obstacle-to-base distance  $l/d$  downstream the left-hand obstacle  $d/H = 0.19$  at  $z/H = 0.09$  (a) and  $x/H = 0.03$  (b), the  $\bar{u}_x$  distributions along  $y_d/d = 0$  in (b) are detailed in (c). (d) Evolution of the space-averaged mean vertical velocity  $\langle \bar{u}_z \rangle$  with  $l/d$  for the reference configuration, the line used for space-averaging is indicated in (b) (see text for details).

of momentum after the obstacle with increasing  $l/d$ . In regime I and the plateau, the length of the recirculation bubble of the obstacles should be constant since the pressure gradient describing wake closure collapses on a single curve in figure 4.7(a). Hence the length of the bubble in regime I should equal to the  $l/d$  value of the dividing point, which is around  $1.45 \leq l/d \leq 1.56$  according to the scaling in §4.3.1.

A mean mass transfer from the main wake to the wakes of the obstacles is observed in figure 4.14(b) by considering the in-plane vector fields. The strength of the mass flux is quantified by space-averaging the mean vertical velocity at the height of the ground clearance in plane YZ over  $-0.5 < y_d/d < 0.5$ , which is shown in figure 4.14(d). In regime II the mass flux has a velocity of approximately 20 % of the free-stream velocity. It is interesting to note here that we also observe a mean mass transfer in regime I, albeit of a smaller strength.

In appendix A, RANS simulations reveal very similar distribution and strength of the mean mass transfer. By tracing the mean mass flux exiting the main body wake contributing to the mean mass transfer, we notice that it comes initially from the free stream and then enters the main body

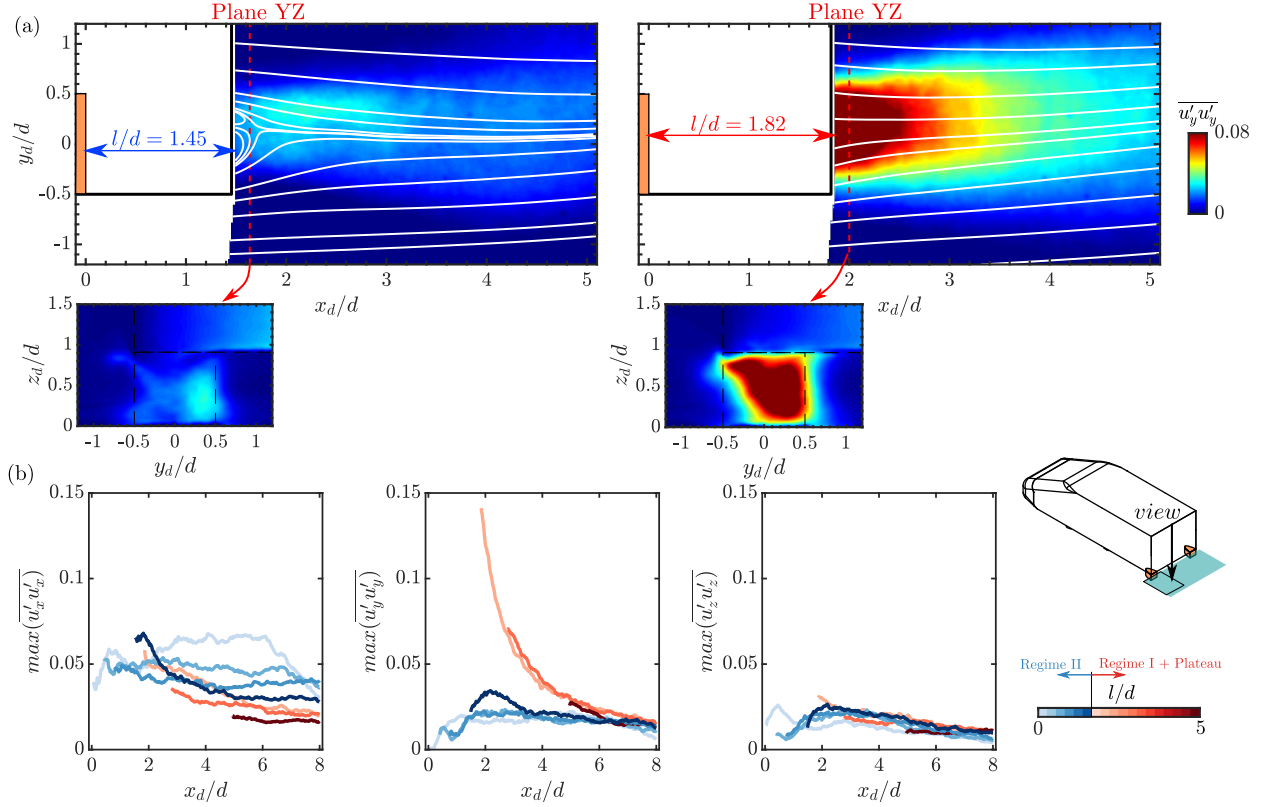


Figure 4.15: Reynolds stresses in the obstacle wake for the reference configuration  $d_{ref}/H = 0.19$ . (a) Normal stress  $\overline{u'_y u'_y}$  of cases  $l/d = 1.45$  and  $l/d = 1.82$  in plane XY and plane YZ. (b) Streamwise profiles of the maximum of Reynolds stresses in plane XY for different regimes.

wake. In this process, the corresponding fluid particles lose their streamwise momentum  $\rho U_0$ . The effect of this momentum loss on the base pressure will be further discussed in §4.5.1 by considering a global momentum balance.

We carry on by analyzing the unsteady characteristics of the wake of the obstacles by showing the Reynolds stresses behind the obstacle in figure 4.15. In accordance with the spectral content of the pressure signal in figure 4.9, the fundamental difference between regime I and II is also noticed in the distribution of Reynolds stresses after the obstacle, which is shown in figure 4.15(a). The unsteady wake of the obstacles in regime I contributes to a higher  $\overline{u'_y u'_y}$  level than in regime II. The increase in  $\overline{u'_y u'_y}$  is also confirmed by the  $\overline{u'_y u'_y}$  distributions in plane YZ as depicted in the inserted figures in figure 4.15(a). Other components of the stresses are also shown in figure 4.15(b); it appears that regime I contributes to lower  $\overline{u'_x u'_x}$  and similar  $\overline{u'_z u'_z}$  compared with regime II.

The underlying coherent unsteady features can be further extracted by means of the proper orthogonal decomposition (POD) (Lumley, 1967). A brief description of the POD method is now presented. The instantaneous velocity field  $\mathbf{u}$  with a snapshot number  $N_s$  is decomposed as:

$$\mathbf{u}(\mathbf{x}, t) = \overline{\mathbf{u}}(\mathbf{x}) + \mathbf{u}'(\mathbf{x}, t) = \overline{\mathbf{u}}(\mathbf{x}) + \sum_{n=1}^{N_s} a_n(t) \Phi_n^u(\mathbf{x}). \quad (4.7)$$

The modes  $\Phi_n(\mathbf{x})$  are determined by solving an eigenvalue problem:

$$\mathbf{R} \Phi_n^u = \lambda_n \Phi_n^u, \quad (4.8)$$

where  $\mathbf{R}$  is the autocorrelation matrix of the velocity fluctuation  $\mathbf{u}'(\mathbf{x}, t)$  and eigenvalues  $\lambda_n$  represent the contribution of each POD mode to the total turbulent kinetic energy which are sorted by descending order. Finally, the temporal coefficients  $a_n(t)$  are calculated by a projection of the velocity fluctuation field  $\mathbf{u}'(\mathbf{x}, t)$  onto the corresponding mode  $\Phi_n^u$ . Since the spatial dimension is far larger than the temporal dimension, the snapshot method proposed by Sirovich (1987) is used.

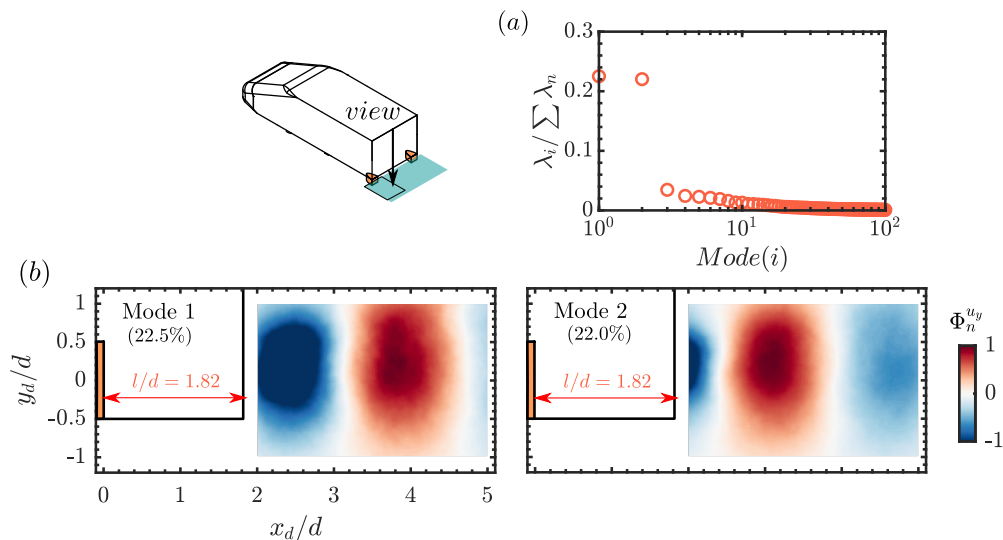


Figure 4.16: POD description for the case  $l/d = 1.82$  of the reference configuration  $d_{ref}/H = 0.19$  in plane XY. (a) Contribution of in-plane turbulent kinetic energy from each POD modes. (b) Mode structures of the first two modes normalized by their maximum value.

The proper orthogonal decomposition is applied to the in-plane fluctuating velocity fields in plane XY of the case  $l/d = 1.82$  spanning  $2 < x_d/d < 5$  and  $-1 < y_d/d < 1$ . The set of measurements consists of 1200 snapshots. The POD shows that the first two modes contain nearly equal turbulent kinetic energy  $k$  (figure 4.16a), suggesting that the two modes constitute a mode pair. They are shown in figure 4.16(b) by the distributions of  $\Phi_n^{u_y}$ , similar topology with almost the same wavelength is observed for the two modes. A phase shift of  $\pi/2$  is found for these two modes which describe traveling waves. These features evidence the signature of a Kármán vortex street downstream of the obstacles (Van Oudheusden *et al.*, 2005), which accounts for a dominant part of the turbulent kinetic energy ( $\sim 40\%$ ). This confirms the mean and fluctuating pressure data in figure 4.7 and 4.9.

## 4.5 Further discussions and concluding remarks

This last section is dedicated to a discussion and a summary of the main results presented. Firstly, we propose a model to gather under a unique framework the results of the present chapter and the base drag modifications obtained in various previous studies. Finally, the concluding remarks are presented.

### 4.5.1 A momentum exchange model to evaluate the mass exchange effects

We call  $\delta\Omega$ , a boundary delimited by the base of the body and the contour of the main separation bubble (see the sketch in figure 4.17a). For the unperturbed baseline situation, a balance of the pressure forces, the shear stresses and the normal stresses occurs in the mean recirculation bubble. Balachandar *et al.* (1997) analyzed this equilibrium in detail in the wake of cylinders. As stated by Grandemange *et al.* (2013b), it may be a rough approximation that  $\delta\Omega$  is usually assumed hermetic in 3-D flows. This statement is particularly true in this work because we have observed a mean transfer of mass flux  $\rho q$  from the main wake to the wakes of the obstacles in the drag-sensitive regimes I and II. The law of mass conservation then guarantees that this mass flux enters the main recirculation bubble through  $\delta\Omega$ . This mechanism is visualized in appendix A using RANS simulations.

The effects of a continuous base suction were studied for a D-shaped cylinder by Bearman (1967) and for a 3-D bluff body by Hsu *et al.* (2021). These authors showed that, for increasing suction flow rate, the base drag increases and the mean wake becomes shorter with higher curvature of the external flow. Hsu *et al.* (2021) also observed a gradual suppression of the symmetry-breaking mode with an increase of the suction flow rate. Very similar trends were discussed in §4.3 and

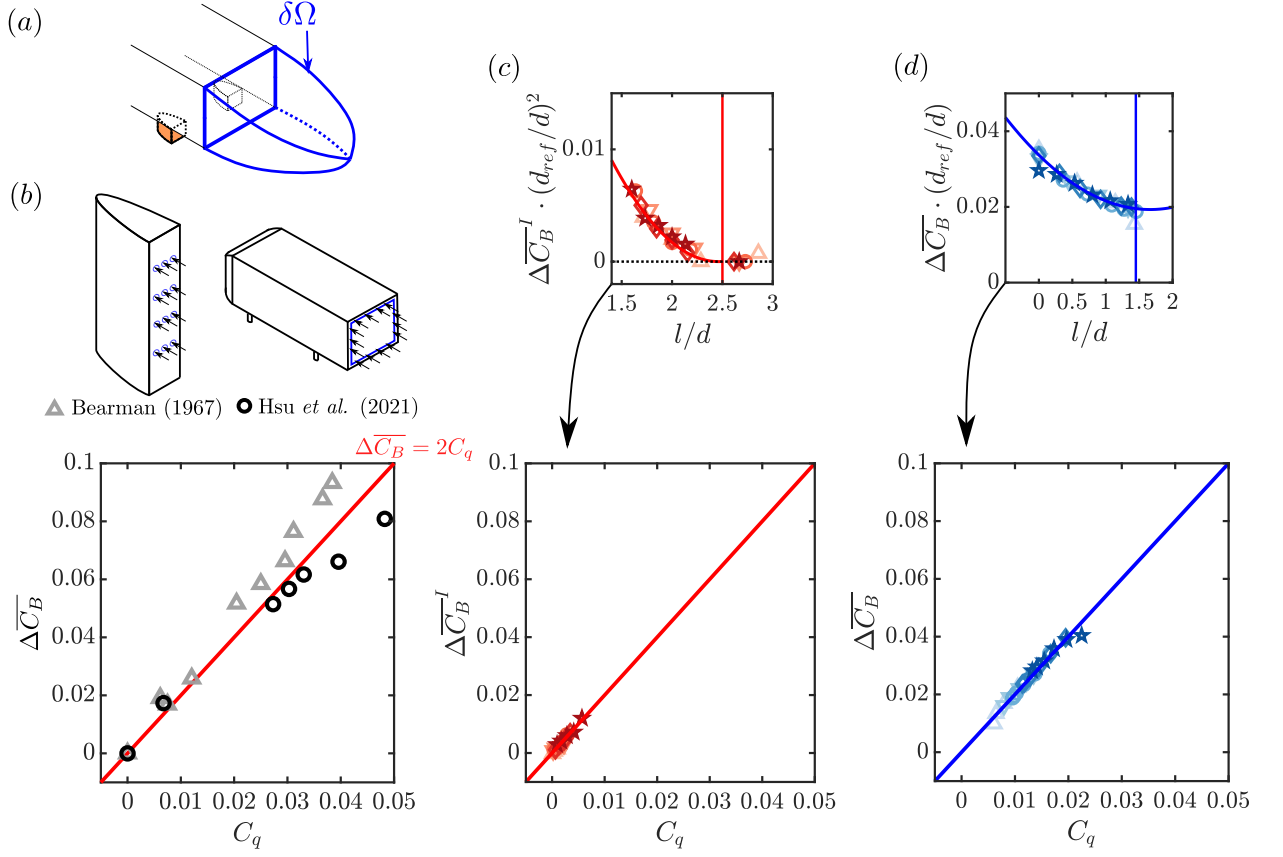


Figure 4.17: (a) Schematic of a boundary delimited by the base of the body and the contour of the main wake bubble. (b – d) Base drag  $\overline{C}_B$  versus suction flow rate coefficient  $C_q$  in previous studies (a), regime I (b) and regime II (c). The suction flow rate in (c) and (d) are obtained from the scalings and fittings in figure 4.4.

§4.4 of the present chapter for decreasing  $l/d$ . In Bearman (1967), the distribution of suction at the base of the 2-D D-shaped body was uniform. On the contrary, suction was provided through a perimetric slit around the base of an Ahmed body in the work of Hsu et al. (2021). While the shapes of the bodies and the ways suction is applied are very different in these two reference works, a global relation linking the suction flow rate and the increase of the pressure drag is observed. If a non-dimensional suction flow rate  $C_q = q/HWU_0$  is defined, figure 4.17(b) shows that a simple relation  $\Delta\overline{C}_B = 2C_q$  is observed to hold between the increase of the base drag and  $C_q$  for small value of suction flow rate ( $C_q < 0.03$  in Hsu et al. (2021)).

We may interpret this result as follows. Upstream of these bluff bodies, the momentum per unit mass of all fluid particles is  $U_0$ . A mean entrainment of mass in the near wake therefore corresponds to a mean deviation of momentum. The deviated longitudinal momentum flux inside the mean near wake is  $(\rho q)U_0$ . If we assume that this deviation is balanced by a variation of the pressure on the base, then the variation of the pressure force on the base induced by the mean momentum entering the near wake is  $\Delta F_x = (\rho q)U_0$ . By normalizing the corresponding quantities, we obtain:

$$\Delta\overline{C}_B = \frac{\Delta F_x}{0.5\rho U_0^2 HW} = \frac{2q}{HWU_0} = 2C_q. \quad (4.9)$$

Let us assume that this relation holds for small  $C_q$  whatever the distribution of the suction. The suction flow rate  $C_q$  imposed by the obstacles in regime I and II can then be estimated from the fitting laws obtained in figure 4.4 (shown again in figure 4.17c and d). Together with the relation  $\Delta\overline{C}_B = 2C_q$ , the suction flow rate  $C_q$  for each case is given by a combination of  $d/H$  and  $l/d$ . The resulting relation between the base drag  $\Delta\overline{C}_B$  and the suction flow rate  $C_q$  is shown in figure 4.17(c) and (d). We see that the maximum value of  $C_q$  is smaller than  $C_q = 0.01$  for regime I and  $C_q = 0.03$  in regime II. Relation 4.9 is therefore expected to hold and can be used to interpret

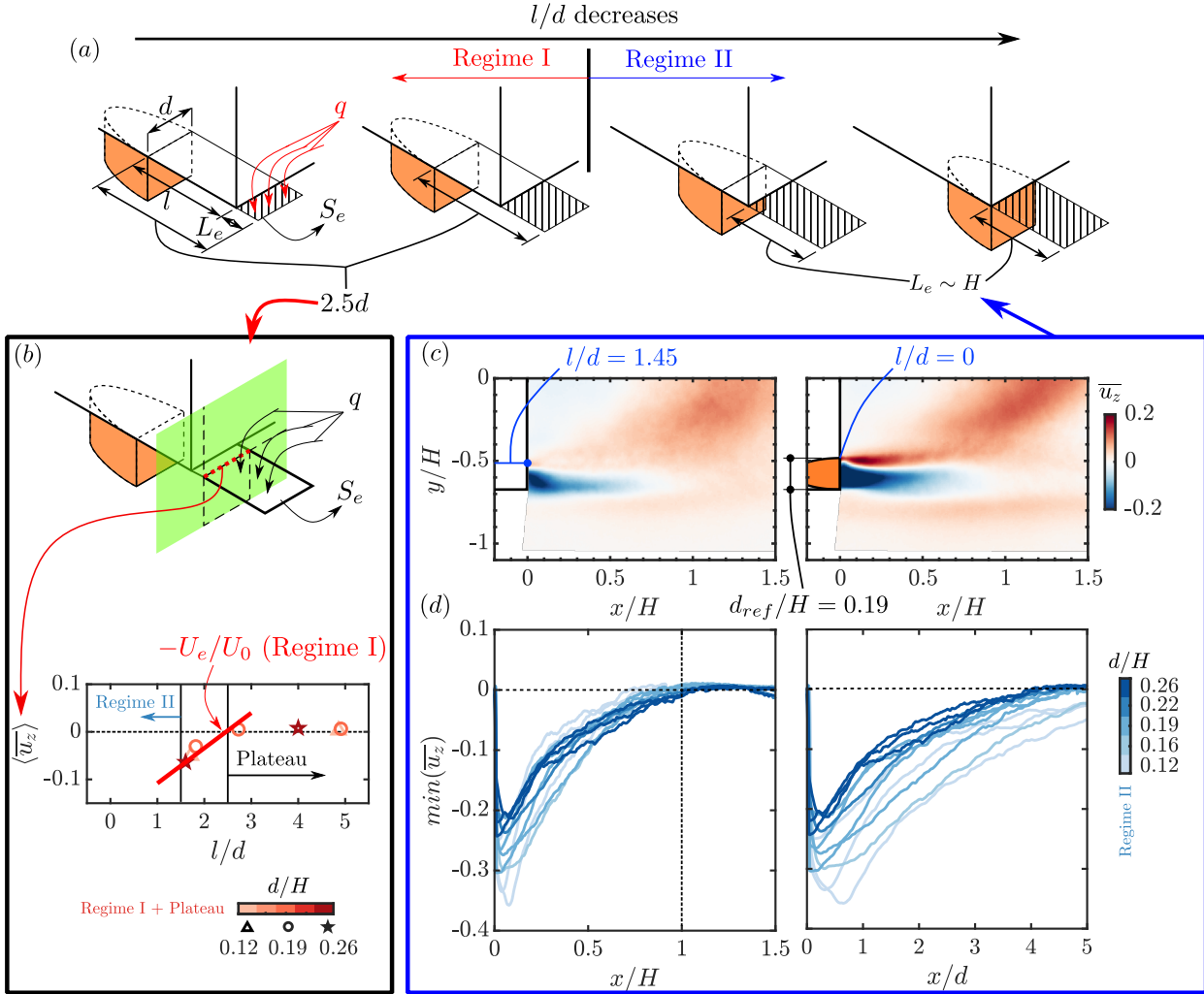


Figure 4.18: (a) Schematics of the surface of the mass exchange in regime I and II. (b) Comparison between the mass exchange velocity  $U_e/U_0$  obtained from the relation  $\Delta \bar{C}_B = 2C_q$  and the space-averaged mean vertical velocity  $\langle \bar{u}_z \rangle$  over the red dotted line indicated (see text for details). (c) Evolution of the vertical velocity  $\bar{u}_z$  in the plane  $z/H = 0.09$  with  $l/d$ , the width of the obstacles is  $d/H = 0.19$ . (d) Streamwise profile of minimum  $\bar{u}_z$  for all the sampled cases, the streamwise distance from the base  $x$  is scaled with the height of the body  $H$  and the width of the obstacles  $d$ .

the different scalings in figure 4.4.

Having two obstacles, the mean volume flow rate  $q$  is simply written as  $q = 2S_e U_e$ . Here  $S_e$  and  $U_e$  are, respectively, the mean exchange surface and the space-averaged mean velocity normal to the surface (figure 4.18a). In what follows, we assume that  $U_e$  depends only on the regime, and therefore on the relative obstacle-to-base ratio  $l/d$ . The  $(d/d_{ref})^2$  scaling (relation 4.1) observed in regime I can then be simply understood by stating that both the length and width of the mean exchange surface  $S_e$  are driven by the obstacle. Therefore the area  $S_e$  is proportional to  $d^2$ . On the other hand, the linear scaling observed in regime II (relation 4.2) shows that the exchange surface  $S_e$  is driven both by the width of the obstacles  $d$  and by the scale of the main wake  $H$ . A set of simple sketches is proposed in figure 4.18(a) where  $S_e$  is simply a rectangular surface of width  $d$  and length  $L_e$ . In regime I, figure 4.7(a) shows that  $x_d \sim 2.5d$  approximately ends the region of strong pressure decrease near the base of the obstacles. This means that there is no significant change in the interactions between the wakes of the obstacles and the main wake when  $l/d > 2.5$ . A simple model for  $S_e$ , that agrees with the scaling 4.1, is then  $S_e \sim dL_e = d(2.5d - l)$ . The mean velocity  $U_e$  can then be estimated with  $U_e/U_0 = HW\Delta \bar{C}_B / (4S_e)$  for each cases in regime I. In order to compare the velocity  $U_e$  with the quantitative data obtained, the mean vertical velocity at the height of the ground clearance in plane YZ is space-averaged in the range of  $-W/2H < y/H < (-W/2H + d/H)$  and  $(W/2H - d/H) < y/H < W/2H$ . The resulting  $\langle \bar{u}_z \rangle$  for

all the sampled cases is presented in figure 4.18(b). It is shown that  $U_e/U_0$  matches satisfactorily with the  $\langle \bar{u}_z \rangle$  for the cases in regime I.

On the other hand, regime II is very different because the wakes are merged. The mean vertical velocity distribution  $\bar{u}_z$  in plane XY at  $z/H = 0.09$  is presented for the reference configuration in figure 4.18(c). The streamwise profiles of the minimum  $\bar{u}_z$  for all sampled cases are shown in figure 4.18(d) with two different longitudinal scalings  $x/H$  and  $x/d$ , where  $x$  is the distance from the base of the body. While the value of  $\bar{u}_z$  varies with  $l/d$  (mass transport is stronger for flush-mounted cases), it is clear in these figures that the streamwise extend of the region with negative  $\bar{u}_z$  scales with  $H$ . Using the scaling 4.2 and  $S_e \sim dL_e = 0.5dH$  with  $0.5H$  being a crude estimation of  $L_e$ , one find for example  $U_e/U_0 = 0.12$  for flush-mounted situations ( $l/d = 0$ ). Figure 4.18(d) shows that this is a good order of magnitude of the downward vertical velocities measured in this complex situation. Our experimental data in both regimes is therefore in agreement with the physical model proposed in this section.

The physical mechanisms proposed by this physical model are visualized in appendix A using simulations. By writing a streamwise momentum balance of a cuboid control volume enclosing the main body wake, the simulations suggest that the mean mass transfer induces a mass exchange between the main body wake and the surrounding high-momentum flow, which corresponds to a longitudinal momentum exchange. This momentum exchange caused by the presence of the obstacles contributes to a dominant part of the base pressure variation. Therefore, in a first-order approximation, the momentum balance can be further simplified to the relation 4.9.

#### 4.5.2 Concluding remarks

The goal of this chapter was to evidence and to analyze, for a model experimental situation, near wake interactions and drag increase regimes. The 3-D near wake of a square-back bluff body in ground proximity was perturbed by placing a pair of D-shaped obstacles under the body. Five obstacle widths  $d$ , from 12 % to 26 % of the height of the body, were used and a sensitivity study of the body's pressure drag was performed by varying the relative distance  $l$  between the obstacle pair and the base. Two successive drag-sensitive regimes are identified for obstacle-to-base distances  $l/d < 2.5$ , where the pressure drag of the body is increased up to 22 %. The flow dynamics measured downstream of the obstacles are found to be very different in different regimes. When the obstacles are the closest to the base  $l/d < 1.5$ , the pressure drag changes of the main body are driven by mean merging between the wakes of the obstacles and of the main body and scale with  $d$ . Contrarily, when the obstacles are located farther from the base  $1.5 < l/d < 2.5$ , the wakes of the obstacles are isolated from the main body wake. The mean pressure at the bottom trailing edge of the body downstream of the obstacles varies significantly with the obstacle-to-base distance and is related to the flow dynamics in the near wake of the obstacles. In particular, a strong signature of vortex shedding is evidenced in this regime while it is absent for merged situation. Here the dynamics of the obstacle wake drive the pressure drag changes of the main body which scale with  $d^2$ .

When reducing the distance to the base and despite these important differences between the two drag increase regimes, the global effects on the main wake are very similar to the effects of a continuous suction located on the base for a D-shaped cylinder studied by Bearman (1967) and for a 3-D bluff body studied by Hsu *et al.* (2021). A mean mass transfer from the wake of the main body to the wakes of the obstacles is indeed evidenced in the present chapter. Therefore, our assumption is that this mechanism of mass transfer from the wake of the main body to the wakes of the obstacles governs the near-wake interactions and the pressure drag changes for the main body. Using our results and the reference studies describing the effect of base suction on the pressure drag of bluff bodies, a physical model based on a flow momentum balance of the wake is proposed to explain the contrasting scalings of the pressure drag increase in the different regimes observed. For the first regime,  $d^2$  scaling can be simply understood by stating that both the width and length of the surface of the mass exchange are driven by the size of the obstacle  $d$ . On the other hand, the linear scaling observed in the second regime implies that the size of the mass exchange surface is governed by both the scale of the obstacle and the scale of the body. Our experimental data are all in agreement with this model.

The drag increase regimes driven by local mass exchange evidenced in this chapter are believed to be a general feature of wake interactions for 3-D bluff bodies that complement our physical understanding of the global reaction of a 3-D recirculating bubble to upstream perturbations (Barros *et al.*, 2017). Moreover, the obstacles also perturb the underflow that leads to global variation in the vertical wake balance. These local and global effects will be studied in the next chapter using more realistic underflow perturbations: rotating wheels, in order to shed further light on the wheel-vehicle interaction problem.

## Chapter 5

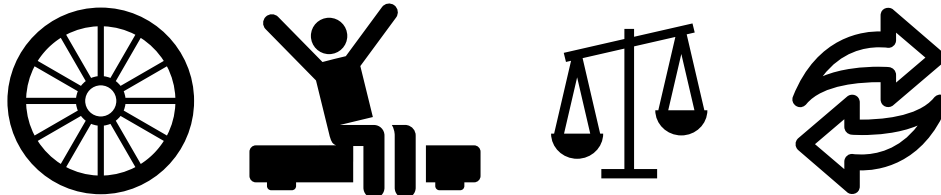
# Salient features of wheel-vehicle interactions: consequences for drag

---

Salient features of wheel-vehicle interactions and their consequences for drag are investigated in this chapter based on the square-back Windsor body with different distances  $l$  between the rear wheels and the base of the vehicle. Two different mechanisms responsible for a base drag increase of up to 12% are distinguished. At the scale of the vehicle, whatever the distance  $l$ , wheels perturb the underflow and induce a global variation of the vertical balance of the vehicle wake. According to the state of the initial wake, significant base drag increase or decrease are observed. Considering the scale of the wheels, if the wheel-to-base distance  $l/w$  ( $w$  being the width of the wheels) is smaller than a threshold of order 3 in the present configuration, the base drag increases and is very sensitive to  $l/w$ . In this situation, a mean mass transfer from the vehicle wake to the wake of the rear wheels is observed. Based on these observations, the physical model proposed in chapter 4 is used to explain this high-sensitivity regime.

Most of these results are published in [Bao et al. \(2023\)](#) in the *Journal of Wind Engineering & Industrial Aerodynamics*.

Main ingredients of wheel-vehicle interactions (Rebus)



## Contents

---

<b>5.1</b>	<b>Introduction</b>	<b>62</b>
<b>5.2</b>	<b>Experimental setup</b>	<b>63</b>
<b>5.3</b>	<b>Salient features of wheel-vehicle interactions</b>	<b>64</b>
5.3.1	Drag sensitivity to wheel-to-base distance	64
5.3.2	Global forcing of vehicle wake by the wheels	65
5.3.3	Near wake interactions for small wheel-to-base distance	67
<b>5.4</b>	<b>Influence of initial asymmetry of the baseline wake</b>	<b>73</b>
<b>5.5</b>	<b>Discussions and concluding remarks</b>	<b>75</b>
5.5.1	Evaluating the effect of mass exchange on the base drag	75
5.5.2	Effects of wheel state: rotating or stationary	76
5.5.3	Influence of tire width on base drag	77
5.5.4	Concluding remarks	77

---

## 5.1 Introduction

In the previous chapter, a parametric study was performed by perturbing the underflow of the square-back vehicle geometry using a pair of two-dimensional (2-D) D-shaped obstacles. By systematically varying the obstacle width and the relative distance from the obstacles to the base of the vehicle, a key mechanism of the local near-wake interactions was found to be a mean mass transfer from the wake of the vehicle to the wakes of the obstacles. In addition, we also found that the obstacles perturb the underflow, leading to a variation in the vertical balance of the vehicle wake. These local and global effects are believed to be the salient features of the wheel-vehicle interaction problem. In this chapter, we seek to validate these findings under a more realistic setup, by installing four rotating wheels on the square-back vehicle geometry.

From an industrial perspective, there are pieces of evidence showing the global and local effects of the wheels on the vehicle wake. Several aspects of wheel-vehicle interactions were considered in previous studies. Adding fixed or rotating wheels to a vehicle results in an important drag increase (Wickern *et al.*, 1997; Regert & Lajos, 2007; Huminic & Huminic, 2017; Wang, 2019; Pavia, 2019). The flow field was studied and it was found that wheels lead to modifications at the scale of the vehicle, such as a reduction in the underflow momentum and a change in the vertical balance of the vehicle wake.

The effect of wheel rotation was specifically studied by actuating the wheels on a fixed ground or by using moving ground facilities (Cogotti, 1983; Mercker & Knape, 1989; Le Good *et al.*, 1998; Elofsson & Bannister, 2002; Heft *et al.*, 2012; Pavia & Passmore, 2017; Wang *et al.*, 2019, 2020; Rejniak & Gatto, 2021; Yu *et al.*, 2022; Aultman *et al.*, 2022). On a given set-up, comparing fixed and rotating wheel configurations, it was found that rotation is responsible for a moderate drag change (mostly drag decreases). Global changes at the scale of the vehicle were also measured for example in Elofsson & Bannister (2002) and Wang *et al.* (2020). Moreover, changes in the local interactions between the rear wheel wakes and the vehicle wake were proposed in Elofsson & Bannister (2002) and Wäschle (2007) as possible reasons for the changes in drag. However, the interaction mechanisms at the scale of the rear wheels were not revealed in these two studies.

In the present chapter, the wheel-vehicle interactions are investigated based on the square-back Windsor body with wheels. We focus on the base drag evolution and large-scale dynamics of the near wake because the base drag is the major drag contributor for this type of vehicle (Schuetz, 2016). Our choice is to follow the investigation in chapter 4, by selecting the distance between the rear wheels and the base of the vehicle as the main parameter. This is also based on the fact that a wide range of relative distances can be found for different car types in the market. Our goal for this chapter is first to analyze how the wake and drag of the vehicle are globally modified by the presence of the wheels. The second goal is to reveal in detail what are the salient features of the local interactions between the rear wheels and the vehicle wake. The experimental apparatus

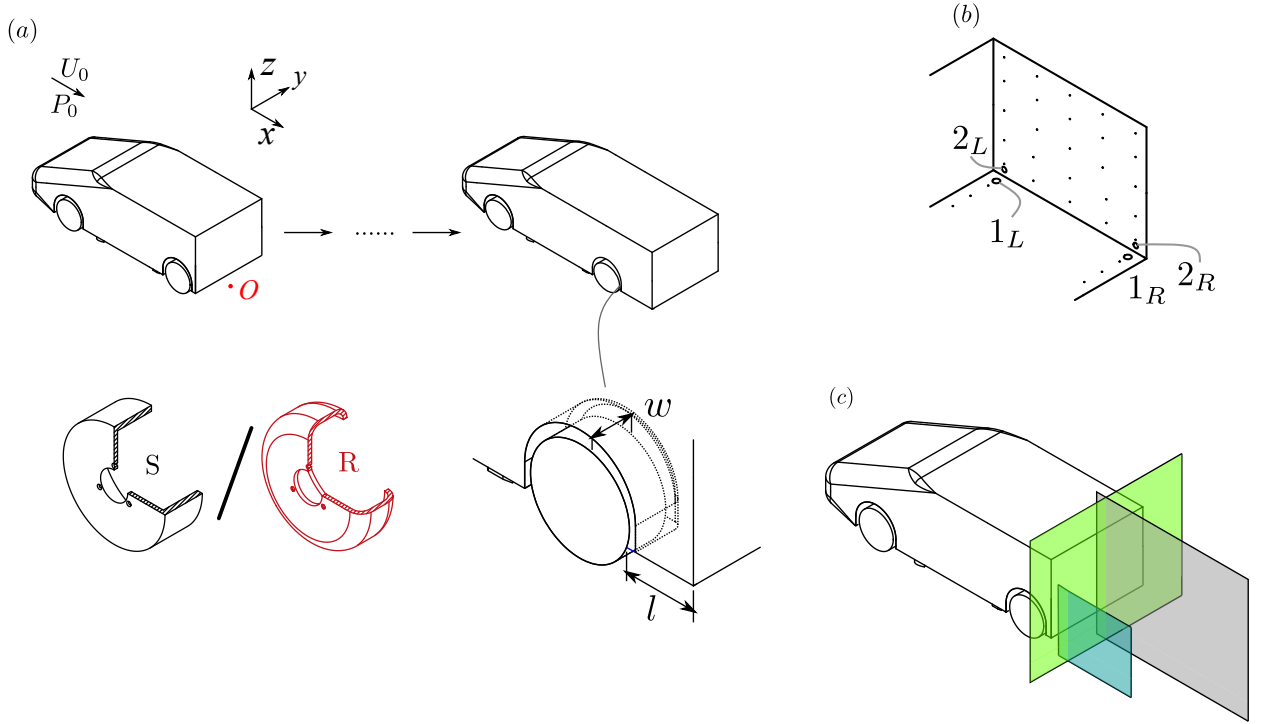


Figure 5.1: Experimental set-up. (a) Arrangement of the vehicle model and the wheels. S and R denote sharp-edged-shoulder and rounded-shoulder wheels, respectively. (b) Locations of pressure taps. Points indicate locations of mean pressure measurements and circles indicate locations of time-resolved pressure measurements. (c) Particle image velocimetry (PIV) fields of view (FOVs) in the symmetry plane of the vehicle ( $y/H = 0$ , colored in gray), the symmetry plane of the left-hand side wheels ( $y/H = -0.58$ , colored in blue), and a cross-flow plane ( $x/H = 0.03$ , colored in green).

used for this chapter are detailed in §5.2. By installing the wheels and varying the wheel-to-base distance, the salient features of wheel-vehicle interactions are revealed in §5.3. The influence of large-scale asymmetry of the vehicle wake is then presented in §5.4. These results are discussed in §5.5, which are followed by concluding remarks.

## 5.2 Experimental setup

The square-back Windsor body with different lengths shown in figure 5.1 is selected for the study in this chapter. Two types of wheels are used and are shown in figure 5.1(a). These wheels are of the same diameter  $0.52H$  and width  $w = 0.19H$ . For the wheel type S, the shoulders are sharp edges. On the other hand, for the wheel type R, the shoulders are rounded with a radius of  $0.3w$ . The wheels are installed on the motors mounted on the floor. The recess between each wheel and the floor is carefully filled using kraft paper (detailed before in §2.2.3 of chapter 2). During the experiments, the wheels are always rotated at the speed of 3187 RPM matching the free-stream velocity. Additional comments and analyses on the effects of wheel state (rotating or stationary) are given in §5.5.2.

All the results presented are collected under a free-stream velocity  $U_0 = 25 \text{ m s}^{-1}$ , corresponding to a height-based Reynolds number  $Re_H = U_0 H / \nu = 4.8 \times 10^5$ , where  $\nu$  is the kinematic viscosity of the air at operating temperature. The same Windsor model equipped with sharp-edged-shoulder wheels was tested in Varney (2020). It was found that the model is Reynolds insensitive when the test is conducted above the Reynolds number selected for the present chapter.

The cases tested are categorized into different groups and are summarized in table 5.1. For the wheel group S (sharp-edged shoulder), different model lengths  $L/H = \{3.41, 3.49, 3.59, 3.68, 3.78, 3.87, 3.97\}$  are tested. On the other hand, for the wheel group R (rounded shoulder), only the shortest and the longest vehicle lengths are tested. The distance  $l$  from the rear wheels to the base (see figure 5.1a) is varied thanks to the variation in the vehicle length, which gives  $l/w = \{0.65,$

$L/H$	3.41	3.49	3.59	3.68	3.78	3.87	3.97
Wheel group S	×	×	×	×	×	×	×
Wheel group R	×	-	-	-	-	-	×

Table 5.1: Cases considered for each test group.

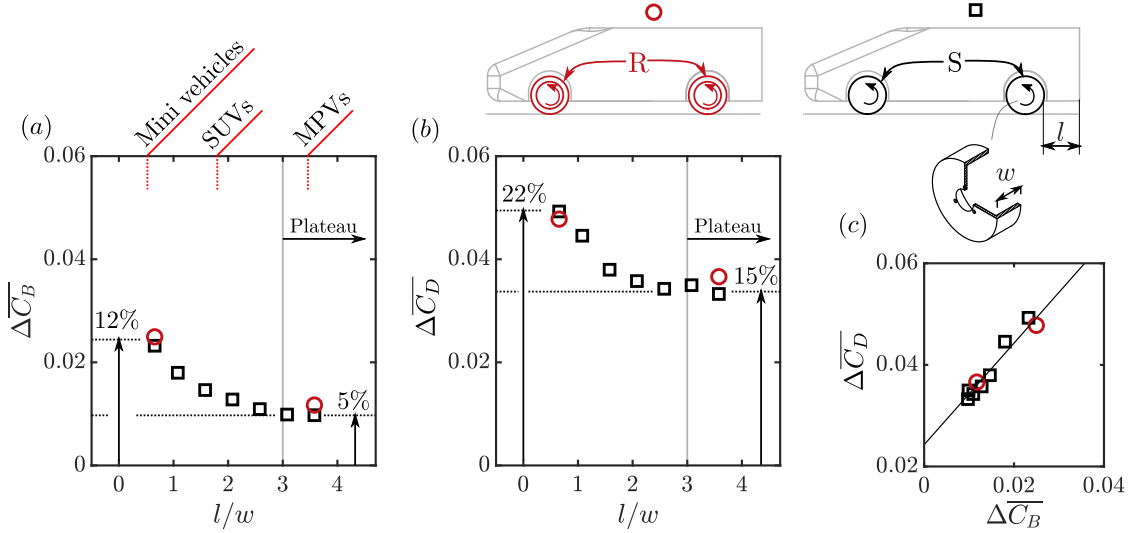


Figure 5.2: Evolution of (a) the base drag  $\Delta \overline{C}_B = \overline{C}_B - \overline{C}_{B0}$  and (b) total drag  $\Delta \overline{C}_D = \overline{C}_D - \overline{C}_{D0}$  of the body as a function of the wheel-to-base distance  $l/w$ . Both sharp-edged-shoulder wheels (S, colored in black) and rounded-shoulder wheels (R, colored in red) are considered. The relationship between  $\Delta \overline{C}_D$  and  $\Delta \overline{C}_B$  is shown in (c).

1.08, 1.58, 2.08, 2.58, 3.08, 3.58}. This  $l/w$  range is designed according to the results in chapter 4, where a strong base drag sensitivity was found for  $l/w < 2.5$ . It also includes the  $l/w$  values for typical road square-back vehicles, from mini vehicles for example Smart Fortwo W453 ( $l/w = 0.52$ ) to big Multi-Purpose Vehicles (MPVs) for example Mercedes-Benz V-class W447 ( $l/w = 3.46$ ).

Two different pressure measurement systems are used to perform surface pressure measurements. The first one used for time-averaged and long-timescale measurements includes two pressure scanners. 25 taps on the base and 6 taps on the underside (see figure 5.1b) are used in the present chapter. The taps on the base and on the underside are connected, respectively, to the two scanners with ranges of  $\pm 1$  and  $\pm 2.5$  kPa. The second system dedicated to time-resolved measurements contains four differential pressure sensors connected to the pressure taps located on the base and the underside. These taps are numbered as  $n_{L,R}$  ( $n \in [1, 2]$ ) as shown in figure 5.1(c), where  $L$  and  $R$  denote the left-hand and right-hand sides, respectively.

The velocity fields in the near wake are measured by the particle image velocimetry (PIV) system. Three two-dimensional fields of view (FOVs) are considered as depicted in figure 5.1(c). The first one located in the cross-flow plane ( $x/H = 0.03$ ) in proximity to the base of the vehicle is of stereoscopic (2-D three-component (2D3C)) set-up, capturing three velocity components. The other two FOVs respectively located in the symmetry planes of the vehicle ( $y/H = 0$ ) and of the left-hand rear wheel ( $y/H = -0.58$ ) are of 2-D two-component (2D2C) set-up, obtaining the streamwise  $u_x$  and vertical  $u_z$  velocity components.

## 5.3 Salient features of wheel-vehicle interactions

### 5.3.1 Drag sensitivity to wheel-to-base distance

The global impact of the wheels on the baseline wake is now investigated. In figure 5.2(a) and (b), the base drag  $\Delta \overline{C}_B = \overline{C}_B - \overline{C}_{B0}$  and total drag  $\Delta \overline{C}_D = \overline{C}_D - \overline{C}_{D0}$  relative to the baseline cases are shown respectively. For each case having a base drag value of  $\overline{C}_B$  and a total drag value of  $\overline{C}_D$ ,  $\overline{C}_{B0}$  and  $\overline{C}_{D0}$  represent the values of the corresponding baseline case with the same vehicle

length. A detailed measurement spanning all the possible wheel-to-base distances is conducted for the configuration using the sharp-edged-shoulder wheels S, while only the minimum and maximum  $l/w$  values are tested for the rounded-shoulder configuration R.

We focus first on the base drag variation in figure 5.2(a) for the configuration S. For the longest baseline case providing the maximum wheel-to-base distance  $\max(l/w)=3.58$ , the wheels are found to increase the base drag by  $\sim 5\%$  ( $\Delta\overline{C_B}/\overline{C_{B0}} \approx 5\%$ ). With decreasing  $l/w$ , we remark that the base drag increase is very similar for  $l/w = 3.58$  and  $l/w = 3.08$ . It is noted here that relative distances larger than  $l/w = 3.58$  were not considered for the present chapter. However, by modeling the wheels as D-shaped obstacles, larger "wheel-to-base" distances were considered in chapter 4. A clear plateau having weak base drag sensitivity to the wheel-to-base distance was identified. In what follows, we will therefore assume that a plateau is reached for  $l/w > 3$ . This will be further confirmed in §5.4 by changing the initial wake balance.

By reducing the length of the vehicle, the wheel-to-base distance  $l/w$  is decreased. From  $l/w = 3$  with decreasing  $l/w$ , a rapid quadratic increase in  $\Delta\overline{C_B}$  is observed until the smallest  $l/w$  is reached, maximally leading to a base drag increase of  $\sim 12\%$ . This suggests the emergence of additional near-wake interactions between the rear wheels and the vehicle wake resulting in an extra base drag increase.

In figure 5.2(b), we consider the total drag acting on the whole vehicle model (wheel drag is not weighted by the balance). In the plateau, the drag increase from the baseline case is  $\sim 15\%$ . With decreasing  $l/w$ , the wheels maximally lead to a  $\sim 22\%$  drag increase at the minimum  $l/w$ . The  $\Delta\overline{C_D}$  evolution with  $l/w$  is very similar to the  $\Delta\overline{C_B}$  evolution as shown before in figure 5.2(a) but presents an overall upward shift of  $\sim 0.024$ . The shift is due to the drag increase at the vehicle surfaces except at the base, for example the wheelhouse drag and/or the change in pressure at the front surfaces. More exactly, we observe that  $\Delta\overline{C_D}(l/w) = 0.024 + \Delta\overline{C_B}(l/w)$  as depicted by showing the relationship between the total drag  $\Delta\overline{C_D}$  and the base drag  $\Delta\overline{C_B}$  in figure 5.2(c). This means that with variation in  $l/w$ , the base drag increase is the only source of total aerodynamic drag increase.

By comparing the configuration R with S in figure 5.2, we note that the variations of the base drag are very similar. In the present chapter, we seek to reveal the general flow mechanisms governing the wheel-vehicle interactions and the base drag changes. The influence of wheel shoulder radius, on the other hand, will be specifically explored in the next chapter.

### 5.3.2 Global forcing of vehicle wake by the wheels

We first focus on the base pressure increase induced by the wheels for the longest body. By installing rotating wheels on a Windsor model, Pavia & Passmore (2017) have shown that the vehicle wake is modified from a well-balanced one to an asymmetric one dominated by a bottom recirculating flow. We therefore suspect the wheels to act as underflow perturbations modifying the global equilibrium of the wake. The largest wheel-to-base distance is considered here in order to focus on these global changes. The local interactions will be considered in the next section.

In figure 3.7 of chapter 3 (shown again in figure 5.3a), we showed that a systematic variation of the vehicle wake can be induced by placing a circular cylinder of varying diameter  $d$  (from  $d/H = 0$  to 0.087) spanning the whole width of the baseline vehicle at  $x/H = -1$  on either the top or bottom surface. A large number of cases are selected in order to have a good description of the effect of global equilibrium modification on the reference body. Their joint p.d.f. and mean base pressure distributions are shown in figure 5.3(a). The whole scenario with a competition between vertical and horizontal wake asymmetries is further pictured in figure 5.3(b) by the relationship between  $\overline{z_b/H}$  and  $|\overline{y_b/H}|$  (the absolute value is used for the horizontal component due to the transient wake switching motion). On the other hand, the variation in the mean vertical asymmetry  $\overline{z_b/H}$  leads to important variations of base drag as shown in figure 5.3(c). The baseline case with small  $|\overline{z_b/H}|$  presenting horizontal bi-modal dynamics has the least mean base drag.

Having this database for the reference body, we are now in a position to examine the effect of the wheels. When the wheels, either S or R, are installed, it is shown in figure 5.3(a) that the mean base pressure distribution is modified from a relatively uniform one with vanishing vertical asymmetry to an uneven one with an obvious positive vertical pressure gradient. More generally,

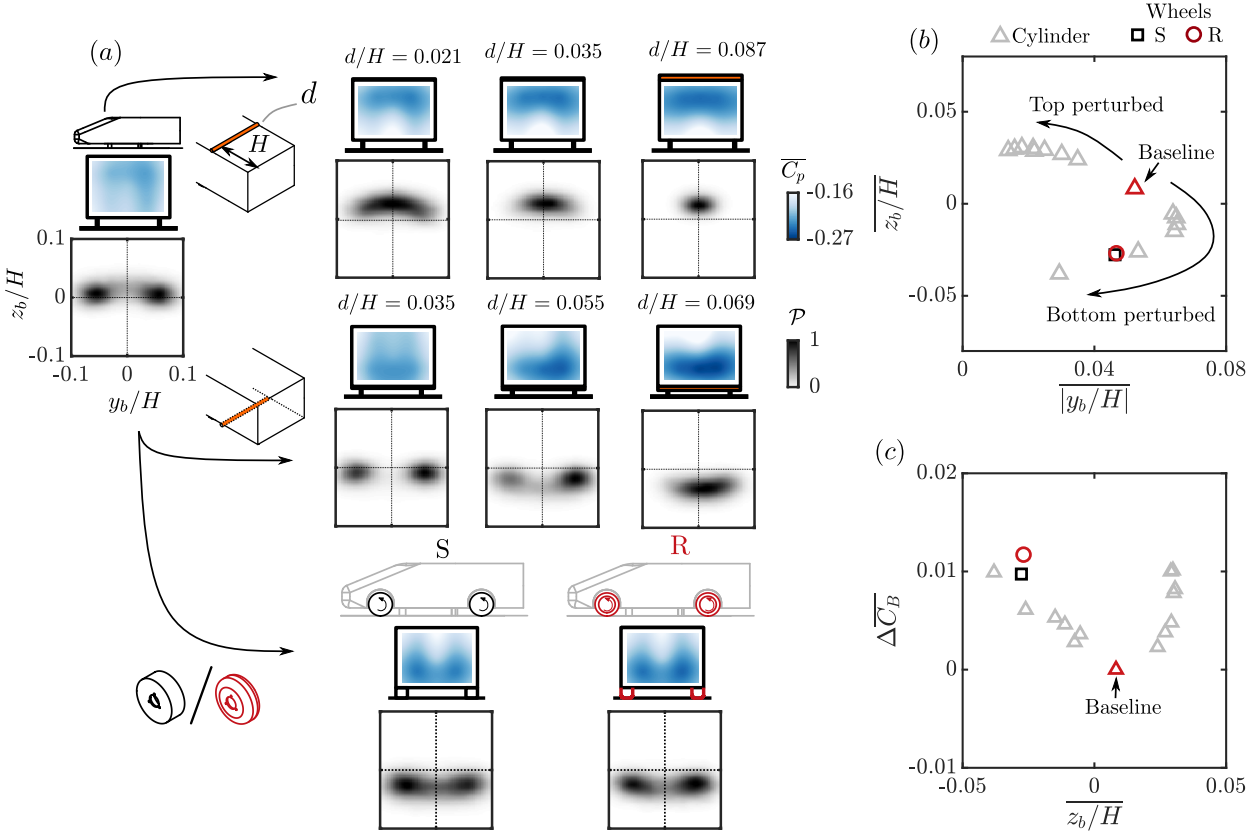


Figure 5.3: Longest baseline vehicle (wheel-to-base distance  $l/w = 3.58$ ) perturbed either by spanwise cylinder or wheels. (a) Effect of spanwise perturbing cylinder or wheels on the base pressure distribution and joint p.d.f. of the base CoP position. The cylinder of varying diameter  $d$  is placed horizontally at  $x/H = -1$  on either the top or bottom surface of the vehicle. (b) Mean vertical position of the base CoP  $\overline{z_b/H}$  versus mean absolute value of the horizontal base CoP position  $|y_b/H|$  for the baseline vehicle perturbed either by spanwise cylinder or wheels. (c) Base drag  $\Delta \overline{C_B}$  versus  $\overline{z_b/H}$  for the same cases in (b).

the mean value of the vertical CoP position  $\overline{z_b/H}$  is decreased by the wheels. Meanwhile, it is noted that the base pressure distributions and the joint p.d.f. of the wheel cases are very similar to that of the  $d/H = 0.055$  case. In figure 5.3(b), it is found that the wheel cases follow the relationship portrayed by the cylinder cases, indicating that the wheels play the same role as the underflow perturbing cylinder on the wake asymmetry. Focusing on figure 5.3(c) where the relationship between the vertical asymmetry and the base drag is discussed, we notice the wheel cases follow approximately the trend measured using the cylinder.

The wake flow is now investigated in figure 5.4 to understand how the wake is modified by the wheels. In figure 5.4(a), the mean streamlines and turbulent kinetic energy  $k$  in the symmetry plane of the longest vehicle are presented. In accordance with the pressure measurements, the wheels, either type S or R, reorganize the structure of the mean vehicle wake, leading to a strong bottom-dominated recirculating flow. The wake reorganization increases the low-pressure imprint at the bottom part of the recirculating flow on the base. At the same time, the interaction mechanism in asymmetric wakes as proposed in Haffner *et al.* (2020a) is enhanced by the growth of the upward cross-flow momentum, evidenced by the stronger flow fluctuation in the top shear layer. This aspect is shown in figure 5.4(b) by integrating the turbulent kinetic energy  $k$  across the measurement plane:

$$\mathcal{K}(x/H) = \int_0^{z_{max}} kd(z/H). \quad (5.1)$$

This quantity reveals the global enhancement of the turbulent fluctuation in the wake. It leads to changes in the intensity of the recirculating flow, which is quantified by defining a quantity:

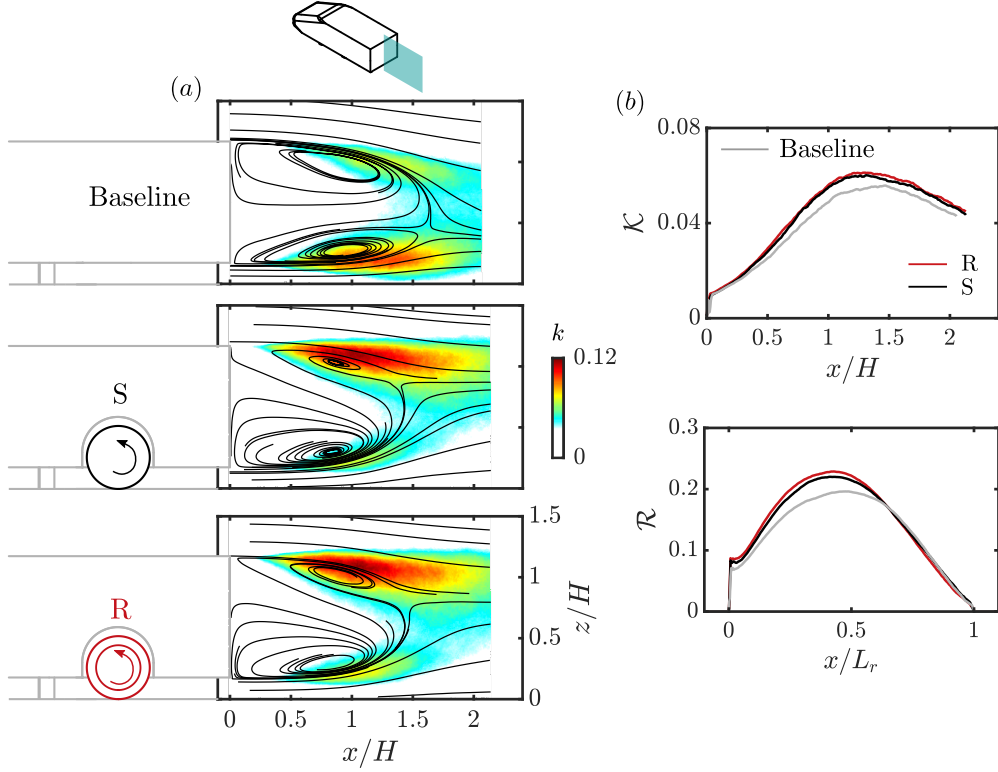


Figure 5.4: Effect of wheels on the wake of the longest baseline vehicle for configurations S and R. (a) Mean streamlines superimposed on the turbulent kinetic energy  $k$  distribution. (b) Streamwise evolution of the integrated turbulent kinetic energy  $\mathcal{K}$  and the recirculation strength  $\mathcal{R}$  for the cases in (a), Gray lines represent the baseline case having no wheels.

$$\mathcal{R}(x) = \int_{\bar{u}_x \leq 0} \sqrt{\bar{u}_x^2 + \bar{u}_z^2} d(z/H), \quad (5.2)$$

As shown in figure 5.4(b), the wheels, either type S or R, lead to an overall enhancement of the recirculating motion from the baseline case, with the maximum of the recirculating strength  $\mathcal{R}$  increases by  $\sim 12\%$ . This enhancement produces a lower pressure at the center of the recirculation region in accordance with the lower pressure footprint measured on the base (Dalla Longa *et al.*, 2019).

### 5.3.3 Near wake interactions for small wheel-to-base distance

In this section, the investigation is focused on the flow mechanisms resulting in the  $\Delta \overline{C_B}$  increase with decreasing  $l/w$  for  $l/w < 3$ . It is important to note here that the global forcing of the vehicle wake found in the last section is also measured for all the  $l/w$  cases in this section.

We start by examining in figure 5.5(a) the base pressure distribution for the longest vehicle ( $l/w = 3.58$ ) and the shortest vehicle ( $l/w = 0.65$ ). On the right-hand side of the base, the distribution of pressure difference  $\Delta \langle \overline{C_p} \rangle$  with respect to the corresponding baseline case is also shown for comparison. For both configurations S and R, the base pressure decreases when  $l/w$  is reduced. The portion of the base that contributes to the increase in  $\Delta \overline{C_B}$  can be obtained by comparing the  $\Delta \langle \overline{C_p} \rangle$  distributions. A decrease in  $\Delta \langle \overline{C_p} \rangle$  is observed at the bottom half of the base near the rear wheels. This region of base pressure decrease is also illustrated in figure 5.5(b) by the continuous decrease in  $\overline{z_b/H}$  with decreasing  $l/w$  at  $l/w < 3$ .

Now the pressure in the vicinity of the rear wheels is considered. The pressure measurements at the taps numbered  $1_L$  and  $2_L$  ( $1_R$  and  $2_R$ ), located in the symmetry plane of the left-hand (right-hand) side wheels (see the sketch in figure 5.5), are used for a comparison in figure 5.5(c). These pressure taps are located on both sides of the bottom trailing edge, representing the pressure levels behind the rear wheels and at the base near the rear wheels. It should be noted here that the

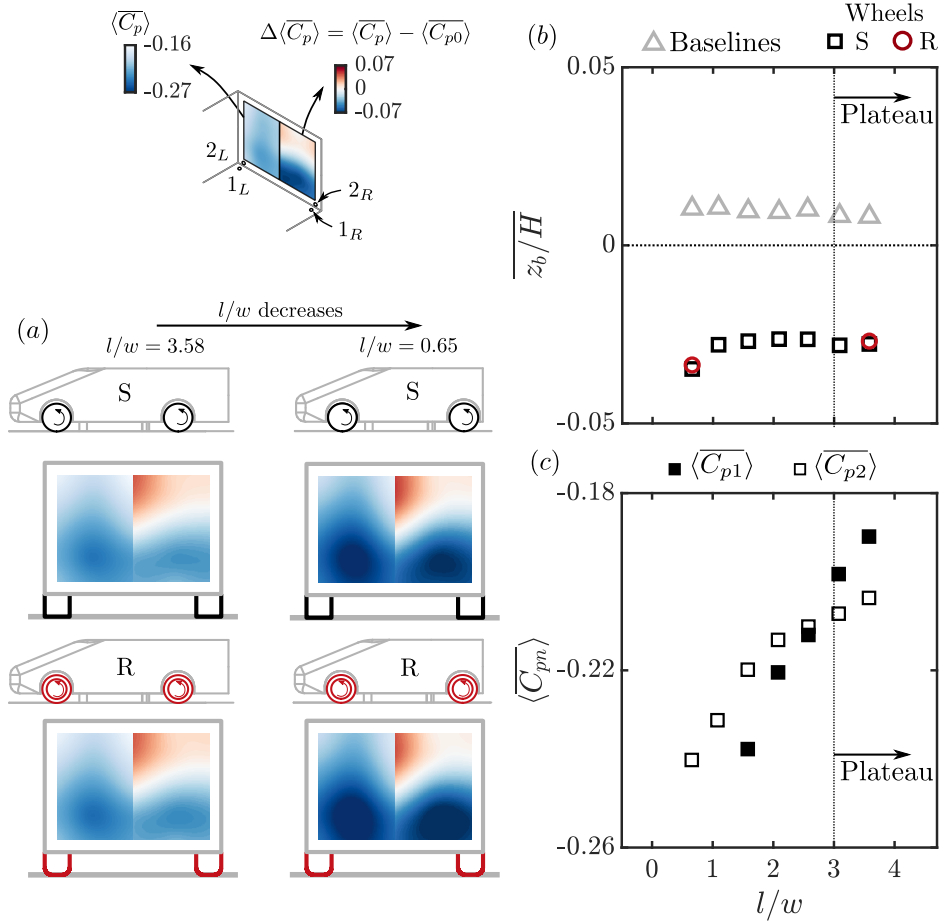


Figure 5.5: Effect of the reduction in the wheel-to-base distance  $l/w$  on the base pressure for configurations S and R. (a) Base pressure distributions for the smallest and the largest  $l/w$  cases, the mean values and the differences with respect to the corresponding baseline case are respectively presented at the left-hand and right-hand sides of the base. (b) Evolution of the mean vertical position of the base CoP  $\overline{z_b}/H$  with  $l/w$ , the values for the baseline cases (no wheels) are shown for comparison using triangles. (c) Comparison between the evolution of  $\langle C_{p1} \rangle$  and  $\langle C_{p2} \rangle$ , the location of the pressure taps are schematically shown above (a).

taps numbered 1 are always located at  $x/H = -0.07$  for different vehicle lengths. For the shorter cases  $l/w = 0.65$  and  $1.58$ , pressure taps  $1_L$  and  $1_R$  are not available due to mechanical constraints. In the plateau ( $l/w > 3$ ),  $\langle C_{p1} \rangle$  is higher than  $\langle C_{p2} \rangle$ . For a canonical separating flow, the pressure condition at separation is similar to the observation here with the separating streamline inducing a lower pressure inside the recirculation region (Bradshaw, 1973). On the other hand, in the drag-sensitive regime  $l/w < 3$ ,  $\langle C_{p1} \rangle$  is lower than  $\langle C_{p2} \rangle$ . The difference  $\langle C_{p2} \rangle - \langle C_{p1} \rangle$  increases with decreasing  $l/w$ .

These observations point out the close relationship between the pressure decrease at the model base and the increasing influence from the rear wheels when the wheel-to-base distance  $l/w$  is decreased in the drag-sensitive regime  $l/w < 3$ . The streamwise development of the rear wheel wake is therefore of particular importance here. We then define a new reference frame in figure 5.6(a) in order to examine this. The rearmost location of the part of the rear wheels exposed to the underflow is set as the origin of this frame with  $x_w = 0$ . For each  $l/w$  case, as shown in the sketch in figure 5.6(b), several pressure taps are located under the vehicle in the symmetry planes of the rear wheels. These pressure measurements are plotted against the distance from the measurement location to the rear wheels  $x_w$  in figure 5.6(b). For case  $l/w = 3.58$  (maximum  $l/w$ ), a rapid pressure increase with increasing  $x_w/w$  is measured at  $x_w/w < 3$  which corresponds to the near-wake region of the rear wheels. For decreasing  $l/w$ , the bottom trailing edge of the vehicle approaches the rear wheels and is gradually influenced by the near-wake region of the rear wheels. This is the reason for the decrease of  $\langle C_{p1} \rangle$  in the drag-sensitive regime  $l/w < 3$ . For all the cases in

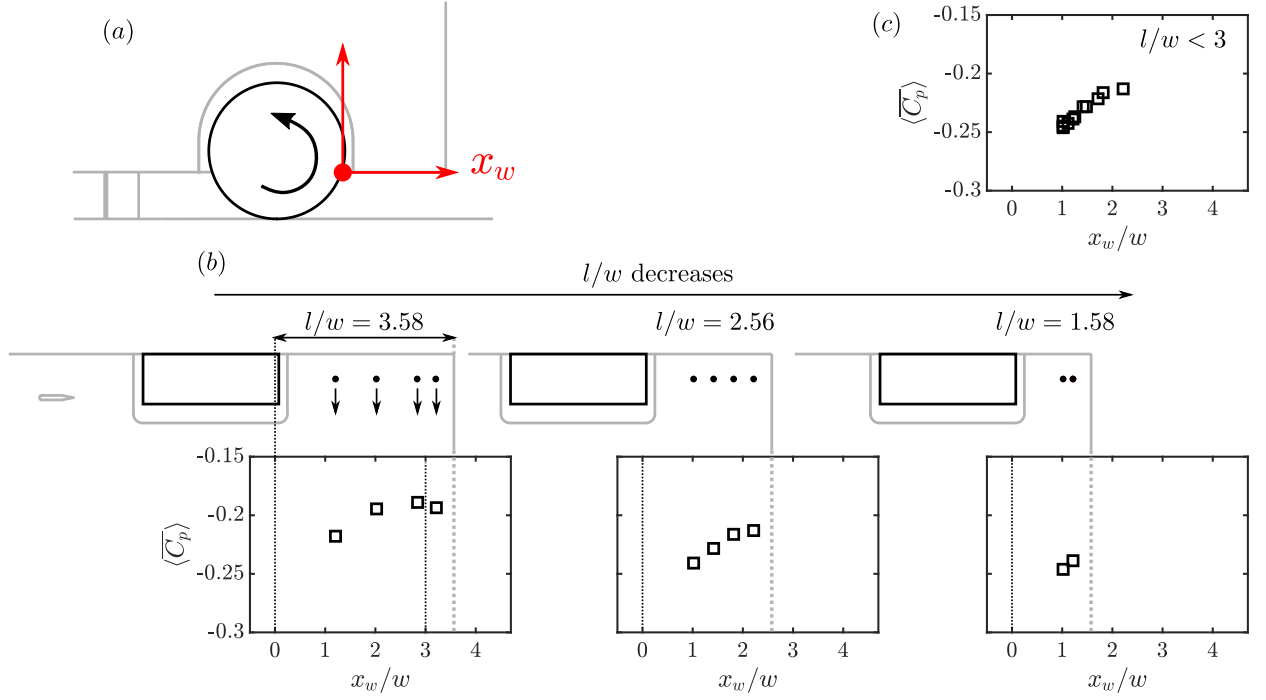


Figure 5.6: Streamwise pressure evolution in the wake of the rear wheels (sharp-edged-shoulder ones). (a) Definition of a wheel-fixed coordinate system. (b) Evolution of  $\langle C_p \rangle$  as a function of  $x_w$  for three different  $l/w$  cases. (c) Superposition of the  $\langle C_p \rangle$  evolution for all the cases in the drag-sensitive regime  $l/w < 3$ .

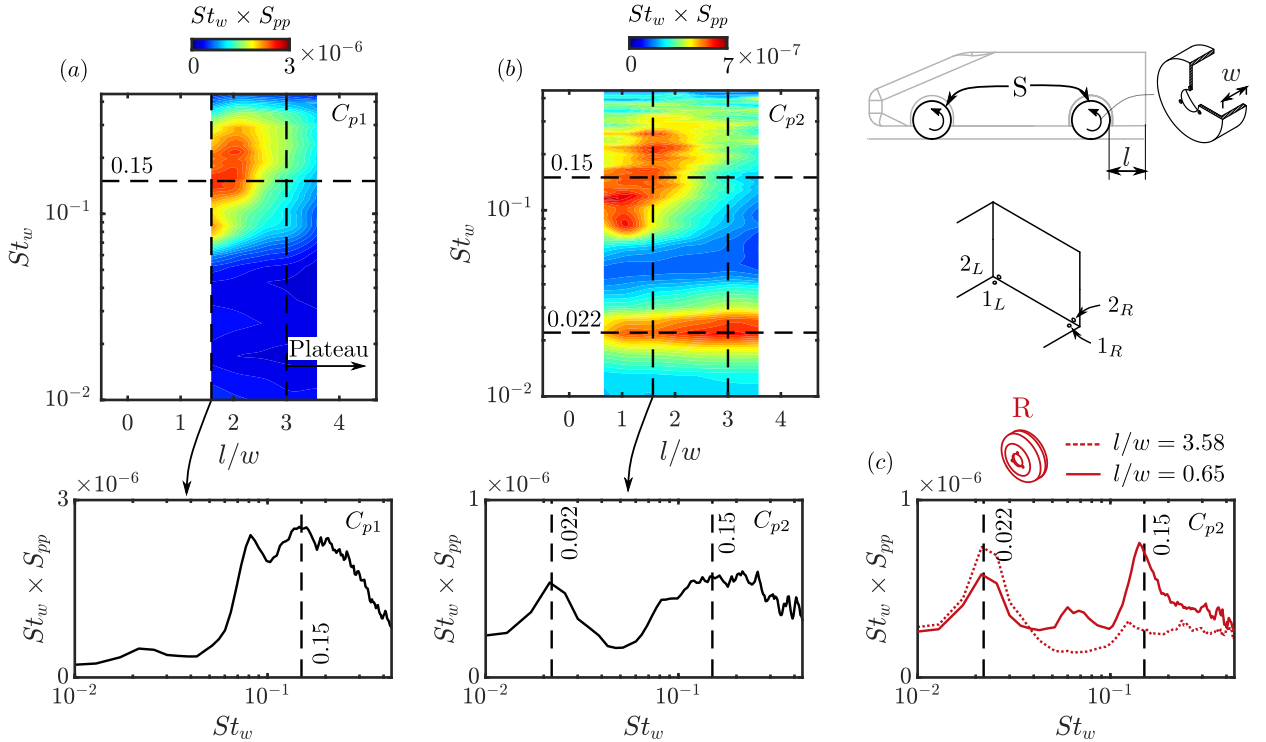


Figure 5.7: For configuration S: evolution of the premultiplied spectra of  $C_{p1}$  (a) and  $C_{p2}$  (b) with the wheel-to-base distance  $l/w$ . At  $l/w = 1.58$ , the spectra are also shown. For configuration R: premultiplied spectrum of  $C_{p2}$  (c) for the maximum and the minimum  $l/w$ .

the drag-sensitive regime ( $l/w < 3$ ), the streamwise pressure developments are gathered together in figure 5.6(c). It is found that all these cases collapse approximately on the same evolution. This means that the wakes of the rear wheels keep their mean properties in the drag-sensitive regime when  $l/w$  is varied. Again, we notice a decrease in pressure with decreasing  $x_w/w$  at  $x_w/w < 3$ .

Noticeably, the bottom trailing edge of the vehicle experiences a gradual increase of periodic

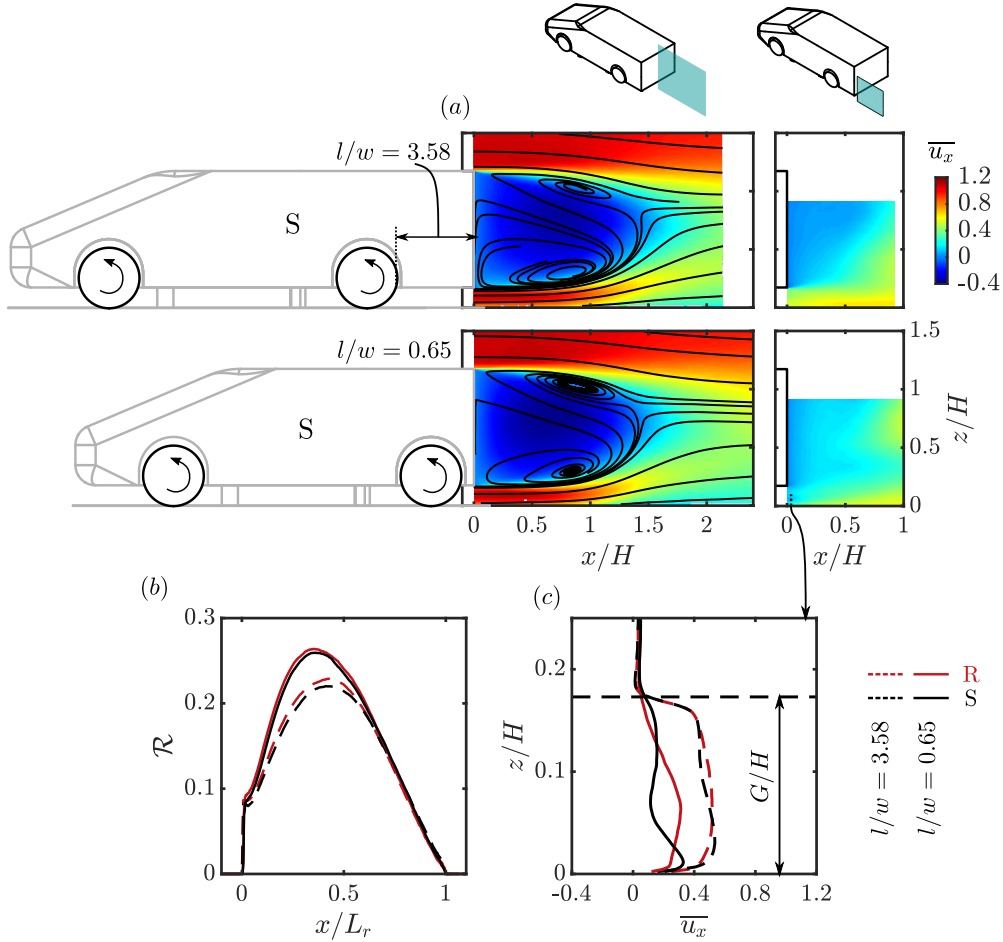


Figure 5.8: Effects of  $l/w$  reduction from the maximum  $l/w$  ( $l/w = 3.58$ ) to the minimum  $l/w$  ( $l/w = 0.65$ ) on the mean flow downstream of the vehicle. (a) Distributions of mean streamwise velocity  $\bar{u}_x$  in the symmetry plane of the vehicle at  $y/H = 0$  and of the left wheels at  $y/H = -0.58$  for configuration S. (b) Recirculation strength  $\mathcal{R}$  for the configurations S and R. (c)  $\bar{u}_x$  profiles along  $x/H = 0.03$  in the symmetry plane of the left wheels for configurations S and R.

dynamics with decreasing  $l/w$ , which is captured by the unsteady pressure sensors numbered 1 and 2. The evolution with  $l/w$  of the premultiplied spectra of the pressure signals obtained from the pressure taps 1 and 2 are shown in figure 5.7(a) and (b). Pressure sensors 1 measure a rapid growth in energy at  $St_w = fw/U_0 = 0.15$  (here  $w$  is the width of the wheels) with decreasing  $l/w$  in the range  $l/w < 3$ . This growing influence of the wheel wake dynamics is also observed at the base (see figure 5.7b). It is noted here that [Croner \*et al.\* \(2013\)](#) experimentally measured a peak at  $St_w = 0.14$  downstream an isolated rotating wheel wake. With the help of numerical simulations, they found the same peak in the spectrum of the side force. Recently, this  $St_w$  was also measured by [Patel \*et al.\* \(2022\)](#). Therefore, the peak measured in the present chapter may be the signature of the horizontal periodic motion of the rear wheel wake. Finally, a peak at a relatively low frequency, about  $St_w = 0.022$  (corresponding to  $St_W = fW/U_0 = 0.16$ , where  $W$  is the width of the vehicle), is measured at the base. This frequency matches with the horizontal periodic dynamics of the vehicle wake measured for example in [Grandemange \*et al.\* \(2013b\)](#) and [Lorite-Díez \*et al.\* \(2020b\)](#). For configuration R, figure 5.7(c) shows the premultiplied spectrum of the pressure signal obtained from the pressure taps 2. We observe the same evolution as in figure 5.7(b) for configuration S. The low-frequency peak at  $St_w = 0.022$  driven by the vehicle wake, is observed in both situations  $l/w = 3.58$  and  $0.65$ . The signature of the wheel wake dynamics at  $St_w = 0.15$  is only detected for  $l/w = 0.65$ . This is because for the case  $l/w = 3.58$ , the rear wheels are located relatively far from the base.

The velocity fields are investigated in order to understand the modifications in the vehicle wake and to reveal the flow mechanisms responsible for the  $\Delta\bar{C}_B$  increase with decreasing  $l/w$

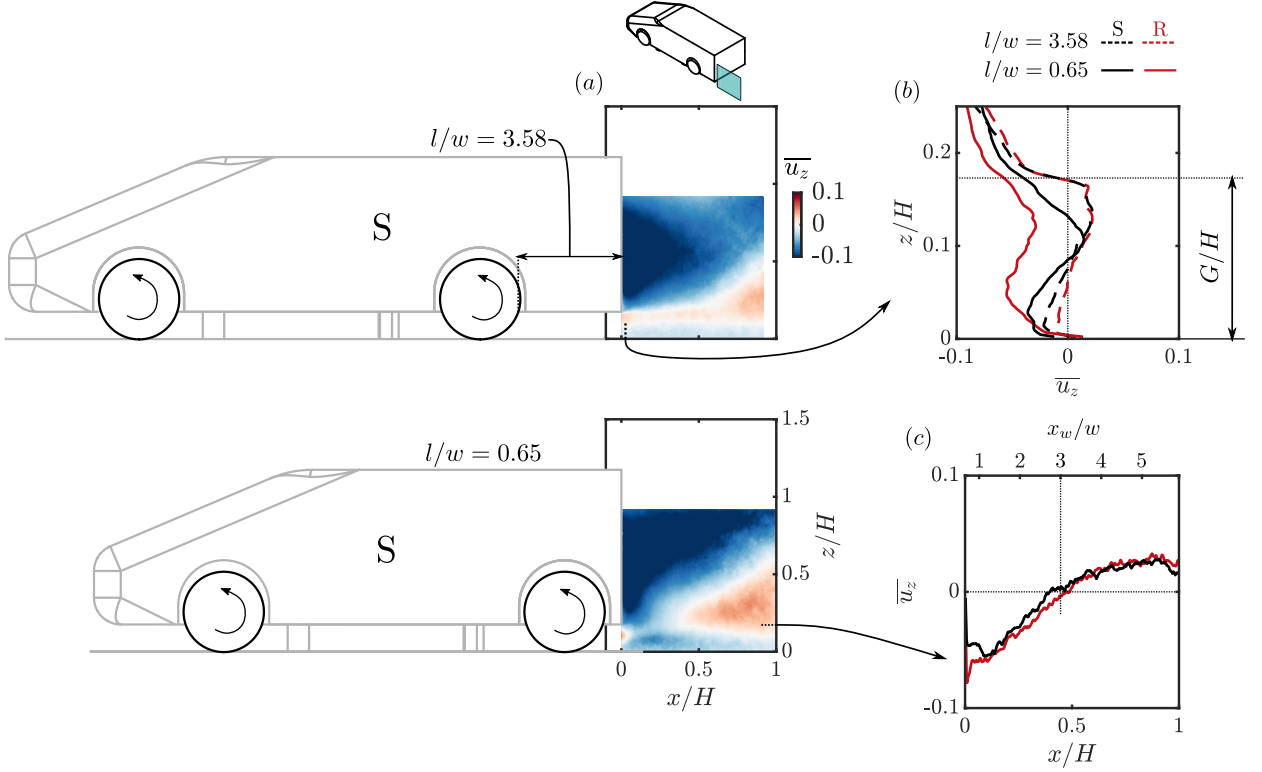


Figure 5.9: (a) Effect of  $l/w$  reduction on the mean vertical velocity  $\bar{u}_z$  in the symmetry plane of the left-hand wheels for configuration S. (b) Vertical profiles of  $\bar{u}_z$  at  $x/H = 0.03$  for configurations S and R. (c)  $\bar{u}_z$  distributions at the height of the ground clearance  $z/H = G/H$  for the  $l/w = 0.65$  cases of the two configurations.

for  $l/w < 3$ . The streamwise velocity  $\bar{u}_x$  downstream the vehicle is presented in figure 5.8(a). Similar mean velocity fields obtained for rounded-shoulder wheels are not shown for brevity. First of all, in the symmetry plane of the vehicle  $y/H = 0$ , no obvious change in the wake topology is noticed. However, by integrating the flow momentum inside the recirculation region, the recirculation strength  $\mathcal{R}$  shows an important change in figure 5.8(b). From  $l/w = 3.58$  to  $l/w = 0.65$ , the maximum of  $\mathcal{R}$  is increased by  $\sim 12\%$ . This is valid for both configurations S and R.

Local velocity measurements shown in figure 5.8(a), downstream of the left-hand wheels, reveal a more pronounced difference between the cases. In the symmetry plane of the left-hand wheels, the streamwise velocity  $\bar{u}_x$  below the vehicle wake is lower for  $l/w = 0.65$  than  $l/w = 3.58$ . This reduces significantly the mean shear between the vehicle wake and the wakes of the rear wheels as illustrated in figure 5.8(c) by plotting the  $\bar{u}_x$  distributions along  $x/H = 0.03$  in this plane. It is shown that no matter the type of wheels, the decrease of  $l/w$  always reduces the mean shear between the vehicle wake and the wakes of the rear wheels.

Along with the mean shear strength with reducing  $l/w$ , an important remark is that a mean mass transfer from the vehicle wake to the wakes of the rear wheels is observed. Indeed, the same observation was made in the last chapter when the wheels are modeled by a pair of 2-D D-shaped obstacles. In figure 5.9, the mass transfer is illustrated by the distribution of the mean vertical velocity  $\bar{u}_z$  in the symmetry plane of the left-hand wheels for the same cases as in figure 5.8(a). A clear difference is found near the base of the vehicle. For the  $l/w = 0.65$  case, there is a downward motion from the recirculation region of the vehicle toward the ground indicated by an overall negative  $\bar{u}_z$  in the flow downstream of the rear wheel. This feature is not observed for the  $l/w = 3.58$  case. The difference is better illustrated by plotting the distribution of  $\bar{u}_z$  along  $x/H = 0.03$  in figure 5.9(b) for both the configurations S and R. For the cases  $l/w = 3.58$ , we notice a sharp change in  $\bar{u}_z$  at the location of the shear  $z/H = G/H$  with different signs above and below this location. On the other hand, case  $l/w = 0.65$  always present a negative  $\bar{u}_z$  near  $z/H = G/H$ .

The streamwise span of the mean mass transfer is quantified in figure 5.9(c) by plotting the

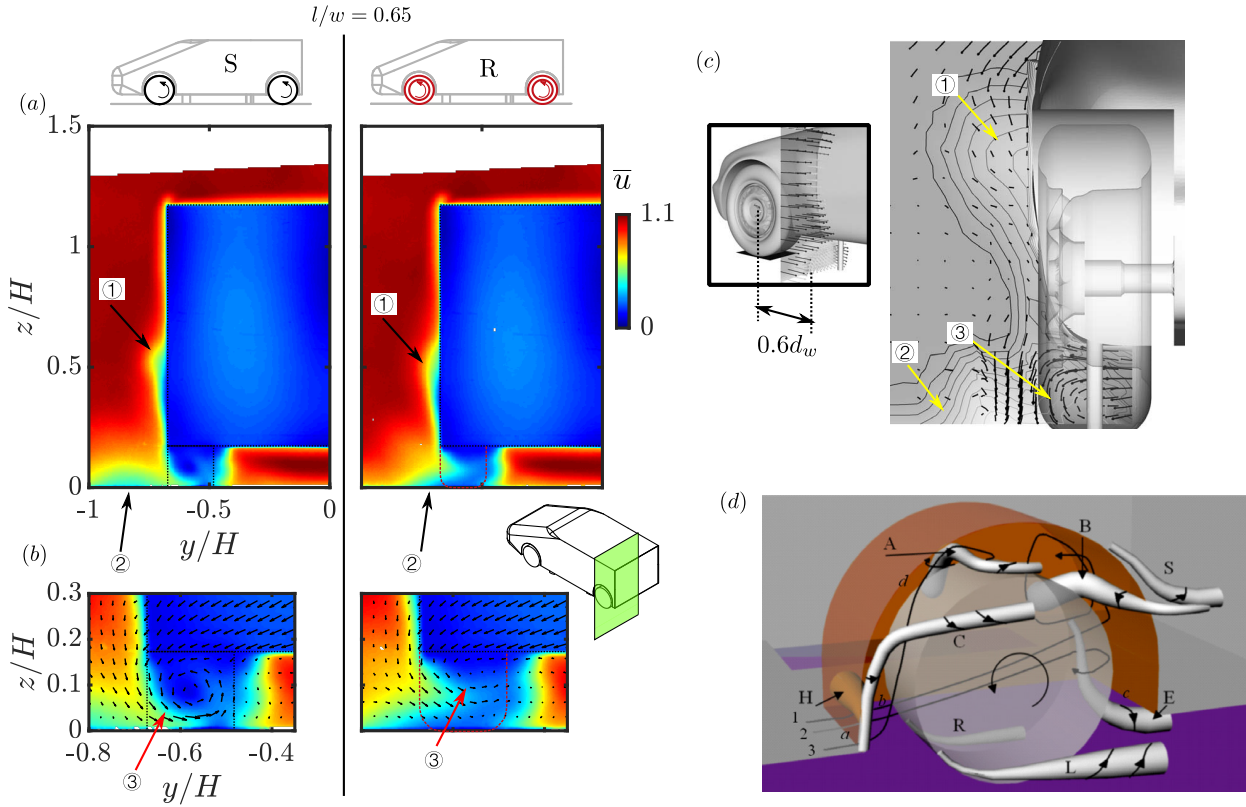


Figure 5.10: For the shortest vehicle case  $l/w = 0.65$ : (a) Mean velocity magnitude  $\bar{u}$  in the cross-flow plane at  $x/H = 0.03$  for configurations S and R. (b) Zoom views of the cases in (a) superimposed by in-plane mean velocity vectors. (c) Mean in-plane velocity vectors in a cross-flow plane at  $0.6 d_w$  ( $d_w$  is the diameter of the wheel) behind the left-hand front wheel of a 1/4 scale car model in Wäschle (2007). (d) Vortex skeleton model proposed by Regert & Lajos (2007).

mean vertical velocity  $\overline{u_z}$ , at the ground clearance height  $G/H$ , as a function of either the distance from the base  $x/H$  or the distance from the rear wheels  $x_w/w$ . The length of the mass exchange interface approximately ends at  $x_w/w = 3$ . It is reminded here that this region behind the rear wheels with  $x_w/w < 3$  was shown to experience a lower pressure than the wake of the vehicle (see figure 5.5c). With variation in  $l/w$ , the length of the region is not expected to be modified since the pressure in the rear wheel wake is measured to be not changed in figure 5.6(c). The physical picture is thus that the rear wheel wakes impose a lower static pressure and a downstream region having the ability to induce mass exchange from the main wake of the vehicle. With the length of this region of order  $x_w/w = 3$ , a decrease of the wheel-to-base distance  $l/w$  then induces a higher mass transfer and a larger drag increase. Further comments on the relation between the mass transfer and the base drag sensitivity are provided in §5.5.1 by adapting the model of chapter 4.

For the  $l/w = 0.65$  case, additional velocity measurements at  $x/H = 0.03$  are shown in figure 5.10(a) to show the flow structures generated by the wheels and to provide the information of mass exchange in the horizontal direction of the interaction interface. The distributions of the mean velocity magnitude  $\bar{u}$  are shown for the two cases S and R. In figure 5.10(a), we see clearly several flow regions that experience a deficit of mean longitudinal momentum. The wake of the left-hand rear wheel has the same velocity level as the recirculation region behind the vehicle. Another region (marked by ①) is observed for both configurations S and R behind the rear wheelhouse. A third region (marked by ②), is situated at the left-hand side of the wheel. This region is clearly visible for configuration S while for configuration R it is closer to the left-hand shear layer of the wheel. When looking closer at the flow behind the wheel in figure 5.10(b), a counter-clockwise mean streamwise vortical structure (marked by ③) is depicted by the in-plane mean velocity vectors. This structure is noticed for both configurations and appears to be less intense for configuration R than for S. In addition, the velocity vectors at the height of the ground clearance show that the mass transfer is always from the vehicle wake to the wakes of the rear wheels. The span of the mass exchange

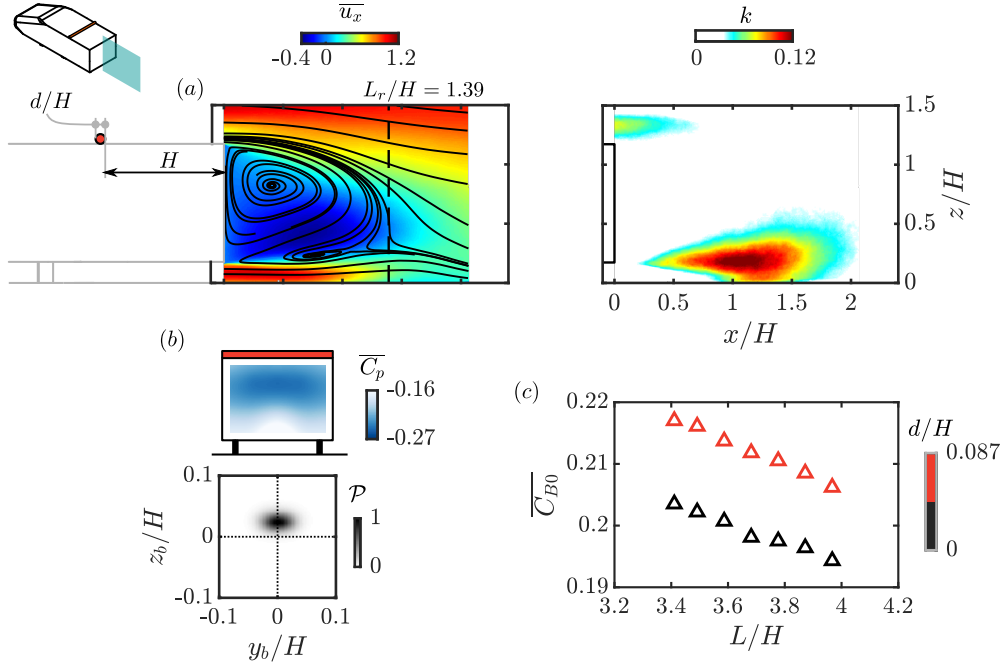


Figure 5.11: Baseline flow for the longest vehicle  $L/H = 3.97$  perturbed by a circular cylinder  $d/H = 0.087$  at  $x/H = -1$  on the top surface. (a) Mean streamwise velocity  $\overline{u_x}$  and turbulent kinetic energy  $k$  in the symmetry plane of the vehicle  $y/H = 0$ . (b) Mean base pressure distribution and the Joint probability density function (p.d.f.) of the base CoP position. (c) Evolution of the base drag  $\overline{C_{B0}}$  with the length of the vehicle  $L/H$ , the baseline cases from chapter 3 with  $d/H = 0$  are shown for comparison.

$L/H$	3.41	3.49	3.59	3.68	3.78	3.87	3.97
$\overline{C_{B0}}$	0.217	0.216	0.214	0.212	0.211	0.209	0.206
$\overline{C_{D0}}$	0.295	0.298	0.295	0.295	0.294	0.292	0.292

Table 5.2: Evolution of the mean aerodynamic coefficients with the model length  $L$ .

surface in the spanwise direction is approximately the width of the wheel.

We now compare the wheel wake structure in the present work with that in previous studies. The experimental measurements behind the front wheel of a car model in Wäschle (2007) are selected for the comparison in figure 5.10(c). A moving ground facility was used and the wheels are solid due to the small scale of the model. Recently in Josefsson *et al.* (2022), the measurements were confirmed by a combination of experiments and numerical simulations using deformable tires. The measurement plane was located at  $0.6d_w$  downstream of the wheel axle, where  $d_w$  represents the diameter of the wheel. In the present chapter, the measurement plane is located at  $0.8d_w$  downstream of the wheel axle. First, the two regions of momentum loss ① and ② were measured. In Wäschle (2007), additional numerical simulations were able to reveal that two streamwise vortical structures are the reasons for the momentum loss regions. In addition, the vortical structure ③ behind the wheel was measured with the same rotation direction as the present work. Finally, the present work is found also in accordance with the vortex skeleton model (see figure 5.10d) proposed by Regert & Lajos (2007) using RANS simulations and confirmed by Krajnović *et al.* (2011) based on Large-eddy simulations.

## 5.4 Influence of initial asymmetry of the baseline wake

In this section, we examine the wheel-vehicle interactions based on a different baseline wake. This baseline wake is derived from the previous one by placing a perturbing cylinder having a diameter of  $d/H = 0.087$  on the top surface (at  $x/H = -1$ , see §5.3.2) for the seven different vehicle lengths  $L/H$ . A picture of this baseline flow is presented in figure 5.11(a) by showing the measurements for

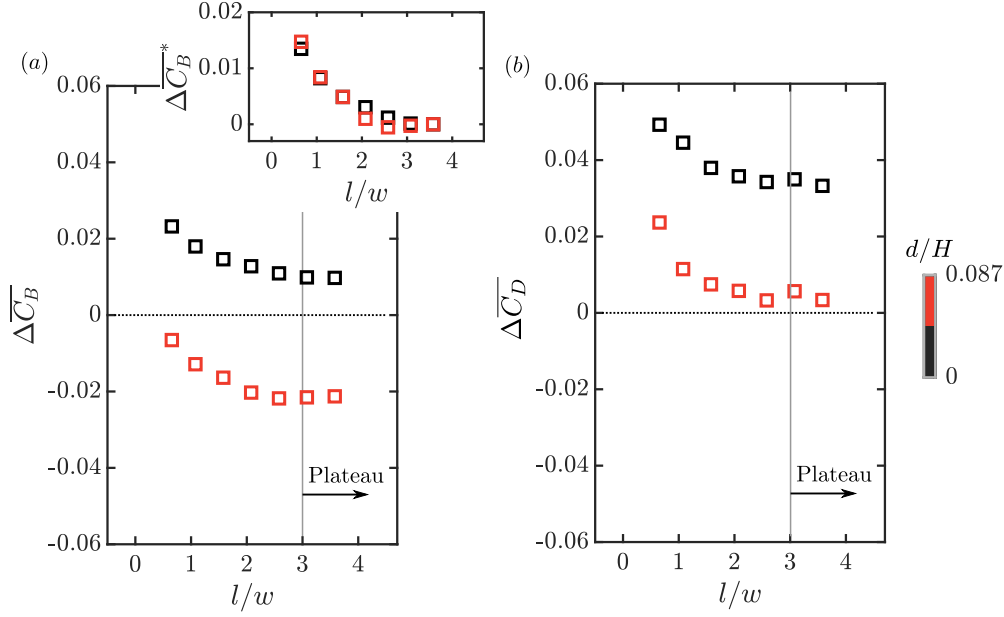


Figure 5.12: Based on a different baseline wake (top perturbing cylinder  $d/H = 0.087$  used here): (a) Base drag  $\Delta \overline{C_B} = \overline{C_B} - \overline{C_{B0}}$  and (b) total drag  $\Delta \overline{C_D} = \overline{C_D} - \overline{C_{D0}}$  of the vehicle perturbed by sharp-edged-shoulder wheels as a function of the wheel-to-base distance  $l/w$ , the base drag variant  $\Delta \overline{C_B}^* = \Delta \overline{C_B} - \Delta \overline{C_B}(\max(l/w))$  versus  $l/w$  is also shown in (a).

the longest vehicle. It is found that the cylinder alters the vehicle wake from a well-balanced one to a vertical asymmetric one dominated by a top recirculating flow. This is shown by both the mean streamlines and the turbulent kinetic energy  $k$  in the symmetry plane of the vehicle. In addition, the horizontal bi-modal dynamics of the wake is inhibited and the wake is locked to a vertical static asymmetric state. The aim of introducing such an asymmetric baseline wake is to generalize the findings described previously, since the wakes of square-back road vehicles present different vertical asymmetries. The mean base drag  $\overline{C_{B0}}$  and total drag  $\overline{C_{D0}}$  coefficients are displayed in table 5.2. The increase in base drag with decreasing vehicle length  $L/H$  is again observed for this baseline (also plotted in figure 5.11c).

The sharp-edged-shoulder wheels S are then tested on the present baseline. The effects on the base drag  $\Delta \overline{C_B} = \overline{C_B} - \overline{C_{B0}}$  and on the total drag  $\Delta \overline{C_D} = \overline{C_D} - \overline{C_{D0}}$  are shown respectively in figure 5.12(a) and (b). The results discussed before in the previous sections (named as  $d/H = 0$ ) are presented for comparison. It is shown in figure 5.12(a) that the  $\Delta \overline{C_B}$  evolution for the new configuration presents an overall downward shift. The wheels now play an opposite role on the base drag in the plateau with a base drag decrease of  $\sim 9\%$ . From the plateau with decreasing  $l/w$ , the same evolution as that of the  $d/H = 0$  configuration is observed. This is evidenced by defining a variant of base drag variation  $\Delta \overline{C_B}^* = \Delta \overline{C_B} - \Delta \overline{C_B}(\max(l/w))$ , where the two curves collapse approximately. When the total aerodynamic drag is considered in figure 5.12(b), an overall upward shift of  $\sim 0.024$  from the  $\Delta \overline{C_B}$  evolution in figure 5.12(a) is noticed. This is similar to the  $d/H = 0$  configuration.

An examination of the mean wake flow is presented in figure 5.13. The global modifications of the vehicle wake by the wheels are exemplified using the case with the longest vehicle in figure 5.13(a). In contrast to the increase in wake asymmetry observed before for the  $d/H = 0$  configuration in figure 5.4(a), here we measure a symmetrization of the vehicle wake as shown by the mean streamlines and the lower turbulent kinetic energy  $k$  in the bottom shear layer.

On the other hand, with decreasing  $l/w$ , the  $\Delta \overline{C_B}$  increase is also accompanied by the emergence of the mass exchange between the rear wheel wakes and the vehicle wake for the  $d/H = 0.087$  configuration. This is shown in figure 5.13(b) by comparison with the  $d/H = 0$  configuration. The  $\overline{u_z}$  distributions at  $x/H = 0.03$  for the shortest vehicle are presented. Inside the vehicle wake, the recirculating flow is very different for these two configurations. However, the mass exchange velocity at the interface  $z/H = G/H$  is not varied significantly. This is depicted by plotting the

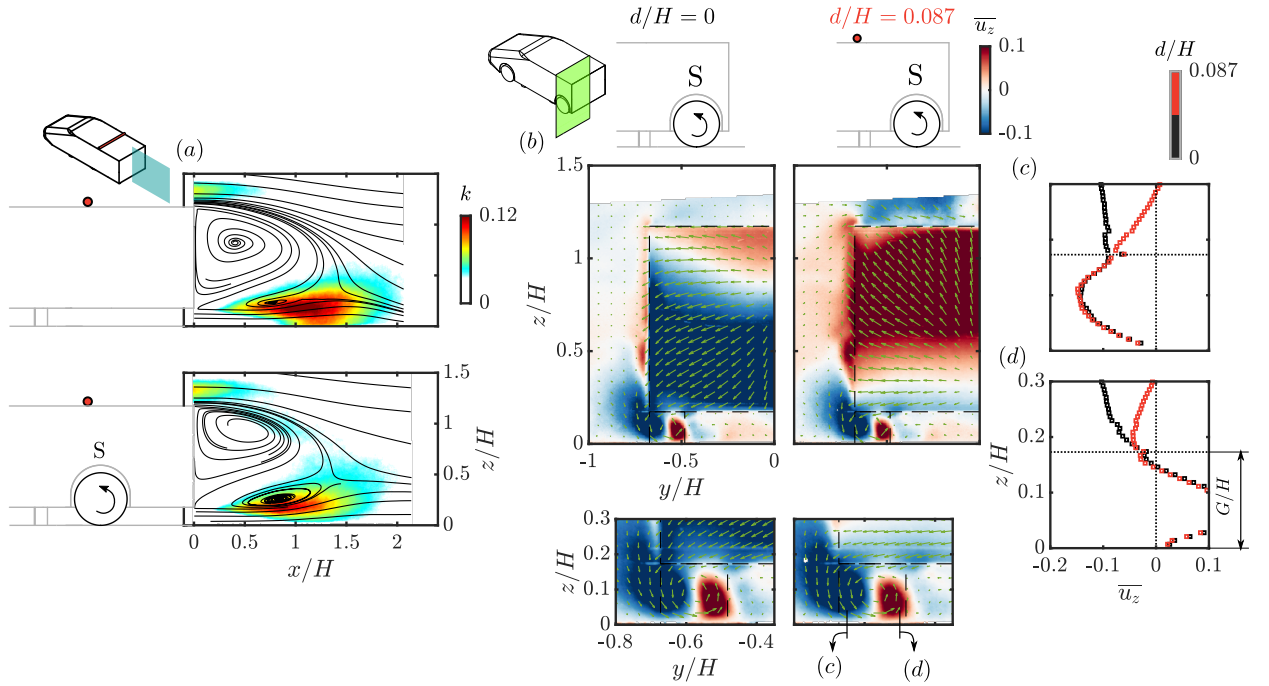


Figure 5.13: (a) Effect of sharp-edged-shoulder wheels on the longest baseline wake, the vehicle is perturbed with a  $d/H = 0.087$  cylinder at the top. (b) For the shortest vehicle with sharp-edged-shoulder wheels: evolution of the mean vertical velocity  $\bar{u}_z$  with the size of the top-perturbing cylinder  $d$  in the cross-flow plane  $x/H = 0.03$ , the vertical profiles at  $y/H = -0.64$  and  $-0.52$  are shown respectively in (c) and (d).

$\bar{u}_z$  profiles at  $y/H = -0.64$  and  $-0.52$ , respectively, in figures 5.13(c) and (d). Despite the very different  $\bar{u}_z$  distributions in the vehicle wake ( $z/H > G/H$ ), the mean vertical velocity  $\bar{u}_z$  at  $z/H = G/H$  is of the same level for the two configurations.

These results show clearly that wheels have two different effects. On one hand, at the scale of the vehicle, they induce a global variation of the wake balance which, according to the initial state of the wake, increases or reduces the global drag (note for example that adding wheels is always beneficial for the base drag of the vehicle perturbed by the cylinder). On the other hand, for moderate wheel-to-base distances, a local interaction driven by the wakes of the wheels takes place. This interaction induces a mass transfer from the main wake and is responsible for a drag increase.

## 5.5 Discussions and concluding remarks

### 5.5.1 Evaluating the effect of mass exchange on the base drag

In chapter 4, a physical model based on a momentum balance of the wake was proposed to link the mass exchange and the concomitant base drag changes. This model was derived from fundamental studies focusing on the effect of base suction on the base pressure of either a 2-D D-shaped cylinder (Bearman, 1967) or a 3-D bluff body (Hsu *et al.*, 2021). In these two reference works, a simple relation between the base drag change  $\Delta \overline{C}_B$  and the suction flow rate  $q$ :

$$\Delta \overline{C}_B = \frac{2q}{HWU_0} = 2C_q, \quad (5.3)$$

was found to hold for small suction flow rate coefficient  $C_q$  ( $C_q < 0.03$  in Hsu *et al.* (2021)). In such situations, fluid particles continuously enter the mean recirculating region and therefore lose their longitudinal momentum. By writing that a pressure decrease at the base is responsible for this momentum flux balance, one gets  $\Delta F_x = (\rho q)U_0$ . Normalizing the corresponding quantities, the simple relation  $\Delta \overline{C}_B = 2C_q$  is then obtained. This model was then found in chapter 4 to be able to explain the results, such as the scalings for the base drag. Considering the overall accordance of the present wheel situation with the obstacle situation, this model is now used to

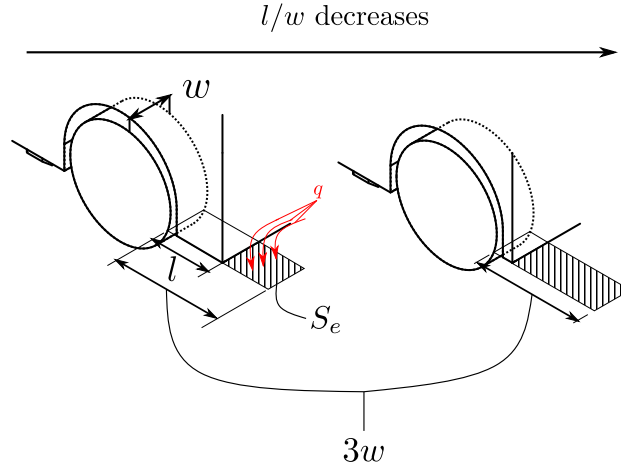


Figure 5.14: Schematics of the surface of mass exchange in the drag-sensitive regime  $l/w < 3$ .

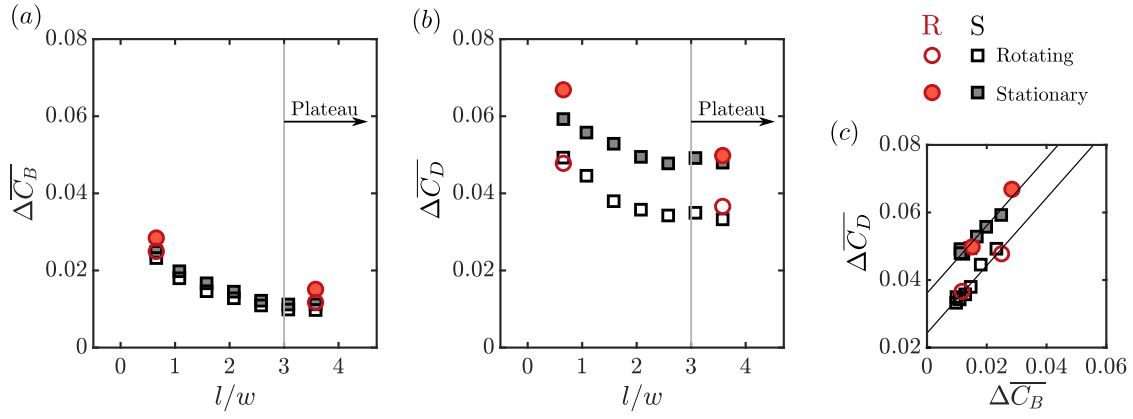


Figure 5.15: Evolution of (a) the base drag  $\Delta \overline{C_B} = \overline{C_B} - \overline{C_{B0}}$  and (b) total drag  $\Delta \overline{C_D} = \overline{C_D} - \overline{C_{D0}}$  of the body as a function of the wheel-to-base distance  $l/w$ . Different wheel shapes (sharp-edged-shoulder wheels (S, colored in black) or rounded-shoulder wheels (R, colored in red)) and different wheel states (rotating or stationary) are considered. The relationship between  $\Delta \overline{C_D}$  and  $\Delta \overline{C_B}$  is shown in (c).

give a global point-of-view linking the base drag variation and the local mass exchange observed in the present chapter.

We start from the base drag evolution shown in figure 5.12. A gradual increase of  $\Delta \overline{C_B}^*$  of  $\sim 0.014$  from  $l/w = 3.09$  to  $l/w = 0.65$  is measured for all configurations. Accompanied by this, pressure measurements show a continuous decrease of pressure and increase of periodic dynamics at the bottom trailing edge of the vehicle with decreasing  $l/w$  at  $l/w < 3$ . Also, the mean properties in the rear wheel wake are measured to be preserved for different  $l/w$  cases. As depicted in the sketches in figure 5.14, we therefore assume a rectangular region with a length of  $3w$  downstream of each rear wheel. When  $l/w < 3$ , this region is exposed downstream of the vehicle base and induces the mean mass transfer. With decreasing  $l/w$ , the area of the mass exchange surface  $S_e = (3w - l)w$  increases linearly. A space-averaged mass transfer velocity  $U_e$  can be defined by  $q = 2S_e U_e$  (2 is here the number of rear wheels). Using relation 5.3,  $U_e/U_0$  can be easily estimated with  $U_e/U_0 = HW \Delta \overline{C_B}^* / (4S_e)$  for all the cases in the drag-sensitive regime ( $l/w < 3$ ). For the cases with the shortest vehicle ( $l/w = 0.65$ ),  $U_e/U_0$  is found to be  $\sim 0.055$ , which is a good order of magnitude of the downward vertical velocities measured in figure 5.9(c) and 5.13(c, d) near  $z/H = G/H$ . Therefore, the impact of the mean mass transfer on the base pressure in the present wheel situation is pictured by the physical model proposed in chapter 4.

### 5.5.2 Effects of wheel state: rotating or stationary

In the present chapter, the wheel-vehicle interactions are investigated using rotating wheels. It is important to question if the conclusions of the present chapter hold, at least qualitatively, for the

configuration with stationary wheels. By repeating the measurements presented in figure 5.2 but with stationary wheels, we examine in figure 5.15 the effects of wheel state.

In figure 5.15(a), the effect of wheel state on the base drag is presented. The two different wheel types, S and R, are considered. For different wheel-to-base distances  $l/w$ , the base drag increases slightly for fixed wheels. This base drag increase is the same for all the  $l/w$  distances. In figure 5.15(b), the total drag  $\overline{\Delta C_D}$  is presented. For stationary cases, figure 5.15(c) shows  $\overline{\Delta C_D}(l/w) = 0.036 + \overline{\Delta C_B}(l/w)$ . The upward shift of  $\sim 0.036$  is bigger than  $\sim 0.024$  for the rotating wheels.

The insensitivity of the base drag to the wheel state is in accordance with the measurements in Pavia & Passmore (2017). Further investigation of the velocity measurements not shown here for brevity confirms that the salient features of wheel-vehicle interactions derived from the rotating cases can be gained in the same way by using the stationary cases. The main aspects of wheel-vehicle interactions for this square-back body, namely the global forcing of the vehicle wake and the local near-wake interactions, are therefore not related to the wheel state.

### 5.5.3 Influence of tire width on base drag

In the present chapter, we discussed the wheel-vehicle interactions by varying one parameter: the wheel-to-base distance  $l/w$ . In the development process for a road vehicle, this parameter is often fixed at the early stage. On the other hand, for a given vehicle, there are often several different tire width choices depending on the usage and load capacities. We now discuss this parameter by focusing on the local near-wake interactions between the rear wheels and the vehicle wake.

We first take the measurements discussed before using a single wheel width  $w_{ref}$  as a reference configuration for the following discussion, the base drag increase in the drag-sensitive regime from the plateau  $\overline{\Delta C_{Bref}}^*$  can be described by a quadratic evolution:

$$\overline{\Delta C_{Bref}}^* = C_1 \left( C_2 - \frac{l}{w_{ref}} \right)^2, \quad (5.4)$$

where  $C_1$  and  $C_2$  are two constants. In the present chapter,  $C_2$  is equal to 3. Based on this reference configuration, we vary the wheel width to  $w_{ref} + \Delta w$ . According to the scaling properties obtained using 2-D D-shaped obstacles in chapter 4, both the width and length of the exchange surface increase with the width  $w$  in this regime (see figure 5.14). As a consequence, the base drag increase from the plateau may be written as:

$$\overline{\Delta C_B}^* = C_1 \left( \frac{w}{w_{ref}} \right)^2 \left( C_2 - \frac{l}{w} \right)^2 = C_1 \left( \frac{w_{ref} + \Delta w}{w_{ref}} \right)^2 \left( C_2 - \frac{l}{w_{ref} + \Delta w} \right)^2. \quad (5.5)$$

The percentage of  $\overline{\Delta C_{Bref}}^*$  increase by the increase in the wheel width  $\Delta w/w_{ref}$  at a specific wheel-to-base distance  $l/w_{ref}$  is therefore:

$$\gamma_B = \frac{\overline{\Delta C_B}^* - \overline{\Delta C_{Bref}}^*}{\overline{\Delta C_{Bref}}^*} = \left( \frac{C_2 \Delta w / w_{ref}}{C_2 - l / w_{ref}} + 1 \right)^2 - 1, \quad (5.6)$$

For different wheel-to-base distances  $l/w_{ref}$ , the increase in base drag  $\overline{\Delta C_B}^* - \overline{\Delta C_{Bref}}^*$  due to the increase in the wheel width is then plotted in figure 5.16. With decreasing  $l/w$ , the sensitivity of base drag to the width of the wheel increases. Normally, the tire width for typical vans can be varied maximally by around 20% (for example Peugeot Bipper 2018 with a tire width varying from 175 mm to 205 mm). This wheel width increase can result in an important base drag increase of the order of 0.01 for  $l/w_{ref} = 0.5$ . Therefore, for a square-back road vehicle with a small  $l/w$ , special attention should be paid when changing the tire width of the wheels. This is because a large drag increase due to the local near-wake interactions can be expected.

### 5.5.4 Concluding remarks

A road vehicle is a complex multi-scale geometry and all flow regions are interacting. Salient features of wheel-vehicle interactions and their consequences for drag were considered in this chapter.

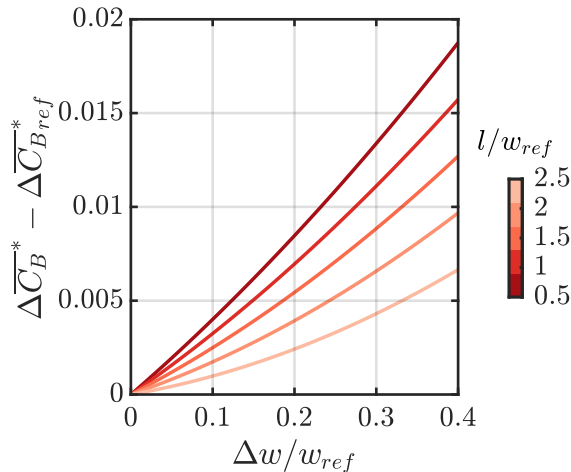


Figure 5.16: Effect of wheel width increase  $\Delta w/w_{ref}$  on the base drag  $\Delta \overline{C}_B^*$  for different wheel-to-base distance  $l/w_{ref}$ . The qualitative measurements in the present chapter are taken as the reference configuration denoted by  $w_{ref}$  (wheel width) and  $\Delta \overline{C}_{B_{ref}}^*$  (base drag increase from the plateau). The variation with the wheel width is derived from the scaling in chapter 4.

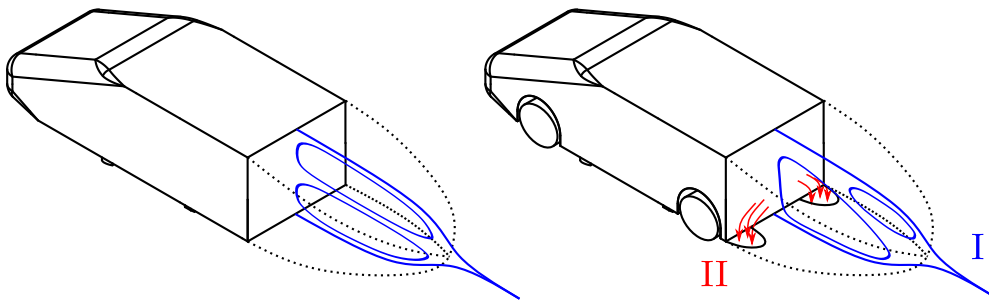


Figure 5.17: A conceptual sketch of the two flow mechanisms of wheel-vehicle interactions responsible for base drag variations. I: global variation of the vertical balance of the vehicle wake. II: mean mass exchange from the wake of the vehicle to the wakes of the wheels.

At first order, we have shown that two different mechanisms can be distinguished, tentatively sketched in figure 5.17. At the scale of the vehicle, wheels perturb the underflow and induce a global variation of the vertical balance of the wake (I in figure 5.17). According to the state of the initial wake, significant base drag increase or decrease is observed. Considering now the scale of the wheels, we have shown that the wake region of the rear wheels imposes a low static pressure having the ability to induce a mean mass exchange from the main wake of the vehicle to the wakes of the rear wheels if the wheel-to-base distance is smaller than a threshold of order  $3w$  ( $w$  is the width of the wheels) in the present situation (II in figure 5.17). A constant mean mass flux extracted from the recirculation region means that this mass flux has to continuously enter the recirculation region of the vehicle wake and that the corresponding fluid particles have lost their mean longitudinal momentum. The physical model proposed in chapter 4 was used to link mass exchange and base drag increase and to check the consistency of the measurements.

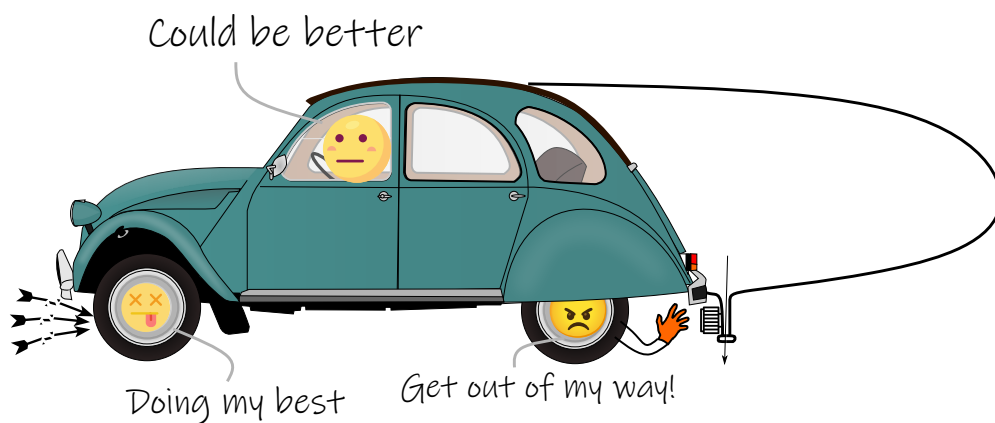
While these two mechanisms for wheel-vehicle interactions are of course coupled at the scale of the vehicle, we insist on the fact that they do have to be distinguished because they imply different physical processes. Moreover, for different initial states of the vehicle wake selected for example in §5.4, it is interesting to figure out that the evolution with the wheel-to-base distance of the base drag increase due to mean mass transfer is very similar in both situations – see insert in figure 5.12(a). This suggests that the mean mass transfer phenomenon and the related drag change are not sensitive to the variation in the vehicle wake balance. In chapter 7, this will be further confirmed by varying the shape of the vehicle from the square-back to a fast-back.

## Chapter 6

# Influence of wheel geometry: importance of front wheels

---

The influence of wheel geometry on the wake and drag of the square-back vehicle geometry is investigated in this chapter. The wheel shoulder radii at the front and rear axles are considered separately or together. The systematic variation of the radii and several additional parameters (distance between the rear wheels and the base  $l$ , mean vertical asymmetry of the vehicle wake) reveals complex interactions between three players: the front wheels, the rear wheels, and the vehicle wake. These interactions lead to a base drag increase of up to 21% from the baseline case without wheels. At the front axle, reducing the front-wheel bluntness increases the base drag and the level of increase depends on the initial wake balance. The facing velocity  $u_f$  for the rear wheels is increased by the reduction in the bluntness which reduces the pressure level inside the rear wheel wakes. In the present situation, when the wheel-to-base distance  $l/w$  ( $w$  is the width of the wheels) is smaller than a threshold of 2.5, the pressure decrease is accompanied by an enhancement of the mean mass transfer discovered in chapter 5 from the vehicle wake to the wakes of the rear wheels. These interactions result in a scaling law with the base drag linearly proportional to  $u_f$ . On the other hand at the rear axle, varying the bluntness of the rear wheels has almost no influence on the base drag regardless of the vehicle wake asymmetry. Finally, a physical model is proposed to illustrate a pressure relationship driving the mean mass transfer, which explains the scaling property for the base drag.



---

**Contents**

<b>6.1</b>	<b>Wheel geometry and drag</b>	<b>80</b>
<b>6.2</b>	<b>Experimental setup</b>	<b>81</b>
<b>6.3</b>	<b>Preliminary parametric survey</b>	<b>82</b>
<b>6.4</b>	<b>Detailed investigation of the effects of front wheels</b>	<b>84</b>
6.4.1	Impact of front-wheel bluntness on drag	84
6.4.2	Global effects of front wheels	87
6.4.3	Influence on near-wake interactions	91
6.4.4	Scaling of drag changes in the drag-sensitive regime	96
<b>6.5</b>	<b>Discussions and concluding remarks</b>	<b>97</b>
6.5.1	Model	97
6.5.2	On the drag sources from near-wake interactions	100
6.5.3	Concluding remarks	101

---

## 6.1 Wheel geometry and drag

With the knowledge of the salient features of the wheel-vehicle interaction problem, the influence of wheel geometry on the wake and drag of the square-back vehicle geometry is investigated in this chapter.

From an industrial perspective, the aerodynamic drag of a ground vehicle has been long noticed to be sensitive to wheel geometry. First, increasing the wheel width has a strong influence on the drag: empirically every 5 mm wheel width increase results in  $0.003\overline{C_D}$  increase (Schuetz, 2016). This point was also illustrated in chapter 5. Moreover, other geometric parameters, such as the shoulder radius, the rim design, and the tire grooves, were identified as significant influencers for the drag. In Wittmeier *et al.* (2013), it was found that tires having a pronounced circumferential edge near the shoulder always increase the drag no matter the geometry of the vehicle. The rim design was found in several previous studies to also have an important effect on the drag (Landström *et al.*, 2009, 2011; Brandt *et al.*, 2019; Josefsson *et al.*, 2022). A smooth cover of the rim was found to be favorable for the drag (approximately  $-0.018\overline{C_D}$  measured in Landström *et al.* (2011)). In addition, adding grooves (rain or pattern grooves) to slick tires was found able to change the drag. Mercker *et al.* (1991) measured a drag increase by adding the rain and pattern grooves together. On the contrary, a decrease of drag was found in Wang *et al.* (2020) by adding rain grooves which is accompanied by a wake symmetrization. Detailed investigations in Wickern *et al.* (1997); Hobeika & Sebben (2018) and in Josefsson *et al.* (2022) show that the effects of these tire patterns on the drag depend on the rim type.

These previous studies, to some extent, provide some guidelines for the optimization of wheel geometry. However, difficulties still exist for automotive manufacturers when choosing rims and tires for a vehicle. There has never been a low-drag wheel shape that works for all vehicles. Rather, a painful process of trial and error is always needed. The physical background for the difficulties lies in the complex interactions between the separation regions around a vehicle. Near the wheels, the flow separation at the tire shoulders interacts with the separation at the rim (Wickern *et al.*, 1997; Wittmeier *et al.*, 2014; Hobeika & Sebben, 2018; Josefsson *et al.*, 2022). The drag was found in Wittmeier *et al.* (2014) to be more sensitive to the rim design for rounded-shoulder tires than for edged-shoulder tires. When looking more globally, the separation regions of the wheels interact with that of the vehicle. This was shown in Elofsson & Bannister (2002); Wäschle (2007); Wang *et al.* (2020) and revealed in chapter 5. Moreover, under a vehicle, the interactions between different components (e.g. front wheels, rear wheels, engine bay flow, and wheel spoilers) are important contributors to the drag (Schuetz, 2016). Here the interactions between the front and rear wheels are particularly important for electric vehicles because the underbody is normally smoothed. Therefore, there is a need for understanding these interactions.

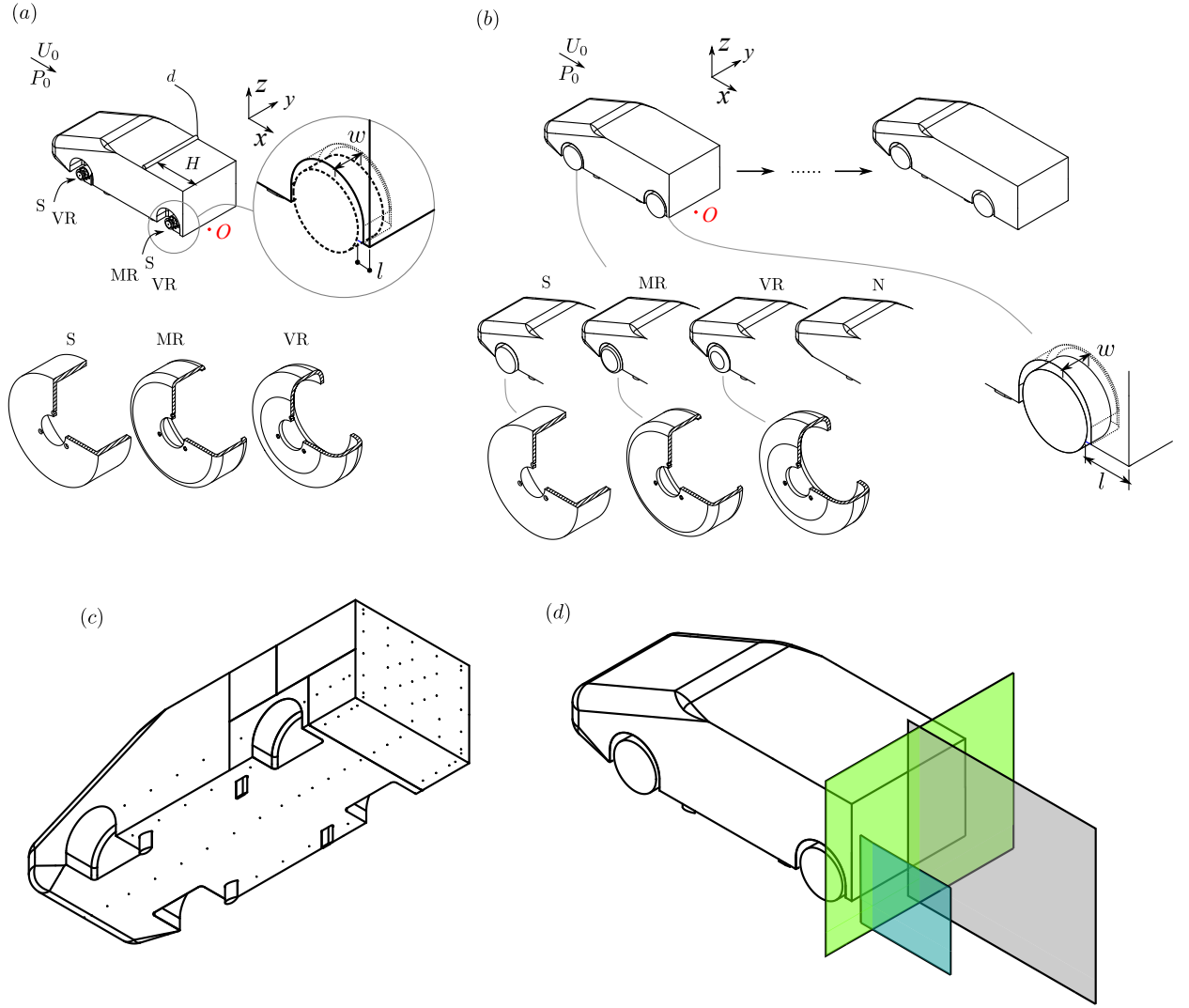


Figure 6.1: Experimental setup. (a) Arrangement of the vehicle perturbed by a spanwise cylinder of diameter  $d$  at the top surface. Different wheel types are installed at the front and rear axles. S, MR and VR denote sharp-edged-shoulder, medium-rounded-shoulder and very-rounded-shoulder wheels, respectively. (b) Arrangement of the vehicle with variable length equipped with sharp-edged rear wheels, different wheel types are considered at the front. (c) Locations of pressure taps. (d) Particle image velocimetry (PIV) fields of view (FOVs) in the symmetry plane of the vehicle ( $y/H = 0$ , colored in gray), symmetry plane of the left wheels ( $y/H = -0.58$ , colored in blue), and cross-flow plane ( $x/H = 0.03$ , colored in green).

The present chapter investigates the influence of wheel geometry based on the simplified square-back vehicle. The chosen variable is the radius of the wheel (tire) shoulder. Our aim is not only to show how the drag and flow are modified by the change in wheel geometry but also to provide more general flow mechanisms in order to improve the optimization process for wheels. In particular, the interactions between the front and rear wheels and their consequences for the drag are focused on. The experimental apparatus used for this chapter are detailed in §6.2. A preliminary parametric survey is conducted in §6.3 by varying the wheel shoulder radii at the front and rear axles separately or together. In §6.4, a detailed investigation of the effects of front wheels is conducted by varying the front wheel radius and the distance between the rear wheels and the vehicle wake. These results are discussed in §6.5, which are followed by concluding remarks.

## 6.2 Experimental setup

The square-back Windsor body shown in figure 6.1 is selected for the study in this chapter. Three types of wheels are tested and are shown in figure 6.1(a). These wheels are of the same diameter

$0.52H$  and width  $w = 0.19H$ . S, MR, and VR represent, respectively, sharp-edged-shoulder, medium-rounded-shoulder and very-rounded-shoulder wheels. The shoulder radii for these three types are  $0$ ,  $0.15w$ , and  $0.3w$ , respectively. All the results presented are collected under a free-stream velocity  $U_0 = 25 \text{ m s}^{-1}$ , corresponding to a height-based Reynolds number  $Re_H = U_0 H / \nu = 4.8 \times 10^5$ , where  $\nu$  is the kinematic viscosity of the air at operating temperature.

Two experimental campaigns with different goals have been conducted. First of all, a preliminary parametric survey shown in figure 6.1(a) is conducted. The vehicle length is  $L/H = 3.41$  giving a short distance between the rear wheels and the wake  $l/w = 0.65$ . Six configurations are considered with different front-rear wheel combinations. Precisely, S and VR are tested at the front axle. For each front wheel type, three rear wheel types (S, MR, and VR) are tested at the rear axle. The wheels are installed on the motors mounted on the floor. During the test, all the wheels are rotated at a speed matching the free-stream velocity. For each configuration, the vertical wake asymmetry is manipulated by placing a circular cylinder at  $x/H = -1$  spanning the whole width on the top surface of the vehicle. The cylinder is of varying diameter  $d$ , ranging from  $d/H = 0$  (no cylinder) to  $0.087$ .

Based on the observations from the preliminary parametric survey, the second campaign shown in figure 6.1(b) is dedicated to understand the effects of the front wheels on the vehicle wake. To this end, we fix the rear wheel type to S and gradually reduce the front wheel bluntness. Four configurations with different front wheel types are tested. They are named as S, MR, VR, and N. Here N denotes no front wheels and the front wheelhouses are filled. All the wheels are directly installed on the vehicle and are therefore not rotated. For each configuration, different vehicle lengths  $L/H = \{3.41, 3.49, 3.59, 3.68, 3.78, 3.87, 3.97\}$  are considered. Thanks to this, the distance from the rear wheels to the base  $l$  is varied, which gives  $l/w = \{0.65, 1.08, 1.58, 2.08, 2.58, 3.08, 3.58\}$ .

Time-averaged and long-timescale pressure measurements are conducted using the pressure scanners. 33 taps on the base, 35 taps on the underbody and 20 taps at side surfaces (see figure 6.1c) are connected to the scanners. Specifically, the pressure taps located before the rear wheelhouses are connected to the scanner with range of  $\pm 2.5 \text{ kPa}$ . The rests are connected to the scanner with range of  $\pm 1 \text{ kPa}$ . For the pressure measurements, unless otherwise stated, the recess between each wheel and the floor is carefully filled by kraft paper (first campaign) or by the combination of high-density foam and aluminum tape (second campaign).

For the second campaign, the aerodynamic drag acting on not only the vehicle but also the wheels is quantified by using the balance. During the force measurements, the recesses are opened. At the same time, supplementary pressure measurements are conducted in order to check if the results match the situation where the recesses are filled.

The velocity fields in the near wake are measured by the particle image velocimetry (PIV) system. Three two-dimensional fields of view (FOVs) are considered as depicted in figure 6.1(d). The first one located in the cross-flow plane ( $x/H = 0.03$ ) in proximity to the base of the vehicle is of stereoscopic (2-D three-component (2D3C)) setup, capturing three velocity components. The other two FOVs respectively located in the symmetry planes of the vehicle ( $y/H = 0$ ) and of the left-hand rear wheel ( $y/H = -0.58$ ) are of 2-D two-component (2D2C) setup, obtaining the streamwise  $u_x$  and vertical  $u_z$  velocity components.

### 6.3 Preliminary parametric survey: unveiling the importance of front wheels

In figure 6.2, the sensitivity of the base drag to the parametric space is considered. The parametric space consists of six configurations having different front-rear wheel combinations. For all the configurations, the base drag evolution  $\overline{C_B}$  with the size of the top-perturbing cylinder  $d/H$  is shown in figure 6.2(a). At a fixed  $d/H$ ,  $\overline{C_B}$  is more sensitive to the shape of the front wheels than the shape of the rear wheels. This is shown by the overall higher  $\overline{C_B}$  for the cases having very-rounded front wheels FVR (colored in red) than the cases having sharp-edged front wheels FS (colored in blue). Taking the configuration with four sharp-edged wheels as an example in figure 6.2(b), reducing the front-wheel bluntness from FS to FVR at most of the situations increases

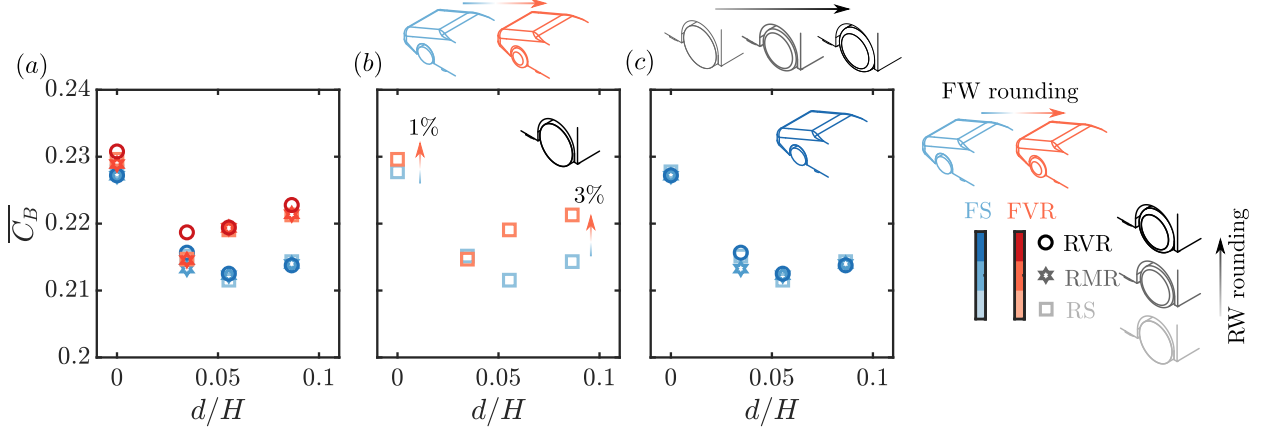


Figure 6.2: (a) Variation of the base drag  $\overline{C}_B$  in the parametric space. The space consists of the diameter of the top-perturbing cylinder  $d/H$ , front-wheel (FW), and rear-wheel (RW) types. At the front axle, FS and FVR represent, respectively, sharp-edged and very-rounded wheels. At the rear axle, RS, RMR, and RVR represent, respectively, sharp-edged, moderate-rounded, and very-rounded wheels. Selected configurations showing front and rear wheel rounding are shown respectively in (b) and (c). All the cases shown here are with rotating wheels having a rotation speed matching the free-stream velocity.

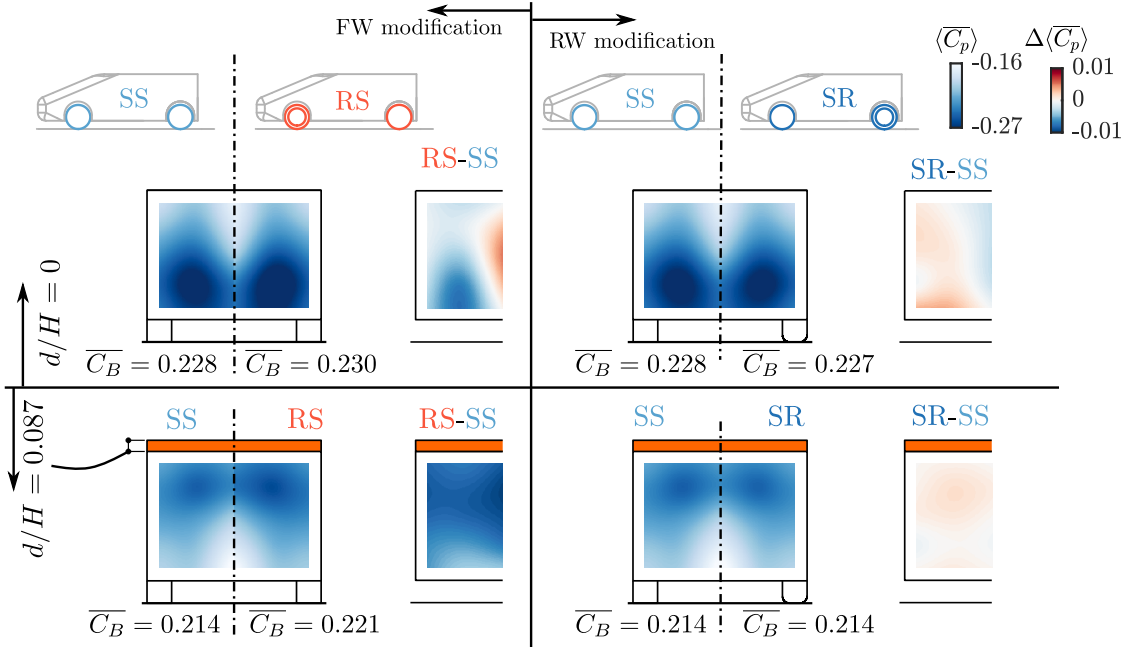


Figure 6.3: Effect of wheel bluntness on the base pressure: Base pressure and base pressure difference distributions for the cases having no ( $d/H = 0$ ) or the biggest ( $d/H = 0.087$ ) perturbing cylinder at the top. The abbreviations denote different front-rear wheel combinations. For example, SR represents the configuration with sharp-edged front wheels and very-rounded rear wheels.

the base drag. It is remarked also that the level of base drag increase depends on the size of the cylinder and therefore on the global wake equilibrium. At  $d/H = 0$ , rounding of the front wheels increases that base drag slightly by  $\sim 1\%$ . On the other hand, a bigger base drag increase of  $\sim 3\%$  is noticed at  $d/H = 0.09$ . As a comparison, a gradual reduction of rear wheel bluntness in figure 6.2(c) at most of the situations has no obvious influence on the base drag.

The base pressure is investigated in figure 6.3 to highlight clearly the base drag changes. The configuration with four sharp-edged wheels is named SS. Changing the front wheels from sharp-edged ones S to very-rounded ones R gives the configuration RS. On the other hand, changing the rear wheels from S to R gives the configuration SR. For these three configurations, the distributions of base pressure and base pressure differences are shown.

When there is no perturbing cylinder at the top of the vehicle ( $d/H = 0$ ), the base pressure

distributions for the three configurations are very similar. The corresponding mean wake topology is characterized by a bottom-dominated recirculating flow. More detailed changes with either front or rear wheel bluntness are pictured by the distributions of the base pressure difference. The pressure near the symmetry plane of the vehicle is recovered when the front wheels are changed from S to R. This indicates a global change in the vertical mean wake equilibrium, which is probably a wake symmetrization. Moreover, a local decrease of pressure is observed near the rear wheels. The combination of these two opposite pressure variations leads to the slight base drag increase of  $\sim 1\%$ . On the other hand as a comparison, when the rear wheels are changed from S to R, we observe very slight and homogeneous changes in base pressure.

When the biggest perturbing cylinder  $d/H = 0.087$  is placed at the top of the vehicle, the mean vehicle wake is reversed vertically with the base pressure distributions picturing a top-dominated recirculating flow. With reducing front-wheel bluntness, the pressure near the symmetry plane of the vehicle is decreased. This is opposite to the cases with  $d/H = 0$  indicating an opposite trend of wake balance change. In addition, the pressure on the base in the vicinity of the rear wheels is found to be decreased. The combination of these two effects gives the moderate base drag increase of  $\sim 3\%$ . For these  $d/H = 0.087$  cases, we measure once again no obvious changes in the base pressure when the rear wheel bluntness is reduced.

This preliminary parametric survey reveals clearly a property underlying the interactions between the wheels and the vehicle wake. When changing the bluntness of the wheels, the front wheels are found to have a stronger impact on the wake of the main body than the rear wheels. Pressure measurements suggest that the variation of front-wheel bluntness modifies the two salient features of wheel-vehicle interactions revealed in chapter 5, namely the vertical equilibrium of the vehicle wake and the local interactions between the rear wheels and the vehicle wake. The physical insights will be investigated in detail in the following parts of the present chapter.

## 6.4 Detailed investigation of the effects of front wheels

In this section, the effects of front-wheel geometry are investigated. Our aim is first to show how front wheels influence the base pressure and then to reveal how the wake of the main body is modified. The answers to these two questions will be used to finally propose a scaling law for the base pressure.

### 6.4.1 Impact of front-wheel bluntness on drag

In figure 6.4(a), we show the base drag  $\Delta\overline{C_B} = \overline{C_B} - \overline{C_{B0}}$  evolution with the distance  $l/w$  from the rear wheels to the base (hereafter abbreviated as wheel-to-base distance). For each case having a base drag value of  $\overline{C_B}$  and a wheel-to-base distance  $l/w$ ,  $\overline{C_{B0}}$  represents the base drag value of the corresponding baseline case (no wheels) having the same  $l/w$ .  $\Delta\overline{C_B}/\overline{C_{B0}}$  is also depicted to show the percentage of base drag increases from the baseline. For all the configurations, a "L" shape evolution is measured and can be divided into a drag-sensitive regime ( $l/w < 2.5$ ) and a large  $l/w$  regime ( $l/w > 2.5$ ). A similar evolution was measured in a situation where the effects of the wheels are modeled by a pair of D-shaped obstacles (chapter 4) and also under the same setup where wheel rotation is considered (chapter 5).

For the base drag evolution in figure 6.4(a), we also notice differences between different configurations. In the large  $l/w$  regime, the front wheels already play an important role in the base drag. Taking the longest  $l/w$  distance as an example, when the front wheels are the bluntest (configuration S), the base drag is increased very slightly from the baseline case (no wheels) by  $\Delta\overline{C_B}/\overline{C_{B0}} \approx 3\%$ . With decreasing front-wheel bluntness, the base drag increases gradually. For the extreme case with no front wheels, a  $\Delta\overline{C_B}/\overline{C_{B0}} \approx 8\%$  increase is measured. In addition, there is a slight difference regarding the slope of the evolution. For the S configuration,  $\Delta\overline{C_B}$  is measured to be quite constant. However, a slight decrease with increasing  $l/w$  is still observed for other configurations.

In the drag-sensitive regime where  $l/w < 2.5$ , the effect of the front wheels also plays an important role. We picture this by defining a base drag variant  $\Delta\overline{C_B}^* = \Delta\overline{C_B} - \Delta\overline{C_B}(l/w = 2.5)$  in figure 6.4(b). It is shown that by reducing front-wheel bluntness, the slope of  $\Delta\overline{C_B}^*$  is increased.

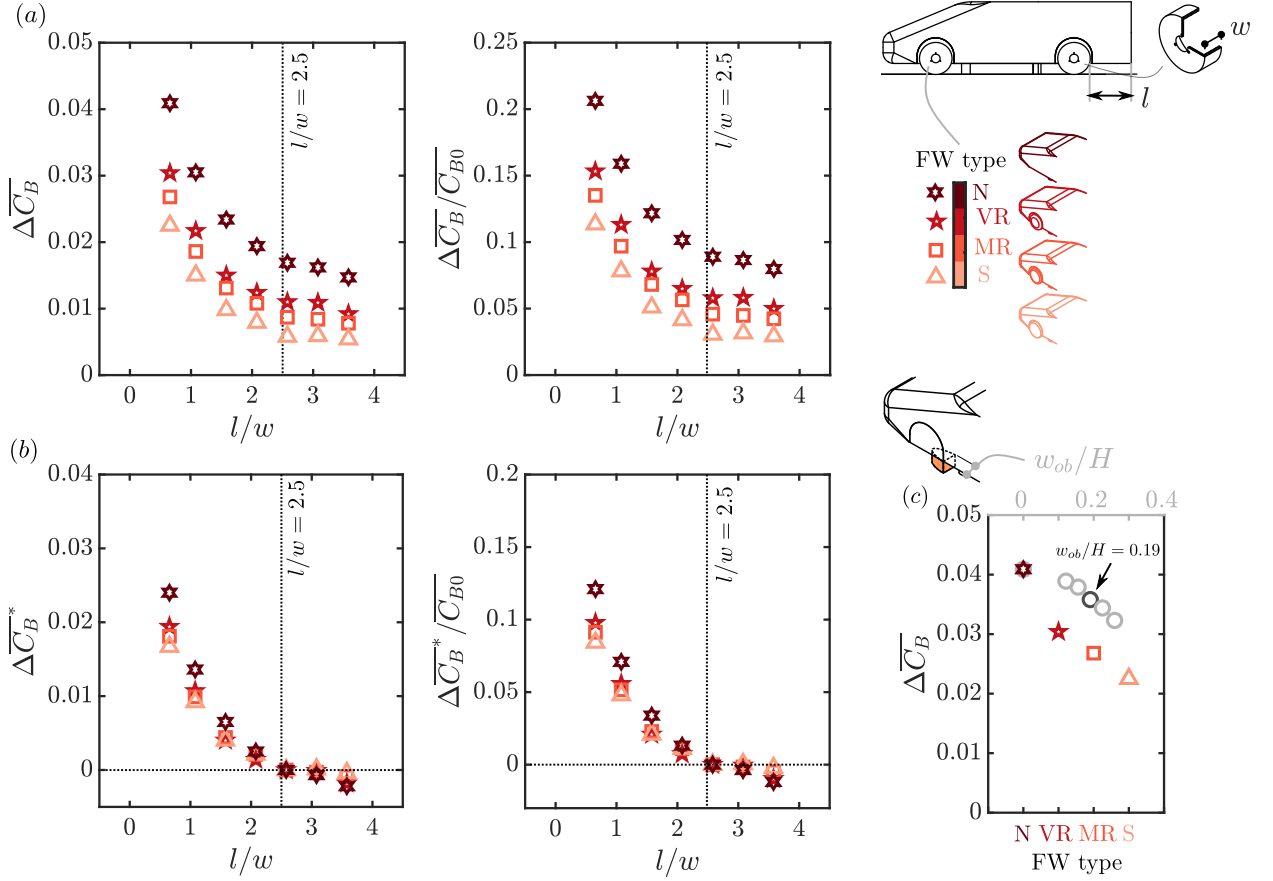


Figure 6.4: (a) Base drag of the body (value  $\Delta \overline{C}_B = \overline{C}_B - \overline{C}_{B0}$  and percentage  $\Delta \overline{C}_B / \overline{C}_{B0}$ ) as a function of the wheel-to-base distance  $l/w$ , different colors indicate different front-wheel (FW) types in combination with sharp-edged rear wheels. (b) Base drag variant  $\Delta \overline{C}_B^* = \Delta \overline{C}_B - \Delta \overline{C}_B(l/w = 2.5)$  versus  $l/w$ . The percentage  $\Delta \overline{C}_B^* / \overline{C}_{B0}$  is also shown. (c) Effects of a D-shaped obstacle pair on the base drag  $\Delta \overline{C}_B$  of the shortest body installed with sharp-edged rear wheels.

This leads to a base drag increase of  $\sim 5\%$  from configuration S to N at  $l/w = 0.65$  as shown by the evolution of  $\Delta \overline{C}_B^* / \overline{C}_{B0}$  in figure 6.4(b). The scaling of the base drag increases in the drag-sensitive regime will be proposed later in §6.4.4.

We examine the robustness of the results based on the shortest body in figure 6.4(c) by considering several additional cases. A D-shaped obstacle pair having variation in width  $w_{ob}/H$  is placed at the same location as the front wheels. Precisely, their base is flush-mounted to the downstream edges of the front wheelhouses. The obstacles have a length of  $1.5w_{ob}$  and a height the same as the ground clearance (see §4.2 in chapter 4 for a detailed description of the obstacles). With increasing  $w_{ob}/H$ , a similar decrease of base drag is measured. It is interesting to note here that the obstacles having the same width as the sharp-edged wheels  $w_{ob}/H = 0.19$  have a weaker effect than all the wheels, probably due to the different types of wakes they generate.

When the recess between each wheel and the floor is opened, force measurements are conducted in order to quantify the aerodynamic drag acting not only on the body but also on the wheels. The opening of the recess has influence on the wakes of the wheels and therefore the interactions between them and the wake of the vehicle. Since this is very different from real on-road situations, considerations of the results shown in figure 6.5 should be under particular caution. In figure 6.5(a), the base drag evolution  $\Delta \overline{C}_B = \overline{C}_B - \overline{C}_{B0}$  is shown. We notice a similar trend as in figure 6.4(a) but the increase of base drag is slightly smaller than when the recess is closed. In figure 6.5(b), the total drag evolution  $\Delta \overline{C}_D = \overline{C}_D - \overline{C}_{D0}$  is given. For different configurations with different front-wheel types, the same "L" trend is observed. However, the configuration with no front wheels gives the smallest  $\Delta \overline{C}_D$  while the configuration with sharp front wheels presents the highest  $\Delta \overline{C}_D$ . This is due to the drag acting on the front wheels and wheelhouses. Finally, the relationship between the base drag increases  $\Delta \overline{C}_B - \Delta \overline{C}_B(\max(l/w))$  and the total drag increases

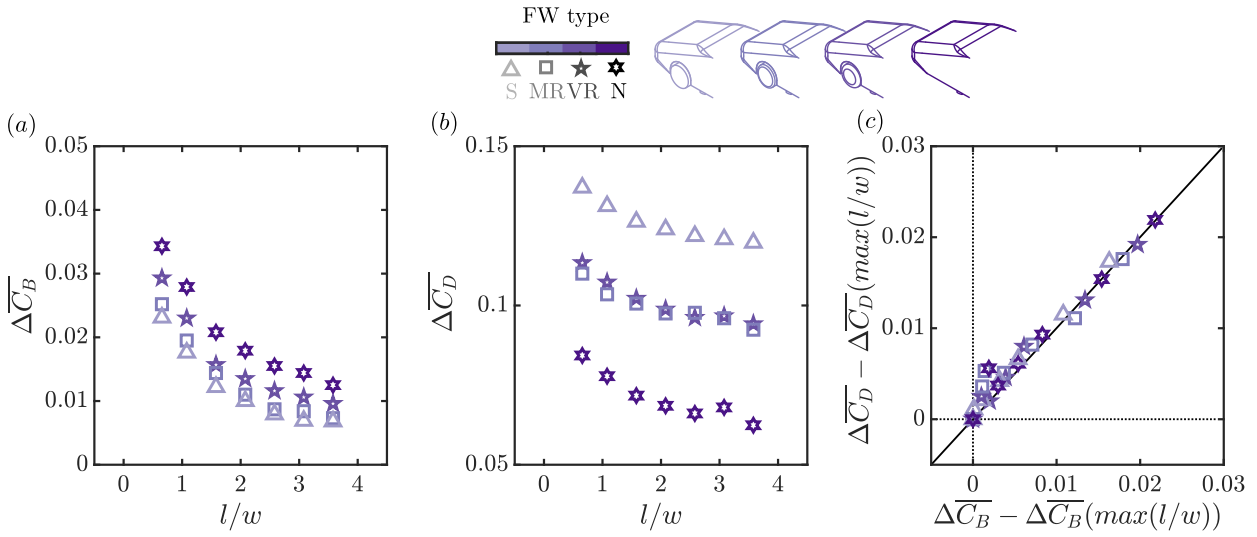


Figure 6.5: For the configurations with the recess between the wheels and the floor open in order to conduct drag measurement: (a) Base drag of the body  $\Delta \overline{C_B} = \overline{C_B} - \overline{C_{B0}}$  as a function of the wheel-to-base distance  $l/w$ . (b) Total drag of the body  $\Delta \overline{C_D} = \overline{C_D} - \overline{C_{D0}}$  as a function of  $l/w$ . (c) Relationship of base drag increase and total drag increase from the maximum  $l/w$  cases.

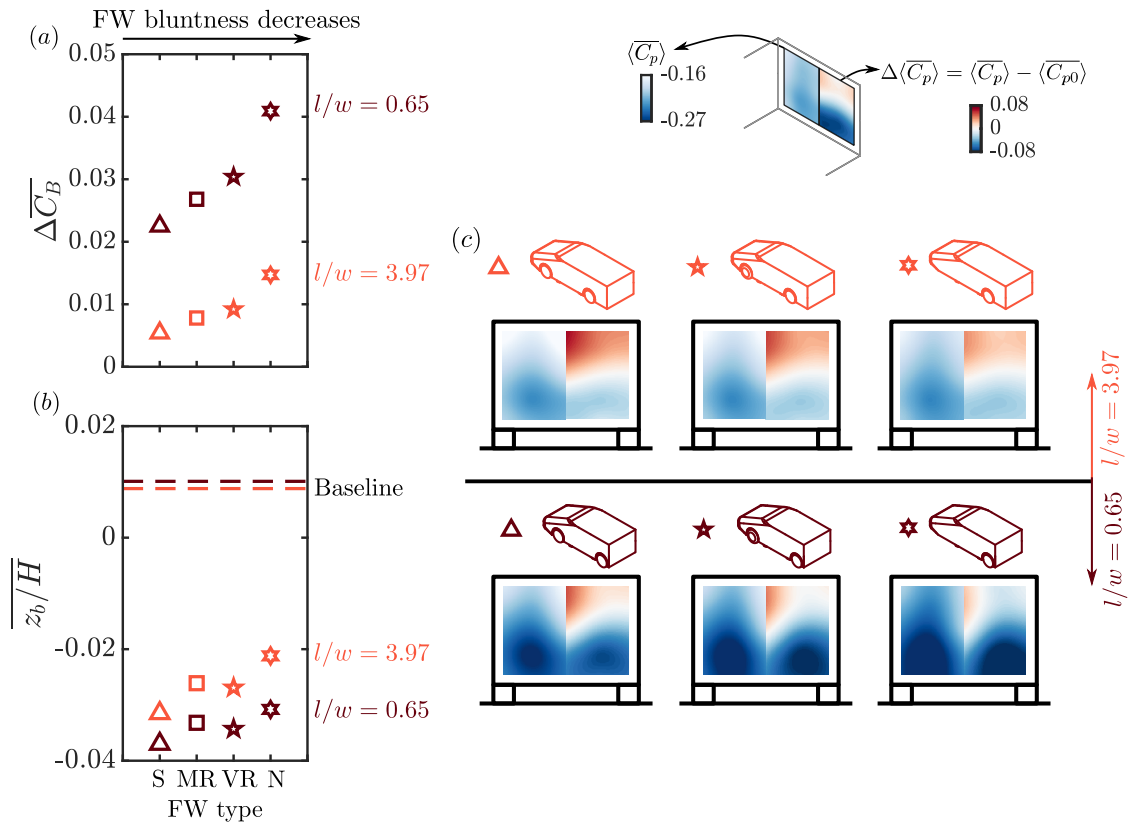


Figure 6.6: For the longest ( $l/w = 3.97$ ) and shortest ( $l/w = 0.65$ ) bodies installed with sharp-edged rear wheels: (a – b) Effects of front-wheel (FW) type on the base drag  $\Delta \overline{C_B}$  (a) and on the mean vertical wake balance denoted by the mean vertical position of the base CoP  $z_b/H$  (b). (c) Base pressure and base pressure difference relative to the baseline for selected cases from (a).

from the maximum  $l/w$  cases is presented in figure 6.5(c). All the configurations with different front-wheel types present a linear law of slope one. This means that with decreasing  $l/w$ , the base drag increase is the only source of total drag increase.

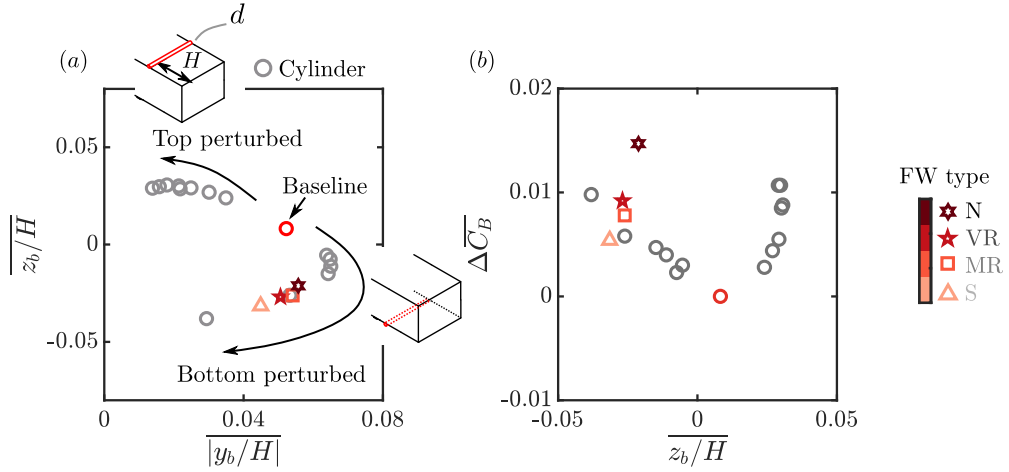


Figure 6.7: For the longest ( $l/w = 3.97$ ) body installed with sharp-edged rear wheels and different types of front wheels (FW): (a) Mean value of the vertical base CoP position  $\overline{z_b/H}$  versus mean absolute value of the horizontal base CoP position  $\overline{|y_b/H|}$ . (b) Relationship between base drag  $\Delta \overline{C_B}$  and  $\overline{z_b/H}$ . The cases with horizontal perturbing cylinder at the top or bottom surfaces of the vehicle from figure 5.3 of chapter 5 are shown as references.

### 6.4.2 Global effects of front wheels

A global look at how the variation in front-wheel bluntness influences the vehicle wake is presented in figure 6.6. First of all, for the largest ( $l/w = 3.97$ ) and smallest ( $l/w = 0.65$ ) wheel-to-base distances, the variations of the base drag  $\Delta \overline{C_B}$  and the mean vertical position of the base center-of-pressure (CoP)  $\overline{z_b/H}$  with the front-wheel bluntness are shown in figure 6.6(a) and (b), respectively. When the wheels are installed, no matter the wheel-to-base distance  $l/w$ , the baseline wake is reversed in the vertical direction with a higher asymmetry strength (denoted by  $\overline{|z_b/H|}$ ) as shown in figure 6.6(b). With variation in the front-wheel bluntness, there is a slight change in  $\overline{z_b/H}$ . Comparing the two  $l/w$  distances, we notice that the asymmetry strength is marginally increased with reducing  $l/w$ . However, the base drag is greatly increased with decreasing  $l/w$ .

In figure 6.6(c), the base drag variation in figure 6.6(a) is explored in detail by showing the distributions of base pressure and base pressure differences with respect to the corresponding baseline cases. For all cases presented, the vertical wake reversal from the baseline cases is visualized. With decreasing front-wheel bluntness from case S (sharp-edged-shoulder front wheels) to N (no front wheels), the mean pressure at the top half of the base is gradually decreased. This trend is not changed when  $l/w$  is varied. On the other hand, at the bottom half of the base near the rear wheels, a gradual pressure decrease with reducing front-wheel bluntness is noticed for the shortest  $l/w$  distance ( $l/w = 0.65$ ) but not for the longest one ( $l/w = 3.97$ ). This explains the higher sensitivity of  $\Delta \overline{C_B}$  to front-wheel bluntness for  $l/w = 0.65$  compared to  $l/w = 3.97$  as shown in figure 6.6(a) and the different slopes observed before in figure 6.4(b).

The modifications in the underflow by the wheels were shown in chapter 5 to have consequences on the vertical equilibrium of the vehicle wake. This can either increase or decrease the base drag depending on the initial wake balance. When the front wheels are modified, we note in figure 6.6 that the vertical balance of the vehicle wake is slightly modified for the shortest and longest bodies. The same method used in chapter 5 is adapted here in figure 6.7 to view the modifications in the wake balance and base pressure. This method was described in detail in chapter 5, here we only provide a brief description. First, the longest baseline body is perturbed by a spanwise circular cylinder having variation in diameter at  $x/H = -1$  either on the top or bottom surface of the vehicle. With this passive perturbation, the whole scenario with a competition between vertical and horizontal wake asymmetries is pictured in figure 6.7(a) by the relationship between  $\overline{z_b/H}$  and  $\overline{|y_b/H|}$  (the absolute value is used for the horizontal component due to the transient wake switching motion). On the other hand, the variation in the mean vertical asymmetry  $\overline{z_b/H}$  leads to important variations of base drag as shown in figure 6.7(b). The baseline case with small  $\overline{|z_b/H|}$  presenting horizontal bi-modal dynamics has the least mean base drag.

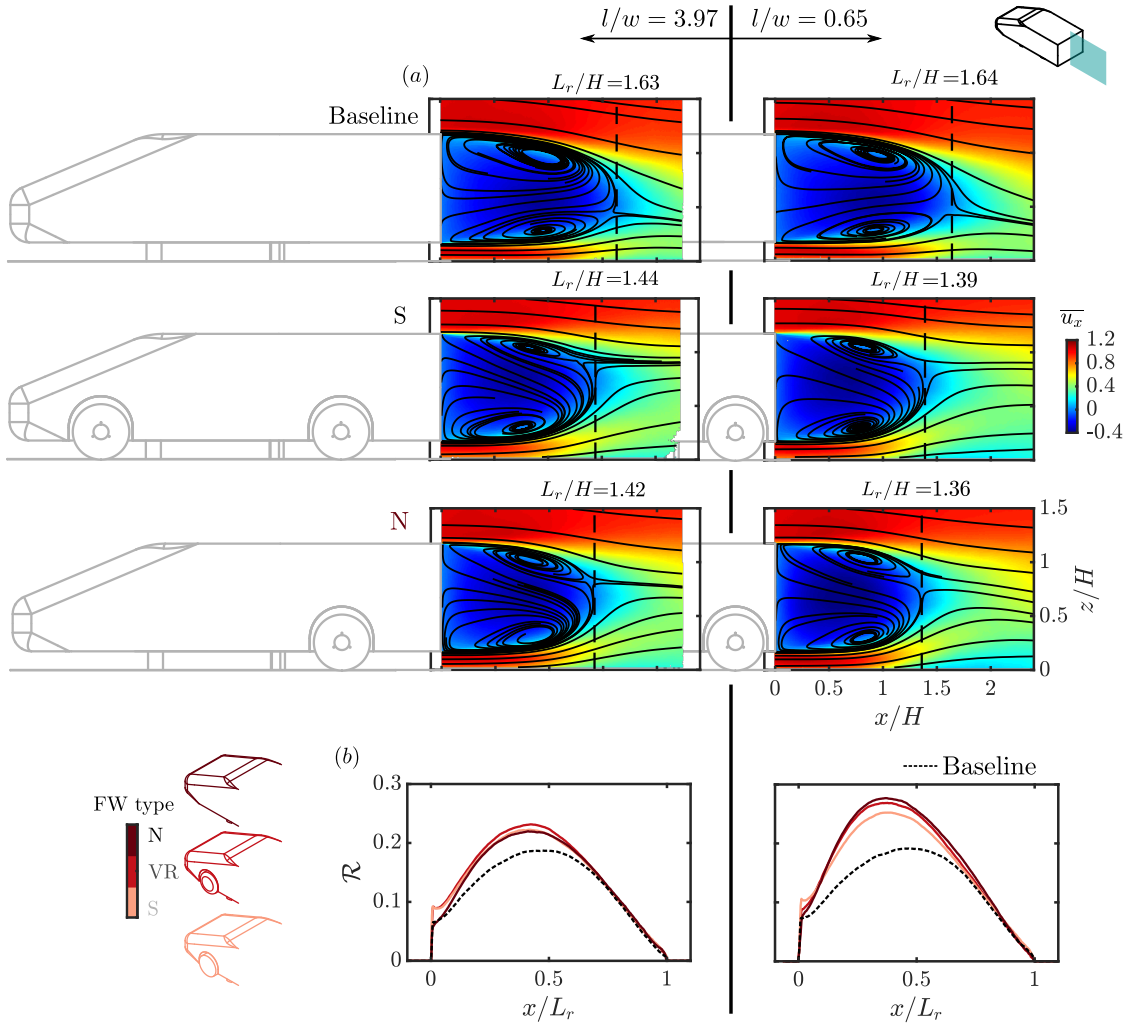


Figure 6.8: For the longest ( $l/w = 3.97$ ) and shortest ( $l/w = 0.65$ ) bodies: (a) Mean streamwise velocity  $\bar{u}_x$  and mean wake topology in the symmetry plane of the vehicle for the baseline case and several cases with different front-wheel types. (b) Streamwise evolution of the recirculation strength  $\mathcal{R}$  for the cases in (a).

With this reference database, the cases considered in the present chapter are examined. When the different sets of wheels having varying front bluntness are installed on the longest baseline body, it is noticed in figure 6.7(a) that these wheel cases follow the relationship portrayed by the cylinder cases. In figure 6.7(b) where the relationship between mean vertical asymmetry and the base drag is discussed, we notice that for the cases having four wheels (cases S, MR and VR), the trend measured using the cylinder is followed approximately. In the extreme situation when the front wheels are not presented (case N), a remarkable deviation from the trend is noticed. When considering the decrease of front-wheel bluntness from case S to N, a very slight change in  $\bar{z}_b/H$  is accompanied by an important increase in base drag. Therefore, the base drag increase is not likely to be caused by the variation in wake asymmetry.

We now turn to the velocity measurements to reveal how the wake of the vehicle is globally modified by the variation in the front-wheel bluntness. In the symmetry plane of the vehicle ( $y/H = 0$ ), the distributions of the mean streamwise velocity  $\bar{u}_x$  superimposed by the mean streamlines are presented in figure 6.8(a) for the largest ( $l/w = 3.97$ ) and smallest ( $l/w = 0.65$ ) wheel-to-base distances. For both distances, the four sharp-edged-shoulder wheels (case S) greatly reorganize the recirculating bubble of the vehicle. The vertical balance of the baseline wake is reversed and the recirculation length  $L_r/H$  is reduced. When the front-wheel bluntness is varied from case S to N, no noteworthy change is found for both  $l/w$  distances when looking at the mean wake topology. On the other hand, differences are noticed when comparing these two  $l/w$  distances. For both configurations S and N, the decrease in  $l/w$  leads to a slight reduction in the recirculation length. In addition, the recirculation strength defined as:

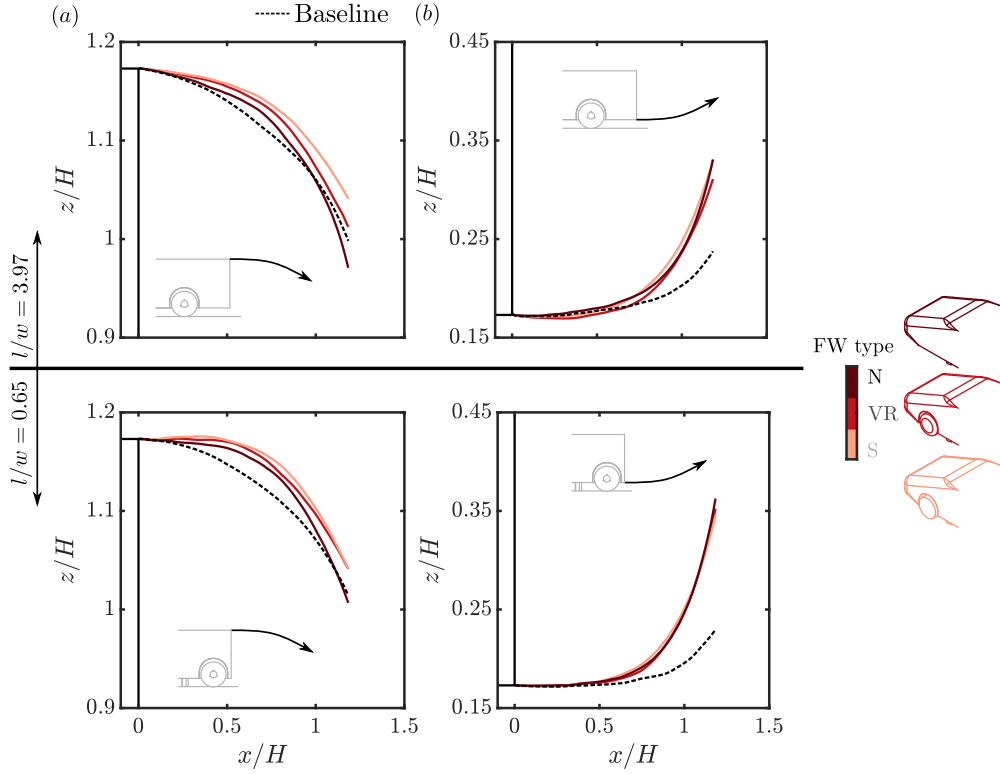


Figure 6.9: For the longest ( $l/w = 3.97$ ) and shortest ( $l/w = 0.65$ ) bodies: effects of front-wheel (FW) type on the mean separating streamlines from the top (a) and bottom (b) trailing edges in the symmetry plane of the vehicle ( $y/H = 0$ ).

$$\mathcal{R}(x) = \int_{\bar{u}_x \leq 0} \sqrt{\bar{u}_x^2 + \bar{u}_z^2} d(z/H), \quad (6.1)$$

shows important differences between the two  $l/w$  distances. The streamwise evolution of this quantity is shown in figure 6.8(b). For the longest wheel-to-base distance  $l/w = 3.97$ , the variation in front wheels has no obvious influence on  $\mathcal{R}$ . With reducing  $l/w$  from  $l/w = 3.97$  to  $0.65$ , there is a substantial enhancement in  $\mathcal{R}$  for all the front-wheel configurations (from  $\sim 14\%$  to  $\sim 26\%$  depending on the configuration). For the smallest wheel-to-base distance ( $l/w = 0.65$ ), we notice that the recirculation strength  $\mathcal{R}$  increases progressively with reducing front-wheel bluntness. From case S to N, it is increased by  $\sim 10\%$ .

The mean curvature of the top and bottom shear layers is described in figure 6.9 by the spatial evolution of the mean separating streamlines in the symmetry plane of the vehicle ( $y/H = 0$ ). With reducing front-wheel bluntness from case S to N, we notice that the curvature of the top shear layer is gradually increased no matter the wheel-to-base distance  $l/w$ . On the other hand for the bottom shear layer, the curvature is insensitive to the front-wheel bluntness. The mean curvature is an indicator of the local pressure gradient as shown by the mean momentum balance (Bradshaw, 1973) in the normal direction of a separating streamline:

$$\frac{\partial \bar{C}_p}{\partial n} = 2\bar{C}_s \bar{u}_s^{-2} - 2 \frac{\partial \bar{u}'_n \bar{u}'_n}{\partial n}, \quad (6.2)$$

where  $\bar{u}_s$  and  $\bar{u}'_n \bar{u}'_n$  are respectively the tangential velocity and Reynolds stress of the normal velocity.  $\mathcal{C}$  is the local curvature of the separatrix. A higher mean curvature  $\mathcal{C}$  then is directly related to a higher normal pressure gradient and therefore a lower pressure inside the recirculation region. This is in accordance with the base pressure measurements in figure 6.6(c), where a gradual pressure decrease is observed at the top half of the vehicle base with reducing front-wheel bluntness.

A detailed examination of the Reynolds stresses in the symmetry plane of the vehicle is presented in figure 6.10. The distributions of the normal stress  $\bar{u}'_x \bar{u}'_x$  are shown in figure 6.10(a). For both  $l/w$  distances, when the four sharp-edged-shoulder wheels (case S) are installed on the

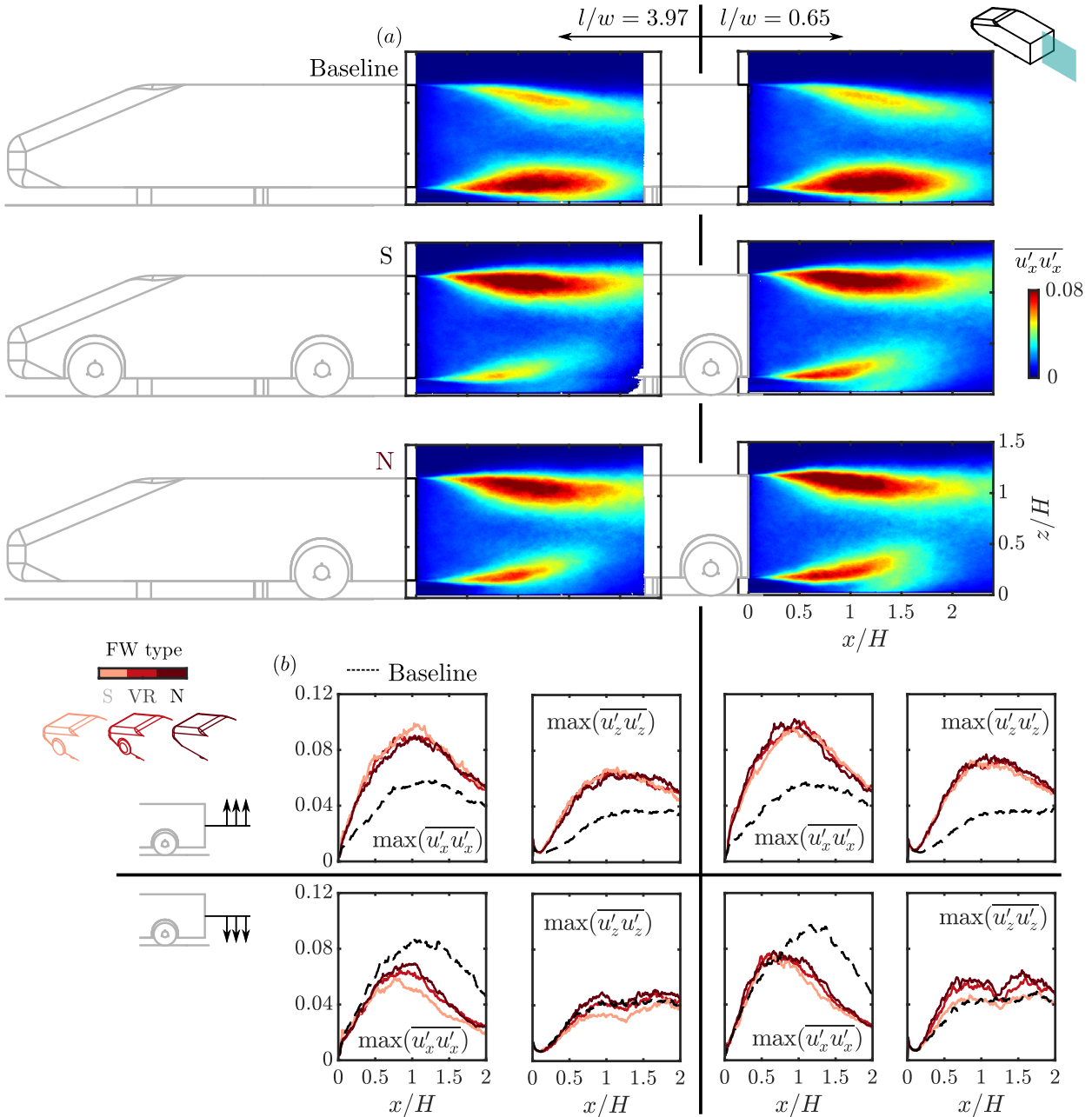


Figure 6.10: For the longest ( $l/w = 3.97$ ) and shortest ( $l/w = 0.65$ ) bodies: effects of front-wheel (FW) type on the Reynolds normal stress  $\overline{u'_x u'_x}$  in the wake of the vehicle (a). The maximum of different components in the top or bottom shear layer are shown in (b).

baseline body, the change in asymmetry is again visualized by the different levels of stress in the top and bottom shear layers. Then, with the reduction in the front-wheel bluntness from case S to N, the flow fluctuations inside the top shear layers are not observed to be modified. However, the stress inside the bottom shear layers is enhanced. This difference in the top and bottom shear layers is characterized by showing the maximum of different Reynolds stress components in the top or bottom shear layer in figure 6.10(b). For the top shear layer, we observe no noteworthy change in all the normal and shear (not shown here for brevity) components of the Reynolds stress tensor. On the other hand, with reducing front-wheel bluntness, the flow fluctuations inside the bottom shear layer are gradually increased.

At this stage, we have described the global effects of the front wheels on the vehicle wake. When the bluntness of the front wheels is varied, the mean flow curvature around the separation bubble and the flow fluctuations inside the wake are modified. These modifications are insensitive to the distances between the rear wheels and the base. Therefore, they are responsible for the

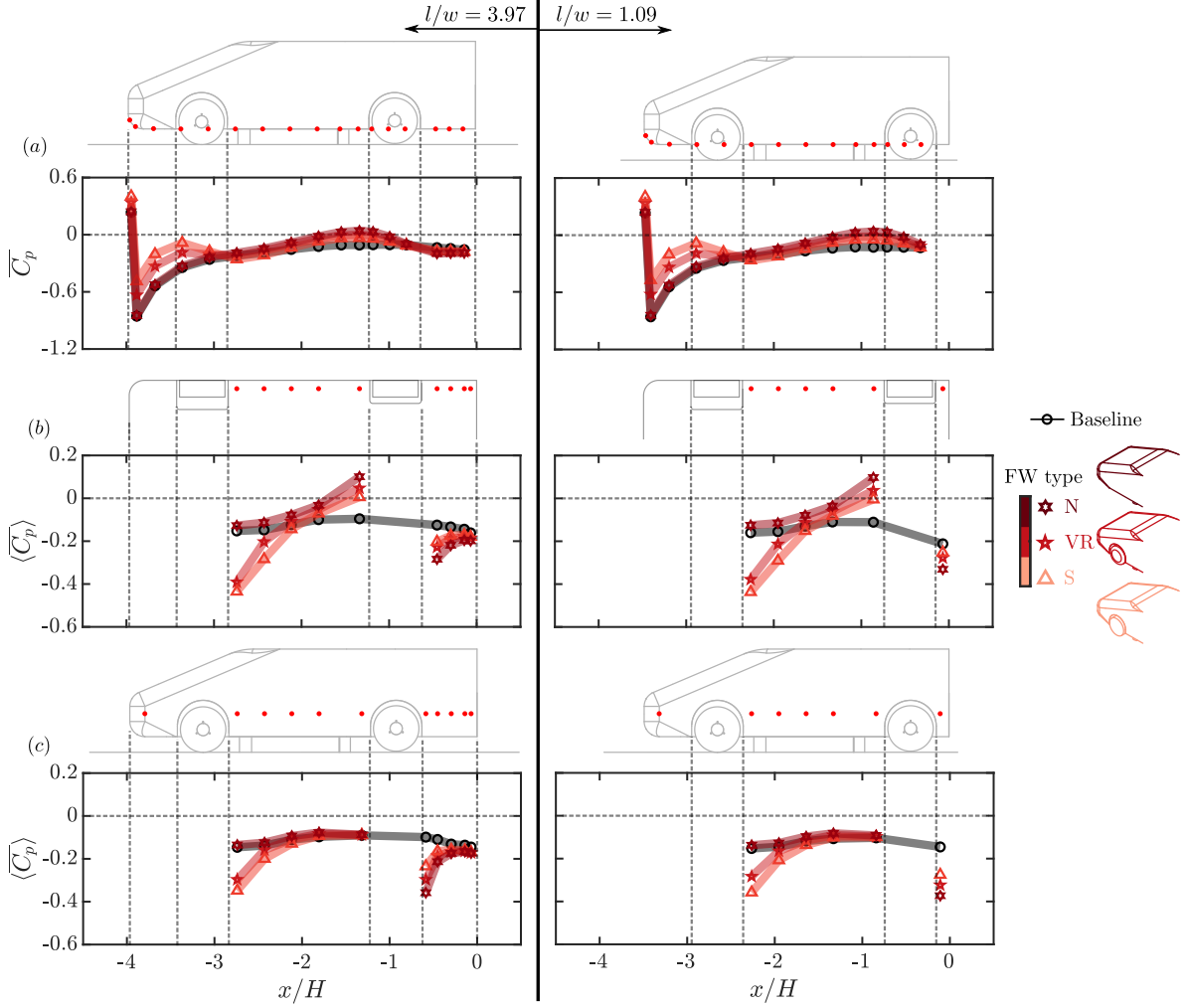


Figure 6.11: For the longest ( $l/w = 3.97$ ) and a short ( $l/w = 1.09$ ) bodies: mean pressure variations in the symmetry plane of the body (a), in the symmetry plane of the left-/right-hand side wheels (b), and in a horizontal plane at  $z/H = 0.43$  (c) with front-wheel (FW) type.

upward shift in  $\Delta \overline{C_B}$  with reducing front-wheel bluntness observed before in figure 6.4(a). On the other hand, in the drag-sensitive regime with  $l/w < 2.5$ , several observations indicate that the front wheels influence the local interactions between the rear wheels and the vehicle wake. Specifically, we noticed that the pressure on the base in the vicinity of the rear wheels is decreased with reducing front-wheel bluntness. Accompanied by this, the flow momentum inside the recirculation region is enhanced. The flow mechanisms leading to these consequences will be detailed in the next section by focusing on the local flow fields near the wheels.

### 6.4.3 Influence on near-wake interactions

In this section, the influence of the front-wheel bluntness on the drag-sensitive regime at  $l/w < 2.5$  is investigated based on a detailed analysis of the local flow near the front and rear wheels. For the largest ( $l/w = 3.97$ ) and smallest ( $l/w = 0.65$ ) wheel-to-base distances, the pressure distributions around the body are presented in figure 6.11. We focus first on the case with the largest  $l/w$  distance at the left-hand side of this figure.

In the symmetry plane of the body ( $y/H = 0$ ), the pressure variation in the underflow with front-wheel type is shown in figure 6.11(a). At the bottom leading edge, the baseline case presents a sharp pressure decrease due to local flow curvature. This is followed by a gradual recovery of pressure until the trailing edge of the model. When the sharp-edged wheels (configuration S) are installed on the baseline case, we observe an increase of pressure at approximately  $x/H < -1.5$ . This is probably due to the blockage induced by the front wheels and therefore the lower flow rate

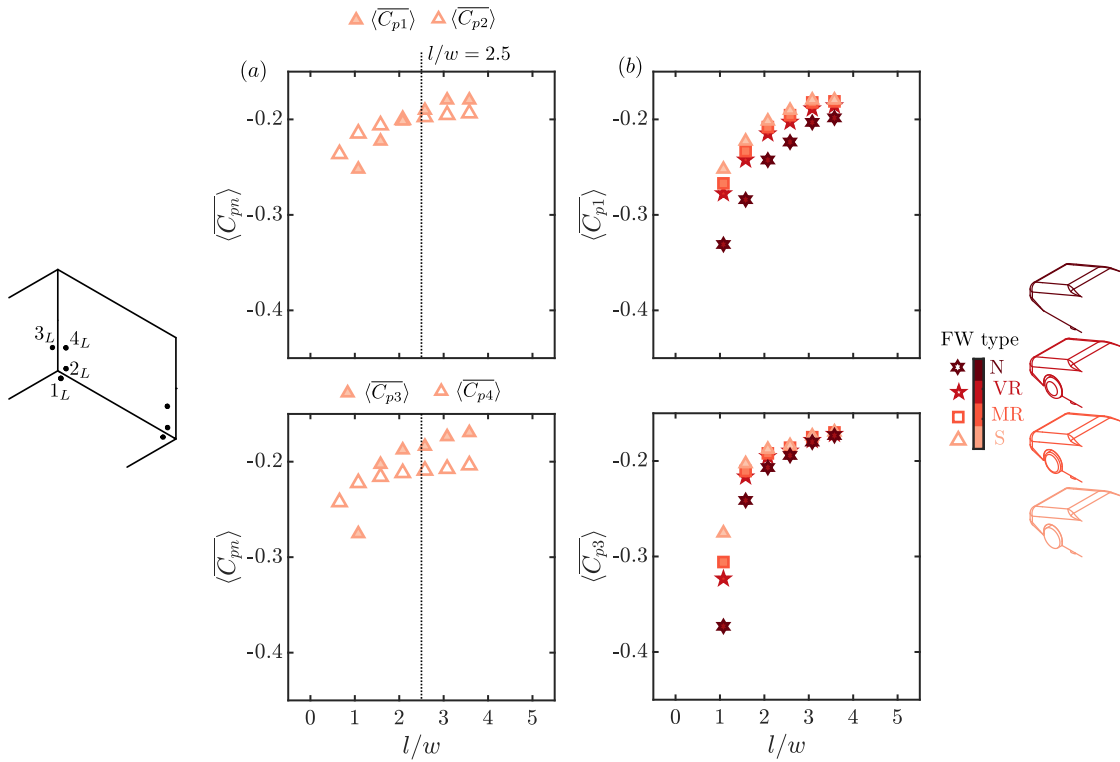


Figure 6.12: With increasing  $l/w$ : (a) Comparisons between either  $\langle C_{p1} \rangle$  and  $\langle C_{p2} \rangle$  or  $\langle C_{p3} \rangle$  and  $\langle C_{p4} \rangle$  for the four sharp-edged wheel configuration. (b) Different pressures imposed by different configurations near the trailing edge of the vehicle.

entering the underflow at the front. With decreasing front-wheel bluntness, the pressure gradually decreased to the value of the baseline case. Downstream of  $x/H = -1.5$  before the rear wheels, the front-wheel bluntness is found to govern the local pressure level. With decreasing front-wheel bluntness, the pressure level is gradually increased in the symmetry plane of the model. This means that the flow rate in the rear part of the underbody is influenced by the flow blockage induced by the rear wheels.

Moreover, the streamwise pressure evolution in the symmetry plane of the left-/right-hand side wheels in figure 6.11(b) shows the separation regions behind the wheels, i.e., the wakes of the front and rear wheels. Behind the front wheels at  $x/H < -2$ , the reduction of front-wheel bluntness gradually increases the local pressure. Further downstream of  $x/H = -2$  in front of the rear wheels, the front wheels also govern the local pressure level. With reducing front-wheel bluntness, the pressure in front of the rear wheels denoting flow stagnation increases. Based on this observation, it is expected that the facing flow velocity for the rear wheels is increased when the front-wheel bluntness is reduced. Accompanied by this, inside the wake of the rear wheels, a gradual decrease of pressure is noticed.

Downstream of the front wheelhouses in a horizontal plane at the half height of the nose  $z/H = 0.43$  (see figure 6.11(c)), flow separation exists and the pressure inside the separation bubble increases to the baseline value with the reduction in front-wheel bluntness. On the contrary inside the separation region behind the rear wheelhouses, the local pressure decreases when the front-wheel bluntness is reduced. It is interesting to note that the pressure variation behind the rear wheelhouses is not related to the flow in front of them. Therefore, the formation of the separation regions behind the rear wheelhouses may be triggered by the underflow in front of the rear wheels. This proposition is in accordance with the model in Regert & Lajos (2007) and Krajnović *et al.* (2011) describing the flow inside a wheelhouse.

With reducing  $l/w$  from  $l/w = 3.97$  to  $l/w = 1.09$ , the separation regions behind the rear wheels and wheelhouses are situated closer to the vehicle wake as shown in figure 6.11(b) and (c). Therefore, the interaction strength between these regions and the vehicle wake is expected to be enhanced. A finer examination of the interactions is provided in figure 6.12. The pressure measured

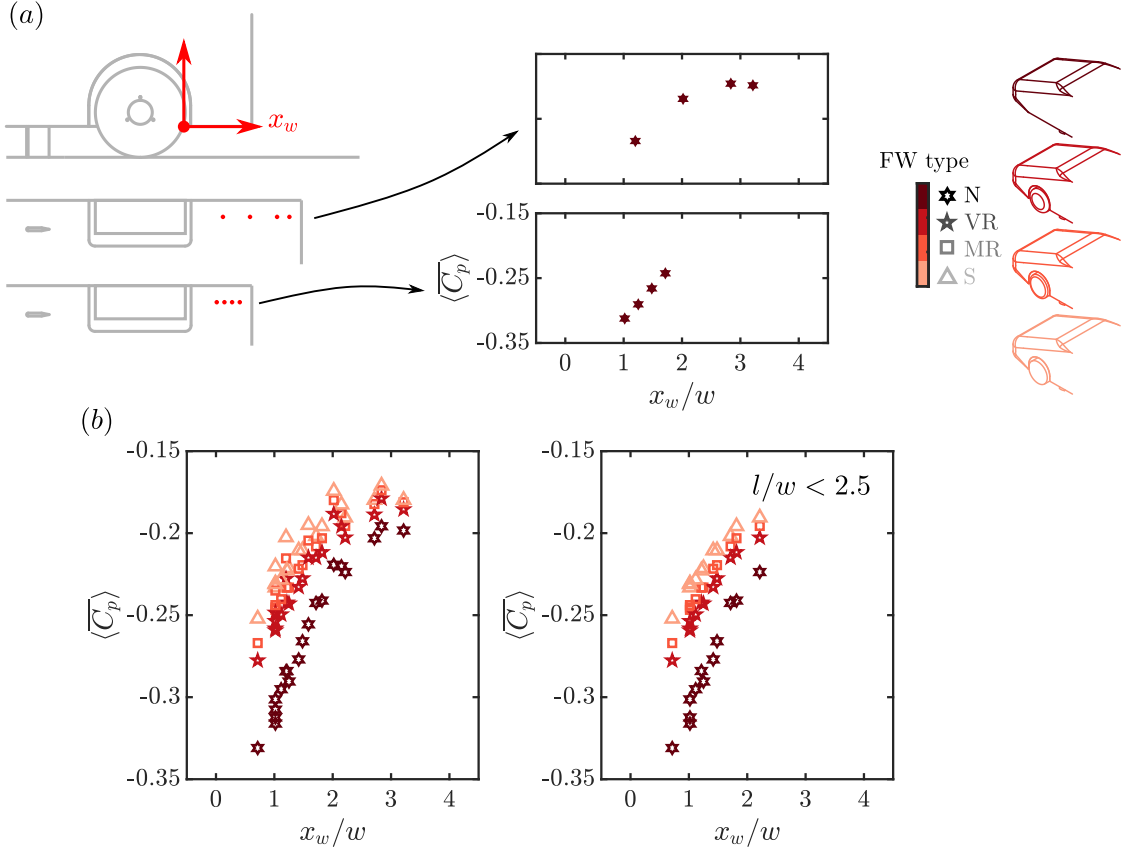


Figure 6.13: Streamwise pressure distribution in the wake of the rear wheels depending on front-wheel (FW) type. (a) Definition of the wheel-fixed reference system. (b) Mean pressure evolution in the wake of the rear wheels for all the  $l/w$  cases and for the cases in the drag-sensitive regime  $l/w < 2.5$ .

near the trailing edges of the vehicle downstream of the rear wheels and wheelhouses is focused. These locations are shown before in figure 6.11 to be representative of the separation regions formed by the rear wheels and wheelhouses, which are found to be greatly influenced by the bluntness of the front wheels. In order to better understand how the front wheels influence the wake of the vehicle, we show in figure 6.12 the mean pressure evolution for the measurements at four locations either downstream of the separation regions or at the base. For different  $l/w$ , the pressure taps before the trailing edges are located at a fixed distance from the base. For the configuration having the highest front-wheel bluntness (S), the comparison of  $\langle C_{p1} \rangle$  and  $\langle C_{p2} \rangle$  is shown in figure 6.12(a). At  $l/w > 2.5$ ,  $\langle C_{p1} \rangle$  is higher than  $\langle C_{p2} \rangle$ . This is similar to a canonical separating flow where the pressure outside the recirculation region is higher than the pressure inside due to local mean flow curvature. On the other hand, in the drag-sensitive regime  $l/w < 2.5$ ,  $\langle C_{p1} \rangle$  is lower than  $\langle C_{p2} \rangle$ . The difference  $\langle C_{p2} \rangle - \langle C_{p1} \rangle$  increases with decreasing  $l/w$ . In addition, the comparison between  $\langle C_{p3} \rangle$  and  $\langle C_{p4} \rangle$  shows a similar evolution. However, only at  $l/w < 1.5$ ,  $\langle C_{p3} \rangle$  is smaller than  $\langle C_{p4} \rangle$ . Therefore, we expected that the separation regions after the rear wheelhouses have a strong influence on the wake only at  $l/w < 1.5$ . This suggests that the characteristic length scale for the separation regions downstream of the rear wheelhouses is smaller than that of the rear wheel wakes. The influence of the wheelhouse flow on the base pressure will be further checked in §6.5.2 by closing the wheelhouses using aluminum tapes.

The front wheels have a strong influence on the pressure inside the separation regions behind the rear wheels and wheelhouses as briefly evoked before in figure 6.11. In figure 6.12(b), the variations of  $\langle C_{p1} \rangle$  and  $\langle C_{p3} \rangle$  with front-wheel bluntness is shown. For short bodies with small  $l/w$  values, the front-wheel bluntness has a strong influence on both  $\langle C_{p1} \rangle$  and  $\langle C_{p3} \rangle$ . With decreasing  $l/w$ , the influence is progressively enhanced. This indicates that the front wheels have a gradually stronger effect on the interactions between the separation regions and the vehicle wake.

In figure 6.13, we seek to quantify the pressure inside the wake of the rear wheels in order to show the influence of the front wheels on the wake of the rear wheels. First, a new reference frame

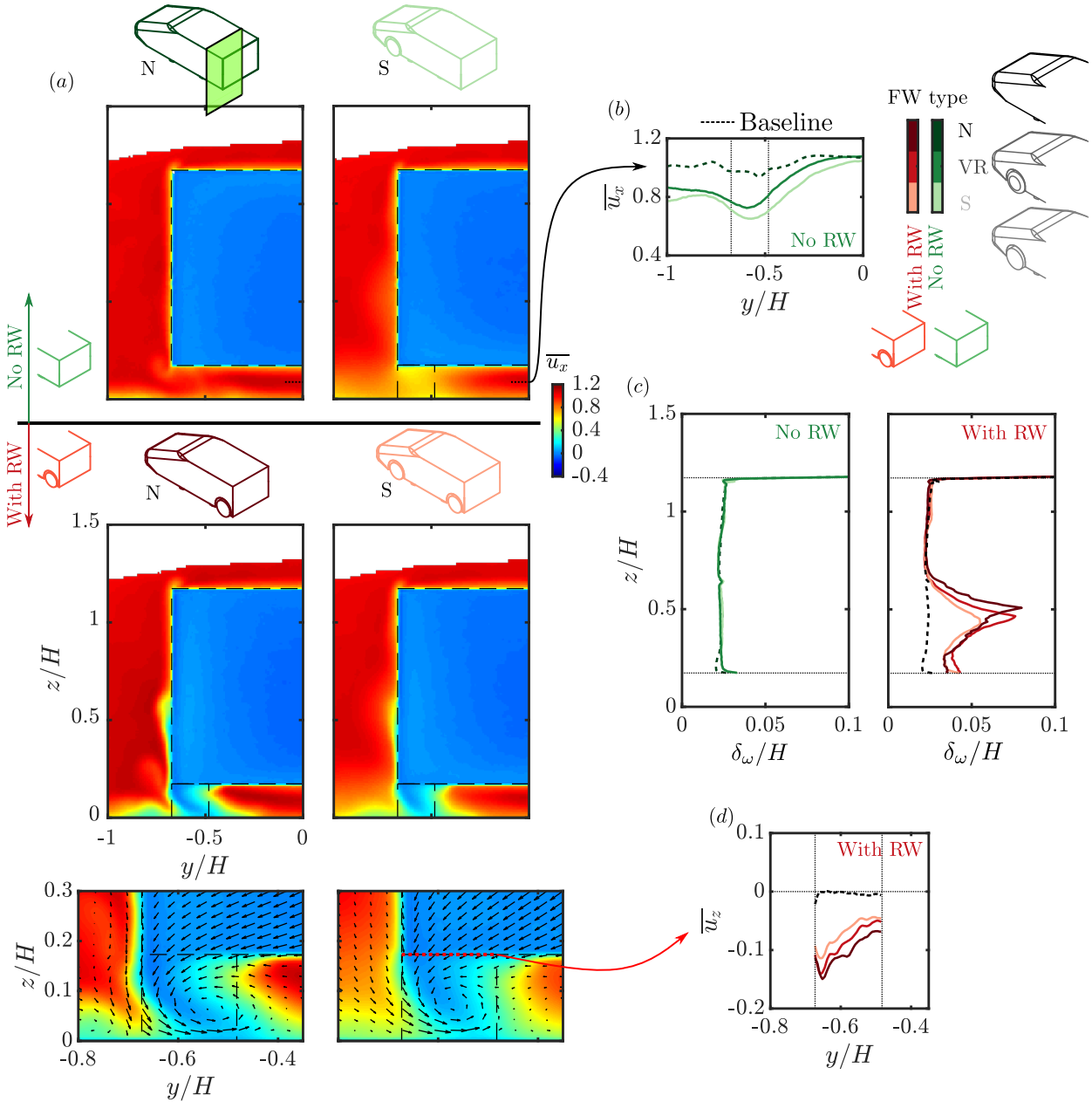


Figure 6.14: For the shortest body with or without rear wheels (RW): effects of front-wheel (FW) type on the mean streamwise velocity  $\overline{u_x}$  in the cross-flow plane  $x/H = 0.03$  (a), on the  $\overline{u_x}$  profile at the half height of the ground clearance (b), on the vorticity thickness  $\delta_\omega/H$  of the side shear layer (c), and on the mean vertical velocity  $\overline{u_z}$  at the height of the ground clearance (d).

is defined in figure 6.13(a). The rearmost location of the part of the rear wheels exposing to the underflow is set as the origin of this frame where  $x_w = 0$ . For each  $l/w$  case, several pressure taps are located in the symmetry planes of the left-/right-hand side wheels and on the underside of the body. The pressure measurements are plotted against the distance to the rear wheels  $x_w$ .

For all the  $l/w$  cases, inside the wake of the rear wheels in figure 6.13(b), the streamwise pressure evolution shows a sharp pressure increase from  $x_w/w = 0$  to approximately  $x_w/w = 2.5$  for all the configurations. With reducing front-wheel bluntness, the pressure inside the wake of the rear wheels is decreased. In the drag-sensitive regime  $l/w < 2.5$ , the sharp mean pressure gradient is pictured, which is found to be increased by the reduction in the front-wheel bluntness.

We now turn to the velocity measurements to reveal how the wake of the vehicle is locally modified by the variation in the front-wheel bluntness. The shortest body with the smallest wheel-to-base distance  $l/w = 0.65$  is investigated. We first consider the modifications in the cross-flow plane at  $x/H = 0.03$  by placing only the front wheels. The distributions of the mean streamwise

velocity  $\overline{u_x}$  are shown in figure 6.14(a). From the baseline case with quite uniform  $\overline{u_x}$  in the underflow (here the baseline case is also the case with no front wheels N), when the sharp-edged wheels are mounted on the front axle, we notice a moderate reduction of  $\overline{u_x}$  downstream of the wheels. The  $\overline{u_x}$  reduction is not only located right behind the front wheels but also at around  $y/H = -1$  probably due to the streamwise structures generated by the front wheels. This  $\overline{u_x}$  reduction is quite surprising when considering the long longitudinal distance between the front wheels and the measurement plane ( $\sim 12w$ ). Furthermore, the  $\overline{u_x}$  profiles along a horizontal line at the half height of the ground clearance are displayed in figure 6.14(b). Note here that the mean velocity magnitude  $\overline{u} = \sqrt{\overline{u_x^2} + \overline{u_y^2} + \overline{u_z^2}}$  shows the same profiles as  $\overline{u_x}$ , meaning that the flow is dominant in the streamwise direction. With reducing front-wheel bluntness, the velocity downstream of the front wheels is recovered gradually and finally reaches the baseline value. When the rear wheels are installed, they therefore experience different facing velocities for different front-wheel types. This has already been indicated by the different pressure levels right in front of the rear wheels in figure 6.11(a).

Furthermore, the side shear layers are quantified by the vorticity thickness, defined as:

$$\delta_\omega = \frac{\overline{u}_{max} - \overline{u}_{min}}{|\frac{\partial \overline{u_x}}{\partial y}|}, \quad (6.3)$$

where  $\overline{u}$  is the mean velocity magnitude, calculated as  $\overline{u} = \sqrt{\overline{u_x^2} + \overline{u_y^2} + \overline{u_z^2}}$ . Between the cases with no rear wheels, we notice no obvious difference in figure 6.14(c) since the front wheelhouses are located relatively far from the measurement plane.

The effects of the front wheels on the vehicle wake are discussed now with the presence of the rear wheels. In figure 6.14(a), the mean streamwise velocity  $\overline{u_x}$  in the cross-flow plane  $x/H = 0.03$  is shown. From the baseline case, we notice that the part of the side shear layers behind the rear wheelhouses becomes thicker when four sharp-edged wheels are installed. From case S (sharp-edged front wheels) to case N (no front wheels) with reducing front-wheel bluntness, the perturbations from the rear wheelhouses to the side shear layers become more pronounced. This evolution with front-wheel bluntness is better pictured in figure 6.14(c) by plotting the vorticity thickness  $\delta_\omega/H$  of the side shear layers. With decreasing front bluntness,  $\delta_\omega/H$  is increased gradually.

Moreover, the near wake of the rear wheels is observed in the underflow. The concomitant momentum loss reduces greatly the mean shear bounding the bottom part of the vehicle wake. From the zoom view given in figure 6.14(a), no noteworthy change in the flow structures inside the near wake of the rear wheels is measured by considering the in-plane mean velocity vectors. At the height of the ground clearance, the vectors show a mean mass transfer from the wake of the vehicle to the wakes of the rear wheels. This feature is in good accordance with the measurements in chapters 4 and 5. The horizontal span of the mean mass transfer is found to be the whole width of the wheel wake which is approximately the same as the width of the rear wheels (see the dotted line in the zoom view for the projection of the rear wheels). Moreover, the strength of the mean mass transfer is found to be sensitive to the front-wheel bluntness. An idea of the mass transfer velocity is given in figure 6.14(d) by plotting the mean vertical velocity  $\overline{u_z}$  at the height of ground clearance in the present PIV plane. It is shown that by reducing the front-wheel bluntness, the strength of the mean mass transfer is enhanced.

A more global idea of the streamwise distribution of the mean mass transfer is presented in figure 6.15(a) by showing the mean vertical velocity  $\overline{u_z}$  in the symmetry plane of the left wheels at  $y/H = -0.67$ . With reducing front-wheel bluntness, an increase in downward velocity is noticed behind the rear wheels. The  $\overline{u_z}$  profiles at the height of the ground clearance are plotted in figure 6.15(b) to quantify the mean mass transfer. An increase in the mean mass transfer is measured by reducing front-wheel bluntness. At  $x_w/w \approx 1$ , the maximum of negative  $\overline{u_z}$  is almost doubled from the configuration S to N. It is noted that the length of the mass exchange surface ends at  $x_w/w \approx 2.5$  and is not varied with front-wheel bluntness.

With increasing  $l/w$ , the mean mass transfer is suppressed gradually for all the configurations. The velocity measurements are very similar to the measurements in chapter 5 and are therefore not shown here for brevity. For the cases with  $l/w > 2.5$ , it is noted that the mean mass transfer is not measured.

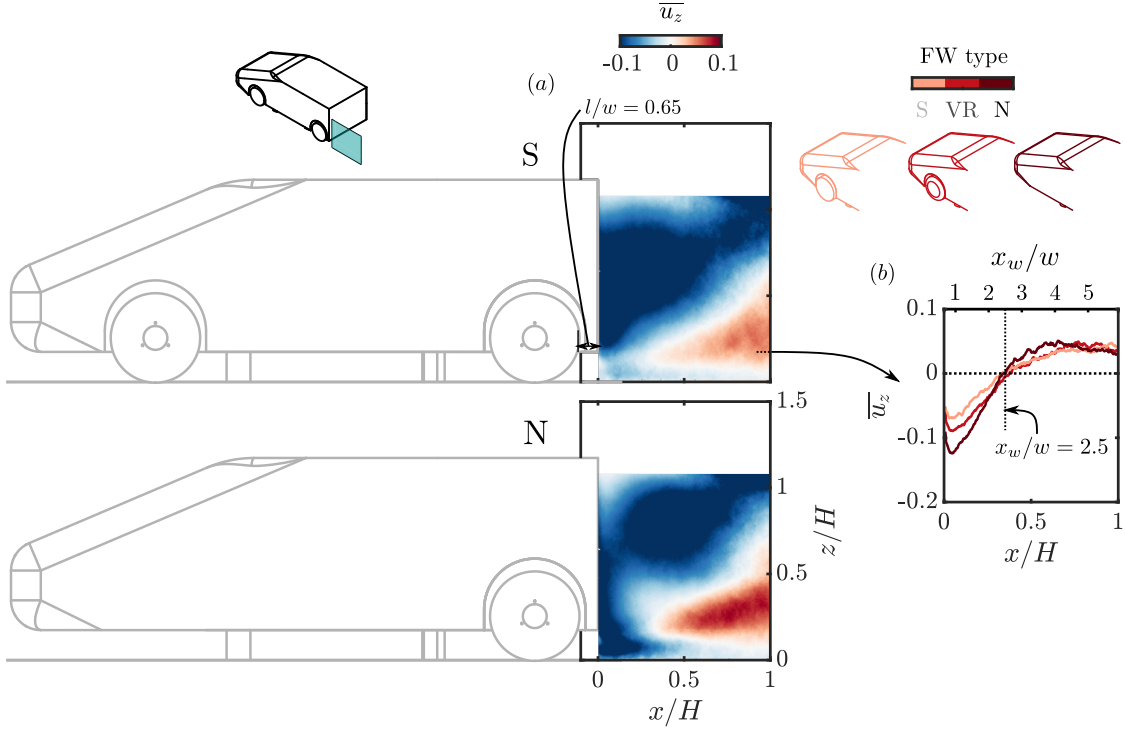


Figure 6.15: For the shortest body with sharp-edged rear wheels: mean vertical velocity  $\overline{u_z}$  in the symmetry plane of the left wheels for configurations S and N (a), and for all the configurations (b) by plotting  $\overline{u_z}$  along a horizontal line at the height of the ground clearance.

#### 6.4.4 Scaling of drag changes in the drag-sensitive regime

We have shown that the front wheels play an important role in the wakes of the rear wheels and consequently in the interactions between the rear wheels and the wake of the body. The facing velocity given by the wakes of the front wheels to the rear wheels governs the mean pressure inside the wakes of the rear wheels and also the local interactions between the rear wheels and the wake of the body. To have a clearer idea of the link between the front wheels and the base drag, in this section we present a scaling for the base drag changes shown before in figure 6.4.

The first step for the scaling relies on the quantification of the facing velocity for the rear wheels. The distributions of the mean streamwise velocity  $\overline{u_x}$  in the cross-flow plane at  $x/H = 0.03$  are shown in figure 6.16(a) for the shortest body with no rear wheels. With increasing front-wheel bluntness, the flow momentum behind the front wheels is gradually reduced. Furthermore, the  $\overline{u_x}$  profiles along the half height of the ground clearance are shown in figure 6.16(b). We note here that the present PIV plane is located very near the base. The channel formed by the floor and the underbody is expected to preserve the  $\overline{u_x}$  values till the location of the rear wheels. Therefore, in the situation where the rear wheels are installed, the rear wheels are expected to experience the same level of upstream velocity as the space-averaged velocity  $\langle \overline{u_x} \rangle$  in the region limited by the width of the wheels (marked by vertical dotted lines). The space-averaged velocity  $\langle \overline{u_x} \rangle$  for different front-wheel type is then plotted at the right-hand side of figure 6.16(b) and are defined as the facing velocity for the rear wheels  $u_f$ .

The base drag is then scaled in figure 6.16(c). As we have shown in section 6.4.2, for all the  $l/w$  cases the global effects of the wheels on the vehicle wake always exist. Therefore, the local near-wake interactions are focused by using the base drag variant  $\Delta \overline{C_B^*} = \Delta \overline{C_B} - \Delta \overline{C_B}(l/w = 2.5)$  defined in figure 6.4(c). This variant then is found to scale linearly with the normalized facing velocity  $u_f$ . The physical argument for this scaling property will be detailed in §6.5.1 with the help of a model explaining the physical mechanisms.

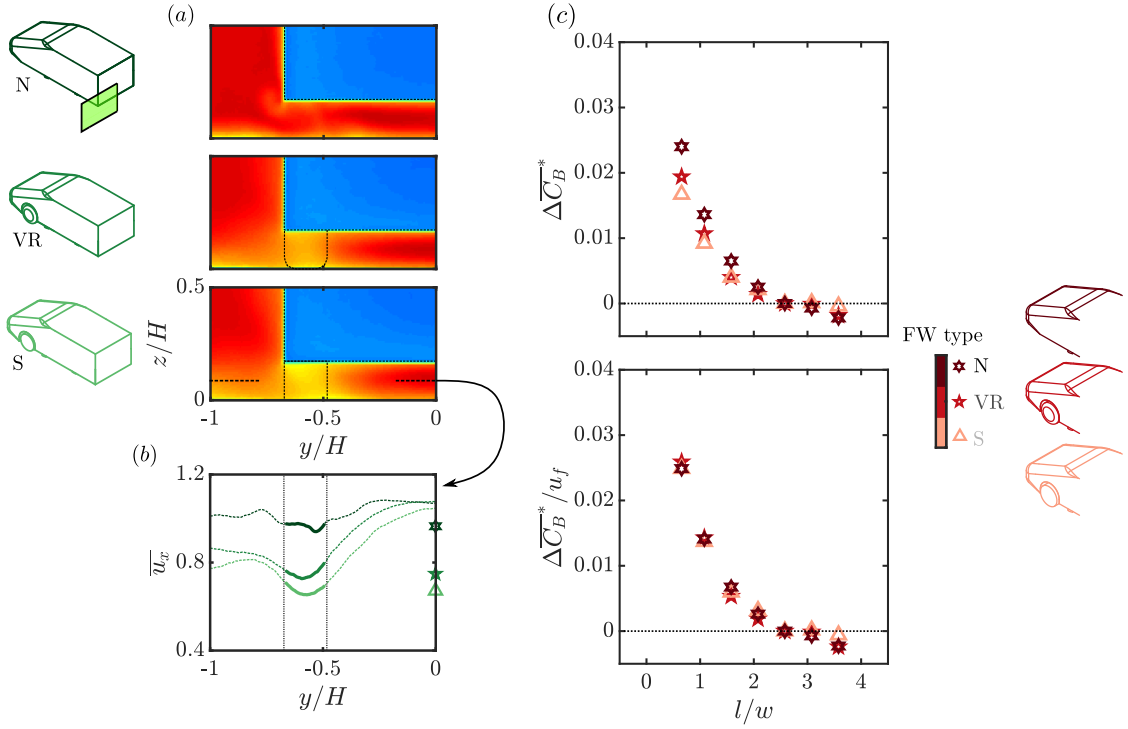


Figure 6.16: (a) Evolution of streamwise velocity  $\bar{u}_x$  in the cross-flow plane ( $x/H = 0.03$ ) with the front-wheel (FW) bluntness, the body length is the shortest. (b)  $\bar{u}_x$  profiles at the half-ground-clearance height for the cases in (a), space-averaged values  $\langle \bar{u}_x \rangle$  for the region limited by the wheel width are shown at the right-hand side of the plot and are defined as the facing velocity for the rear wheels  $u_f$ . (c) Scaling of the base drag increase in the drag-sensitive regime.

## 6.5 Discussions and concluding remarks

This last section is dedicated to a discussion and a summary of the main results presented. First, a physical model is proposed to explain how the interactions between the rear wheels and the vehicle wake are influenced by the front wheels and how the base drag is varied in this process. In addition, different sources of base drag and their contributions are discussed. Finally, the concluding remarks are presented.

### 6.5.1 Model

A conceptual sketch of the underflow around the rear wheels is shown in figure 6.17(a). We found that because of the front wheels, the upstream flow velocity  $U_f$  for the rear wheels is smaller than the free-stream velocity  $U_0$ . Furthermore, a sketch of the global pressure distribution behind the vehicle is presented in figure 6.17(b). Here we follow the measurement in Grandemange *et al.* (2014) and the RANS simulations conducted in appendix A. The background pressure level  $C_{pg} = (p_g - p_0)/(0.5\rho U_0^2)$  in the region under the vehicle wake (the red line represents the mean separatrix) is dictated by the pressure inside the vehicle wake. We assume here that these two quantities  $U_0$  and  $p_g$  are the main factors in setting the pressure level inside the rear wheel wakes. Considering that the Reynolds number investigated is high enough, the pressure coefficient inside the rear wheel wakes  $C_{pw}^* = (p_w - p_g)/(0.5\rho U_f^2)$  is therefore a fixed value when  $p_g$  and  $U_f$  are varied. Using the reference pressure  $p_0$  and velocity  $U_0$  of the present work, the pressure coefficient inside the wake of the rear wheels is then written as:

$$\overline{C_{pw}} = \overline{C_{pg}} + u_f^2 \overline{C_{pw}^*}. \quad (6.4)$$

This model is of course very simplified because the velocity upstream of the rear wheel is not uniform at the value  $u_f = U_f/U_0$ . In what follows, we will use the value of  $u_f$  calculated in figure 6.16, which is a space-averaged value in the region limited by the wheel width at the half-ground-

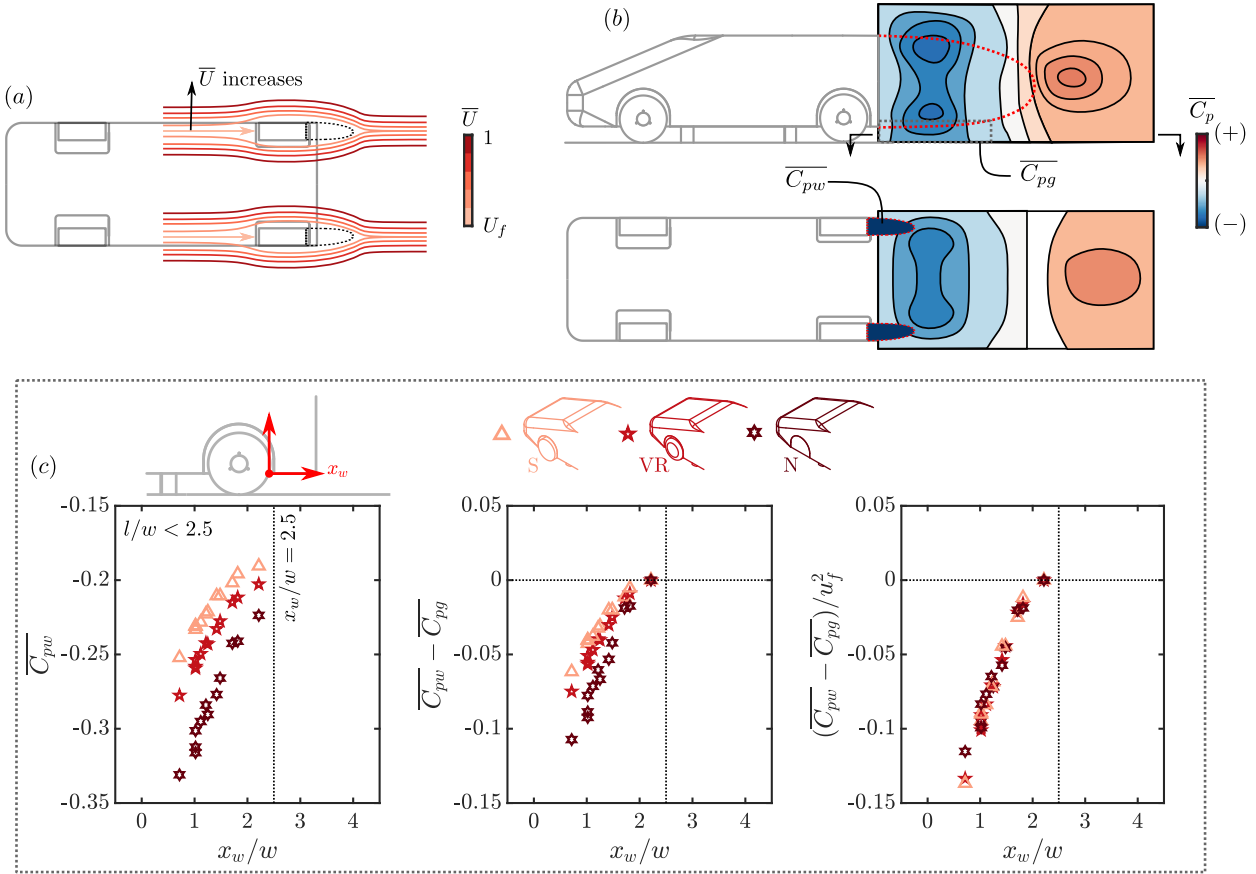


Figure 6.17: (a–b) A conceptual sketch of the global pressure distribution around the model: Local pressure variation around the rear wheels due to facing velocity modification (a). Global pressure distribution in the vehicle wake following the measurement in Grandemange *et al.* (2014) and the RANS simulations conducted in appendix A (b). (c) Scaling of the streamwise pressure development in the rear wheel wake from figure 6.13 considering the sketch.

clearance height. This equation considering the relation between global and local pressure is now visualized based on our experimental data.

When the front-wheel type is changed, the vehicle wake topology and the facing velocity for the rear wheels are found to be modified. This means that the two terms at the right-hand side of equation 6.4 are changed. For the cases in the drag-sensitive regime ( $l/w < 2.5$ ), the streamwise pressure evolution in the wake of the rear wheels from figure 6.13 is shown again in figure 6.17(c). For all the configurations, the  $\bar{C}_{pw}$  evolution features a sharp increase of pressure from  $x_w/w = 1$  to  $x_w/w = 2.5$ . This sharp pressure increase is followed by a plateau as shown before in figure 6.13. For different configurations, the plateau has different  $\bar{C}_{pw}$  levels which are set by the vehicle wake as proposed in figure 6.17(b). We approximate here the most downstream measurements of  $\bar{C}_{pw}$  at  $x_w/w = 2.5$  as  $\bar{C}_{pg}$ . It is then shown that the pressure difference  $\bar{C}_{pw} - \bar{C}_{pg}$  scale with the square of the facing velocity  $u_f^2$ .

When the relative distance between the rear wheels and the base is smaller than  $2.5w$ , we measured a mean mass transfer from the vehicle wake to the wakes of the rear wheels. The strength of this mean mass transfer is sensitive to the type of front wheels. In figure 6.18(a), a sketch of the mass exchange process is schematically shown. The recirculation region of the vehicle wake bears a pressure level of  $\sim \bar{C}_{pb}$  (mean base pressure coefficient), which is higher than the pressure level inside the rear wheel wake (see figure 6.12 for the experimental data). Accompanied by this, a mean mass transfer was measured. In appendix A, using RANS simulations, we noticed that locally near the mean mass transfer, the pressure difference between the regions above and below the interface drives the mass exchange. If this is the case for the present work, the total pressure of the mean flow is a constant along any streamline passing through the interaction interface (schematically shown in figure 6.18a):

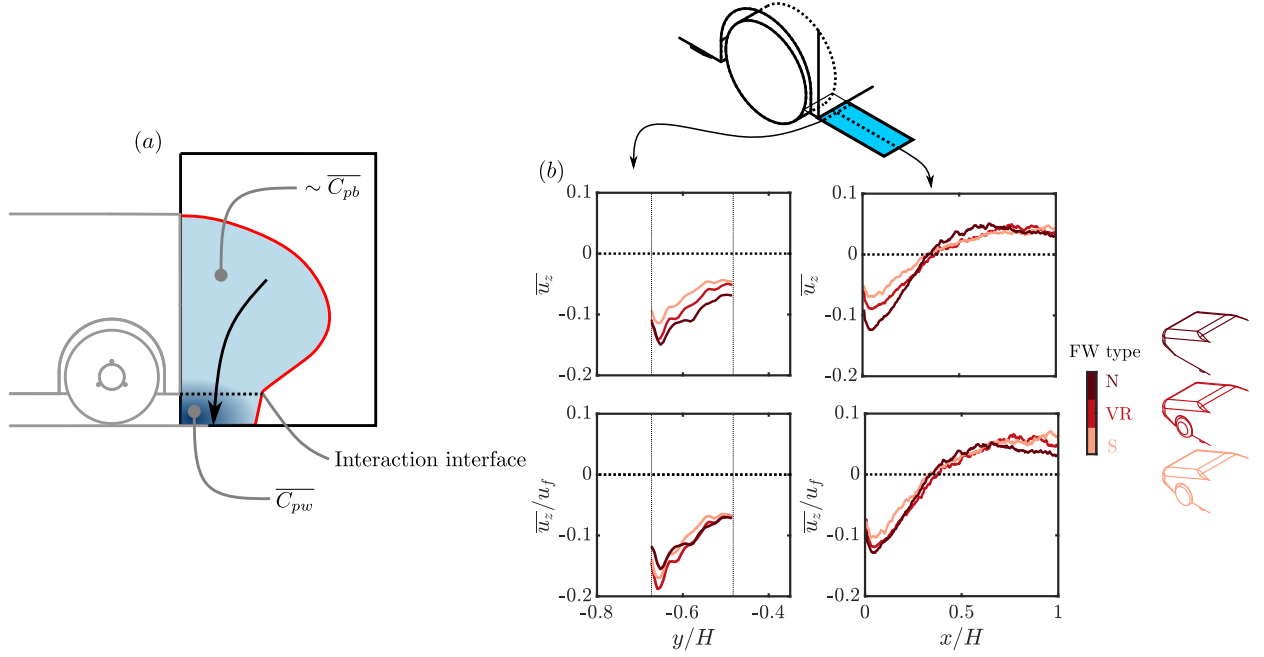


Figure 6.18: (a) A conceptual sketch illustrating the mean mass transfer through the interaction interface between the vehicle wake and the rear wheel wake driven by the pressure difference between the wakes. (b) Scaling of the mass exchange velocity at the interface characterized by the mean vertical velocity measured in figure 6.14(d) and 6.15(b).

$$u_e^2 + \overline{C_{pw}} = u_r^2 + \overline{C_{pb}}, \quad (6.5)$$

where  $u_e$  is the normalized mass exchange velocity at the interface and  $u_r$  is the velocity inside the recirculation region of the vehicle. When the facing flow velocity  $u_f$  for the rear wheels is varied slightly, the slight change in all components of equation 6.5 then leads to:

$$2u_e\delta u_e + \delta\overline{C_{pw}} = 2u_r\delta u_r + \delta\overline{C_{pb}}. \quad (6.6)$$

We further assume that the velocity inside the recirculation region of the vehicle is only slightly modified ( $\delta u_r \approx 0$ ). Moreover, the pressure variation  $\delta\overline{C_{pb}}$  is approximated as the variation of the background pressure level under the vehicle wake  $\delta\overline{C_{pg}}$ . The component of the mass exchange velocity  $2u_e\delta u_e$  can therefore be further written as:

$$2u_e\delta u_e \approx \delta(\overline{C_{pg}} - \overline{C_{pw}}). \quad (6.7)$$

The term  $\overline{C_{pg}} - \overline{C_{pw}}$  scales quadratically with the facing velocity  $u_f$  as shown before in figure 6.17(d). As a consequence, we should expect the mass exchange velocity  $u_e$  to scale linearly with the facing velocity  $u_f$ . As shown in figure 6.18(b), the measurements in the cross-flow plane and in the symmetry plane of the left-hand side wheels both confirm this. Therefore, our experimental data is in good agreement with the physical model proposed in this section. The insensitivity of the mean mass transfer and the related base pressure change to the vertical asymmetry of the vehicle wake shown before in chapter 5 can be also explained by considering the proposed model. When the vertical asymmetry is modified, the pressure relationship (equation 6.4) leads to always the same pressure difference  $\overline{C_{pg}} - \overline{C_{pw}}$  above and below the interaction interface. Therefore the strength of the mean mass transfer is not varied.

Further explanation of the scaling of the base drag in figure 6.16 is provided by the model proposed in chapter 4. This model was derived from fundamental studies focusing on the effect of base suction on the base pressure of either a 2-D D-shaped cylinder (Bearman, 1967) or a 3-D bluff body (Hsu *et al.*, 2021). In these two reference works, a simple relation between the base drag change  $\Delta\overline{C_B}$  and the suction flow rate  $q$ :

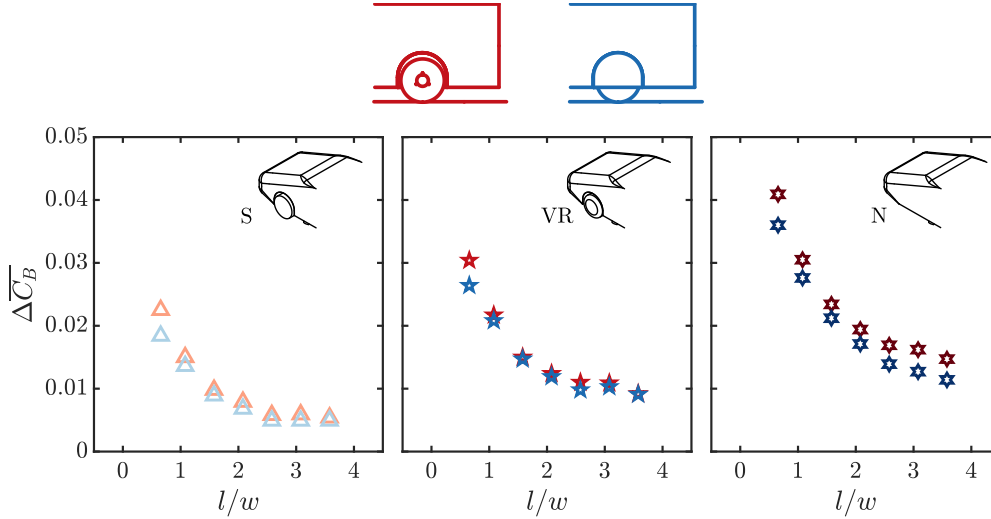


Figure 6.19: For configurations S, VR, and N: effect of flow separation from the rear wheelhouses on the base drag evolution  $\Delta\overline{C}_B$  with the distance  $l/w$  between the rear wheels and the base.

$$\Delta\overline{C}_B = \frac{2q}{HWU_0} = 2C_q, \quad (6.8)$$

was found to hold for small suction flow rate coefficient  $C_q$  ( $C_q < 0.03$  in [Hsu et al. \(2021\)](#)). The suction flow rate  $q$  is written in the form of  $q = S_e U_e$ , where  $S_e$  and  $U_e$  are respectively the surface area and the velocity of the suction. In such situations, fluid particles continuously enter the mean recirculating region and therefore lose their longitudinal momentum. By writing that a pressure decrease at the base is responsible for this momentum flux balance, one gets  $\Delta F_x = (\rho q)U_0$ . Normalizing the corresponding quantities, the simple relation  $\Delta\overline{C}_B = 2C_q$  is then obtained. This model was then found to be able to explain the results, such as the scalings for the base drag. In the present chapter, when the facing flow velocity  $u_f$  is varied for a fixed  $l/w$  value, the surface area is not varied as measured in figure 6.14(a) and in 6.15(b). Using the model, the linear scaling for the base drag is then linked with the scaling for the mass exchange velocity in figure 6.18(b), highlighting the importance of the mass exchange in the drag-sensitive regime where  $l/w < 2.5$ .

### 6.5.2 On the drag sources from near-wake interactions

The separation regions around a ground vehicle and the interactions between them are direct or indirect sources of aerodynamic drag. In the present work, we have shown two sources of base drag from the interactions between the vehicle wake and two separation regions. These two separation regions, as shown before in figure 6.14(a), are located behind the rear wheels and the rear wheelhouses. Their respective contributions are now discussed.

#### From the mean mass transfer (for small wheel-to-base distances $l/w < 2.5$ )

First of all, the near-wake interactions between the separation regions behind the rear wheels (i.e. the rear wheel wakes) and the vehicle wake locally was found to be a mean mass transfer. An order of magnitude evaluation of its base drag contribution can be gained by using the simple relation of  $\Delta\overline{C}_B = 2C_q$  proposed in chapter 4. The surface of mass exchange is represented by two rectangles  $S_e = 2W_e L_e$  with the width  $W_e$  approximated as the width of the rear wheels  $W_e = w$  (see figure 5.14 for an illustration). The length  $L_e$  of the exchange surface is given by the exposed part of the region downstream of the rear wheels having the ability to induce the mean mass transfer from the vehicle wake  $L_e = 2.5w - l$ . This was shown before in figure 6.15(b). With this approximation, the mass exchange velocity can be calculated by the relation  $U_e/U_0 = HW\Delta\overline{C}_B^*/2S_e$ . When dividing the two sides of this equation by the facing velocity for the rear wheels  $u_f = U_f/U_0$ , a new relation for the present situation  $U_e/U_f = HW\Delta\overline{C}_B^*/2u_f S_e$  is obtained. For all the configurations having the same  $\overline{C}_B^*/u_f$  in the drag-sensitive regime  $l/w < 2.5$  (see figure 6.16c),  $U_e/U_f$  is calculated to

be  $\sim 0.06$  for the  $l/w = 0.65$  cases. This is a good order of magnitude of the downward velocity in figure 6.18(b). Therefore, the mean mass transfer governs the near-wake interactions and base drag increase for the present situation.

### From rear wheelhouses

An investigation of the base drag contribution from the wheelhouses is carried out in figure 6.19. The flow separation from the rear wheelhouses is prevented by sealing the gaps at the sides of the model between the rear wheels and the wheelhouses using aluminum tapes. Then, the same measurements as in figure 6.19 are repeated. For all the configurations, we notice that the evolution of  $\Delta\overline{C}_B$  with  $l/w$  is only slightly modified by the flow separation at the rear wheelhouse. Therefore, the interactions between the separation behind the rear wheelhouses and the vehicle wake are believed to have very limited effects on the base drag in the present situation.

### 6.5.3 Concluding remarks

The separation regions around a ground vehicle and the interactions between them are direct or indirect sources of aerodynamic drag. In some situations, local drag reduction induces modifications in the interactions between the separation regions which may compensate or even dominate the local gain. A specific situation was studied in the present chapter by investigating the influence of wheel geometry on the wake and drag of a square-back vehicle geometry. The wheel shoulder radii at the front and rear axles were considered. The systematic variation of the radii and several additional parameters (distance between the rear wheels and the base  $l$ , mean vertical symmetry of the vehicle wake) shows a substantial increase of base drag by up to 21% from the baseline case without wheels. This drag increase is a result of the complex interactions between three players: the front wheels, rear wheels, and the vehicle wake.

At the front axle, reducing the front-wheel bluntness increases the base drag and the level of increase depends on the initial wake balance. The facing velocity  $u_f$  for the rear wheels is increased with the reduction in the bluntness which reduces the pressure level inside the rear wheel wake. In the present situation, when the wheel-to-base distance  $l/w$  ( $w$  is the width of the wheels) is smaller than a threshold of 2.5, the pressure decrease was found to be accompanied by an enhancement of the mean mass transfer discovered in chapter 5 from the vehicle wake to the wakes of the rear wheels. These interactions lead to a scaling law with the base drag linearly proportional to  $u_f$ . On the other hand at the rear axle, varying the bluntness of the rear wheels has almost no influence on the base drag regardless of the vehicle wake asymmetry.

Finally, by proposing a relationship between the global pressure level established by the vehicle wake, the facing flow velocity for the rear wheels  $u_f$ , and the development of the rear wheel wake, a physical model was developed. Our assumption was that the pressure difference between the two sides of the interaction interface (where the mean mass exchange happens) governs the velocity of the mean mass transfer. This model was then found in accordance with the experimental data measured in the present chapter. Moreover, the application of the momentum exchange model proposed in chapter 4 further explains the linear scaling of the base drag with the facing velocity  $u_f$ .

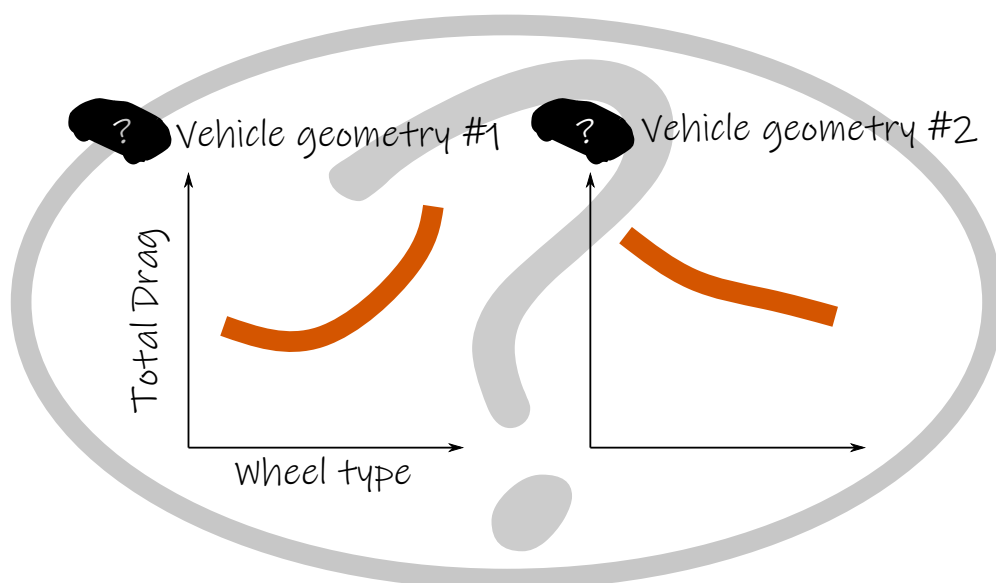
The findings in the present chapter refine our physical understanding of the interactions between the wheels and the vehicle wake in the automotive industry and between separation regions in a more general situation with complex bluff body flow. The physical model proposed was found able to illustrate the insensitivity of the mean mass transfer and the related drag changes to the vertical asymmetry of the vehicle wake found in chapter 5 (see figure 5.13). This is expected to hold when the shape of the vehicle back is modified which will be investigated in the next chapter.



## Chapter 7

# Extension to a different vehicle back shape

The dependency of wheel-vehicle interactions on vehicle back shape is investigated experimentally. Based on the  $20^\circ$  fast-back Windsor body, additional measurements repeating the investigations in previous chapters using the square-back Windsor body are carried out. By placing a pair of D-shaped obstacles under the vehicle or by installing wheels on the vehicle, similarities and differences in the wheel-vehicle interactions are found when comparing the results from the two different vehicles. We show that the mean mass transfer from the vehicle wake to the wake of the rear wheels (or obstacles) and the related pressure drag change are insensitive to the vehicle shape. When varying the distance between the obstacles and the vertical base of the vehicle, the same flow regimes and pressure drag sensitivity as in chapter 4 are found. Here the pressure drag changes are still governed by the scaling properties found for the square-back vehicle. When the wheels are installed, the mean mass transfer and the related pressure drag change are found to be enhanced by reducing the front-wheel bluntness. This is in accordance with the finding in chapter 6 for the square-back model. On the other hand, differences between the two different vehicle types are revealed. Most importantly, the vertical balance of the recirculating flow behind the vertical base of the fast-back is relatively insensitive to the presence of obstacles or wheels.



## Contents

7.1	Dependency of wheel-vehicle interactions on vehicle shape . . . . .	104
7.2	Experimental setup . . . . .	105
7.3	Baseline flow . . . . .	107
7.4	Effects of underflow perturbations . . . . .	109
7.5	Effects of wheels . . . . .	114
7.6	Concluding remarks . . . . .	118

## 7.1 Dependency of wheel-vehicle interactions on vehicle shape

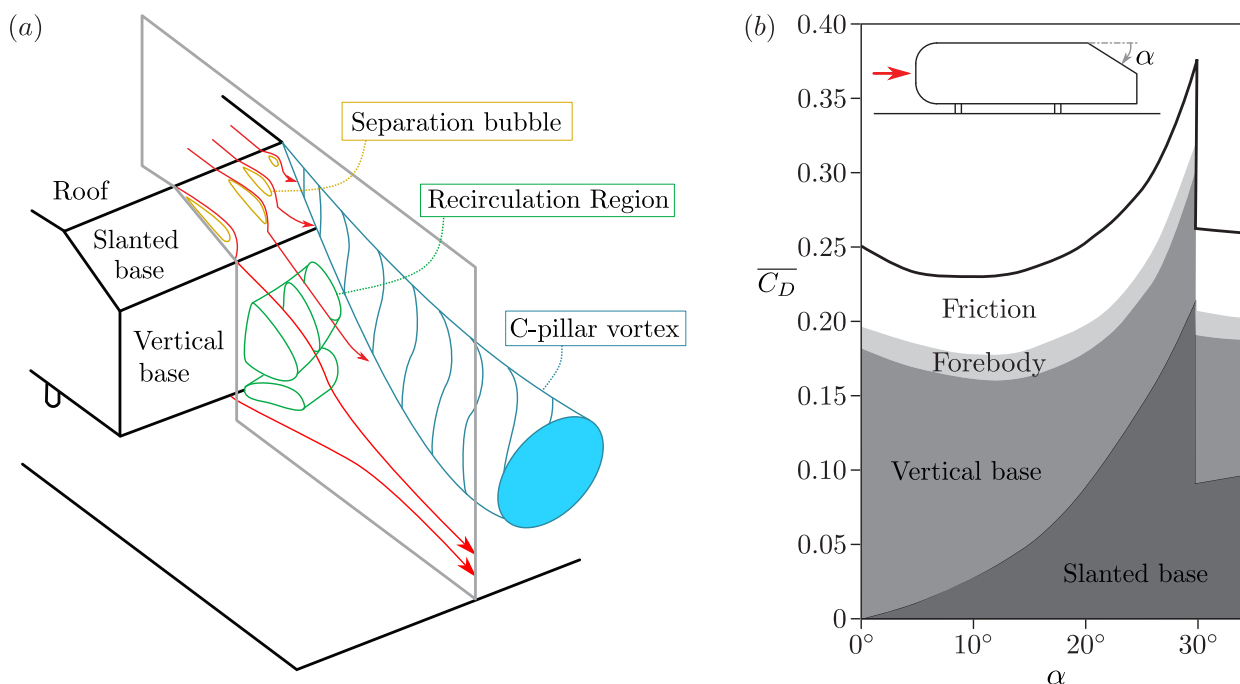


Figure 7.1: (a) Mean wake topology of the 25° fast-back Ahmed body. (b) Drag evolution of the Ahmed body with the angle of the rear window  $\alpha$ . The figure is adapted from Grandemange (2013) with data from Ahmed *et al.* (1984).

In the previous chapters, we examined the wheel-vehicle interactions and their sensitivity to different parameters based on the square-back Windsor body. However, road vehicles are designed to fulfill different needs. This means that the shapes of the main vehicle body can be varied greatly. To this end, additional measurements are carried out in this chapter based on the 20° fast-back Windsor body.

In the automotive community, it has long been noticed that different vehicles have different sensitivities to the modifications on wheels. Wittmeier *et al.* (2013) tested a group of tires on several road vehicles, including a sedan, an estate, and several square-backs. It was found that the ranking by the total drag of different tires depends on the vehicle geometry. In Hobeika *et al.* (2013), two different types of the Volvo S60 were tested, namely a sedan (similar to a fast-back) and a sport wagon (square-back). When adding geometric features on the slick tires, for example rain grooves and edge patterns, the aerodynamic drag of the vehicle shows different levels of changes for different types. Moreover, when the wheel state (rotating or stationary) is investigated on different vehicle shapes, different sensitivities are again noticed (Elofsson & Bannister, 2002; Heft *et al.*, 2012). In Elofsson & Bannister (2002), a sedan and a square-back were used. When the wheels state changes from stationary to rotating, the sedan presents a higher drag decrease of  $0.019\overline{C_D}$  compared to the square-back ( $0.008\overline{C_D}$ ). This observation is similar to Heft *et al.* (2012),

where a Fast-back and a Notch-back present higher drag decreases of up to  $0.015\overline{C_D}$  compared to a square-back ( $0.004\overline{C_D}$ ).

All these observations from previous studies suggest that differences in wheel-vehicle interactions exist between different vehicles. This suggestion is reasonable when considering that the flow features of different vehicle types are indeed very different. For academic models such as the Ahmed body (Ahmed *et al.*, 1984) or the Windsor body (Le Good & Garry, 2004; Howell & Le Good, 2005), the mean flow structures in the wake of a fast-back version are very different from that of a square-back version. The mean wake of the  $25^\circ$  fast-back Ahmed body is pictured in figure 7.1(a). Inside the wake, three main flow structures exist: a separation bubble over the slanted base, a pair of counter-rotating C-pillar vortices, and a recirculation region behind the vertical base. The drag is related to these structures and the interactions between them. This is well depicted when the angle of the rear window  $\alpha$  is varied as shown in figure 7.1(b). The pressure variations at the rear surfaces, namely the slanted base and the vertical base, are the main sources of the total drag changes. From  $\alpha = 0^\circ$  to  $30^\circ$ , the drag from the slanted base increases rapidly. This is due to the increases in the strength of the C-pillar vortices and the size of the separation bubble above the slanted base. On the other hand, the drag from the vertical base is gradually decreased with increasing  $\alpha$  from  $\alpha = 0^\circ$  to  $30^\circ$ . This is accompanied by a gradual reduction in the bluntness of the recirculation region behind the vertical base. The opposite trends at the slanted base and the vertical base lead to a slight decrease in the total drag from  $\alpha = 0^\circ$  to  $12.5^\circ$  and a rapid increase in drag from  $\alpha = 12.5^\circ$  to  $30^\circ$ . Beyond  $\alpha = 30^\circ$ , a fully separated flow is formed behind both base surfaces with a burst of the C-pillar vortices. This results in a sharp decrease in drag.

In the present work, our aim is to examine the dependency of the salient features of wheel-vehicle interactions on vehicle back shape. Our choice is the  $\alpha = 20^\circ$  fast-back by modifying the rear section of the square-back vehicle used before. The experimental apparatus used for this chapter is detailed in §7.2, followed by a description of the baseline flow without the wheels in 7.3. By placing a pair of D-shaped obstacles under the vehicle and varying the relative distance from the obstacles to the base, the same sensitivity study as in chapter 4 is conducted in §7.4. Then, in §7.5, the effects of wheels on the wake of the vehicle are investigated. A systematic variation of the front wheel shape is also applied in order to show if the findings in chapter 6 are still valid. Finally, in §7.6, concluding remarks are proposed.

## 7.2 Experimental setup

The  $\alpha = 20^\circ$  fast-back Windsor body having a length of  $L/H = 3.41$  shown in figure 7.2 is selected for the study in this chapter. Two test groups are considered. For the first group shown in figure 7.2(a), the wake of the model is perturbed by placing a pair of D-shaped obstacles under the model. This is the same as the sensitivity study in chapter 4. The two-dimensional (2-D) obstacles have a half-elliptic cross-section, whose length is 1.5 times the width  $d$ . The width of the obstacles is  $d/H = 0.19$  and the height is  $h/H = 0.17$ . Between each obstacle and the model, a gap of 1.5 mm exists and is carefully filled with high-density foam to reduce the complexity of the flow and to focus on the interactions between the obstacles and the model wake. The obstacle pair is always placed symmetrically to the symmetry plane of the model, with its rear surface parallel to the vertical base of the body and its left-hand/right-hand side tangents to the left-hand/right-hand side of the body. The degree of freedom of the pair in the streamwise direction is fixed by the obstacle-to-base distance  $l$ , which is defined as the streamwise distance from the base of the obstacles to the vertical base of the body. The parameter  $l$  ranges from  $0 d$  (flush-mounted to the base) to  $4 d$ .

On the other hand, the second test group considers the influence of the wheels. Four sharp-edged wheels with a width of  $w/H = 0.19$  are installed directly on the model (detailed in figure 2.4b of chapter 2) as shown in figure 7.2(b). The length of the model gives a distance from the vertical base to the rear wheels  $l/w = 0.65$ . For the square-back Windsor body, this small  $l/w$  distance provides strong near-wake interactions between the rear wheels and the wake. On top of this, the role of the front wheels as examined for the square-back model in chapter 6 is tested. With decreasing front bluntness, S, MR, VR, and N represents sharp-edged, medium-rounded,

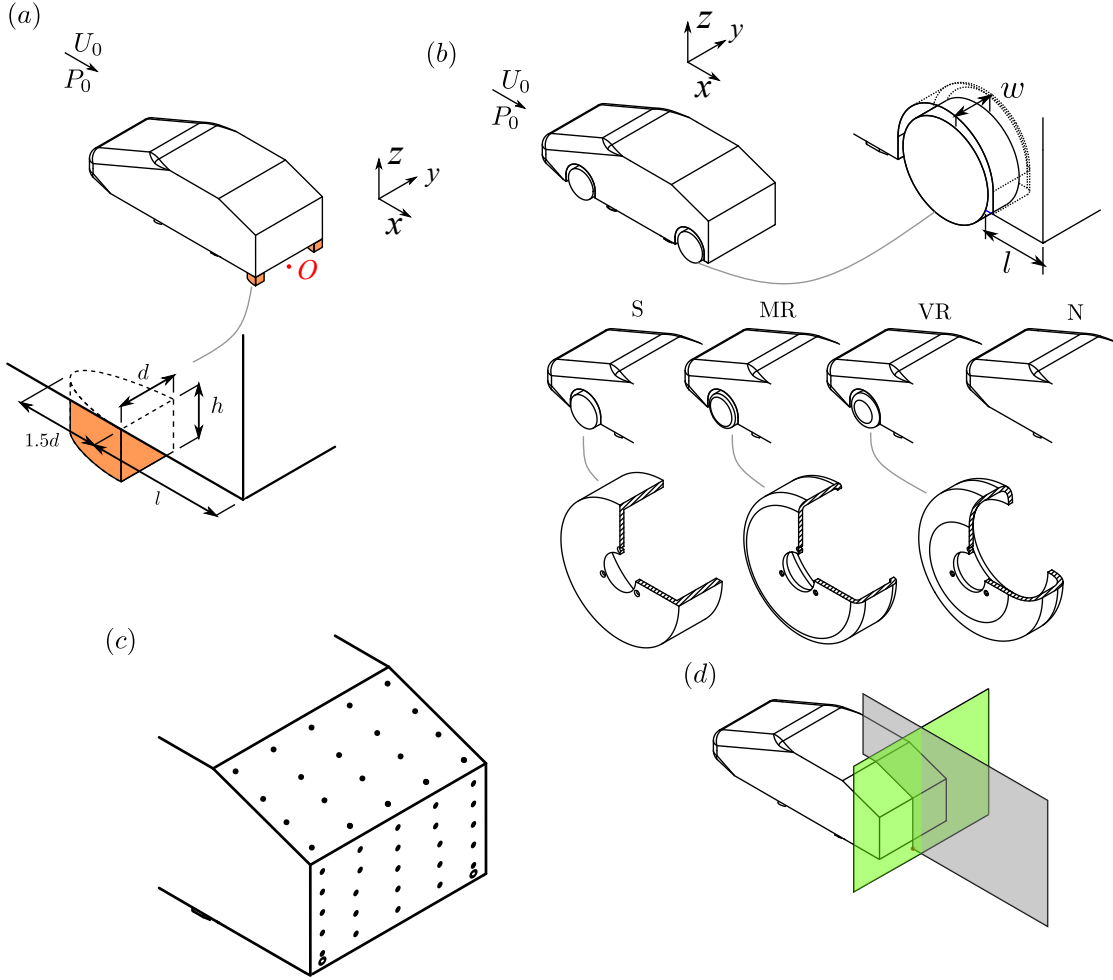


Figure 7.2: Experimental setup. (a) Arrangement of the model and the underflow perturbing obstacle pair. (b) Arrangement of the model equipped with wheels, different wheel types are considered at the front. (c) Locations of pressure taps on the base. Points indicate locations of mean pressure measurements and circles indicate locations of time-resolved pressure measurements. (d) Particle image velocimetry (PIV) fields of view (FOVs) in the symmetry plane ( $y/H = 0$ , colored in gray), and in the cross-flow plane ( $x/H = 0.03$ , colored in green).

very-rounded, and no front wheels. The radius of the rounding for the MR and VR profiles are respectively  $0.15w$  and  $0.3w$ .

Unless otherwise stated, all the results presented are collected under a free-stream velocity  $U_0 = 25 \text{ m s}^{-1}$ , corresponding to a height-based Reynolds number  $Re_H = U_0 H / \nu = 4.8 \times 10^5$ , where  $\nu$  is the kinematic viscosity of the air at operating temperature.

Two different pressure measurement systems are used to perform surface pressure measurements. The first one used for time-averaged and long-timescale measurements uses the pressure scanner. 20 taps on the slanted base and 25 taps on the vertical base (see figure 7.2c) are connected to the scanner with a range of  $\pm 1 \text{ kPa}$ . On the vertical base near the bottom trailing edge, two pressure taps are connected to the second system dedicated to time-resolved measurements using the differential pressure sensors.

The base pressure of the slanted base (BS) and the vertical base (BV) are calculated via:

$$C_{pbS} = \frac{\int_{BS} C_p ds}{\int_{BS} ds}, C_{pbV} = \frac{\int_{BV} C_p ds}{\int_{BV} ds}. \quad (7.1)$$

The pressure drag from the base is quantified by the base drag coefficient:

$$C_B = -\frac{\sin(20^\circ) \int_{BS} C_p ds + \int_{BV} C_p ds}{HW}. \quad (7.2)$$

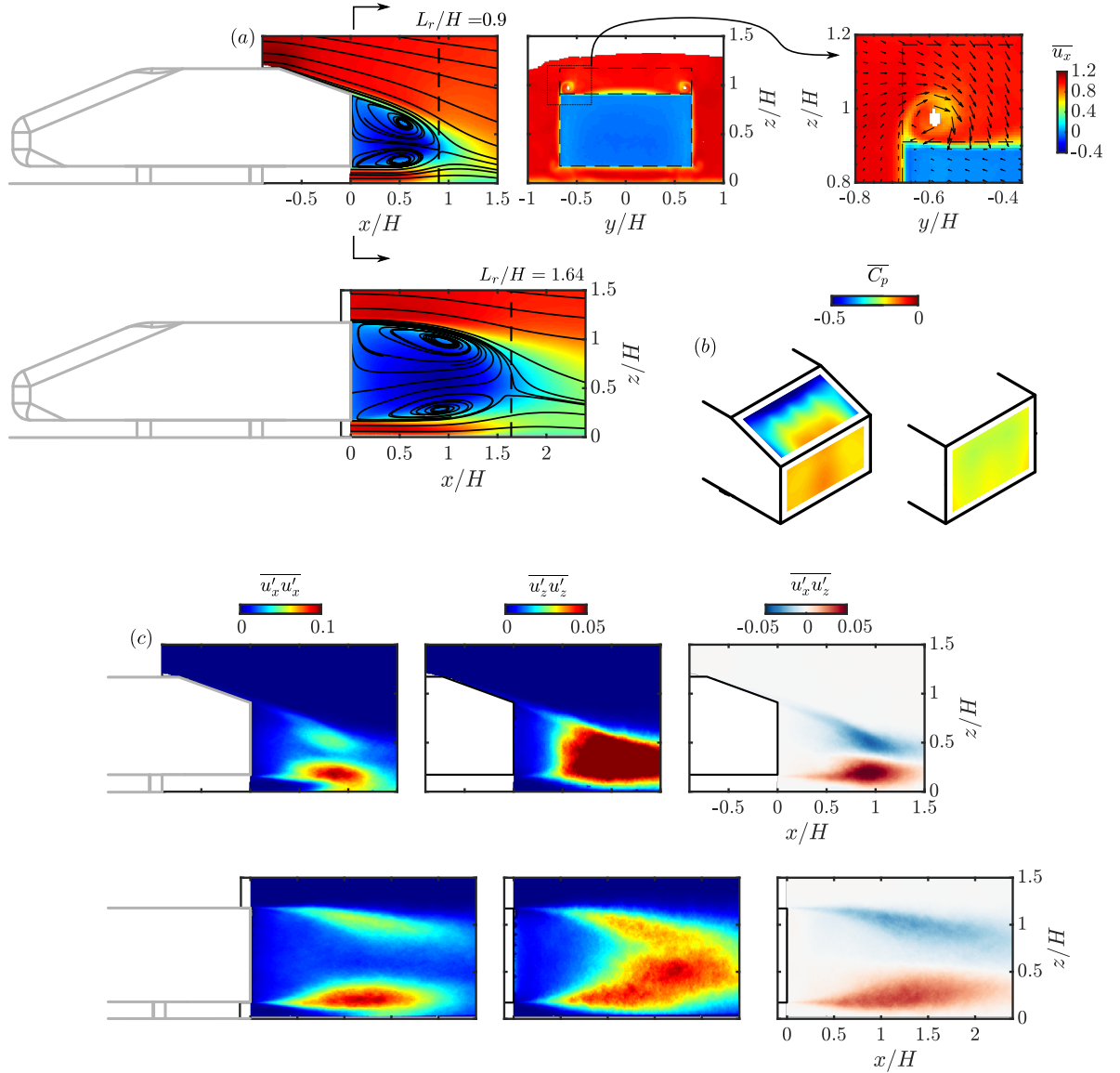


Figure 7.3: Baseline flow around the fast-back Windsor body with reference to the corresponding square-back having the same length. (a) Mean streamwise velocity  $\bar{u}_x$  distributions in the symmetry plane of the body ( $y/H = 0$ ) and in the cross-flow plane at  $x/H = 0.03$ . In the symmetry plane, the mean streamlines are superimposed. A zoom view is given for the cross-flow plane superimposed by in-plane mean velocity vectors. (b) Mean pressure distributions on the base surfaces of the model. (c) Reynolds stress distributions in the symmetry plane of the body ( $y/H = 0$ ).

The velocity fields in the near wake are measured by the particle image velocimetry (PIV) system. Two two-dimensional fields of view (FOVs) are considered as depicted in figure 7.2(d). The first one located in the symmetry plane of the body ( $y/H = 0$ ) is of 2-D two-component (2D2C) setup, obtaining the streamwise  $u_x$  and vertical  $u_z$  velocity components. Another FOV locates in a cross-flow plane in proximity to the base of the body ( $x/H = 0.03$ ). This FOV is of stereoscopic (2-D three-component (2D3C)) setup, capturing three velocity components.

### 7.3 Baseline flow

We first describe the baseline flow of the present chapter which is produced by the fast-back Windsor body without wheels. The corresponding square-back body having the same length from chapter 3 is compared. In figure 7.3(a) the mean streamwise velocity  $\bar{u}_x$  superimposed with mean streamlines in the symmetry plane  $y/H = 0$  is shown. From the top surface of the model, we notice a strong flow curvature near the leading edge of the slanted base. Then, the flow is fully

attached over the slanted base with no observable separation bubble<sup>1</sup>. At the trailing edge of the slanted base, the flow separates and forms a recirculation region extending towards  $x/H = 0.9$ . This recirculation length is reduced by  $\sim 45\%$  from the corresponding square-back. This means that the distance for the bottom shear layer from the flow separation to the proximity of the top shear layer is shorter for the fast-back than the square-back. If the separation condition at the bottom trailing edge is similar for both bodies, the vortices inside the bottom shear layer of the fast-back body may not have enough time to grow and to impact the mean topology of the wake. In [Lorite-Díez et al. \(2020b\)](#), steady blowing parallel to the streamwise direction was applied along the bottom trailing edge of a square-back Ahmed body. It was shown that even at very small blowing flow rate  $C_q = U_b S_b / (U_0 H W) < 0.02$  ( $U_b$  and  $S_b$  represents, respectively, blowing velocity and surface size), the development of the bottom shear layer is fundamentally changed which impacts the mean vertical balance of the wake and the base pressure. On the other hand, similar steady blowing parallel to the streamwise direction was applied along the bottom trailing edge of a fast-back Ahmed body ([Zhang et al., 2018](#)). Although the flow rate  $C_q$  is two order of magnitude higher than in [Lorite-Díez et al. \(2020b\)](#), the drag is only varied maximally by  $\sim 2\%$ . Therefore, when the underflow of the fast-back body is perturbed later by either the obstacles or the wheels, we expect a weaker influence on the development of the bottom shear layer and the global wake topology compared to the square-back body.

The pressure distributions on the slanted and vertical base surfaces are shown in figure 7.3(b). The flow curvature at the leading edge of the slanted surface induces a local decrease in pressure. Then, the progressive reduction of the body cross-section results in a pressure recovery before the flow separation and a higher base pressure of  $\overline{C_{pbV}} = -0.150$  on the vertical surface compared to  $\overline{C_{pb}} = -0.202$  for the corresponding square-back. The wake in the cross-flow plane at  $x/H = 0.03$  is shown in figure 7.3(a). Apart from the recirculation region behind the vertical base, the C-pillar vortex pair developed from the two side edges of the slanted base is observed (see also the zoom in figure 7.3a). It is formed from the separation of the side boundary layers at the two side edges of the slanted base, as indicated by the trace of low-momentum flow inside the streamwise vortex. These structures are responsible for the low-pressure regions measured in figure 7.3(b) near the two side edges of the slanted base.

The velocity fluctuations in the wake are pictured by the distributions of the Reynolds stresses as shown in figure 7.3(c). No unsteady dynamics are observed above the slanted base, confirming that the flow is fully attached. Behind the vertical base, a qualitative similarity compared with the square-back is found. However, the normal stress  $\overline{u'_z u'_z}$  and the shear stress  $\overline{u'_x u'_z}$  overall present higher values compared to the square-back, probably due to the closer distance between the top and bottom shear layers.

The aerodynamic coefficients for this baseline case are summarized in table 7.1. The base drag  $\overline{C_{B0}}$  has a slightly smaller value than the corresponding square-back having the same length. The total drag is also marginally smaller than the square-back case. This is in accordance with the measurement by [Howell \(2013\)](#). The lift coefficient  $\overline{C_{z0}}$  presents a positive value for the present case mainly due to the negative pressure on the slanted surface.

	$U_0$ [m s <sup>-1</sup> ]	$\overline{C_{B0}}$	$\overline{C_{pbS0}}$	$\overline{C_{pbV0}}$	$\overline{C_{x0}}$	$\overline{C_{z0}}$
Fast-back	25	0.197	-0.331	-0.150	0.219	0.258
Square-back	25	0.202	-	-	0.225	-0.123

Table 7.1: Mean aerodynamic coefficients of the fast-back and the corresponding square-back Windsor body having the same length at  $U_0 = 25$  m s<sup>-1</sup>.

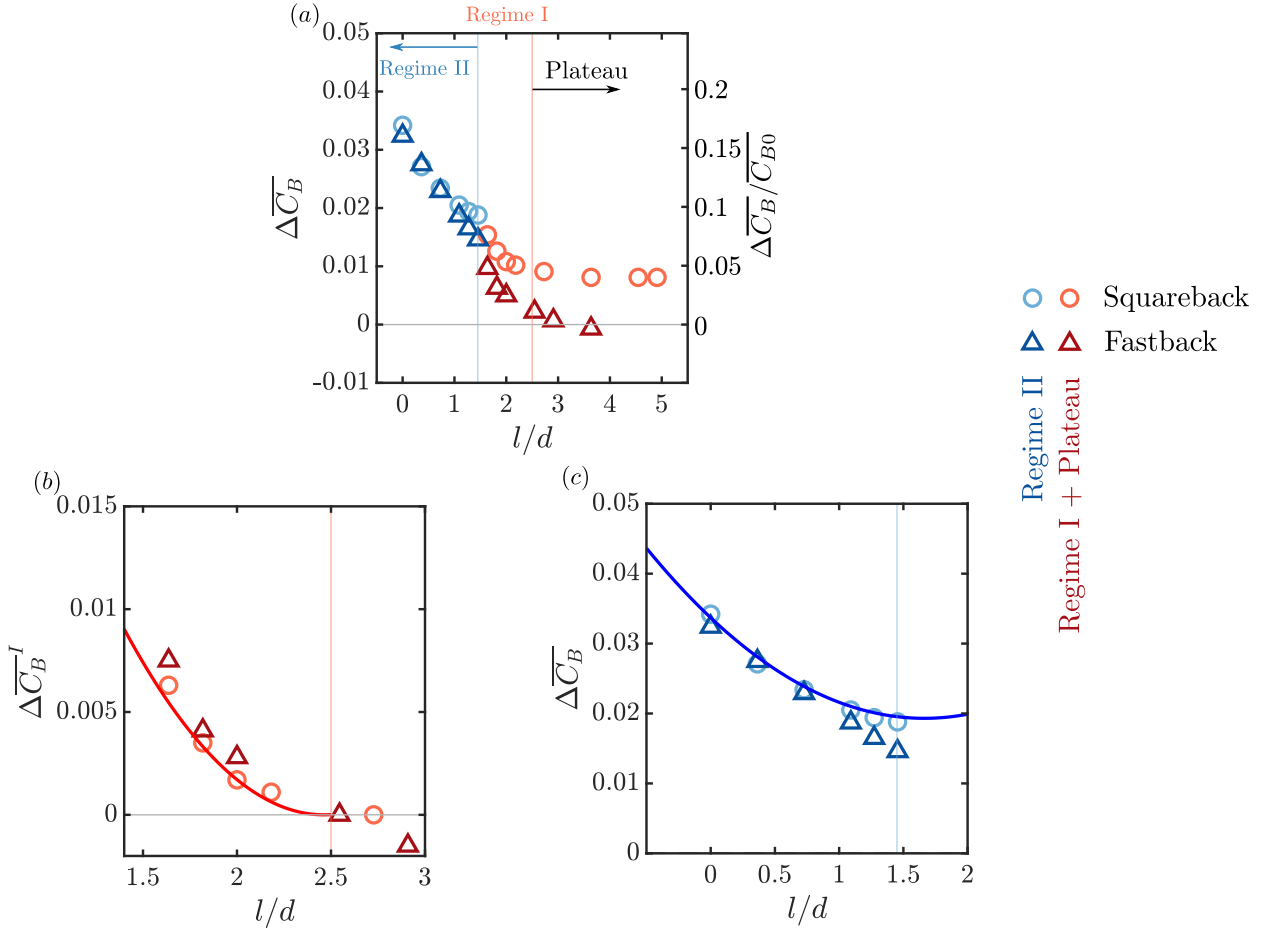


Figure 7.4: (a) Base drag of the body  $\Delta\overline{C}_B = \overline{C}_B - \overline{C}_{B0}$  as a function of the obstacle-to-base distance  $l/d$ , the corresponding square-back configuration from chapter 4 is shown for comparison (the percentage of increase  $\Delta\overline{C}_B/\overline{C}_B$  does not apply for the square-back). (b – c) Comparison with the scaling laws in regime I (b) and regime II (c) from chapter 4.

## 7.4 Effects of underflow perturbations

In this section, we focus on the first test group where the wake of the fast-back Windsor body is perturbed by a pair of 2-D D-shaped obstacles. The aim is to show if the near-wake interactions and drag-increase regimes observed in chapter 4 for a square-back Windsor body are general features for different ground vehicles having different back shapes. Hereafter we abbreviate the configuration in chapter 4 using the same obstacles as the square-back configuration.

First of all, the base drag variation  $\Delta\overline{C}_B = \overline{C}_B - \overline{C}_{B0}$  with the relative obstacle-to-base distance  $l/d$  is shown in figure 7.4(a). A major difference between the fast-back and the square-back configurations is noticed. When the obstacles are placed the most upstream of the base at the maximum  $l/d$ , no obvious change in the base drag is measured. Nevertheless, the trends of these two configurations are very similar. Moving the obstacles from the most upstream position (maximum  $l/d$ ) towards the base with decreasing  $l/d$ , a slight increase in base drag is noticed before  $l/d = 2.5$ . From  $l/d = 2.5$  to 0 with reducing obstacle-to-base distance, a rapid increase in base drag is noticed. Maximally, we measure a base drag increase of  $\Delta\overline{C}_B/\overline{C}_{B0} \approx 16\%$ .

Promoted by the overall consistency of the present study with the square-back configuration as will be shown later using detailed measurements, the range  $l/d > 2.5$  is named the plateau following the nomenclature used in chapter 4. Moreover, by looking at the pressure fluctuations in the wake of the obstacles, two drag-sensitive regimes, regime I and II, are defined for the range  $l/d < 2.5$ . The fluctuating pressure measurements will be detailed later in figure 7.5(e). The  $l/d$

<sup>1</sup>The fast-back part of the vehicle model is manufactured using composite material. Therefore the surface curvature at the top leading edge of the slanted base is reduced (with a radius of  $\sim 0.5$  mm). This curvature, according to [Rossitto et al. \(2016\)](#), has a fundamental influence on the flow separation over the slanted base.

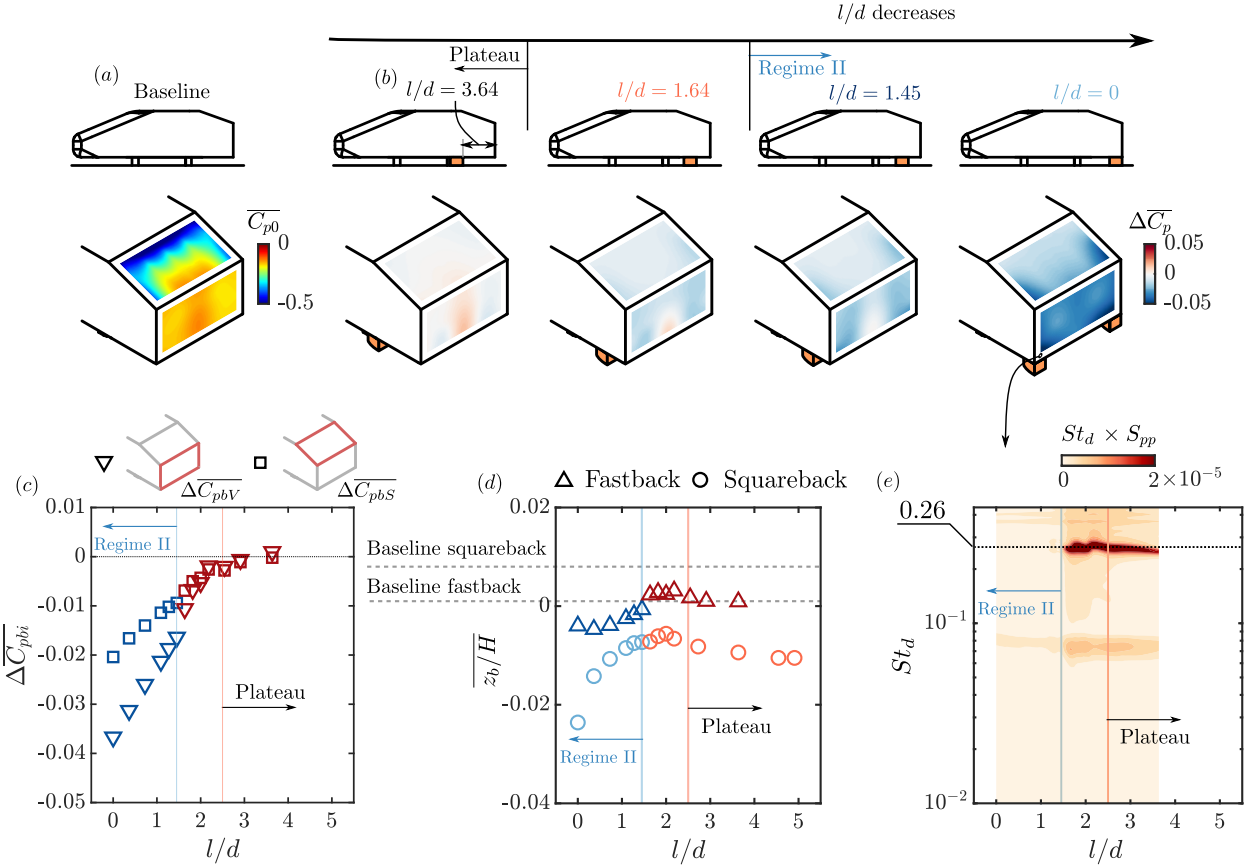


Figure 7.5: (a) Mean base pressure distribution for the baseline body. (b) Distributions of base pressure differences for different  $l/d$  cases. (c) Base pressure variations of the slanted surface and the vertical surface with  $l/d$ . (d) Evolution of the mean vertical position of the base center-of-pressure (CoP)  $z_b/H$  with  $l/d$  for the two configurations.  $z_b/H$  is calculated using the vertical base for the fast-back. (e) Evolution of the premultiplied spectrum from the pressure sensor with  $l/d$ .

ranges for these two regimes are  $1.5 < l/d < 2.5$  and  $l/d < 1.5$ , respectively.

We further compare the variations of the base drag in regime I and II with the square-back configuration respectively in figure 7.4(b) and (c). The level of base drag increase in regime I from the plateau  $\Delta \overline{C_B}^I = \overline{C_B} - \overline{C_B}(l/d = 2.5)$  is not varied by the shape of the body. In regime II, the base drag increase  $\Delta \overline{C_B}$  is measured to be only slightly modified. In chapter 4,  $\Delta \overline{C_B}^I$  was found to scale quadratically with the square of the width of the obstacles  $d^2$ . On the other hand,  $\Delta \overline{C_B}$  was measured to scale linearly with the width of the obstacles  $d$ . These observations mean that the base drag changes for the fast-back model are still governed by the scaling properties found for the square-back model.

The mean pressure distributions on the base are analyzed in figure 7.5 to better understand how the base pressure is modified by the obstacles. In figure 7.5(a) the pressure distribution on the base of the baseline case is shown. With respect to this case, the distributions of pressure difference for different  $l/d$  cases are presented in figure 7.5(b). When the obstacle pair is placed the most upstream of the base, a slight decrease of pressure at the left- and right-hand sides of the vertical base is compensated by a pressure recovery near the centerline of the vertical base. On the slanted base, the pressure is not measured to be varied. All these features give the observation in figure 7.4(a) with no observable base drag change. With decreasing  $l/d$  from the plateau to regime I, a quite homogeneous decrease of pressure is measured both on the vertical base and the slanted base. In regime II with decreasing  $l/d$ , a further decrease of base pressure is noticed. On the slanted base, the pressure decrease is primarily located near the bottom trailing edge at the left- and right-hand sides. On the vertical base, an important drop is noticed near the obstacles. The pressure evolution on the base surfaces with  $l/d$  is further shown in figure 7.5(c) by the evolution of  $\Delta \overline{C_{pbV}} = \overline{C_{pbV}} - \overline{C_{pbV0}}$  (mean pressure change on the vertical base) and  $\Delta \overline{C_{pbS}} = \overline{C_{pbS}} - \overline{C_{pbS0}}$

(mean pressure change on the slanted base). On both base surfaces, a decrease in pressure is measured in the drag-sensitive regimes with reducing  $l/d$ .

In figure 7.5(d), the vertical asymmetry of the recirculation region is quantified by the vertical position of the base center-of-pressure (CoP):

$$z_b = \frac{\int_{base} (z - z_c) C_p ds}{\int_{base} C_p ds}. \quad (7.3)$$

where  $z_c$  is the vertical coordinate of the center of the base. For the square-back configuration, a large decrease in the mean vertical position of the base CoP  $\overline{z_b/H}$  is measured from the baseline to the cases in the plateau. With decreasing  $l/d$ , it varies slightly in regime I and decreases tremendously in regime II. On the other hand for the fast-back configuration, the main recirculation region is located downstream of the vertical base. Therefore,  $\overline{z_b/H}$  is calculated for the vertical base. From the corresponding baseline, there is no variation in  $\overline{z_b/H}$  when the obstacles are located the most upstream of the base. With decreasing  $l/d$ , a weaker but similar variation in  $\overline{z_b/H}$  as the square-back configuration in both regimes is measured. Overall, the vertical wake balance of the fast-back body is less sensitive to the presence of the obstacles in the underflow, especially when they are located relatively far from the base. This is probably the reason for the different  $\Delta \overline{C_B}$  values measured in the plateau.

The pressure measurements for the square-back configuration in chapter 4 showed that the pressure decrease on the base with decreasing  $l/d$  is driven by the approaching of the near-wake regions of the obstacles. In particular, in regime I, the wake of the main body experiences a growing perturbation from the Kármán vortex shedding in the obstacle wakes. On the other hand in regime II, the wake of the main body merges with the wakes of the obstacles. The mean wake merging and the accompanying near-wake interactions alter the wake of the obstacles resulting in a suppression of the vortex shedding. In different regimes, the different flow dynamics downstream of the obstacles are also measured in the present chapter. This is shown in figure 7.4(e) by the evolution of the premultiplied spectrum from the pressure sensor. In the plateau and regime I, a peak at  $St_d = fd/U_0 = 0.26$  ( $d$  is the width of the obstacles) is measured. With decreasing  $l/d$  from regime I to II, the peak suddenly disappears at  $l/d = 1.5$ . This is used as the criterion to separate the regimes. These measurements near the obstacles are very similar to the measurements in chapter 4, suggesting that the obstacle wake dynamics are insensitive to the variation in the body shape.

Velocity measurements in the near wake of the main body are presented in figure 7.6 to show how the wake of the body is globally modified by the obstacles. The distributions of the mean streamwise velocity  $\overline{u_x}$  in the symmetry plane of the body ( $y/H = 0$ ) and in the cross-flow plane at  $x/H = 0.03$  are shown respectively in figure 7.6(a) and (b). When the obstacle pair is situated in the underflow, it is found that the wake of the body in the symmetry plane is not subjected to any noteworthy changes no matter the value of  $l/d$ . This is quite surprising especially when considering the large pressure variation on the vertical base. However, we should always keep in mind that the wakes of the fast-back bluff bodies are of higher complexity than the square-back ones (Zhang *et al.*, 2015; Liu *et al.*, 2021). Specifically, the complex interactions between the C-pillar vortices and the recirculation region (Venning *et al.*, 2015), which probably include mass and momentum exchanges, cannot be precisely quantified using the present setup. These interactions, to the understanding of the authors, may play an important role in the local mean mass transfer (will be evidenced later) from the vehicle wake to the obstacle wakes.

Moreover, in the cross-flow plane at  $x/H = 0.03$  as shown in figure 7.6(b), more obvious changes due to the presence of the obstacles are found locally under the recirculating bubble of the main body. From the baseline case with a quite homogeneous  $\overline{u_x}$  distribution in the underflow, a decrease in flow momentum downstream of the obstacles is already noticed when the obstacles are placed at the most upstream of the base. From the plateau with decreasing  $l/d$ , the momentum deficit becomes obvious in regime I. When  $l/d$  is further decreased, we notice that the wakes of the obstacles and the wake of the main body are merged in regime II as depicted by the same blue color downstream of the obstacles and of the body.

An examination of the velocity fluctuations in the wake is presented in figure 7.7. The distributions of turbulent kinetic energy  $k$  in the symmetry plane ( $y/H = 0$ ) and in the cross-flow plane

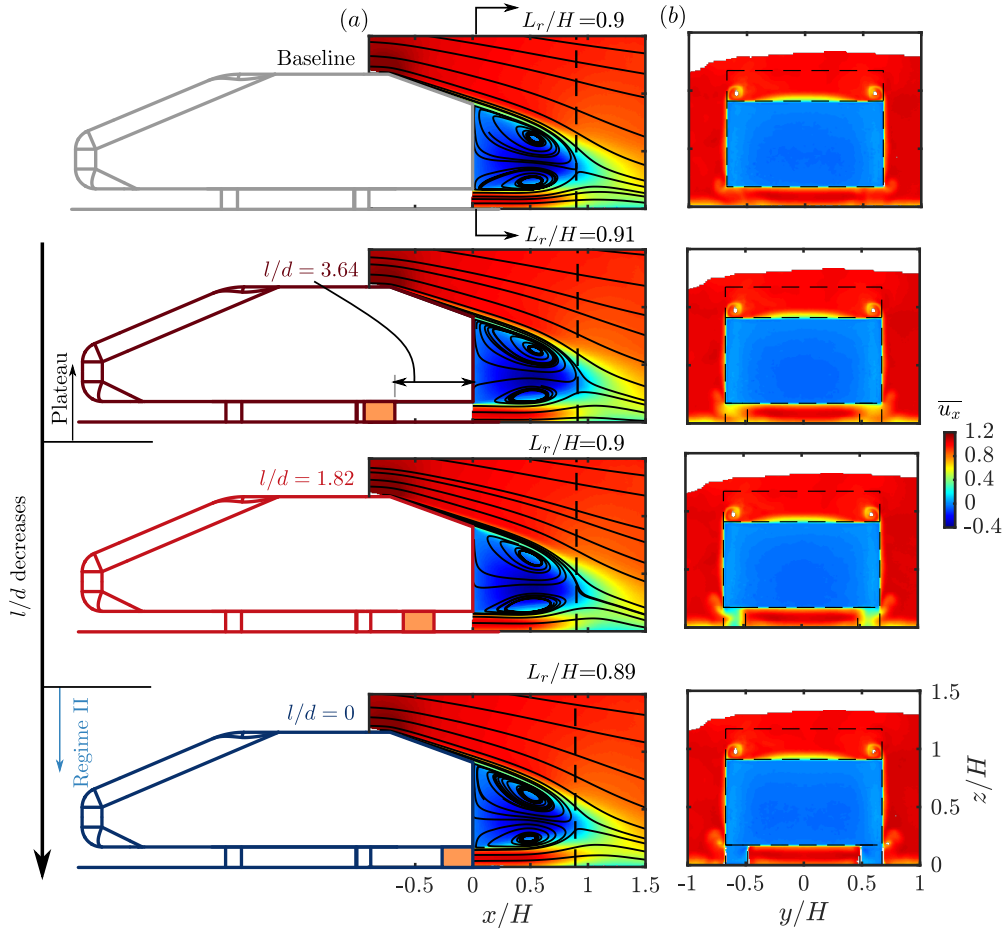


Figure 7.6: Distributions of mean streamwise velocity  $\bar{u}_x$  in the symmetry plane of the body at  $y/H = 0$  (a) and in the cross-flow plane at  $x/H = 0.03$  (b) for the baseline case and several cases with the obstacle pair in the underflow. In the symmetry plane, the mean streamlines are superimposed.

at  $x/H = 0.03$  are shown, respectively, in figure 7.7(a) and (b). In the symmetry plane, when the obstacles are placed at the maximum  $l/w$  location, the velocity fluctuations in the bottom shear layer near the wake closure ( $x/H \approx 0.9$ ) are enhanced. This enhancement is strengthened when  $l/d$  is reduced from the plateau to regime I. However, from regime I to regime II, there is a suppression of flow fluctuations in the bottom shear layer. The whole variation is better pictured in figure 7.7(c) by the streamwise evolution of the maximum of  $k$ . It is noted that from the baseline case to  $l/d = 0$  case, the maximum of  $k$  is almost not varied. These features in the symmetry plane are different from the observations for the square-back, where the flow fluctuations in the symmetry plane increase monotonously with reducing  $l/d$  (see figure 4.12).

In the cross-flow plane, the distributions of turbulent kinetic energy  $k$  (see figure 7.7b) are similar to the square-back configurations. In the plateau and regime I, the strong unsteady dynamics behind the obstacles observed by unsteady pressure measurements are again noticed. On the other hand in regime II, the flow fluctuations are suppressed<sup>2</sup>.

We focus in figure 7.8 on the local flow fields near the obstacles. The distributions of mean streamwise velocity  $\bar{u}_x$  in the cross-flow plane are superimposed by in-plane velocity vectors in figure 7.8(a). First of all, the gradual reduction of flow momentum in the underflow downstream of the obstacles is shown by plotting  $\bar{u}_x$  along the centerline of the obstacle in figure 7.8(b). With reducing  $l/d$  from the plateau to regime I, the reduction of flow momentum in the underflow also reduces the mean shear between the main body wake and the wake of the obstacles. In regime II, the merging of the wakes gives no mean shear between the wakes.

<sup>2</sup>May be due to the small distance between the PIV plane and the obstacle base but it is noted that the unsteady dynamics of the obstacle wake are suppressed by the mean wake merging as already shown by the unsteady pressure measurements in figure 7.5(e).

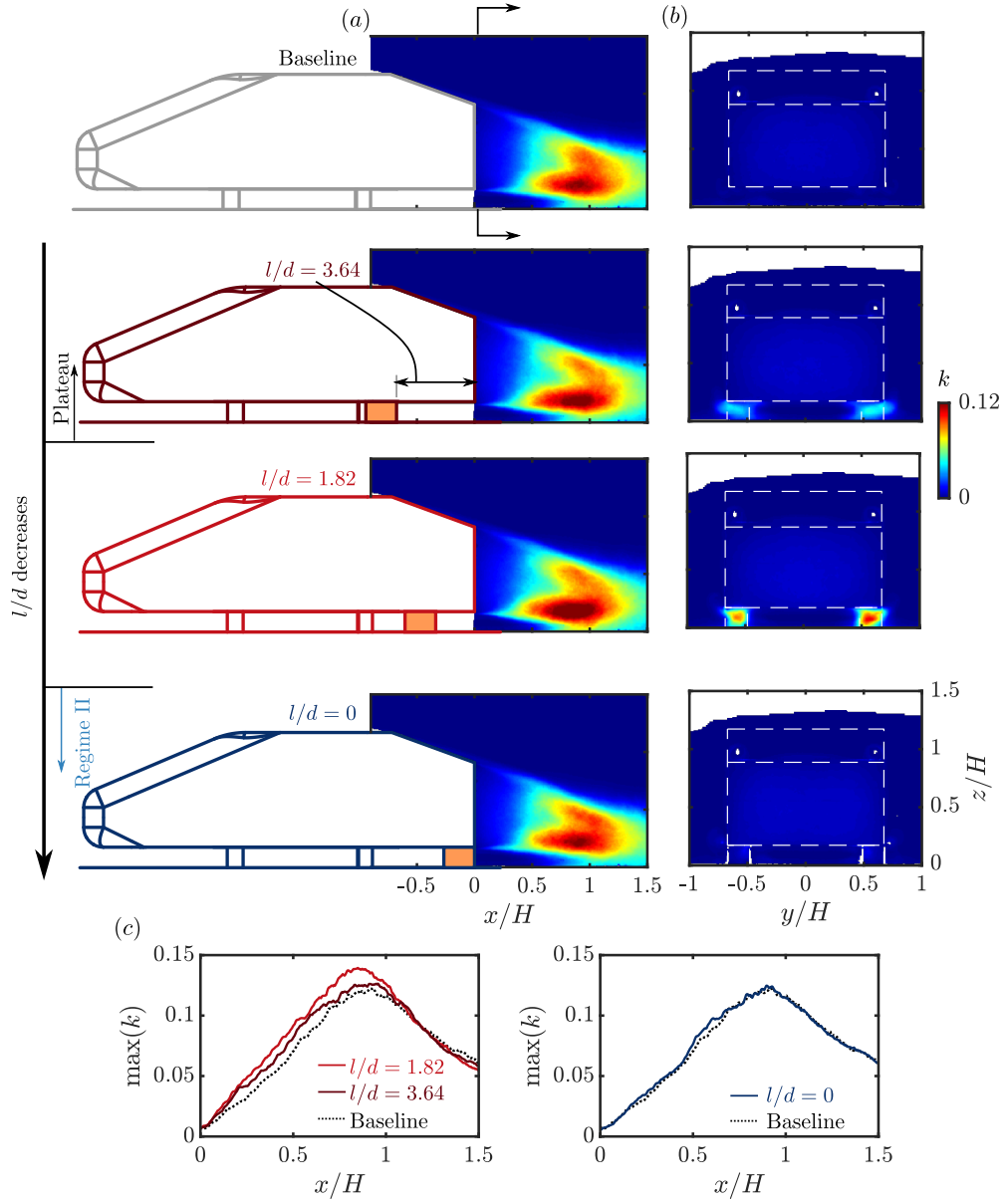


Figure 7.7: Distributions of turbulent kinetic energy  $k$  in the symmetry plane of the body at  $y/H = 0$  (a) and in the cross-flow plane at  $x/H = 0$  (b) for the baseline case and several cases with the obstacle pair in the underflow. The streamwise evolution of the maximum  $k$  is shown in (c).

When focusing on the in-plane velocity vectors, a mean mass transfer from the main body wake to the wakes of the obstacles is observed in regime II. By space-averaging the mean vertical velocity  $\overline{u_z}$  across the surface of mass exchange having the same width as the obstacles, it is shown in figure 7.8(c) that the mean mass transfer is of quite strong strength in regime II having a velocity of  $\sim 20\%$  of the free-stream velocity. On the other hand in regime I, the mass transfer also exists but is of a smaller strength. These local velocity distributions are very similar to the square-back configuration measured in chapter 4 (see figure 4.14), meaning that the obstacles have strong authority over the flow near them.

We recall here the physical model developed in chapter 6. It suggests that the mean mass transfer is driven by the pressure difference between the regions above and below the interaction interface. By considering a relationship between local and global pressure levels, the model proposes that this pressure difference is related to the upstream flow condition and local wake development of the obstacles. Therefore, in the present situation where the back shape of the body is modified, the pressure difference and consequently the mean mass transfer are not expected to be varied. This is indeed measured in figure 7.8(c) by comparing the  $\langle \overline{u_z} \rangle$  evolution of different configurations.

To balance the mass flux exiting the recirculation region via the mean mass transfer, the

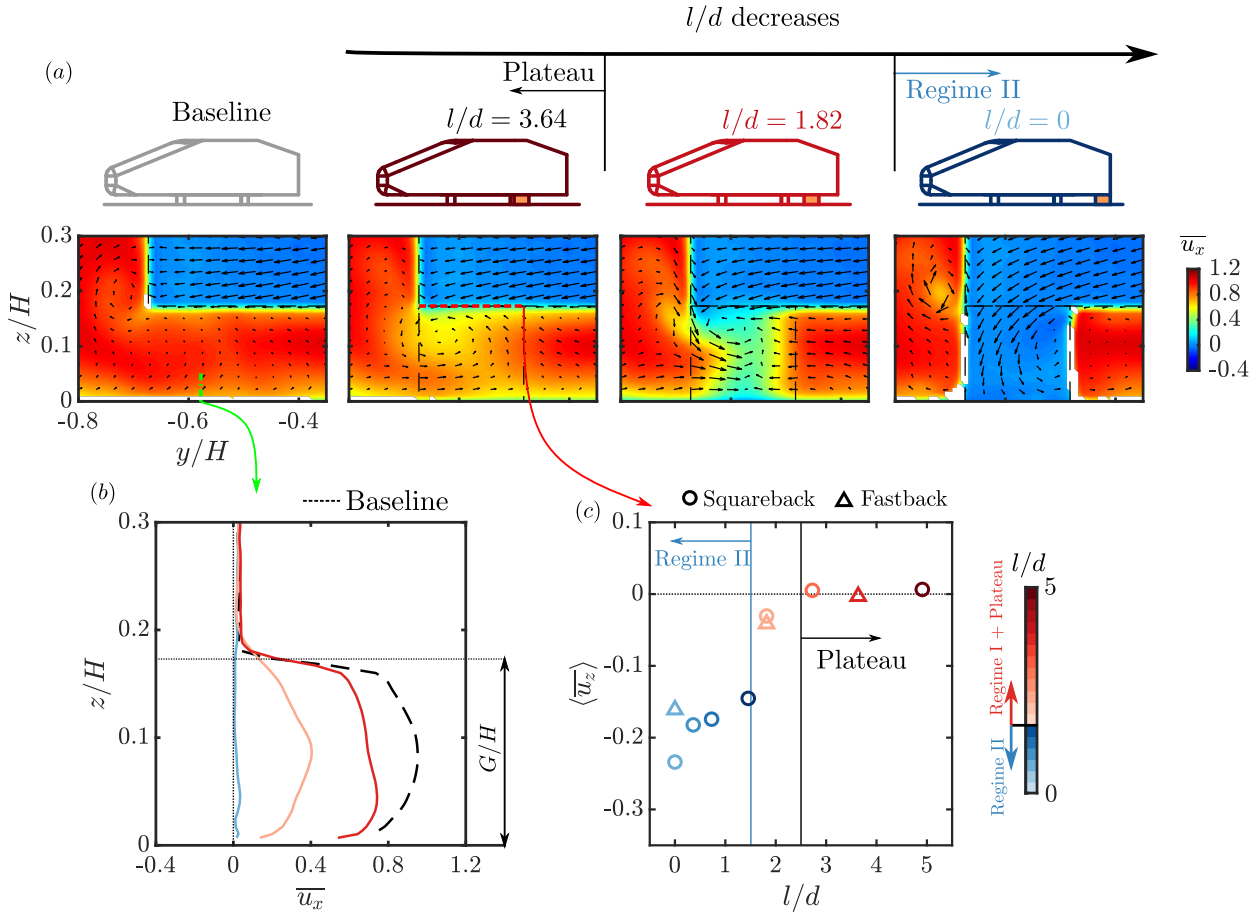


Figure 7.8: (a) Local distributions of the mean streamwise velocity  $\bar{u}_x$  in the cross-flow plane at  $x/H = 0.03$  for the same cases in figure 7.6(b), the  $\bar{u}_x$  profiles along the centerline of the obstacles are plotted in (b). (c) Space-averaged mean vertical velocity  $\langle \bar{u}_z \rangle$  across the width of the left obstacle at the height of the ground clearance.

wake has to obtain the flux bearing high streamwise momentum from the surrounding flow. The corresponding fluid particles lose their initial streamwise momentum  $\rho U_0$  in this process. According to the model proposed in chapter 4, the momentum loss has to be balanced by a pressure decrease on the base. Therefore, the same level of mean mass transfer corresponds to the same level of base pressure changes.

In chapter 4, two different base drag parameters were defined in the same fashion as in figure 7.4. These two parameters, namely  $\Delta \overline{C_B^I}$  for regime I and  $\Delta \overline{C_B}$  for regime II, were found to be dictated by the mean mass transfer through the two scaling properties. Therefore, the insensitivity of these two parameters in the two regimes is related to the insensitivity of mean mass transfer to model shape.

## 7.5 Effects of wheels

In this section, the results from the second test group are analyzed where the wake of the fast-back Windsor body is perturbed by the wheels. The corresponding square-back configuration having the same distance between the rear wheels and the base is shown for comparison. The aim of this section is first to show if the salient features of wheel-vehicle interactions observed in chapter 5 for a square-back Windsor body are valid also for the fast-back body. In particular, the two main features, namely the modification in the mean vertical equilibrium of the main body wake and the mean mass transfer from the main body wake to the wakes of the rear wheels, were found to have strong impacts on the pressure drag of the main body and therefore are focused on. In addition, the second aim is to show if the front wheels also play the same role as in chapter 6.

In figure 7.9(a), the base drag variation  $\Delta \overline{C_B} = \overline{C_B} - \overline{C_{B0}}$  relative to the baseline case is shown.

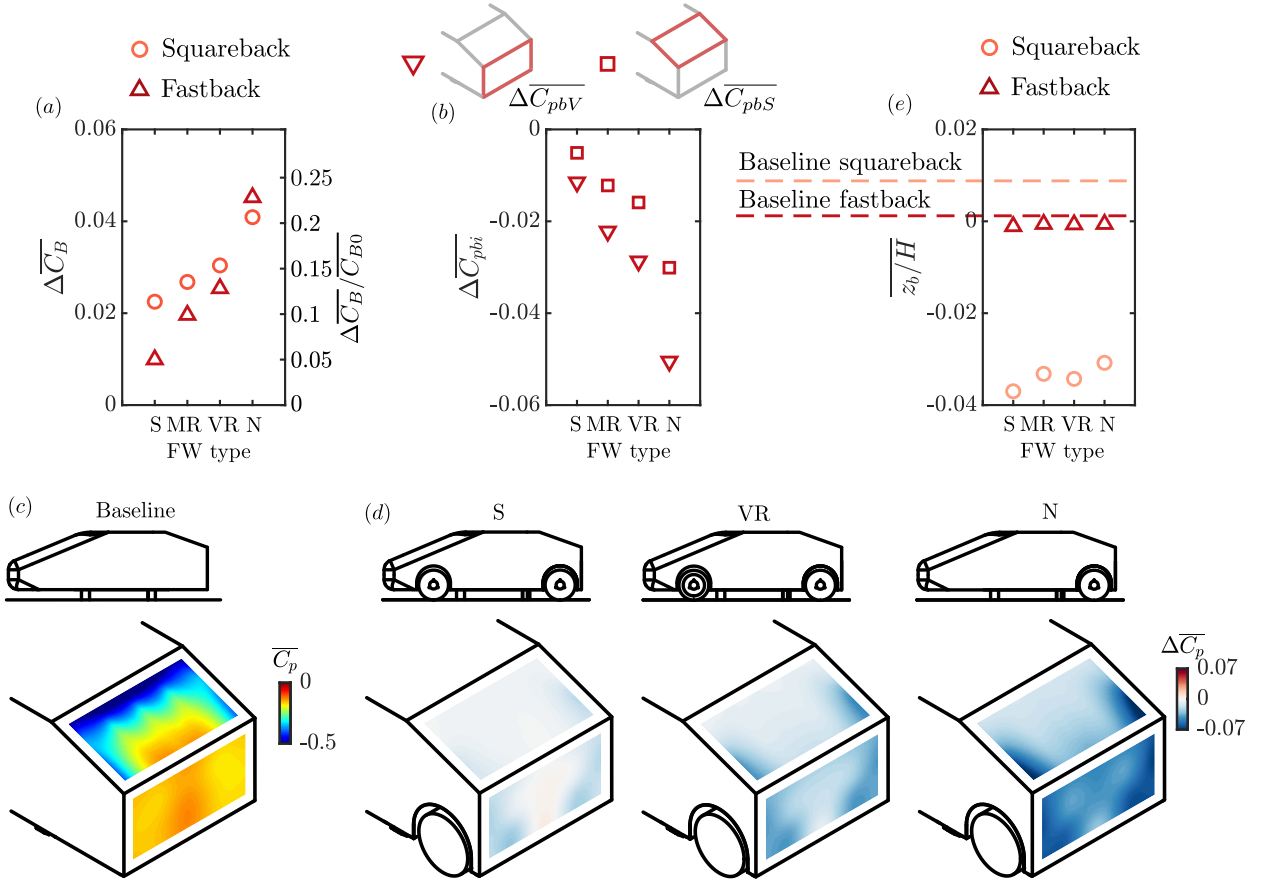


Figure 7.9: (a) Base drag of the body  $\Delta \overline{C_B} = \overline{C_B} - \overline{C_{B0}}$  as a function of the front wheel (FW) type, the corresponding square-back configuration from chapter 6 is shown for comparison (the percentage of increase  $\Delta \overline{C_B} / \overline{C_{B0}}$  does not apply for this configuration). (b) Base pressure variations of the slanted surface and the vertical surface with the FW type. (c) Mean base pressure distribution for the baseline case. (d) Distributions of base pressure difference with respect to the baseline case for three cases with different FW types. (e) Mean vertical position of the base CoP  $z_b/H$  versus  $l/d$  for the two configurations.  $z_b/H$  is calculated using the vertical base for the fast-back.

The installation of the four shape-edged wheels (case S) increases the base drag by  $\sim 5\%$ . A higher base drag increase of  $\sim 10\%$  was measured for the square-back configuration. With decreasing front-wheel bluntness, there is a gradual increase in base drag till no wheels are presented at the front axle (case N). The slope of this base drag increase is steeper than that of the square-back configuration leading to a substantial base drag increase of  $\sim 23\%$  for case N. The mean pressure on the slanted base  $\Delta \overline{C_{pbS}}$  and on the vertical base  $\Delta \overline{C_{pbV}}$  are shown in figure 7.9(b). It is shown that the base drag increase with reducing front-wheel bluntness is caused by the pressure decrease on both base surfaces.

The distributions of the base pressure are provided in figure 7.9(c) and (d) to better understand how the presence of wheels modifies the base pressure. In figure 7.9(c) the mean base pressure distribution is shown for the baseline case while in figure 7.9(d) the distribution of pressure difference with respect to the baseline case is shown for the wheel cases. It is shown that when the four sharp-edged wheels are installed, a slight decrease in pressure is located at the left- and right-hand sides of the two base surfaces. Specifically, the pressure decrease is primarily located on the vertical base near the rear wheels. With reducing front wheel bluntness from case S to N, the level of pressure decrease is gradually enhanced.

Similar to the test group using obstacles, the mean equilibrium of the recirculating flow behind the vertical base is not sensitive to the presence of different sets of wheels. This is better depicted in figure 7.9(e) by the mean vertical position of the base CoP  $z_b/H$ . For the square-back configuration, the presence of four sharp-edged-shoulder wheels (case S) greatly decreases  $z_b/H$  from the baseline case. With reducing front-wheel bluntness, the vertical asymmetry of the mean body wake is

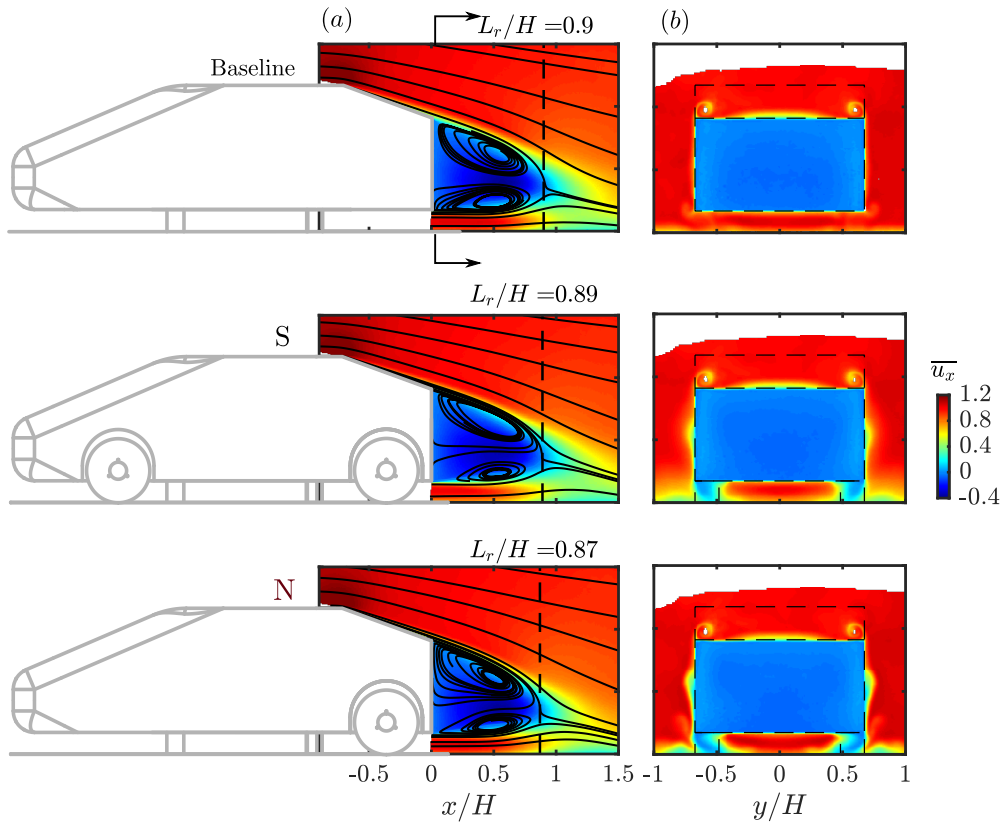


Figure 7.10: Distributions of mean streamwise velocity  $\overline{u_x}$  in the symmetry plane of the body at  $y/H = 0$  (a) and in the cross-flow plane at  $x/H = 0.03$  (b) for the baseline case and several cases with different front wheel types. In the symmetry plane, the mean streamlines are superimposed.

slightly varied. On the other hand for the fast-back configuration, different sets of wheels have no obvious influence on the initial wake asymmetry of the baseline case.

The wake flow is examined in figure 7.10 to show how the wake is modified by the presence of wheels. The mean streamwise velocity  $\overline{u_x}$  in the symmetry plane of the main body at  $y/H = 0$  and in the cross-flow plane at  $x/H = 0.03$  is shown. Similar to the test group using obstacles, the mean wake topology depicted by the mean streamlines in the symmetry plane is almost not changed by the presence of different sets of wheels. On the other hand in the cross-flow plane, the four sharp-edged wheels (case S) modify the baseline flow in two aspects. The first one is the momentum deficit behind the rear wheels in the underflow and the second aspect is the thickening of the side shear layers downstream of the rear wheelhouses. When the front wheel bluntness is reduced from case S to N, the  $\overline{u_x}$  level around the rear wheel wakes is increased as marked by the darker red color. This indicates a stronger facing velocity for the rear wheels. These features measured in the cross-flow plane are qualitatively the same as the square-back configuration shown in chapter 6.

The flow fluctuations are examined in figure 7.11(a) by showing the distributions of turbulent kinetic energy  $k$  in the symmetry plane ( $y/H = 0$ ). When the four sharp-edged wheels are installed, the turbulent kinetic energy  $k$  in the wake is slightly reduced. From this case S with reducing front wheel bluntness, we notice that the flow fluctuations in the bottom shear layer near wake closure ( $x/H \approx 0.9$ ) are greatly enhanced. In figure 6.10 of chapter 6, very similar observations were found for the square-back configuration. We further plot the streamwise evolution of the maximum of  $k$  in figure 7.11(b). The gradual enhancement of flow unsteadiness in the bottom shear layer is pictured. Indeed, the maximum  $k$  in the wake is significantly increased by  $\sim 50\%$  from case S to N.

The flow near the rear wheels is investigated in detail in figure 7.12(a). The mean streamwise velocity  $\overline{u_x}$  in the cross-flow plane is shown in figure 7.12(a) for the cases displayed in figure 7.10. These local flow fields are very similar to the measurements in chapter 6 (see figure 6.14). When the four sharp-edged wheels are installed, a significant reduction of mean shear between the wake

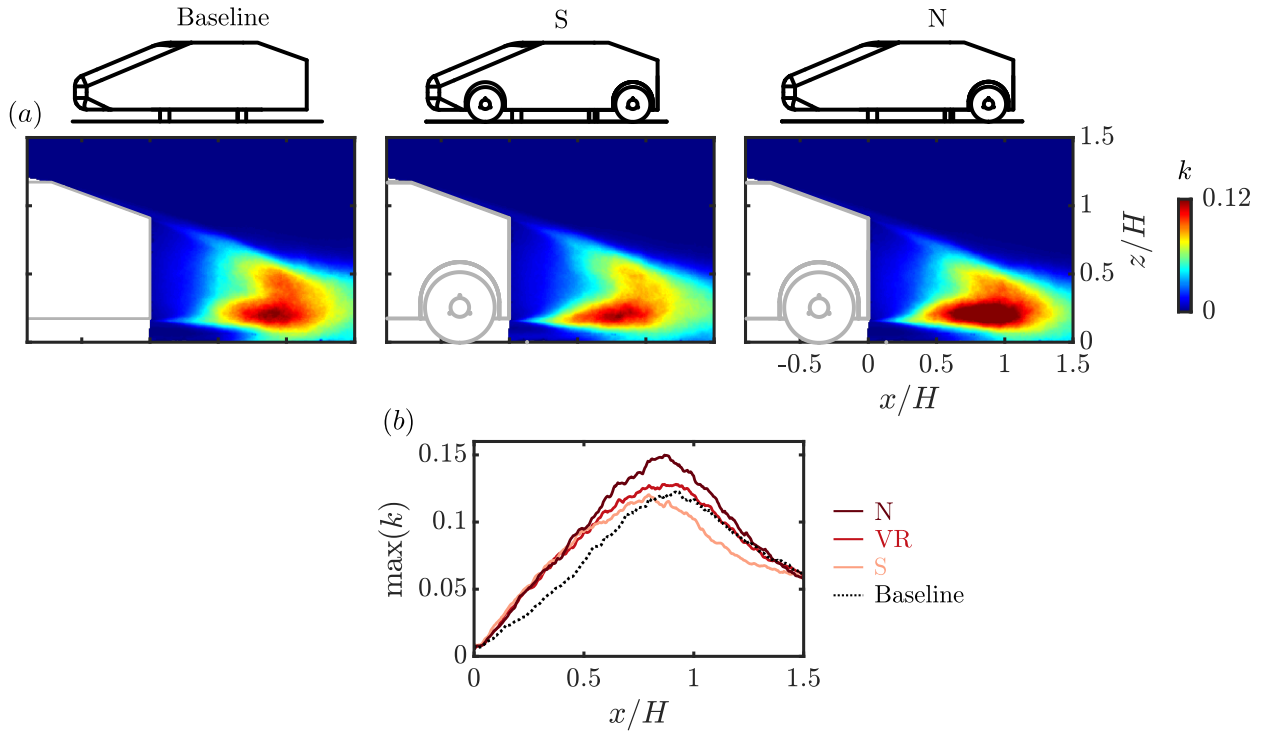


Figure 7.11: (a) Distributions of turbulent kinetic energy  $k$  in the symmetry plane of the body at  $y/H = 0$  for the baseline case and several cases with different front wheel types. (b) Effect of front wheel type on the streamwise evolution of the maximum of  $k$ .

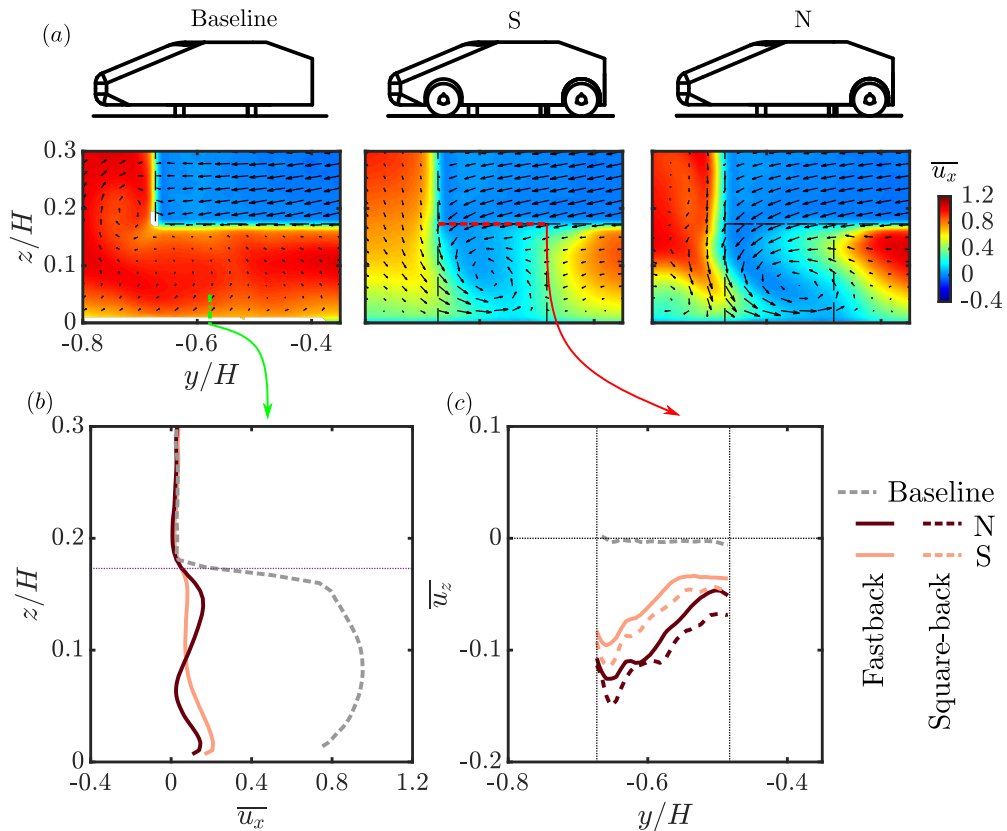


Figure 7.12: (a) Local distributions of the mean streamwise velocity  $\overline{u_x}$  in the cross-flow plane at  $x/H = 0.03$  for the same cases in figure 7.10(b), the  $\overline{u_x}$  profiles along the centerline of the obstacles are plotted in (b). The  $\overline{u_z}$  profiles along the width of the wheels at the height of the ground clearance are plotted in (c).

of the main body and the wake of the rear wheels is noticed. This is depicted in figure 7.12(b)

by the  $\overline{u_x}$  profiles along the centerline of the left-hand wheels. By looking at the in-plane vectors, the reduction of mean shear between the wakes is accompanied by a mean mass transfer from the wake of the main body to the wakes of the rear wheels. The mean vertical velocity  $\overline{u_z}$  profiles across the width of the rear wheels at the ground-clearance height are plotted in figure 7.12 for the three cases. When the front wheel bluntness is reduced from case S to N, the strength of the mass transfer is enhanced. When comparing these  $\overline{u_z}$  profiles with that of the square-back configuration, we notice that the mean mass transfer is not sensitive to the shape of the model.

## 7.6 Concluding remarks

The dependency of wheel-vehicle interactions on vehicle back shape was investigated. Additional measurements repeating the investigations in previous chapters using a square-back vehicle were carried based on a  $20^\circ$  fast-back vehicle. This vehicle features a highly 3-D wake topology with a complex interaction between several flow structures. By placing a pair of D-shaped obstacles under the vehicle or by installing wheels on the vehicle, differences and similarities in the wheel-vehicle interactions were found when comparing the results from the two different vehicles. Differences were noticed when looking globally at the wake of the main vehicle body, which reacts very differently to the presence of the wheels or the obstacles. The investigations on the mean and fluctuating properties of the wake both confirmed this. Most importantly, the strong sensitivity of the vertical wake equilibrium of the square-back vehicle to the wheels (or the obstacles) was not found for the fast-back geometry. This is believed to be the key to further understanding the different wheel shape sensitivity for different vehicle shapes (Wittmeier *et al.*, 2013).

On the other hand, when looking locally at the flow near the rear wheels or the obstacles, we showed that the flow near the rear wheels or the obstacles is barely modified by the variation in the vehicle wake. Accompanied by this, the mean mass transfer from the vehicle wake to the wakes of the rear wheels (or obstacles) was found quantitatively to be not sensitive to the vehicle shape. When a mass flux exits a wake, the mass conservation guarantees that the wake has to obtain the mass flux from the high-momentum surrounding flow. According to the model proposed in chapter 4, the streamwise momentum loss of the fluid particles entering the wake is balanced by a pressure drop on the base. Therefore the same level of mean mass loss corresponds to the same level of base pressure change. This was successfully measured by systematically varying the relative distance between the obstacles and the vertical base of the vehicle. In fact, the same flow regimes and pressure drag sensitivity as in chapter 4 using a square-back model was measured. Here the pressure drag changes are still governed by the scaling properties found for the square-back vehicle. From another perspective, the present work also confirmed that the physical model proposed in chapter 4 is robust even for a complex 3-D wake.

Moreover, the role of the front wheels remains the same as for the square-back model investigated in chapter 6. When reducing the front-wheel bluntness, the mean mass transfer is enhanced and the base drag is increased.

These similarities between the two vehicles showed that the front-rear wheel interactions and the local interactions between the rear wheels and the vehicle wake are insensitive to vehicle type. The latter one had been partly confirmed in chapter 5 by investigating two different initial wake states of the square-back model.

## Chapter 8

# General synthesis and perspectives

---

### 8.1 General synthesis

For a road vehicle, flow separations occur all around it and are of a multi-scale nature. The separation regions and the interactions between them are direct or indirect sources of aerodynamic drag. We focused on a specific problem by considering the interactions between the wheels and the main body of a vehicle. Our objective was first to reveal the key flow mechanisms governing the interactions and their impacts on the drag of the vehicle. The second objective was to show, from a more general perspective, how these flow mechanisms evolve with the shape of the vehicle or the wheels.

Dedicated experiments were conducted to achieve these objectives. Based on a simplified vehicle geometry with rigid wheels, we studied the contributions of front wheels, rear wheels and vehicle wake in the wheel-vehicle interaction problem. From a global and local analysis, we found that two main mechanisms originate from wheel-wake and wheel-wheel interactions and contribute to a base drag increase of up to 21 %. We summarize our main findings in what follows.

#### 8.1.1 Mean mass transfer: sensitivity, origin, and consequences

Two approaches were utilized in the present work to elucidate the underlying flow mechanisms based on a simplified vehicle geometry. In the first approach, a pair of 2-D D-shaped obstacles was placed under the vehicle and the relative obstacle-to-base distance  $l$  was varied. In the second approach, four rigid wheels were installed on the vehicle with different relative distances  $l$  between the rear wheels and the base. Using these two approaches, we highlighted a mean mass transfer from the vehicle wake to the wakes of the rear wheels. Under the present experimental setup, this phenomenon happens when the relative wheel-to-base distance  $l$  is smaller than a threshold of 2.5 times the wheel width  $w$  (or the obstacle width  $d$ ). The associated base drag increase of this phenomenon was estimated to be up to 22%<sup>1</sup> (12%) for the obstacle (wheel) situation, which corresponds to a drag penalty of  $0.040\overline{C_D}$  ( $0.024\overline{C_D}$ ). This suggests a large drag reduction potential.

Moreover, systematic sensitivity analyses were carried out to answer one important question: what are the parameters that drive the mean mass transfer? These analyses involve varying the relative distance  $l$  along with different parameters, such as the vehicle shape (a square-back and a 20° fast-back were tested), the vertical balance of the vehicle wake, the width of the obstacles  $d$ , and the wheel shoulder radius. Examination and analysis of these results have led us to answer the question and to propose scaling laws for the associated drag changes. These sensitivity analyses are classified into four parts:

---

<sup>1</sup>In reference to the baseline case without any underflow perturbations.

- **Vehicle shape influence:** One surprising finding from the sensitivity analyses is that the mean mass transfer is not sensitive to the variations in the topology of the vehicle wake. This was demonstrated through two scenarios in which the backshape of the vehicle was altered or the large-scale vertical asymmetry of the vehicle wake was manipulated. Despite these changes, the strength of the mean mass transfer and the associated base pressure change remained relatively constant.
- **Wheel-to-base distance influence:** For both obstacle and wheel situations, we showed that the relative distance  $l$  is a critical parameter in the mean mass transfer and the related drag changes. At  $l/w < 2.5$  for the wheel situation or  $l/d < 2.5$  for the obstacle situation, the base drag increases rapidly with reducing  $l/w$  or  $l/d$ . This is accompanied by an enhancement of the mean mass transfer.
- **Wheel width influence:** At a fixed wheel-to-base distance  $l$ , increasing the width of the rear wheels  $w$  is expected to reduce the normalized relative distance  $l/w$  and increase the width of the mean mass transfer surface. This was demonstrated under the obstacle situation. We united the relationship between the relative distance  $l$  and the obstacle width  $d$  by examining the effects of obstacle width  $d$  at fixed  $l/d$  values. When the obstacles are the closest to the base,  $l/d < 1.5$ , the base drag changes scale with  $d$ . This suggests that the size of the mass exchange surface is governed by both the scale of the obstacle and the scale of the body. Contrarily, when the obstacles are located farther from the base  $1.5 < l/d < 2.5$ , the base drag changes scale with  $d^2$ . This implies that both the width and the length of the mass exchange surface are driven by the size of the obstacles. An evaluation using these scaling properties for the wheel situation shows a base drag increase of up to 5% (equivalent to a drag penalty of  $0.01\overline{C_D}$ ) by increasing the width of the rear wheels by 20%.
- **Rear-wheel upstream flow condition:** In addition to the wheel dimensions, we revealed another crucial parameter for the mean mass transfer and the related drag change. When the shoulder radius of the front wheels was reduced, the base drag is increased. Meanwhile, the normalized facing velocity  $u_f$  for the rear wheels is increased which reduces the pressure level inside the rear wheel wakes. When the wheel-to-base distance  $l/w$  is smaller than a threshold of 2.5, the pressure decrease is accompanied by an increase in the mean mass transfer velocity while the size of the mass exchange surface remains unchanged for a fixed  $l/w$ . These interactions result in a scaling law with the base drag linearly proportional to  $u_f$ .

Based on the detailed pressure and velocity measurements from these sensitivity studies, a physical scenario was proposed in order to answer two main questions: (i) what causes the mean mass transfer? and (ii) what are the consequences of this transfer? We have shown that the difference in mean pressure between the wakes of the rear wheels and the wake of the body drives the mean mass transfer. This mean pressure difference was related to the mean upstream flow condition for the rear wheels and the local mean wake development of the rear wheels. As the second question is concerned, if a mean mass flux exits the main wake, the law of mass conservation then guarantees that this mass flux has to enter the mean recirculating bubble. The corresponding fluid particles, coming from upstream unperturbed flow, therefore lose their mean streamwise momentum. By assuming that this momentum loss is balanced by a pressure drop at the vehicle base, a linear relationship between the base drag penalty and the mass transfer flow rate was obtained.

These physical models were found in accordance with all the experimental data displayed in the present work. Further RANS (Reynolds-Averaged Navier-Stokes) simulations reproducing the obstacle situation were able to provide supplementary information, for example by computing an integral mean longitudinal momentum balance for the near wake. Using this understanding, the different sensitivities of the mean mass transfer and the related drag penalty to different parameters were explained. This includes the reasons for the insensitivity to the vehicle shape and for the sensitivity to several wheel-related parameters.



Figure 8.1: Bluff bodies involving the interactions between multi-scale separation regions: An offshore facility, a yacht, and a building.

### 8.1.2 Variation in vehicle wake balance

For the wake of a square-back vehicle, the orientation of the recirculating flow is very sensitive to small flow modifications around the model, such as variations in yaw/pitch angle, changes in ground clearance, or perturbing objects located in the underflow. The resulting wake asymmetry, in the form of either bi-modal asymmetry in the direction along the main axis of the vehicle base or permanent asymmetry in the direction along the minor axis of the base, is an important source of aerodynamic drag (see chapter 1 for a detailed review).

In the present work, we started by perturbing the underflow of the simplified square-back vehicle geometry using either the obstacle pair or the four rigid wheels. Two different initial wake asymmetries were tested. We found that the wheels (or the obstacles) induce changes in the underflow, which consequently leads to a global variation in the vertical balance of the mean vehicle wake. This phenomenon happens for all the wheel(obstacle)-to-base distances  $l$  investigated. Moreover, according to the state of the initial wake, significant base drag increase of  $\sim 5\%$  (corresponding to  $0.01\overline{C_D}$ ) or decrease of  $\sim 9\%$  ( $0.02\overline{C_D}$ ) was observed. This drag increase (decrease) corresponds to an enhancement (reduction) of vertical wake asymmetry.

The same experiments were then repeated on the  $20^\circ$  fast-back vehicle geometry. We found that the vertical wake balance for this geometry is relatively insensitive to the presence of either obstacles or the wheels in the underflow. Considering the insensitivity of the mean mass transfer phenomenon to vehicle shape, this difference in vehicle wake balance variation is believed to be the key to further understanding the different wheel shape sensitivity for different vehicle shapes (Wittmeier *et al.*, 2013).

## 8.2 Perspectives

The physical mechanisms underlying the wheel-vehicle interaction problem highlighted in the present work may open some perspectives for several research topics. Some guidelines are provided now for tackling these possibilities.

### 8.2.1 Interactions of multi-scale separation regions

In the present work, we focused specifically on the wheel-vehicle interaction problem, which involves the interactions between a large-scale separation region (the vehicle wake) and several small-scale separation regions (the wheel wakes). Indeed, similar situations can be found in nature and industry, as illustrated in figure 8.1. For these situations, the main separation region is generated by the large-scale bluff bodies, which may interact with the flow separations from the small-scale bluff bodies (highlighted by red dotted lines in the figure). We believe that the flow mechanisms found in the present work could be further extended from this point-of-view of multi-scale separation region interactions.

The study of the local wheel-vehicle interactions has provided the key mechanism causing the drag increase: the mean mass transfer phenomenon. This was found under two different configurations with the small-scale separations generated by the rear wheels or two 2-D D-shaped

obstacles. Therefore, it is believed to be a general feature for bluff body flows. In figure 8.1, this phenomenon may exist from the wake of the offshore facility to the wakes of the four supporting cylinders, from the air wake of the yacht to the wake of the top deck, or from the building wake to the chimney wake. The physical scenario proposed in the present work could be useful in these situations when trying to link the mass exchange phenomenon and the drag increase. Additionally, this phenomenon may also play an important role in the dynamics of the large-scale separation region. For a 3-D wake, [Hsu \*et al.\* \(2021\)](#) showed that a continuous base suction is able to fully suppress the static mode of the wake. This is also noted in the present work that the static mode is slightly suppressed in some situations of the obstacle configuration<sup>2</sup>. Nonetheless, there is still a need for further elaboration to fully explain the relationship between the mass exchange and the static wake mode. There are two questions to be answered: (i) where and how the mass extraction should be applied in order to efficiently reduce the transient wake asymmetry? (ii) why under mass extraction the steady state of the recirculation region changes from the bi-stable asymmetric state to the symmetric state?

Moreover, we found that the wheels induce changes in the underflow, which consequently leads to the variation in the vertical balance of the mean vehicle wake of the square-back geometry. This phenomenon is reminiscent of the previous studies by modifying the underflow condition ([Grandemange \*et al.\*, 2013a](#); [Barros \*et al.\*, 2017](#); [Castelain \*et al.\*, 2018](#)) or by perturbing the side boundary layer ([Haffner \*et al.\*, 2022](#)) of square-back bluff bodies. In this process, the changes in the underflow (sideflow), the development of shear layers, and the formation of the wake are crucial physical elements. We suggest that the link between these elements should be further pursued. In particular, we have shown that by changing the backshape from the square-back to the fast-back, the mean vertical wake balance becomes less sensitive to the variations in the underflow. These different sensitivities could serve as a promising key to evidence the relationship between the underflow and the wake of a bluff body.

### 8.2.2 A road towards industrial applications

The flow mechanisms driving the wheel-vehicle interactions were revealed based on a simplified vehicle geometry. We admit that this model vehicle, although designed with a more industrial look than the Ahmed body ([Ahmed \*et al.\*, 1984](#)), still can not reproduce all the flow features of real road vehicles. In particular, the complex underflow condition caused by the rough underbody and cooling airflow from the engine bay is not represented. Therefore, further applications of the present conclusions on real road vehicles require first a dedicated experimental setup in automotive wind tunnels using real cars at the industrial scale. This can be supplemented numerically by Reynolds-averaged or time-resolved simulations, which have been shown able to reproduce the key mechanisms of the wheel-vehicle interaction problem. With the RANS simulations shown in appendix A, we have noticed that the mean mass transfer phenomenon can be reproduced. In addition, as shown in [Su \*et al.\* \(2023\)](#), time-efficient hybrid RANS-LES (Large-Eddy Simulations) methods are useful when the wake balance problem is considered.

Driven by the new regulation of the Real-Driving Emission (RDE) ([Hooftman \*et al.\*, 2018](#)), the aerodynamic design of road vehicles requires more considerations of real on-road conditions. In particular, the presence of side flow leading to the variation of yaw angle is one of the important factors to be considered. [D’Hooge \*et al.\* \(2015\)](#) showed that the yaw angle range between  $0^\circ$  and  $6^\circ$  covers the majority of possible situations. Therefore, it is important to consider the wheel-vehicle interaction problem under different yaw angles.

Based on the experimental setup used in chapter 6, preliminary tests are conducted by varying the yaw angle  $\beta$  for the shortest square-back body with or without wheels (sharp-edged-shoulder ones). The results are shown in figure 8.2. This body length gives the smallest distance between the rear wheels and the base  $l/w = 0.65$  with strong interactions between the rear wheels and the vehicle wake (see chapter 5) at  $\beta = 0$ . When the yaw angle is increased, we notice in figure 8.2(a) that the base drag  $\overline{C_B}$  increases slower for the wheel configuration than the no-wheel configuration. By looking at the mean base pressure distributions, it is surprising to note that the evolution of the mean horizontal wake asymmetry is very different between the two configurations. This is pictured

---

<sup>2</sup>See figure 4.10 of chapter 4.

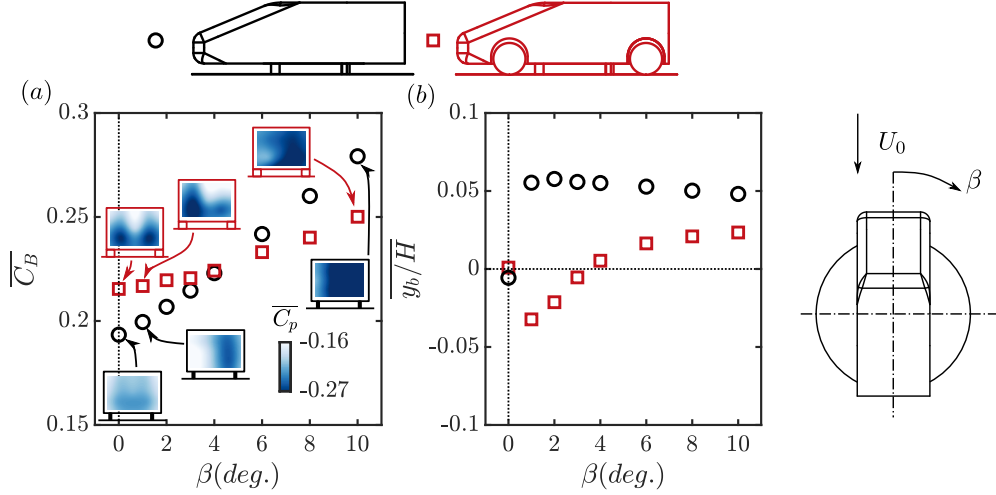


Figure 8.2: For the shortest square-back body ( $l/w = 0.65$ ) with and without sharp-edged-shoulder wheels: evolution of mean base drag  $\overline{C_B}$  and mean horizontal position of the base center-of-pressure (CoP)  $\overline{y_b/H}$  with the yaw angle  $\beta$  of the body.

by the evolution of the mean horizontal position of the base center-of-pressure (CoP)  $\overline{y_b/H}$  with  $\beta$  in figure 8.2(b). When the yaw angle  $\beta$  is increased,  $\overline{y_b/H}$  increases suddenly to  $\overline{y_b/H} \approx 0.05$  for the no-wheel configuration due to the selection of horizontal asymmetry states by the wake. On the other hand, for the wheel configuration, there exists a complex evolution of horizontal mean wake asymmetry with the yaw angle  $\beta$ .

These preliminary results show that for a road vehicle at yaw, there exists a complex coupling between the vehicle wake asymmetry and the wheels. This coupling has an important impact on the drag. In addition, under yaw conditions, the facing velocity for the rear wheels is expected to be increased. This facing velocity is crucial for the mean mass transfer phenomenon and the related drag changes as shown in chapter 6.

### 8.2.3 Drag-reduction strategies

The understanding of the wheel-vehicle interaction problem also enables us to propose drag-reduction strategies for road vehicles. In our situation, it was evaluated that the mean mass transfer phenomenon accounts for a drag penalty of up to  $0.024\overline{C_D}$ . On the other hand, the wheels are an important influencer of the mean wake asymmetry. This asymmetry-related drag is often estimated to account for up to  $0.020\overline{C_D}$  (Haffner *et al.*, 2020a).

By focusing on the wheel-vehicle interactions, further drag reduction of road vehicles may be achieved through two different approaches. First of all, the aerodynamic optimization process could be improved. For some automotive companies<sup>3</sup>, after a main vehicle body shape is fixed, several wheelsets (combinations of tires and rims) are tested and the optimum one is then selected. For the wheelset leading to the minimum local drag (the sum of wheel drag and mass exchange drag), the coupling with the mean wake balance may in total cause a higher drag compared to other wheelsets. If all four wheels are required to be identical, we proposed that an additional procedure of wake symmetrization should be followed for each wheelset. This can be done by adjusting the angle of the rear spoiler or the angle of the diffuser for example.

Moreover, we may propose several devices targeting the local mean mass transfer that appears for mini cars having a small relative distance between the rear wheels and the base. The present work showed that this mean mass transfer can be suppressed or at least reduced in three ways: increasing the wheel-to-base distance, reducing the width of the rear wheels, and decreasing the facing velocity for the rear wheels. Limited by functionality and maneuverability, the wheel-to-base distance and the width of the rear wheels are normally fixed. However, alternative ways could be sought to increase the wheel-to-base distance at highway speeds for example the adaptive rear cavity used on the concept vehicle IAA (Mercedes-Benz). In addition, the facing velocity for the

<sup>3</sup>Private communications with MFP Michelin and Shanghai Automotive Wind Tunnel Center (SAWTC).

rear wheels could be reduced by placing obstacles in front of the rear wheels, for example the wheel spoiler. We note that this spoiler should be carefully designed to cope with flow condition variations, e.g. the yaw angle, and to have the least local drag.

# Appendix A

## Numerical simulations for the square-back Windsor body

---

Numerical computations using Reynolds-Averaged Navier-Stokes (RANS) simulations are performed to model the experiments described in chapter 4, where the three-dimensional wake of a square-back bluff body in ground proximity is perturbed by placing a pair of D-shaped obstacles under the body. When the obstacles are placed close to the base of the body and their wakes are merged with the wake of the body, the simulations successfully reproduce the increase in pressure drag and the modifications in the wake of the body observed in the experiments. The mean mass transfer from the body wake to the wakes of the obstacles is found to have a similar distribution to that observed in the experiments. The pressure difference between the wakes is identified as the main driving factor for the mean mass transfer. Furthermore, we show the consequences of the mass transfer on the mass and momentum exchange between the body wake and the surrounding flow in a more global aspect. Finally, the momentum exchange model proposed in chapter 4 is validated, and its physical implications are revealed.

### Contents

---

<b>A.1 Methodology</b>	<b>126</b>
A.1.1 Model geometry and numerical setup	126
A.1.2 Underflow perturbations	128
<b>A.2 Comparison between numerical and experimental results</b>	<b>128</b>
<b>A.3 Further insights of near-wake interactions</b>	<b>130</b>
A.3.1 Global pressure distributions	131
A.3.2 Origin of the mean mass exchange	132
A.3.3 Effect of mean mass exchange on base pressure	133

---

In this appendix, we conduct numerical computations to model the experiments described in chapter 4. Our primary objective is twofold: firstly, to demonstrate whether the simulations can replicate the observations made in chapter 4; secondly, to provide additional insights into the near-wake interactions using the 3-D numerical data.

## A.1 Methodology

The simulations reproduce the experiments in chapter 4. A sensitivity study was performed under a free-stream velocity  $U_0 = 25 \text{ m s}^{-1}$ , corresponding to a height-based Reynolds number  $Re_H = U_0 H / \nu = 4.8 \times 10^5$ .  $\nu$  is the kinematic viscosity of the air at operating temperature. The underflow of the Windsor body was perturbed by a pair of 2-D D-shaped obstacles. The model geometry and the numerical setup are presented in §A.1.1, followed by a description of the underflow perturbations in §A.1.2.

### A.1.1 Model geometry and numerical setup

The square-back Windsor body shown in figure A.1(a) having width  $W = 0.389 \text{ m}$ , height  $H = 0.289 \text{ m}$ , and length  $L = 1.147 \text{ m}$  is used. The supports used for the experiments are not considered in order to simplify the mesh. Considering the profiled shape of the supports, they are expected to have very little effect on the flow. This model is placed inside a computational domain with a ground clearance of  $G = 0.05 \text{ m}$  as shown in figure A.1(b). The domain has the same width and height as the region above the raised floor in the test section of the wind tunnel. The inlet of the domain is at  $8H$  in front of the model and the outlet is at  $20H$  behind the model. Different boundary conditions are given for the domain surfaces. A uniform velocity profile at  $25 \text{ m s}^{-1}$  with turbulence intensity of 0.3 % and turbulence length scale of 0.1 m is set for the inlet. A pressure outlet condition with a gauge pressure of zero is used for the outlet. For the model surface, a no-slip condition is given. The ground is divided into two parts. From the inlet to  $1.8H$  in front of the model, a slip boundary condition is given. The rest of the ground is set to a no-slip boundary condition. This boundary condition for the ground is designed in order to give the same boundary layer thickness approaching the model as the experiments (Östh *et al.*, 2014). In addition, the walls of the domain are specified to a slip boundary condition.

The unstructured mesh inside the computational domain as shown in figure A.1(c) is generated using the commercial code Star-ccm+ following the suggestions of Page & Walle (2022). The mesh contains prism layers near the no-slip boundaries and hexahedral grids in the rest of the domain. The hexahedral grids downstream of the model are refined in two regions. For the first region near the model, the size of the grids is set to the same dimension as that near the model. For the second region located more downstream, the size of the grids is doubled compared to the first region. Four sets of mesh, namely coarse, medium, fine, and very fine, are tested as shown in table A.1. The size of the first prism layer at the model surface is expressed in wall units calculated using the friction velocity measured in table 3.1. The total number of cells is gradually increased following two steps. First, for the first prism layer, the thickness  $y^+$  is fixed and the wall-parallel dimension  $x^+/z^+$  is gradually reduced. Moreover, the size of all the hexahedral grids in the domain varies in the same proportion as  $x^+/z^+$ .

	Course	Medium	Fine	Very fine
Number of cells ( $\times 10^6$ )	1.4	2.4	5.5	22.0
Wall-normal resolution $y^+$	150	150	150	150
Wall-parallel resolution $x^+/z^+$	670	470	330	200
$\overline{C_{B0}}$	0.168	0.160	0.153	0.153
$\overline{C_{x0}}$	0.247	0.236	0.228	0.227

Table A.1: Spatial resolution and mean force coefficients for four sets of meshes.

The incompressible RANS equations are solved iteratively based on a finite volume discretization with the Reynolds stresses modeled by the two-equation Realizable  $k - \epsilon$  model (Shih *et al.*,

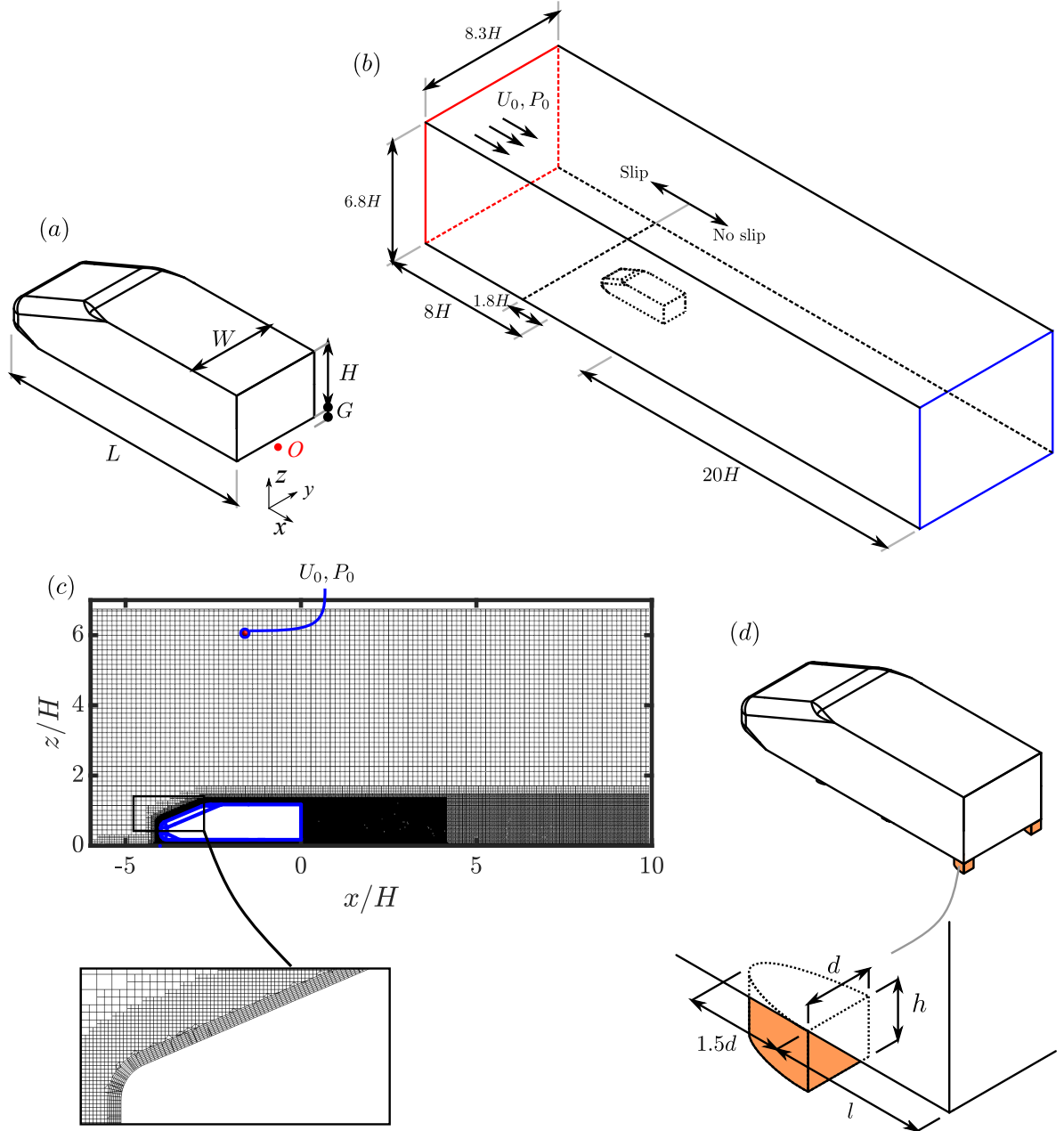


Figure A.1: Numerical setup. (a) Model geometry and coordinate system. (b) Computational domain and boundary conditions, red and blue rectangles represent inlet and outlet, respectively. (c) Distribution of mesh in the symmetry plane of the model at  $y/H = 0$ . (d) Locations of the underflow perturbing D-shaped obstacles.

1995). We are aware that all eddy-viscosity models are unable to model accurately the complex dynamics of 3-D wakes (Page & Walle, 2022). However, we will see in what follows that while modifications of the wake balance and wheel vehicle interactions in plateau or regime I regions cannot be predicted by this model, the near-wake interaction features are quantitatively captured in the strong interaction regime II. The use of simple CFD approaches, therefore, permits to obtain further insights into the near-wake interactions in this situation.

Due to the high Reynolds number of the present study, the wall functions are used. The second-order upwind scheme is used to discretize the convection and diffusion terms in the equations. The coupling between pressure and velocity is implemented with the SIMPLE algorithm.

The origin of the coordinate system  $O$  (shown in figure A.1a behind the model) is located at the intersection point of the floor surface, the rear surface, and the symmetry plane of the model. The axes of the system are defined as streamwise ( $x$ ), spanwise ( $y$ ) and floor-normal ( $z$ ) directions. Under this system, the velocity vector is decomposed into  $\mathbf{U} = (U_x, U_y, U_z)$ . Unless

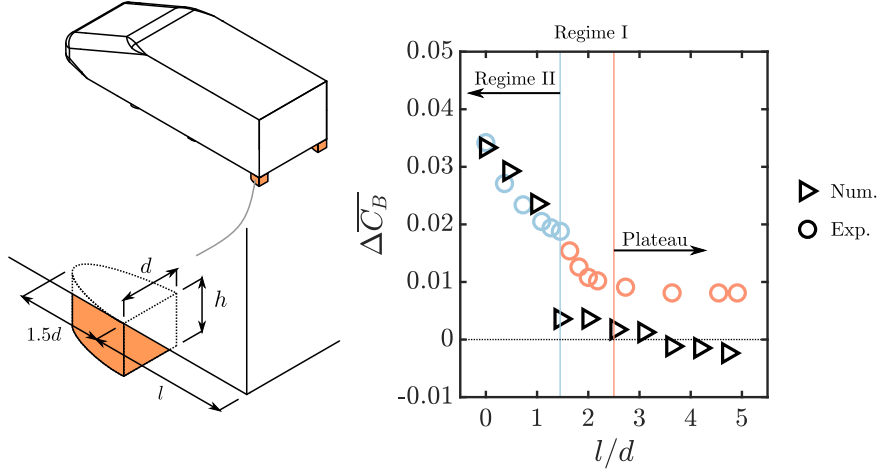


Figure A.2: Comparison of the base drag evolution  $\Delta \overline{C}_B = \overline{C}_B - \overline{C}_{B0}$  with obstacle-to-base distance  $l/d$  between numerical and experimental results.

otherwise stated, all physical quantities are normalized by any appropriate combination of the model height  $H$ , the reference free-stream velocity  $U_0$ , the reference pressure  $p_0$  and the air density  $\rho$  at  $15^\circ\text{C}$ . For convenience, the normalized velocity vector is denoted by lowercase letters, i.e.  $\mathbf{u} = (u_x, u_y, u_z) = (U_x/U_0, U_y/U_0, U_z/U_0)$ . The reference velocity  $U_0$  and the reference pressure  $p_0$  are obtained at the location of the pitot tube for the experiments as shown in figure A.1(c).

In table A.1, we focus on the variations of the base drag  $\overline{C}_{B0}$  (opposite of the space-averaged pressure coefficient on the base) and the total drag  $\overline{C}_{x0}$  of the model. With increasing cell number, we notice that  $\overline{C}_{B0}$  and  $\overline{C}_{x0}$  are mesh insensitive when the cell number is bigger than 5.5 million. Therefore, the corresponding grid (fine grid) is used for the investigation in figure 3.5 of chapter 3 and the investigations presented later when the underflow of the model is perturbed.

### A.1.2 Underflow perturbations

The same as the experimental setup in chapter 4, a pair of D-shaped obstacles as shown in figure A.1(d) is placed in the underflow of the model. The two-dimensional (2-D) obstacles have a half-elliptical cross-section, with a width of  $d = 0.19H$  and a length of  $1.5d$ . The obstacle height is the same as the ground clearance  $G$ . When the obstacles are used, care was taken for the mesh with the cell size near the obstacles reduced by 5 times (proper refinement in the wake region is also considered). The obstacle pair is always placed symmetrically to the symmetry plane of the model, with its rear surface parallel to the base of the body and its left-hand/right-hand side tangents to the left-hand/right-hand side of the body. The degree of freedom of the pair in the streamwise direction is fixed by the obstacle-to-base distance  $l$ , which is defined as the streamwise distance from the base of the obstacles to the base of the body. The parameter  $l$  ranges from  $0$   $d$  (flush-mounted to the base) to  $5$   $d$ .

## A.2 Comparison between numerical and experimental results

In this section, we compare the simulations with the experiments in chapter 4. We focus on the global and local wake modifications by the obstacles leading to a substantial base drag increase of up to 18%. In particular, the mean mass transfer from the wake of the model to the wakes of the obstacles is targeted. This was identified as the main drag increase mechanism.

The base drag variation  $\Delta \overline{C}_B = \overline{C}_B - \overline{C}_{B0}$  of the model with the distance from the obstacles to the base  $l/d$  is shown in figure A.2. Using the experimental results, we were able to identify a plateau and two drag-sensitive regimes. In the plateau ( $l/d > 2.5$ ), the obstacles increase slightly the base drag by  $\Delta \overline{C}_B / \overline{C}_{B0} \approx 5\%$  and the base drag is not sensitive to  $l/d$ . From the plateau with decreasing  $l/d$ , the two successive drag-sensitive regimes are marked by a sharp increase of  $\Delta \overline{C}_B$ . The maximum drag increase is  $\Delta \overline{C}_B / \overline{C}_{B0} \approx 18\%$  at  $l/d = 0$ . In different regimes, the flow

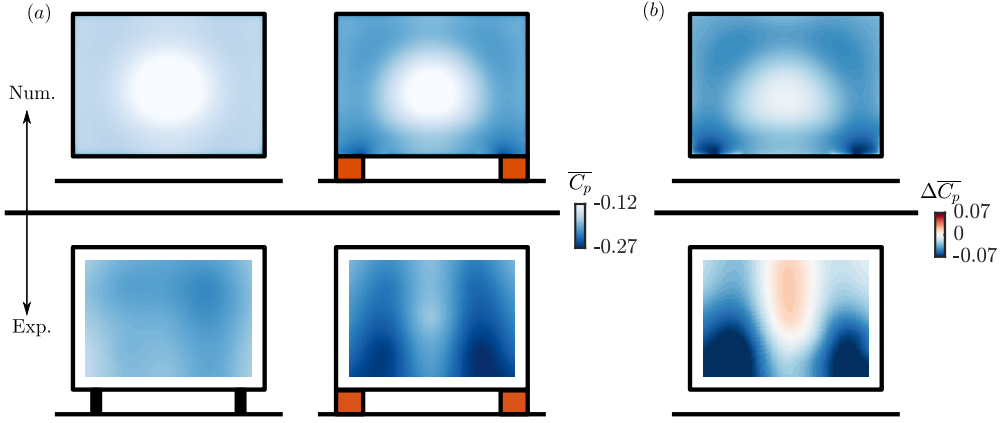


Figure A.3: Comparison of the base pressure  $\overline{C_p}$  (a) and base pressure difference  $\Delta\overline{C_p} = \overline{C_p} - \overline{C_{p0}}$  (b) between numerical and experimental results for the cases without and with obstacles (obstacles are flush-mounted to the base with  $l/d = 0$ ).

dynamics behind the obstacles were found to be very different. In regime I ( $1.5 > l/d > 2.5$ ), the wakes of the obstacles can be separately identified and signatures of vortex shedding were measured behind the obstacles. In regime II, the obstacle wakes and the model wake are merged and the vortex shedding is suppressed.

We now compare the numerical results with the experimental results. In the plateau, we note that the simulations fail to reproduce the base drag increase of 5 %. From the plateau with decreasing  $l/d$ , in regime I the drag sensitivity to  $l/d$  is not observed. This is probably due to the failure of the RANS simulations in modeling the complex wake dynamics of the obstacles and their interactions with the main body wake. However, in regime II, we notice the same level of base drag increase  $\Delta\overline{C_B}$  and the drag sensitivity to  $l/d$ . Therefore, in what follows, the flush-mounted case  $l/d = 0$  is selected for the comparisons and is named as the case with obstacles.

In figure A.3, we present the mean base pressure distributions  $\overline{C_p}$  for the case with and without obstacles. When the obstacles are not placed, we note that the  $\overline{C_p}$  distribution is very different from that of the experiments. It presents a low-pressure region near the trailing edges and a higher-pressure region at the center of the base. This is similar to the RANS simulations in [Khalighi \*et al.\* \(2001\)](#); [van Raemdonck \*et al.\* \(2016\)](#) and in [Bonnayon \(2018\)](#). When the underflow of the model is perturbed by the obstacles, we observe a uniform drop in pressure around the edges of the base. Focusing on the distribution of the base pressure difference  $\Delta\overline{C_p}$  between the two cases, we notice that the base pressure variation due to the obstacles is different from that of the experiments. In the experiments, a change in vertical asymmetry and a decrease in pressure near the obstacles were observed.

The mean streamwise velocity distributions  $\overline{u_x}$  superimposed by in-plane streamlines in the symmetry plane of the model  $y/H = 0$  are shown in figure A.4(a) for the cases with and without obstacles. For the case without obstacles, the wake structure is qualitatively similar to the PIV measurements. The recirculation length  $L_r/H = 1.96$  is longer than that of experiments  $L_r/H = 1.65$  ( $L_r$  defined as:  $L_r = \max(x)_{\overline{u_x} \leq 0}$ ). When the obstacles are placed, we notice a reduction of  $L_r/H$  by  $\sim 10\%$ . This trend is similar to the experiments. The recirculation strength is also found to be enhanced as shown in figure A.4(c) by the evolution of  $\mathcal{R}$ , which is defined as:

$$\mathcal{R}(x) = \int_{\overline{u_x} \leq 0} \sqrt{\overline{u_x^2} + \overline{u_z^2}} d(z/H). \quad (\text{A.1})$$

For the simulations, the maximum of  $\mathcal{R}$  is increased by  $\sim 14\%$ . In the cross-flow plane at  $x/H = 0.03$  (see figure A.4b), the presence of the obstacles greatly reduces the flow momentum behind them. This reduction decreases the shear between the wake of the model and the wakes of the obstacles as visualized in figure A.4(d) by plotting  $\overline{u_x}$  along the centerline of the left-hand side obstacle. All these changes due to the presence of obstacles are similar to the experimental measurements.

Better similarities with the experiments are found when examining the local flow field near

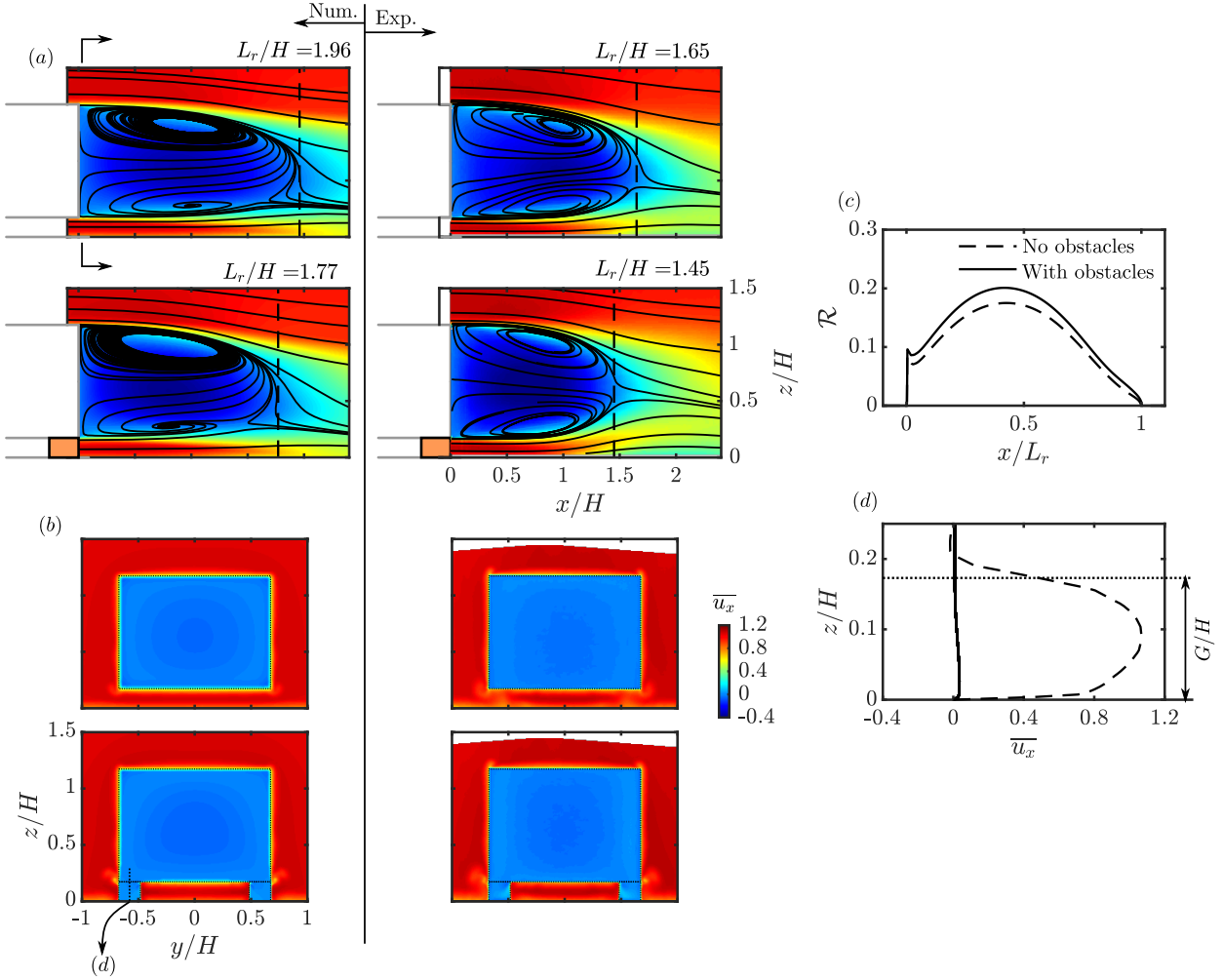


Figure A.4: Comparison of the mean streamwise velocity  $\overline{u}_x$  in the symmetry plane of the model  $y/H = 0$  (a) and in a cross-flow plane at  $x/H = 0.03$  (b) between numerical and experimental results for the cases without and with obstacles (obstacles are flush-mounted to the base with  $l/d = 0$ ). For the numerical simulations, the streamwise evolution of the recirculation strength  $\mathcal{R}$  and the vertical profiles of  $\overline{u}_x$  along the centerline of the left-hand side obstacle from (b) are shown in (c) and (d), respectively.

the obstacles in figure A.5. The mean vertical velocity distributions  $\overline{u}_z$  in the cross-flow plane at  $x/H = 0.03$  and in the half-ground-clearance plane at  $z/H = 0.09$  are shown. Comparing the cases with and without obstacles, a mean mass transfer from the wake of the model to the wakes of the obstacles is noticed. The mean mass transfer and the related flow structures are in very good accordance with that of the experiments. Indeed, we only observe a slight difference in the magnitude of the mass transfer. Therefore, the essential features of near-wake interactions between the model and the obstacles, namely the base drag increase and the mean mass transfer, are captured by the numerical simulations.

### A.3 Further insights of near-wake interactions

The experimental investigation in chapter 4 and the present numerical study both highlight the mass exchange between the model wake and the obstacle wakes. With the 3-D flow data available now, we are in a position to further investigate the mass exchange. The pressure fields are investigated first. Then the origin of the mass flux is examined. Finally, an analysis of the influence of the mass exchange on the base pressure is presented.

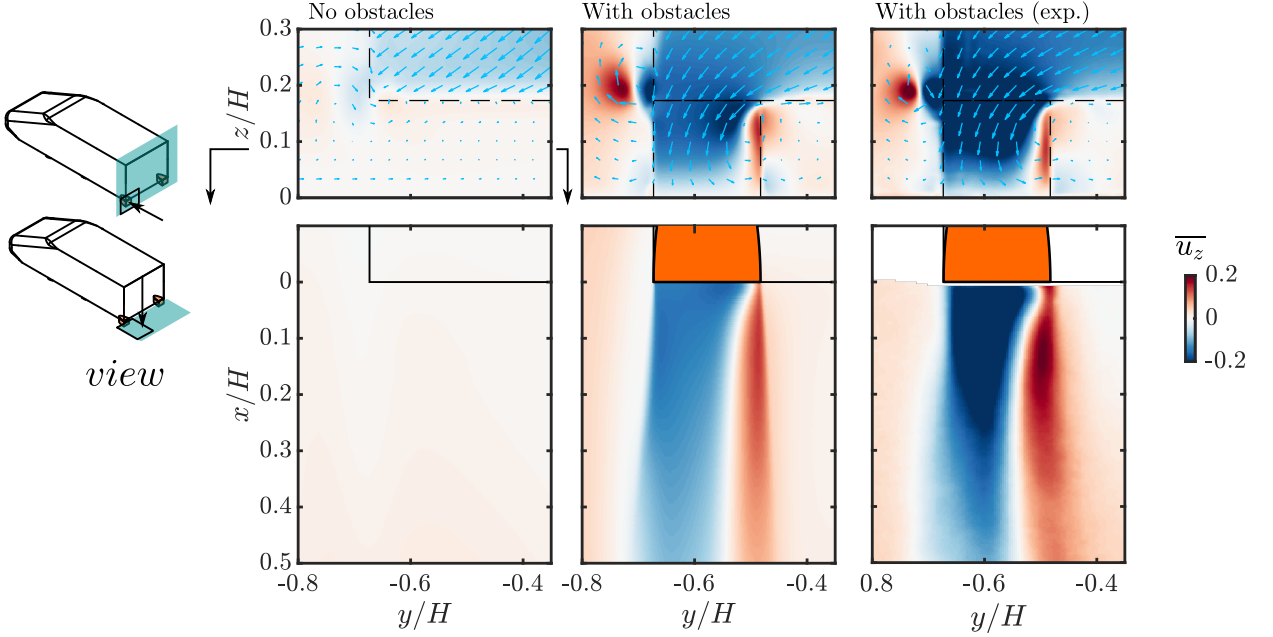


Figure A.5: Comparison of the mean vertical velocity  $\overline{u}_z$  in a cross-flow plane at  $x/H = 0.03$  (top) and in the half-ground-clearance plane  $z/H = 0.09$  (bottom) between numerical and experimental results for the cases without and with obstacles (obstacles are flush-mounted to the base with  $l/d = 0$ ).

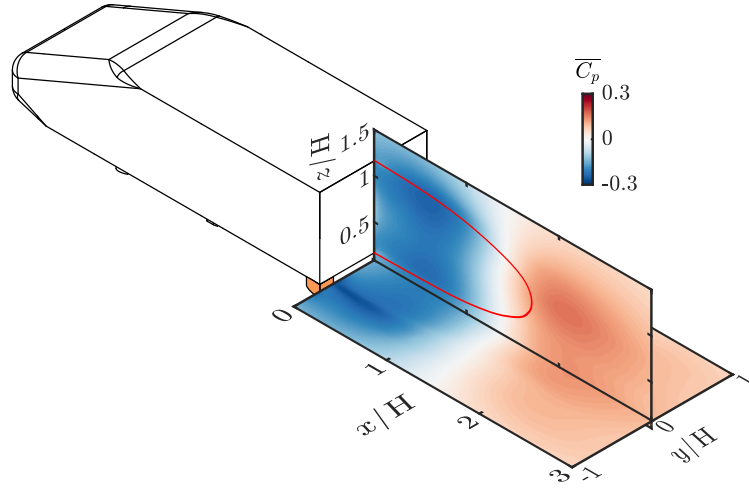


Figure A.6: Mean pressure distributions in the symmetry plane of the model ( $y/H = 0$ ) and in the half-ground-clearance plane ( $z/H = 0.09$ ) for the case with the obstacles. The red line in the symmetry plane is the mean separatrix.

### A.3.1 Global pressure distributions

In figure A.6, the mean pressure distributions in the symmetry plane of the model ( $y/H = 0$ ) and in the half-ground-clearance plane ( $z/H = 0.09$ ) are shown. Downstream of the base of the main body, a strong pressure increase is observed between  $x/H = 1$  and 2 near the end of the recirculation region. The low-pressure region inside the main body wake influences greatly the pressure distribution in the region under the main body wake. This means that the main body wake sets the background pressure level in the region where the wakes of the obstacles are located. The development of the obstacle wakes further reduces the local pressure level as can be noticed in the horizontal plane behind the obstacles.

The above investigation is important when considering different vehicle shapes. For example, when the vertical asymmetry of the wake is varied, the background pressure level around the obstacle wakes should be modified. If the wakes of the obstacles remain the same in this situation, the pressure inside them should be changed by the same level as the background pressure. In a

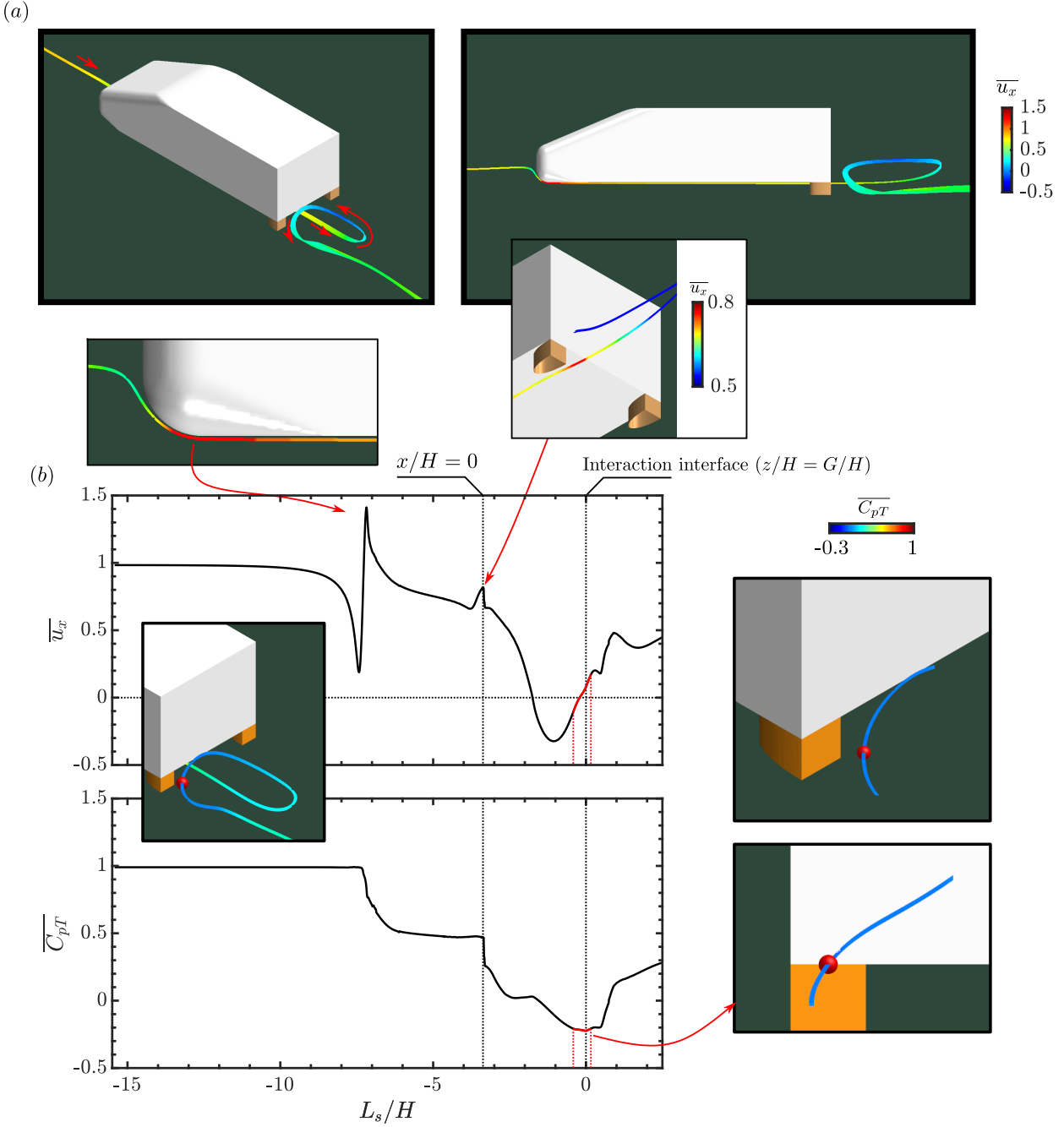


Figure A.7: For the case with obstacles: (a) Mean streamlines colored by mean streamwise velocity  $\bar{u}_x$  seeded from the interaction interface at  $z/H = G/H$ . (b) Evolution of mean streamwise velocity  $\bar{u}_x$  and total pressure  $\overline{C_{pT}}$  along one streamline from (a).  $L_s$  is the length of the streamline from the source seed (denoted by the red point in the streamline pictures). A region near the interaction interface with a conserved  $\overline{C_{pT}}$  is colored in red.

more complex situation when the back shape of the body is modified from the square-back to a fast-back, the same suggestion is again expected to hold.

### A.3.2 Origin of the mean mass exchange

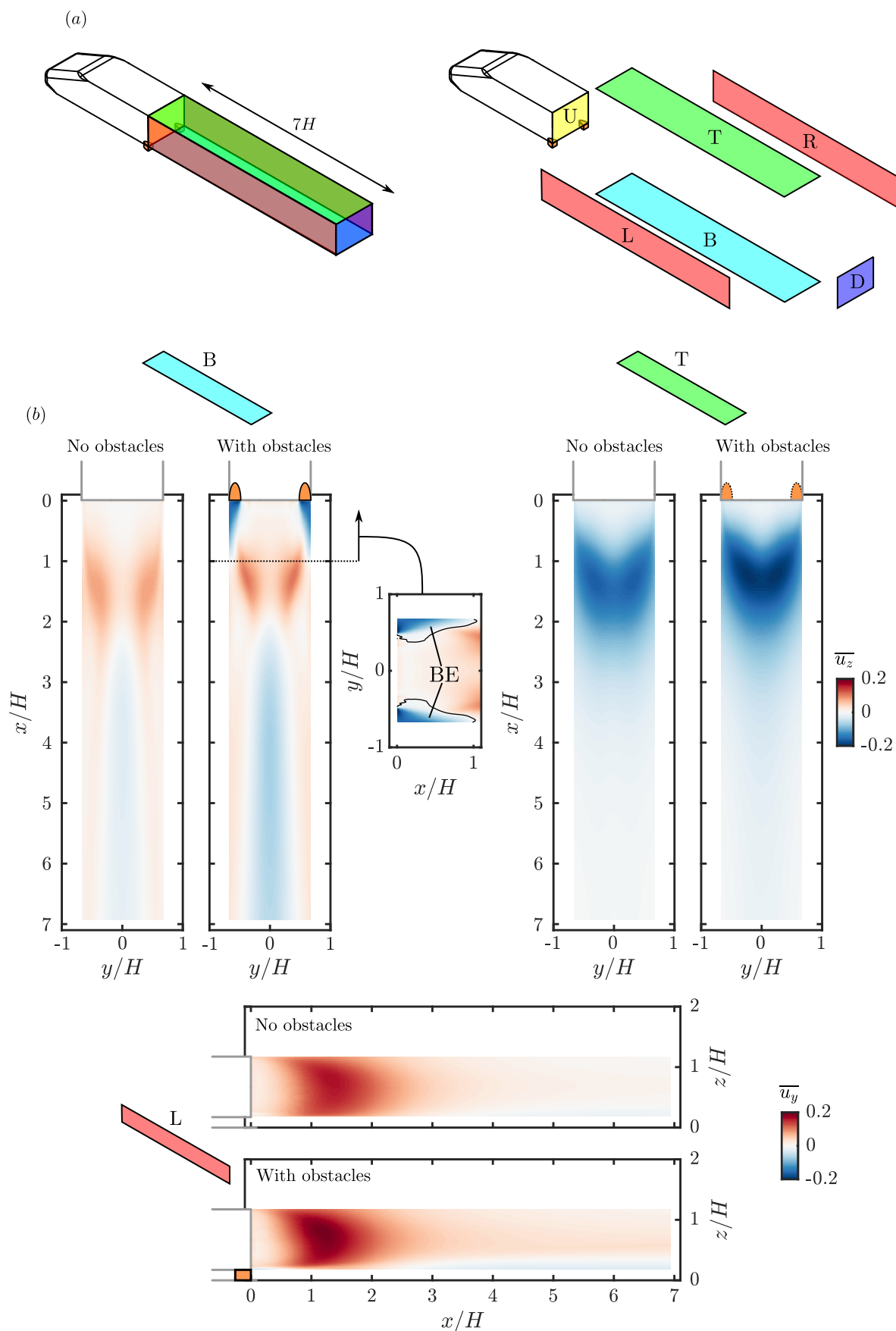
In figure A.7(a), a group of streamlines is issued from the interaction interface ( $z/H = G/H$ ) to both forward and backward directions. The mean streamwise velocity  $\bar{u}_x$  is used to color the streamlines. It is noticed that the mass flux exiting the model wake originally comes from the potential flow region in front of the model. It passes the model first and then enters the recirculation region of the model. Finally, it exits the recirculation region through the mass

exchange. A quantitative representation is provided in figure A.7(b) by focusing on one of the streamlines from figure A.7(a). At any location of the streamline, the value of  $L_s$  represents the length of the streamline from the location to the source seed at the interaction interface (marked by the red point in the inserted pictures of figure A.7b). The sign of  $L_s$  denotes the integration direction of the streamline, with a negative (positive) sign representing the forward (backward) direction. At  $L_s/H = -15$ , the mass flux is located near the inlet of the computational domain, it has a streamwise momentum of  $\overline{u_x} \approx 1$ . Moving downstream with increasing  $L_s/H$ , the flux reaches the nose of the model at  $L_s/H \approx 8$ . We notice a gradual drop of  $\overline{u_x}$ . This is followed by a sharp drop of pressure induced by the curvature effect at the bottom side of the nose (not shown here for brevity) and an increase of  $\overline{u_x}$ . With increasing  $L_s/H$ ,  $\overline{u_x}$  gradually decreases until the trailing edge of the model ( $x/H = 0$ ), where a local flow acceleration is noticed. Behind the trailing edge, the mass flux is entrained by the model wake and the streamwise momentum  $\overline{u_x}$  is decreased. When  $\overline{u_x} = 0$ , the streamline enters the recirculation region and then crosses the mass exchange surface at  $L_s/H = 0$ . It finally goes into the wake of the left-hand side obstacle.

Moreover, the total pressure coefficient  $\overline{C_{pT}}$  along the streamline is plotted in figure A.7(b). Near the nose of the body at  $L_s/H \approx 8$ , we notice a gradual decrease of  $\overline{C_{pT}}$ , indicating that the mass flux enters the bottom boundary layer of the model. With increasing  $L_s/H$ , at the trailing edge of the model ( $x/H = 0$ ), a gradual decrease of  $\overline{C_{pT}}$  is noticed when the mass flux enters the recirculation region. However, inside the recirculation region near the interaction interface at  $z/H = G/H$ ,  $\overline{C_{pT}}$  is relatively conserved. For a part of the streamline shown at the right-hand of figure A.7(b),  $\overline{C_{pT}}$  is maximally varied by  $\sim 7\%$ . Accordingly, along this part of the streamline,  $\overline{C_{pT}} = \overline{C_p} + \overline{u^2}$  ( $\overline{u}$  is the normalized velocity modulus) is approximately constant. This means that locally the mass exchange is mainly driven by the pressure difference between the obstacle wakes and the recirculation region of the body. When a different wake is perturbed using the same obstacles, the global variation in the pressure field as depicted before in figure A.6 suggests that the pressure difference remains the same. Therefore, the level of mass exchange and the related drag change are expected to be independent on vehicle shape.

### A.3.3 Effect of mean mass exchange on base pressure

We have shown that the mass flux exiting the model wake through the mean mass transfer initially comes from the free stream. It enters the recirculation region and loses its streamwise momentum. Therefore, the mean mass transfer caused by the presence of the obstacles induces a mean momentum exchange between the model wake and the surrounding flow. This momentum exchange can be linked to the base drag increase by writing a streamwise momentum balance. To this aim, a control volume is defined in figure A.8(a). The volume has a rectangular cuboid shape and a length of  $7H$ . The length of the volume can be chosen arbitrarily, but here the decision is made so that the base pressure is the main contributor to the surface force acting on the control volume. The upstream surface U of the volume is the base surface. The top, bottom, left-hand side, right-hand side, and downstream surfaces are denoted by T, B, L, R, and D, respectively. The sum of all the surfaces is denoted by S. In figure A.8(b), the mass flux crossing the surfaces of the control volume is shown by the velocity component perpendicular to the corresponding surface. At the bottom surface, the mean mass transfer is noted by the negative  $\overline{u_z}$  behind the obstacles until  $x/H = 1$ . At the surfaces T and L (R), we notice that the obstacles increase the mass flux entering the control volume. For each surface, the mean mass flow rate  $\mathcal{M} = \int_S \rho \overline{\mathbf{U}} \cdot d\mathbf{S} / (\rho U_0 HW)$  exiting/entering the control volume is shown in figure A.9(a). It is noted here that a positive  $\mathcal{M}$  means an outflow. The mass exchange at each surface corresponds to a momentum exchange between the control volume and the surrounding flow. This momentum exchange is linked to the base pressure as shown by the streamwise momentum balance:



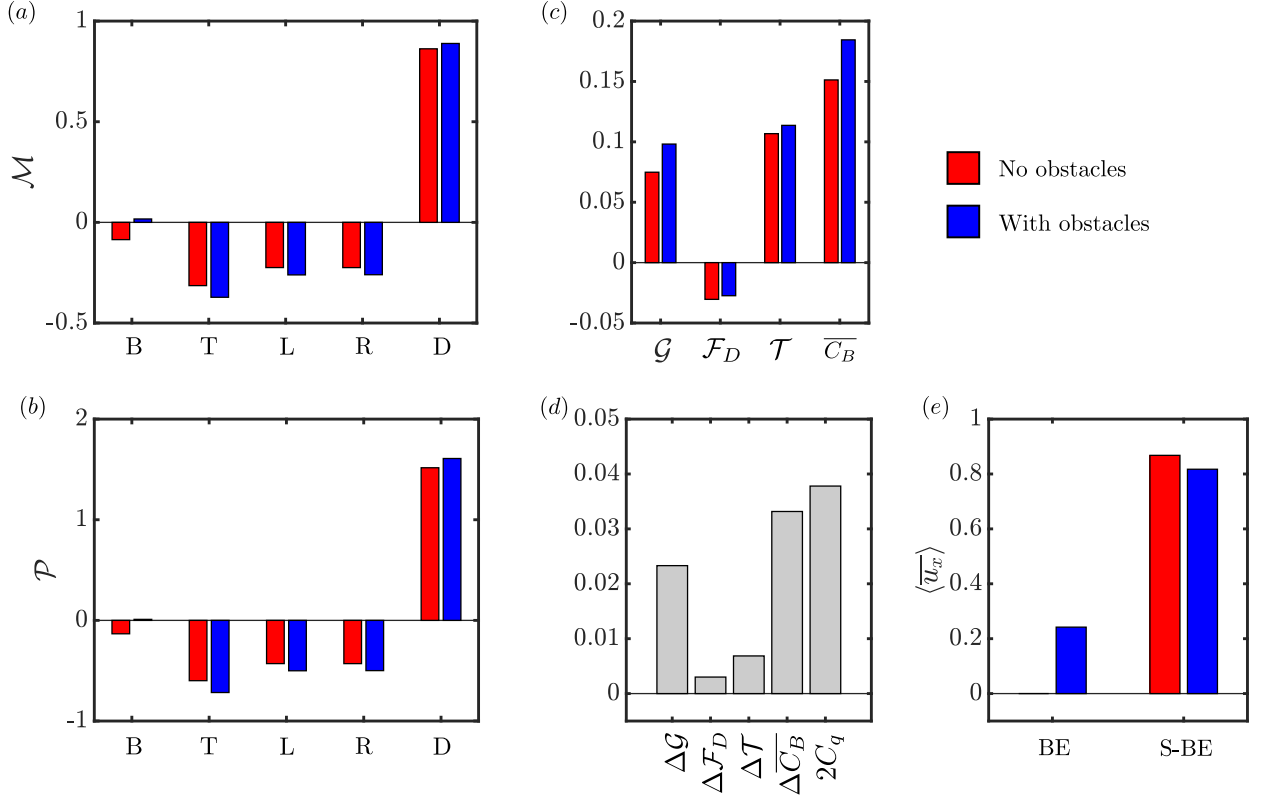


Figure A.9: Time-averaged description of the mass and momentum balance of the control volume defined in figure A.8(a) for the cases without and with obstacles. (a) Mass flow rate  $\mathcal{M}$  and (b) streamwise momentum flow rate  $\mathcal{P}$  at the surfaces of the control volume. (c) Contributions to the base drag  $\overline{C}_B$  of the mean momentum exchange  $\mathcal{G}$ , the downstream pressure modification  $\mathcal{F}_D$ , and the turbulence  $\mathcal{T}$  calculated using equation A.2. (d) The differences of the components in (c) between the cases with and without the obstacles.  $C_q$  is the mass flow rate of the mean mass transfer from the vehicle wake to the obstacle wakes. (e) Space-averaged streamwise velocity  $\langle \overline{u}_x \rangle$  at the surfaces of the control volume.

$$\begin{aligned}
0.5\rho U_0^2 HW \overline{C}_B &= - \int_S \rho \overline{U}_x (\overline{\mathbf{U}} \cdot d\mathbf{S}) \\
&\quad - \int_D \overline{P} d\mathbf{S} \cdot \mathbf{x} \\
&\quad - \int_D \rho \overline{U'_x U'_x} d\mathbf{S} \cdot \mathbf{x} - \int_{L+R} \rho \overline{U'_x U'_y} d\mathbf{S} \cdot \mathbf{y} - \int_{T+B} \rho \overline{U'_x U'_z} d\mathbf{S} \cdot \mathbf{z}.
\end{aligned} \tag{A.2}$$

After all the terms are normalized by  $0.5\rho U_0^2 HW$ , the three parts at the right-hand side of this equation are denoted by  $\mathcal{G}$ ,  $\mathcal{F}_D$ , and  $\mathcal{T}$ , respectively. They represent the contributions to the base drag of the mean momentum exchange, the downstream pressure modification, and the turbulence. The contribution to  $-\mathcal{G}$  from each surface  $\mathcal{P} = \int \rho \overline{U}_x (\overline{\mathbf{U}} \cdot d\mathbf{S}) / (\rho U_0 HW)$  is calculated in figure A.9(b).

Furthermore, the contributions to the base drag  $\overline{C}_B$  from the mean momentum exchange  $\mathcal{G}$  and downstream pressure modification  $\mathcal{F}_D$  are shown in figure A.9(c). Note that the turbulence term  $\mathcal{T}$  is obtained directly to satisfy the momentum balance. We notice that for the case with or without the obstacles, the contributions of the mean momentum exchange  $\mathcal{G}$  and turbulence  $\mathcal{T}$  to the base drag  $\overline{C}_B$  are dominant because the surface D is quite far from the base. When considering the changes in the terms shown in figure A.9(c) by the obstacles, we observe in figure A.9(d) that the change in the momentum exchange  $\Delta\mathcal{G}$  is the dominant part of  $\Delta\overline{C}_B$  ( $\sim 70\%$ ). This indicates that the enhancement in the momentum exchange between the volume and the surrounding flow is the main contributor to the base drag increase.

Since  $\Delta\mathcal{G}$  is the major contributor to  $\Delta\overline{C}_B$ , the momentum balance can be written, in a first-

order approximation, as:

$$0.5\rho U_0^2 HW \Delta \overline{C_B} \approx -\Delta \int_S \rho \overline{U_x} (\mathbf{U} \cdot d\mathbf{S}). \quad (\text{A.3})$$

We then divide the surface of the control volume into two parts, the mass transfer surface BE behind the obstacles with  $\overline{u_z} < 0$  and the rest S-BE (see figure A.8b). This equation is further written as:

$$0.5\rho U_0^2 HW \Delta \overline{C_B} \approx -\int_{BE} \rho \overline{U_z} dS \overline{U_x} - \Delta \int_{S-BE} \rho \overline{U_x} (\mathbf{U} \cdot d\mathbf{S}). \quad (\text{A.4})$$

We consider the mass conservation for the control volume, where  $\Delta \int_{S-BE} \rho (\mathbf{U} \cdot d\mathbf{S}) = \int_{BE} \rho \overline{U_z} dS$ . On the surface  $S - BE$ ,  $\overline{U_x}$  is approximately the same order of magnitude as the free-stream velocity  $U_0$  as shown in figure A.9(c) by the space-averaged streamwise velocity  $\langle \overline{u_x} \rangle$  on surface S-BE. The equation is therefore transformed into:

$$0.5\rho U_0^2 HW \Delta \overline{C_B} \approx -\int_{BE} \rho \overline{U_z} dS (\overline{U_x} + U_0). \quad (\text{A.5})$$

On  $BE$  the velocity distribution is mainly vertical, thus  $\overline{U_x} \ll U_0$ . Normalizing each term by  $0.5\rho U_0^2 HW$ , we finally find:

$$\Delta \overline{C_B} \approx 2 \frac{-\int_{BE} \overline{u_z} dS}{HW U_0} = 2C_q. \quad (\text{A.6})$$

By comparing the terms  $2C_q$  and  $\Delta \overline{C_B}$ , it is shown in figure A.9(d) that the simplification of the momentum balance gives a satisfactory result. In chapter 4, this relation of  $\Delta \overline{C_B} = 2C_q$  was found to govern the base suction experiments in Bearman (1967) for a 2-D D-shaped bluff body and in Hsu *et al.* (2021) for a 3-D Ahmed body. The momentum exchange model based on this relation was also found to be in accordance with the experimental results in chapter 4 for the obstacle situation, and in chapter 5, 6 for the wheel situation. Therefore, the momentum exchange model proposed in chapter 4 is validated and its physical insight is revealed using the numerical simulations.

# References

- AHMED, D & MORGAN, A.S. 2022 The effect of boundary layer dynamics on wake bi-modality for a squareback ahmed body. In *14th European Fluid Mechanics Conference*.
- AHMED, S.R., RAMM, G. & FALTIN, G. 1984 Some salient features of the time-averaged ground vehicle wake. *Tech. Rep.* 840300. Society of Automotive Engineers, Inc.
- ALJURE, D. E., LEHMKUHL, O., RODRÍGUEZ, I. & OLIVA, A. 2014 Flow and turbulent structures around simplified car models. *Comput. Fluids* **96**, 122–135.
- AULTMAN, M., AUZA-GUTIERREZ, R., DISOTELL, K. & DUAN, L. 2022 Effects of wheel rotation on long-period wake dynamics of the driver fastback model. *Fluids* **7** (1), 19.
- BALACHANDAR, S., MITTAL, R. & NAJJAR, F.M. 1997 Properties of the mean recirculation region in the wakes of two-dimensional bluff bodies. *J. Fluid Mech.* **351**, 167–199.
- BAO, D., BORÉE, J., HAFFNER, Y. & SICOT, C. 2022 Near wake interactions and drag increase regimes for a square-back bluff body. *J. Fluid Mech.* **936**, A2.
- BAO, D., BORÉE, J., SICOT, C. & ROEBROECK, C. 2023 Salient features of wheel-vehicle interactions: consequences on drag. *J. Wind Eng. Ind. Aerodyn.* **236**, 105366.
- BARROS, D. 2015 Wake and drag manipulation of a bluff body using fluidic forcing. PhD thesis, Chasseneuil-du-Poitou, Ecole Nationale Supérieure de Mécanique et d’Aérotechnique.
- BARROS, D., BORÉE, J., CADOT, O., SPOHN, A. & NOACK, B.R. 2017 Forcing symmetry exchanges and flow reversals in turbulent wakes. *J. Fluid Mech.* **829**, R1.
- BARROS, D., BORÉE, J., NOACK, B.R., SPOHN, A. & RUIZ, T. 2016a Bluff body drag manipulation using pulsed jets and coanda effect. *J. Fluid Mech.* **805**, 422–459.
- BARROS, D., BORÉE, J., NOACK, B. R. & SPOHN, A. 2016b Resonances in the forced turbulent wake past a 3d blunt body. *Phys. Fluids* **28** (6), 065104.
- BATCHELOR, G.K. 1956 A proposal concerning laminar wakes behind bluff bodies at large reynolds number. *J. Fluid Mech.* **1** (4), 388–398.
- BEARMAN, P.W. 1965 Investigation of the flow behind a two-dimensional model with a blunt trailing edge and fitted with splitter plates. *J. Fluid Mech.* **21** (2), 241–255.
- BEARMAN, P.W. 1967 The effect of base bleed on the flow behind a two-dimensional model with a blunt trailing edge. *Aeronaut. Q.* **18** (3), 207–224.
- BEARMAN, P.W. & HARVEY, J.K. 1976 Golf ball aerodynamics. *Aeronaut. Q.* **27** (2), 112–122.
- BERGER, E., SCHOLZ, D. & SCHUMM, M. 1990 Coherent vortex structures in the wake of a sphere and a circular disk at rest and under forced vibrations. *J. Fluids Struct.* **4** (3), 231–257.
- BONNAVION, G. 2018 Dynamics of the unstable wake modes in automotive aerodynamics: from simplified models to real vehicles. PhD thesis, Université Paris Saclay (COMUE).

- BONNAVION, G., BORÉE, J. & HERBERT, V. 2022 On the use of kinetic energy balance for the volumetric identification of drag sources of a blunt body. application to road vehicles. *Int. J. Heat Fluid Flow* **96**, 108977.
- BONNAVION, G. & CADOT, O. 2018 Unstable wake dynamics of rectangular flat-backed bluff bodies with inclination and ground proximity. *J. Fluid Mech.* **854**, 196–232.
- BONNAVION, G. & CADOT, O. 2019 Boat-tail effects on the global wake dynamics of a flat-backed body with rectangular section. *J. Fluids Struct.* **89**, 61–71.
- BRACKSTON, R. D., DE LA CRUZ, J.M. G., WYNN, A., RIGAS, G. & MORRISON, J.F. 2016 Stochastic modelling and feedback control of bistability in a turbulent bluff body wake. *J. Fluid Mech.* **802**, 726–749.
- BRADSHAW, P. 1973 Effects of streamline curvature on turbulent flow. *Tech. Rep.*. Advisory Group for Aerospace Research and Development Paris (France).
- BRANDT, A., BERG, H., BOLZON, M. & JOSEFSSON, L. 2019 The effects of wheel design on the aerodynamic drag of passenger vehicles. *Tech. Rep.* 2019-01-0662. Society of Automotive Engineers, Inc.
- BRILLOUIN, M. 1911 Les surfaces de glissement de helmholtz et la resistance des fluides. *Ann. Chim. Phys* **23**, 145–230.
- BURTON, D., WANG, S., SMITH, D. T., SCOTT, H.N., CROUCH, .TN. & THOMPSON, M.C. 2021 The influence of background turbulence on ahmed-body wake bistability. *J. Fluid Mech.* **926**.
- CADOT, O., ALMARZOOQI, M., LEGEAI, A., PAREZANOVIĆ, V. & PASTUR, L. 2020 On three-dimensional bluff body wake symmetry breaking with free-stream turbulence and residual asymmetry. *C. R.. Méc.* **348** (6-7), 509–517.
- CADOT, O., EVRARD, A. & PASTUR, L. 2015 Imperfect supercritical bifurcation in a three-dimensional turbulent wake. *Phys. Rev. E* **91** (6), 063005.
- CASTELAIN, T., MICHARD, M., SZMIGIEL, M., CHACATON, D. & JUVÉ, D. 2018 Identification of flow classes in the wake of a simplified truck model depending on the underbody velocity. *J. Wind Eng. Ind. Aerodyn.* **175**, 352–363.
- COGOTTI, A. 1983 Aerodynamic characteristics of car wheel. *Int. J. of Vehicle Design* **SP3**.
- CRONER, E., BÉZARD, H., SICOT, C. & MOTHAY, G. 2013 Aerodynamic characterization of the wake of an isolated rolling wheel. *Int. J. Heat Fluid Flow* **43**, 233–243.
- DE LA CRUZ, J. M. G., BRACKSTON, R. D. & MORRISON, J. F. 2017a Adaptive base-flaps under variable cross-wind. *Tech. Rep.*. SAE Technical Paper.
- DE LA CRUZ, J. M. G., OXLADE, A. R. & MORRISON, J. F. 2017b Passive control of base pressure on an axisymmetric blunt body using a perimetric slit. *Phy. Rev. Fluids* **2** (4), 043905.
- DALLA LONGA, L., EVSTAFYEVA, O. & MORGANS, A.S. 2019 Simulations of the bi-modal wake past three-dimensional blunt bluff bodies. *J. Fluid Mech.* **866**, 791–809.
- DARABASZ, T., BONNAVION, G., CADOT, O., GORAGUER, Y. & BORÉE, J. 2023 Drag reduction using longitudinal vortices on a flat-back ahmed body. *Exp. Fluids* **64** (1), 20.
- DAVIS, S. C. & BOUNDY, R. G. 2021 Transportation energy data book: Edition 39. *Tech. Rep.*. Oak Ridge National Lab.(ORNL), Oak Ridge, TN (United States).
- D’HOOGE, A., REBBECK, L., PALIN, R., MURPHY, Q., GARGOLOFF, J. & DUNCAN, B. 2015 Application of real-world wind conditions for assessing aerodynamic drag for on-road range prediction. *Tech. Rep.* 2015-01-1551. Society of Automotive Engineers, Inc.

- DUELL, E. G. & GEORGE, A.R. 1999 Experimental study of a ground vehicle body unsteady near wake. *SAE transactions* pp. 1589–1602.
- EASANESAN, G., BURTON, D. & THOMPSON, M. C. 2020 The effects of nose-shape and upstream flow separation on the wake of a cylindrical square-backed body. *Exp. Therm. Fluid Sci.* **118**, 110142.
- ELOFSSON, P. & BANNISTER, M. 2002 Drag reduction mechanisms due to moving ground and wheel rotation in passenger cars. *Tech. Rep.* 2002-01-0531. Society of Automotive Engineers, Inc.
- EVRRARD, A., CADOT, O., HERBERT, V., RICOT, D., VIGNERON, R. & DÉLERY, J. 2016 Fluid force and symmetry breaking modes of a 3d bluff body with a base cavity. *J. Fluids Structures* **61**, 99–114.
- EVSTAFYEVA, O., MORGANS, A.S. & DALLA LONGA, L. 2017 Simulation and feedback control of the ahmed body flow exhibiting symmetry breaking behaviour. *J. Fluid Mech.* **817**, R2.
- FAN, Y. & CADOT, O. 2023 Reynolds number effect on the bistable dynamic of a blunt-base bluff body. *Phys. Rev. E* **107** (2), 025103.
- FAN, Y., PAREZANOVIĆ, V. & CADOT, O. 2022 Wake transitions and steady-instability of an ahmed body in varying flow conditions. *J. Fluid Mech.* **942**.
- FAN, Y., XIA, C., CHU, S., YANG, Z. & CADOT, O. 2020 Experimental and numerical analysis of the bi-stable turbulent wake of a rectangular flat-backed bluff body. *Phys. Fluids* **32** (10), 105111.
- FAVRE, T. & EFRAIMSSON, G. 2011 An assessment of detached-eddy simulations of unsteady crosswind aerodynamics of road vehicles. *Flow Turbul. Combust.* **87** (1), 133–163.
- GERRARD, J.H. 1966 The mechanics of the formation region of vortices behind bluff bodies. *J. Fluid Mech.* **25** (2), 401–413.
- GRANDEMANGE, M. 2013 Analysis and control of three-dimensional turbulent wakes: from axisymmetric bodies to road vehicles. PhD thesis, Palaiseau, Ecole polytechnique.
- GRANDEMANGE, M., CADOT, O. & GOHLKE, M. 2012 Reflectional symmetry breaking of the separated flow over three-dimensional bluff bodies. *Phys. Rev. E* **86** (3), 035302.
- GRANDEMANGE, M., GOHLKE, M. & CADOT, O. 2013a Bi-stability in the turbulent wake past parallelepiped bodies with various aspect ratios and wall effects. *Phys. Fluids* **25** (9), 095103.
- GRANDEMANGE, M., GOHLKE, M. & CADOT, O. 2013b Turbulent wake past a three-dimensional blunt body. part 1. global modes and bi-stability. *J. Fluid Mech.* **722**, 51.
- GRANDEMANGE, M., GOHLKE, M. & CADOT, O. 2014 Turbulent wake past a three-dimensional blunt body. part 2. experimental sensitivity analysis. *J. Fluid Mech.* **752**, 439–461.
- GRANDEMANGE, M., MARY, A., GOHLKE, M. & CADOT, O. 2013c Effect on drag of the flow orientation at the base separation of a simplified blunt road vehicle. *Exp. Fluids* **54**, 1–10.
- HAFFNER, Y. 2020 Manipulation of three-dimensional turbulent wakes for aerodynamic drag reduction. PhD thesis, Chasseneuil-du-Poitou, Ecole Nationale Supérieure de Mécanique et d’Aérotechnique.
- HAFFNER, Y., BORÉE, J., SPOHN, A. & CASTELAIN, T. 2020a Mechanics of bluff body drag reduction during transient near-wake reversals. *J. Fluid Mech.* **894**, A14.
- HAFFNER, Y., BORÉE, J., SPOHN, A. & CASTELAIN, T. 2020b Unsteady coanda effect and drag reduction for a turbulent wake. *J. Fluid Mech.* **899**, A36.

- HAFFNER, Y., CASTELAIN, T., BORÉE, J. & SPOHN, A. 2021 Manipulation of three-dimensional asymmetries of a turbulent wake for drag reduction. *J. Fluid Mech.* **912**, A6.
- HAFFNER, Y., LI, R., MELDI, M. & BORÉE, J. 2022 Drag reduction of a square-back bluff body under constant cross-wind conditions using asymmetric shear layer forcing. *Int. J. Heat Fluid Flow* **96**, 109003.
- HEARST, R. J., GOMIT, G. & GANAPATHISUBRAMANI, B. 2016 Effect of turbulence on the wake of a wall-mounted cube. *J. Fluid Mech.* **804**, 513–530.
- HEFT, A. I., INDINGER, T. & ADAMS, N. A. 2012 Introduction of a new realistic generic car model for aerodynamic investigations. *Tech. Rep.* 2012-01-0168. Society of Automotive Engineers, Inc.
- HOBEIKA, T. & SEBBEN, S. 2018 Tyre pattern features and their effects on passenger vehicle drag. *Tech. Rep.* 2018-01-0710. Society of Automotive Engineers, Inc.
- HOBEIKA, T., SEBBEN, S. & LANDSTROM, C. 2013 Investigation of the influence of tyre geometry on the aerodynamics of passenger cars. *Tech. Rep.* 2013-01-0955. Society of Automotive Engineers, Inc.
- HOOFTMAN, N., MESSAGIE, M., VAN MIERLO, J. & COOSEMANS, T. 2018 A review of the european passenger car regulations—real driving emissions vs local air quality. *Renew. Sust. Energ. Rev.* **86**, 1–21.
- HOWELL, J. 2013 The influence of ground simulation on the aerodynamics of simple car shapes with an underfloor diffuser. *Tech. Rep.* 1994-11-0103. Society of Automotive Engineers, Inc.
- HOWELL, J. & LE GOOD, G. 2005 Vortex drag for a simple bluff body at incidence in ground proximity. *Tech. Rep.* 2005-01-0869. Society of Automotive Engineers, Inc.
- HSU, E.C., PASTUR, L., CADOT, O. & PAREZANOVIĆ, V. 2021 A fundamental link between steady asymmetry and separation length in the wake of a 3-d square-back body. *Exp. Fluids* **62** (5).
- HUERRE, P. & MONKEWITZ, P. A. 1990 Local and global instabilities in spatially developing flows. *Annu. Rev. Fluid Mech.* **22** (1), 473–537.
- HUMINIC, A. & HUMINIC, G. 2017 Aerodynamic study of a generic car model with wheels and underbody diffuser. *Int. J. Automot. Technol.* **18** (3), 397–404.
- JIMÉNEZ-GONZÁLEZ, J.I., SEVILLA, A., SANMIGUEL-ROJAS, E. & MARTÍNEZ-BAZÁN, C. 2014 Global stability analysis of the axisymmetric wake past a spinning bullet-shaped body. *J. Fluid Mech.* **748**, 302–327.
- JOSEFSSON, E., HOBEIKA, T., SEBBEN, S. & URQUHART, M. 2022 Investigation of tyre pattern effect on the aerodynamics of a passenger vehicle. *J. Fluids Eng.* **144** (11), 111209.
- KANG, N., ESSEL, E. E., ROUSSINOVA, V. & BALACHANDAR, R. 2021 Effects of approach flow conditions on the unsteady three-dimensional wake structure of a square-back ahmed body. *Phys. Rev. Fluids* **6** (3), 034613.
- KENDALL, A. & KOCHESFAHANI, M. 2008 A method for estimating wall friction in turbulent wall-bounded flows. *Exp Fluids* **44** (5), 773–780.
- KHALIGHI, B., ZHANG, S., KOROMILAS, C., BALKANYI, S.R., BERNAL, L. P., IACCARINO, G. & MOIN, P. 2001 Experimental and computational study of unsteady wake flow behind a bluff body with a drag reduction device. *SAE transactions* pp. 1209–1222.
- KHAN, T. I., PAREZANOVIĆ, V., PASTUR, L. & CADOT, O. 2022 Suppression of the wake steady asymmetry of an ahmed body by central base bleed. *Phys. Rev. Fluids* **7** (8), 083902.

- KIRCHHOFF, G. 1869 Zur theorie freier flüssigkeitsstrahlen. *Journal für die reine und angewandte Mathematik* **70**, 289–298.
- KLOTZ, L., GOUJON-DURAND, S., ROKICKI, J. & WESFREID, J.E. 2014 Experimental investigation of flow behind a cube for moderate reynolds numbers. *J. Fluid Mech.* **750**, 73–98.
- KONSTANTINIDIS, E., BALABANI, S. & YIANNESKIS, M. 2005 Conditional averaging of piv plane wake data using a cross-correlation approach. *Exp. Fluids* **39** (1), 38–47.
- KRAJNOVIC, S. & DAVIDSON, L. 2003 Numerical study of the flow around a bus-shaped body. *J. Fluids Eng.* **125** (3), 500–509.
- KRAJNOVIĆ, S. & DAVIDSON, L. 2005 Influence of floor motions in wind tunnels on the aerodynamics of road vehicles. *J. Wind Eng. Ind. Aerodyn.* **93** (9), 677–696.
- KRAJNOVIĆ, S., SARMAST, S. & BASARA, B. 2011 Numerical investigation of the flow around a simplified wheel in a wheelhouse. *J. Fluids Eng.* **133** (11).
- LAHAYE, A., LEROY, A. & KOURTA, A. 2014 Aerodynamic characterisation of a square back bluff body flow. *Int. J. Aerod.* **4** (1-2), 43–60.
- LANDSTRÖM, C., LÖFDAHL, L. & WALKER, T. 2009 Detailed flow studies in close proximity of rotating wheels on a passenger car. *Tech. Rep.* 2009-01-0778. Society of Automotive Engineers, Inc.
- LANDSTRÖM, C., WALKER, T., CHRISTOFFERSEN, L. & LÖFDAHL, L. 2011 Influences of different front and rear wheel designs on aerodynamic drag of a sedan type passenger car. *Tech. Rep.* 2011-01-0165. Society of Automotive Engineers, Inc.
- LE GOOD, G.M., HOWELL, J.P., PASSMORE, M.A. & COGOTTI, A. 1998 A comparison of on-road aerodynamic drag measurements with wind tunnel data from pininfarina and mira. *Tech. Rep.* 980394. Society of Automotive Engineers, Inc.
- LE GOOD, G. M. & GARRY, K. P. 2004 On the use of reference models in automotive aerodynamics. *Tech. Rep.* 2004-01-1308. Society of Automotive Engineers, Inc.
- LEGEAI, A. & CADOT, O. 2020 On the recirculating flow of three-dimensional asymmetric bluff bodies. *Exp. Fluids* **61** (12), 1–6.
- LI, R. 2017 Aerodynamic drag reduction of a square-back car model using linear genetic programming and physic-based control. PhD thesis, Chasseneuil-du-Poitou, Ecole Nationale Supérieure de Mécanique et d’Aérotechnique.
- LI, R., BARROS, D., BORÉE, J., CADOT, O., NOACK, B.R. & CORDIER, L. 2016 Feedback control of bimodal wake dynamics. *Exp. Fluids* **57** (10), 158.
- LI, R., BORÉE, J., NOACK, B.R., CORDIER, L. & HARAMBAT, F. 2019 Drag reduction mechanisms of a car model at moderate yaw by bi-frequency forcing. *Phys. Rev. Fluids* **4** (3), 034604.
- LIU, K., ZHANG, B.F., ZHANG, Y.C. & ZHOU, Y. 2021 Flow structure around a low-drag ahmed body. *J. Fluid Mech.* **913**, A21.
- LO, K. H. & KONTIS, K. 2017 Flow around an articulated lorry model. *Exp. Therm. Fluid Sci.* **82**, 58–74.
- LORITE-DÍEZ, M., JIMÉNEZ-GONZÁLEZ, J.I., GUTIÉRREZ-MONTES, C. & MARTÍNEZ-BAZÁN, C. 2017 Drag reduction of slender blunt-based bodies using optimized rear cavities. *J. Fluids Struct.* **74**, 158–177.
- LORITE-DÍEZ, M., JIMÉNEZ-GONZÁLEZ, J.I., PASTUR, L., CADOT, O. & MARTÍNEZ-BAZÁN, C. 2020a Drag reduction of three-dimensional bodies by base blowing with various gas densities. *Phys. Rev. E* . **102** (1), 011101.

- LORITE-DÍEZ, M., JIMÉNEZ-GONZÁLEZ, J.I., PASTUR, L., MARTÍNEZ-BAZÁN, C. & CADOT, O. 2020*b* Experimental analysis of the effect of local base blowing on three-dimensional wake modes. *J. Fluid Mech.* **883**.
- LUCAS, J.-M., CADOT, O, HERBERT, V, PARPAIS, S & DÉLERY, J 2017 A numerical investigation of the asymmetric wake mode of a squareback ahmed body—effect of a base cavity. *J. Fluid Mech.* **831**, 675–697.
- LUMLEY, J. L. 1967 The structure of inhomogeneous turbulent flows. In *Atmospheric turbulence and radio wave propagation* (ed. A.M. Yaglom & V.I. Tatarski), pp. 166–178. Nauka.
- MARIOTTI, A., BURESTI, G. & SALVETTI, M. V. 2015 Connection between base drag, separating boundary layer characteristics and wake mean recirculation length of an axisymmetric blunt-based body. *J. Fluids Struct* **55**, 191–203.
- MERCKER, E., BREUER, N., BERNEBURG, H. & EMMELMANN, H.J. 1991 On the aerodynamic interference due to the rolling wheels of passenger cars. *Tech. Rep.* 910311. Society of Automotive Engineers, Inc.
- MERCKER, E., COOPER, K.R., FISCHER, O. & WIEDEMANN, J. 2005 The influence of a horizontal pressure distribution on aerodynamic drag in open and closed wind tunnels. *SAE transactions* pp. 921–938.
- MERCKER, E. & KNAPE, H.W. 1989 Ground simulation with moving belt and tangential blowing for full-scale automotive testing in a wind tunnel. *Tech. Rep.* 890367. Society of Automotive Engineers, Inc.
- MLINARIC, P. & SEBBEN, S. 2008 Investigation of the influence of tyre deflection and tyre contact patch on cfd predictions of aerodynamic forces on a passenger car. In *7th MIRA International Vehicle Aerodynamics Conference*.
- MORRIS, S. C. & FOSS, J. F. 2003 Turbulent boundary layer to single-stream shear layer: the transition region. *J. Fluid Mech.* **494**, 187–221.
- MUSKER, A.J. 1979 Explicit expression for the smooth wall velocity distribution in a turbulent boundary layer. *AIAA Journal* **17** (6), 655–657.
- ÖSTH, J., NOACK, B. R., KRAJNOVIĆ, S., BARROS, D. & BORÉE, J. 2014 On the need for a nonlinear subscale turbulence term in pod models as exemplified for a high-reynolds-number flow over an ahmed body. *J. Fluid Mech.* **747**, 518–544.
- OXLADE, A. 2013 High-frequency pulsed jet forcing of an axisymmetric bluff body wake. PhD thesis, Imperial College London.
- PAGE, G. J. & WALLE, A. 2022 Towards a standardized assessment of automotive aerodynamic cfd prediction capability-autocfd 2: Windsor body test case summary. *Tech. Rep.* 2022-01-0898. Society of Automotive Engineers, Inc.
- PARK, H., LEE, D., JEON, W., HAHN, S., KIM, J., KIM, J., CHOI, J. & CHOI, H. 2006 Drag reduction in flow over a two-dimensional bluff body with a blunt trailing edge using a new passive device. *J. Fluid Mech.* **563**, 389.
- PARKIN, D. J., THOMPSON, M. C. & SHERIDAN, J. 2014 Numerical analysis of bluff body wakes under periodic open-loop control. *J. Fluid Mech.* **739**, 94–123.
- PARKINSON, GV & JANDALI, T 1970 A wake source model for bluff body potential flow. *J. Fluid Mech.* **40** (3), 577–594.
- PATEL, D., GARMORY, A. & PASSMORE, M. 2022 On the wake of an isolated rotating wheel: An experimental and numerical investigation. *J. Wind Eng. Ind. Aerodyn.* **227**, 105049.

- PAVIA, G. 2019 Characterisation of the unsteady wake of a square-back road vehicle. PhD thesis, Loughborough University.
- PAVIA, G. & PASSMORE, M. 2017 Characterisation of wake bi-stability for a square-back geometry with rotating wheels. In *FKFS Conference*, pp. 93–109. Springer.
- PAVIA, G., PASSMORE, M. & SARDU, C. 2018 Evolution of the bi-stable wake of a square-back automotive shape. *Exp Fluids* **59** (1), 1–20.
- PAVIA, G., PASSMORE, M.A., VARNEY, M. & HODGSON, G. 2020 Salient three-dimensional features of the turbulent wake of a simplified square-back vehicle. *J. Fluid Mech.* **888**, A33.
- PERRY, A., PAVIA, G. & PASSMORE, M. 2016 Influence of short rear end tapers on the wake of a simplified square-back vehicle: wake topology and rear drag. *Exp. Fluids* **57**, 1–17.
- PERRY, A. K. & PASSMORE, M. 2013 The impact of underbody roughness on rear wake structure of a squareback vehicle. *Tech. Rep.* 2013-01-0463. Society of Automotive Engineers, Inc.
- PFEIFFER, J. & KING, R. 2018 Robust control of drag and lateral dynamic response for road vehicles exposed to cross-wind gusts. *Exp. Fluids* **59** (3), 45.
- PHILIP, J. & MARUSIC, I. 2012 Large-scale eddies and their role in entrainment in turbulent jets and wakes. *Phys. Fluids* **24** (5), 055108.
- PLUMEJEAU, B., DELPRAT, S., KEIRSBULCK, L., LIPPERT, M. & ABASSI, W. 2019 Ultra-local model-based control of the square-back ahmed body wake flow. *Phys. Fluids* **31** (8), 085103.
- PODVIN, B., PELLERIN, S., FRAIGNEAU, Y., BONNAVION, G. & CADOT, O. 2021 Low-order modelling of the wake dynamics of an ahmed body. *Journal of Fluid Mechanics* **927**, R6.
- VAN RAEMDONCK, G. M.R., VAN LEEUWEN, P. & VAN TOOREN, M. J.L. 2016 Comparison of experimental and numerically obtained flow properties of a bluff body. In *The Aerodynamics of Heavy Vehicles III: Trucks, Buses and Trains*, pp. 393–411. Springer.
- REGERT, T. & LAJOS, T. 2007 Description of flow field in the wheelhouses of cars. *Int. J. Heat Fluid Flow* **28** (4), 616–629.
- REJNIK, A. A. & GATTO, A. 2021 Influence of rotating wheels and moving ground use on the unsteady wake of a small-scale road vehicle. *Flow Turbul. Combust.* **106** (1), 109–137.
- ROSHKO, A. 1954 On the drag and shedding frequencies of two dimensional bluff bodies. *NACA TM* **3169** (61), 118.
- ROSHKO, A. 1955 On the wake and drag of bluff bodies. *J. aeronaut. sci.* **22** (2), 124–132.
- ROSHKO, A. 1993 Perspectives on bluff body aerodynamics. *J. Wind Eng. Ind. Aerodyn.* **49** (1-3), 79–100.
- ROSSITTO, G., SICOT, C., FERRAND, V., BORÉE, J. & HARAMBAT, F. 2016 Influence of after-body rounding on the pressure distribution over a fastback vehicle. *Exp. Fluids* **57**, 1–12.
- ROWE, A., FRY, A.L.A. & MOTALLEBI, F. 2001 Influence of boundary-layer thickness on base pressure and vortex shedding frequency. *AIAA journal* **39** (4), 754–756.
- RUIZ, T., SICOT, C., BRIZZI, L. E., LAUMONIER, J., BORÉE, J. & GERVAIS, Y. 2009 Unsteady near wake of a flat disk normal to a wall. *Exp Fluids* **47** (4), 637–653.
- SCHUETZ, T. 2016 *Aerodynamics of road vehicles*. Society of Automotive Engineers, Inc.
- SHIH, T.-H., LIOU, W. W., SHABBAR, A., YANG, Z. & ZHU, J. 1995 A new  $k - \epsilon$  eddy viscosity model for high reynolds number turbulent flows. *Comput. fluids* **24** (3), 227–238.

- SIROVICH, L. 1987 Turbulence and the dynamics of coherent structures. i. coherent structures. *Q. Appl. Math.* **45** (3), 561–571.
- SPALDING, D.B. 1961 A single formula for the law of the wall. *J. Appl. Mech.* **28** (3), 455–458.
- SPOHN, A. & GILLIÉRON, P. 2002 Flow separations generated by a simplified geometry of an automotive vehicle. In *IUTAM Symposium: unsteady separated flows*, , vol. 1. Kluwer Academic,.
- STELLA, F., MAZELLIER, N. & KOURTA, A. 2017 Scaling of separated shear layers: an investigation of mass entrainment. *J. Fluid Mech.* **826**, 851–887.
- STRACHAN, R.K., KNOWLES, K. & LAWSON, N.J. 2007 The vortex structure behind an ahmed reference model in the presence of a moving ground plane. *Exp. Fluids* **42** (5), 659–669.
- SU, X., HE, K., XU, K., GAO, G. & KRAJNOVIĆ, S. 2023 Comparison of flow characteristics behind squareback bluff-bodies with and without wheels. *Phys. Fluids* **35** (3), 035114.
- SYCHEV, V. V. 1982 Asymptotic theory of separated flows. *Mekh. Zhid. i Gaza* .
- SYCHEV, V. V., SYCHEV, V. V., RUBAN, A. I. & KOROLEV, G. L. 1998 *Asymptotic theory of separated flows*. Cambridge University Press.
- TRIP, R. & FRANSSON, J. H.M. 2017 Bluff body boundary-layer modification and its effect on the near-wake topology. *Phys. Fluids* **29** (9), 095105.
- URQUHART, M., SEBEN, S. & STERKEN, L. 2018 Numerical analysis of a vehicle wake with tapered rear extensions under yaw conditions. *J. Wind Eng. Ind. Aerodyn.* **179**, 308–318.
- VAN DYKE, M. 1982 *An album of fluid motion*, , vol. 176. Parabolic Press Stanford.
- VAN OUDHEUSDEN, B.W., SCARANO, F., VAN HINSBERG, N.P. & WATT, D.W. 2005 Phase-resolved characterization of vortex shedding in the near wake of a square-section cylinder at incidence. *Exp. Fluids* **39** (1), 86–98.
- VARNEY, M. 2020 Base drag reduction for squareback road vehicles. PhD thesis, Loughborough University.
- VARNEY, M., PASSMORE, M., SWAKEEN, R. & GAYLARD, A. 2020 Parametric study of reduced span side tapering on a simplified model with wheels. *Tech. Rep.* 2020-01-0680. Society of Automotive Engineers, Inc.
- VENNING, J., LO JACONO, D., BURTON, D., THOMPSON, M. & SHERIDAN, J. 2015 The effect of aspect ratio on the wake of the ahmed body. *Exp. Fluids* **56** (6), 1–11.
- VOLPE, R., DEVINANT, P. & KOURTA, A. 2015 Experimental characterization of the unsteady natural wake of the full-scale square back ahmed body: flow bi-stability and spectral analysis. *Exp. Fluids* **56** (5), 1–22.
- WANG, S., AVADIAR, T., THOMPSON, M. C. & BURTON, D. 2019 Effect of moving ground on the aerodynamics of a generic automotive model: The driver-estate. *J. Wind Eng. Ind. Aerodyn.* **195**, 104000.
- WANG, X.W., ZHOU, Y., PIN, Y.F. & CHAN, T.L. 2013 Turbulent near wake of an ahmed vehicle model. *Exp. Fluids* **54** (4), 1490.
- WANG, Y. 2019 Experimental study of wheel-vehicle aerodynamic interactions. PhD thesis, Chasseneuil-du-Poitou, Ecole Nationale Supérieure de Mécanique et d’Aérotechnique.
- WANG, Y., SICOT, C., BORÉE, J. & GRANDEMANGE, M. 2020 Experimental study of wheel-vehicle aerodynamic interactions. *J. Wind Eng. Ind. Aerodyn.* **198**, 104062.

- WÄSCHLE, A. 2007 The influence of rotating wheels on vehicle aerodynamics-numerical and experimental investigations. *Tech. Rep.* 2007-01-0107. Society of Automotive Engineers, Inc.
- WEST, G.S. & APELT, C.J. 1982 The effects of tunnel blockage and aspect ratio on the mean flow past a circular cylinder with reynolds numbers between 104 and 105. *J. Fluid Mech.* **114**, 361–377.
- WICKERN, G., ZWICKER, K. & PFADENHAUER, M. 1997 Rotating wheels-their impact on wind tunnel test techniques and on vehicle drag results. *Tech. Rep.* 970133. Society of Automotive Engineers, Inc.
- WILLIAMSON, C. H.K. 1996 Vortex dynamics in the cylinder wake. *Ann. rev. fluid mech.* **28** (1), 477–539.
- WITTMEIER, F., KUTHADA, T., WIDDECKE, N. & WIEDEMANN, J. 2014 Model scale based process for the development of aerodynamic tire characteristics. *Tech. Rep.* 2014-01-0585. Society of Automotive Engineers, Inc.
- WITTMEIER, F., WIDDECKE, N., WIEDEMANN, J., LINDENER, N. & ARMBRUSTER, R. 2013 Reifenentwicklung unter aerodynamischen aspekten. *ATZ-Automobiltechnische Zeitschrift* **115** (2), 144–150.
- WOOD, C. J. 1964 The effect of base bleed on a periodic wake. *Aeronaut. J.* **68** (643), 477–482.
- YU, X., JIA, Q., RASHIDI, M. M. & YANG, Z. 2020 Comprehensive investigating on the aerodynamic influences of the wheel contact patch. *J. Appl. Comput. Mech.* **6** (4), 934–955.
- YU, X., JIA, Q. & YANG, Z. 2022 Comprehensive study of the aerodynamic influence of ground and wheel states on the notchback driver. *Energies* **15** (3), 1124.
- ZDRAVKOVICH, M. M. 1997 *Flow around circular cylinders: Volume 1: Fundamentals*, , vol. 1. Oxford university press.
- ZHANG, B.F., LIU, K., ZHOU, Y., TO, S. & TU, J.Y. 2018 Active drag reduction of a high-drag ahmed body based on steady blowing. *J. Fluid Mech.* **856**, 351–396.
- ZHANG, B.F., ZHOU, Y. & TO, S. 2015 Unsteady flow structures around a high-drag ahmed body. *J. Fluid Mech.* **777**, 291–326.



# Résumé étendu

Le secteur des transports terrestres est à l'origine de niveaux élevés d'émissions de gaz à effet de serre, qui ont des effets néfastes sur la santé humaine et l'environnement. La réduction de la traînée aérodynamique des véhicules routiers est l'un des principaux leviers pour diminuer ces impacts environnementaux.

L'écoulement autour d'un véhicule automobile, de par sa forme extérieure, est massivement décollé. Les régions de séparation et les interactions entre elles sont des sources directes ou indirectes de traînée aérodynamique. Les sillages des roues et celui du véhicule représentent les régions décollées les plus importantes, en terme d'échelle, autour du véhicule. Les effets indirects des sillages de roues sur le sillage proche du corps principal, qui entraînent une diminution de la pression de base, ont un effet très négatif sur la traînée aérodynamique du véhicule. Les roues elles-mêmes et leurs interactions avec le corps principal sont responsables de plus de 25 % de la traînée aérodynamique (Wickern *et al.*, 1997).

Dans ce contexte industriel, le présent travail vise à améliorer la compréhension physique des interactions aérodynamiques roue-véhicule et de leurs conséquences sur la traînée. L'objectif est d'améliorer le processus de réduction de la traînée aérodynamique des véhicules en tenant compte de la présence des roues et de leur interaction avec le reste du véhicule.

Nous fournissons ici un résumé étendu en français du manuscrit. Les principaux résultats et conclusions y sont présentés.

## Chapitre 1. Introduction

Dans ce chapitre introductif, nous commençons par passer brièvement en revue les caractéristiques générales des sillages de corps épais. Nous examinons ensuite le sillage de modèles de voiture simplifiés et leur sensibilité à divers paramètres et perturbations. Une attention particulière est accordée à l'influence des roues, qui sont considérées comme des perturbations du sous bassement. Enfin, les problèmes spécifiques abordés par le présent mémoire sont mis en évidence, ce qui conduit à une présentation du plan de la thèse.

Les modèles simplifiés de véhicules routiers sont devenus courants dans la recherche sur l'aérodynamique des véhicules routiers au cours des dernières décennies. Ils offrent en effet un bon compromis entre la prise en compte des dynamiques principales de l'écoulement autour des véhicules routiers réels et la facilité de gestion des expériences et des calculs. Le corps de Ahmed (Ahmed *et al.*, 1984) et le corps appelé 'Windsor' (Le Good & Garry, 2004) sont peut-être les modèles les plus connus. Pour le corps de Ahmed original à culot carré, par Ahmed *et al.* (1984), avec un rapport entre la hauteur  $H$  et la largeur  $W$  inférieur à 1 ( $H/W < 1$ ), nous montrons à la figure A.10 une schématisation de l'écoulement de sillage. Le culot droit impose des séparations d'écoulement massives derrière le modèle, ce qui conduit à la formation d'un sillage tridimensionnel. L'interaction des couches de cisaillement opposées conduit à un lâcher tourbillonnaire dans les directions verticales et horizontales. De plus, dans la direction horizontale du sillage, Grandemange *et al.* (2013b) a révélé un basculement aléatoire de l'orientation du sillage entre deux états conduisant à une symétrie statistique. Une longue échelle de temps de l'ordre de  $O(10^3 H/U_0)$  est normalement nécessaire entre les basculements. Des études complémentaires menées par Barros *et al.* (2017); Bonnavion & Cadot (2018) et Haffner *et al.* (2020a) montrent que le sillage présente toujours une asymétrie sous la forme d'une asymétrie bimodale horizontale ou d'une asymétrie verticale permanente. Ces asymétries sont une source importante de traînée ( $\sim 5\%$  de la traînée

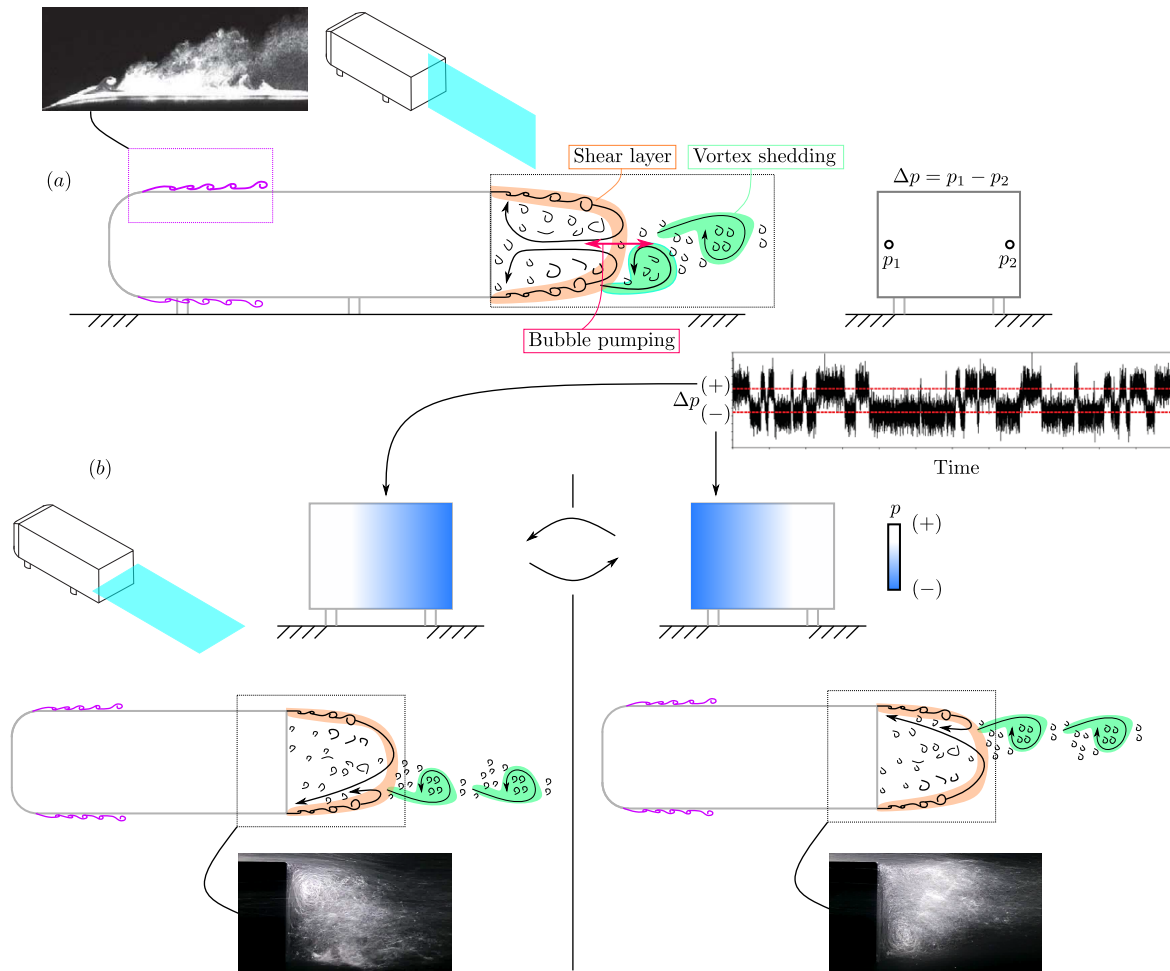


Figure A.10: (a) Schématisation de la séparation de l'écoulement et de la dynamique du sillage du corps d'Ahmed à culot d'origine ; la visualisation de l'écoulement à partir de Grandemange (2013) montre la séparation à l'avant. (b) Description simplifiée de la bi-stabilité du sillage horizontal. L'évolution temporelle de la différence de pression  $\Delta p$  entre deux points de la base  $p_1$  et  $p_2$  montre deux états de sillage présentant une asymétrie horizontale à grande échelle. Les deux états sont illustrés par des croquis et des visualisations de flux provenant de Cadot *et al.* (2015).

totale) comme le suggèrent Grandemange *et al.* (2013b) sur la base de la théorie de la traînée induite et Haffner *et al.* (2020a) sur la base du mécanisme d'interaction entre les couches de cisaillement opposées.

Des études antérieures ont révélé que le sillage de ces modèles est très sensible aux perturbations de l'écoulement, même très faibles. Un sous-ensemble important de perturbations de l'écoulement se situe entre la face inférieure du corps et le sol. L'importance de ce sous-ensemble réside dans le fait qu'il est fréquemment rencontré dans des conditions routières réelles. En général, ces perturbations ont la capacité de modifier l'équilibre naturel du sillage dans la direction verticale et, dans certains cas, de favoriser l'apparition d'une dynamique bimodale (Barros *et al.*, 2017).

Il est intéressant de constater que des modifications très similaires de l'équilibre du sillage ont été trouvées en incluant des roues tournantes/stationnaires sur un corps de Windsor dans Pavia & Passmore (2017); Pavia *et al.* (2020) et dans Su *et al.* (2023). Récemment, Wang *et al.* (2020) ont étudié les effets des roues sur le sillage d'un modèle ASMO à culot droit. Dans cette étude, il a été montré que les roues, qui ont ici une déformation réaliste, influencent de manière importante l'asymétrie verticale du sillage. Il a également été mis en évidence une fusion entre les sillages des roues arrière et le sillage du modèle, qui a été identifiée comme un facteur clé pour les interactions locales donnant lieu à une forte pénalité de traînée. Toutefois, les mécanismes d'interaction sous-jacents doivent encore être analysés plus en détail.

Sur la base de ces études antérieures, plusieurs caractéristiques clés des interactions roue-véhicule et leurs conséquences sur la traînée sont ont été étudiées lors de ce travail :

- Comme le montre Wang (2019), localement à l'échelle des roues, la fusion des sillages des roues arrière avec le sillage du véhicule entraîne une interaction locale et donne lieu à une forte pénalité de traînée. Cependant, le mécanisme d'écoulement qui conduit à cette pénalité de traînée n'a pas encore été révélé.
- La présence des roues et leurs caractéristiques se sont avérées capables d'influencer considérablement les asymétries de sillage (Pavia & Passmore, 2017; Pavia *et al.*, 2020; Wang *et al.*, 2020; Su *et al.*, 2023). Cependant, une étude détaillée est encore nécessaire pour mieux prendre en compte cette caractéristique dans le développement aérodynamique des véhicules routiers.
- Les véhicules routiers sont conçus pour répondre à différents besoins. Cela signifie que les formes de la carrosserie et des roues peuvent varier considérablement. Par conséquent, la dépendance du modèle (forme de la carrosserie et forme de la roue) des interactions roue-véhicule est un autre facteur décisif à prendre en compte.

## Chapitre 2. Méthodes expérimentales

Une description du dispositif expérimental est donnée dans ce chapitre. Le corps épais étudié dans le présent travail est basé sur le modèle de Windsor (Le Good & Garry, 2004), qui présente une section transversale rectangulaire, et un avant incliné avec les bords d'attaque arrondis pour empêcher une séparation massive de l'écoulement. Différents ensembles d'accessoires ont été développés pour adapter le modèle aux différentes configurations expérimentales. Pour examiner l'influence de la géométrie des roues, trois types de roues sont conçus avec des rayons d'épaulement différents. La figure A.11 présente ensuite le montage du modèle dans la section d'essai de la soufflerie S620 de l'ENSMA. Une description de l'intégration des roues dans le modèle est également fournie.

Les techniques de mesure utilisées sont :

- Mesure de la pression moyenne et résolue dans le temps sur le corps.
- Balance à six composantes pour quantifier les forces aérodynamiques moyennes.
- Mesures de la vitesse dans des plans bidimensionnels à l'aide d'un système de vélocimétrie par image de particules (PIV). On utilise un système de PIV bidimensionnel à deux composantes (2D2C) ou bidimensionnel à trois composantes (2D3C).

## Chapitre 3. Configuration de référence

Ce chapitre présente brièvement les caractéristiques de l'écoulement naturel autour du corps de Windsor standard à culot droit sans roue. Cet écoulement sert de référence pour les chapitres suivants. Le nombre de Reynolds  $Re_H$  basé sur la hauteur du modèle varie de 3 à  $7 \times 10^5$ . Dans un premier temps, nous caractérisons l'écoulement moyen en amont du culot du modèle à l'aide de mesures de pression. L'absence de séparation à l'avant du corps est mise en évidence. En outre, les caractéristiques de la couche limite au niveau du culot sont détaillées. L'écoulement de sillage est caractérisé à l'aide de mesures de vitesse et de pression sur le culot du modèle (appelée pression de base). La courbure de l'écoulement et les contraintes de Reynolds autour de la bulle de recirculation sont détaillées. Elles sont importantes pour définir la pression négative significative dans la région de recirculation du sillage et donc l'empreinte de basse pression sur le culot. Les variations de certaines grandeurs aérodynamiques globales (forces, pression de base et longueur de la région de recirculation) en fonction du nombre de Reynolds et de la longueur du modèle sont ensuite présentées. Les explications et les discussions relatives à ces variations sont également fournies.

Comme dans les études précédentes décrites dans le chapitre 1, la symétrie du sillage moyen dans la direction horizontale est composée de deux états équiprobables présentant une forte asymétrie dans la direction horizontale. L'intervalle entre deux événements de basculement des deux états est d'environ  $\sim 10^3$  échelle de temps de convection  $H/U_0$ . Afin d'obtenir un large

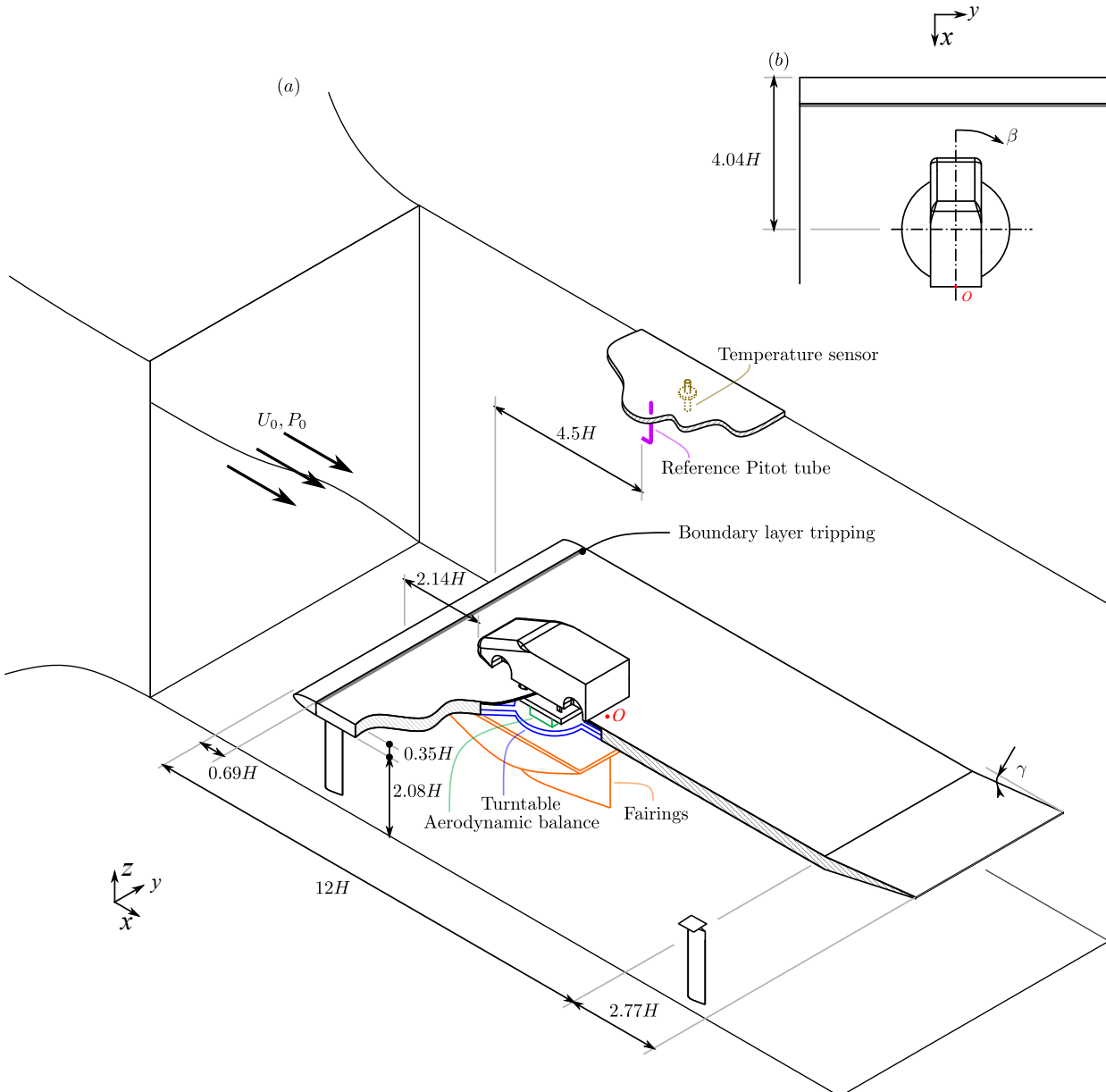


Figure A.11: Installation détaillée dans la section d'essai de la soufflerie. (a) Vue isométrique de la maquette montée sur un plancher surélevé. (b) Vue de dessus de la maquette détaillant le centre de rotation du lacet.

éventail d'orientations de sillage pour le corps de référence, un cylindre circulaire de diamètre variable couvrant toute la largeur du véhicule est placé sur la surface supérieure ou inférieure du modèle. En utilisant cette méthodologie, le scénario de bifurcation avec une compétition entre l'asymétrie statique verticale et l'asymétrie bimodale horizontale est illustré, fournissant des références pour les investigations dans les chapitres suivants lorsque le sillage du véhicule est perturbé par des roues.

## Chapitre 4. Modélisation simplifiée des roues

Une expérience modèle est menée dans ce chapitre afin de permettre une étude paramétrique rigoureuse des modifications dans le sillage d'une géométrie de voiture par des perturbations de l'écoulement de soubassement imitant les effets des roues.

Comme le montre schématiquement la figure A.12, le sillage tridimensionnel du corps de Windsor est perturbé par le placement d'une paire d'obstacles en forme de D sous le corps. Cinq largeurs d'obstacle  $d$ , de 12 à 26 % de la hauteur du corps, sont utilisées pour réaliser une étude de sensibilité

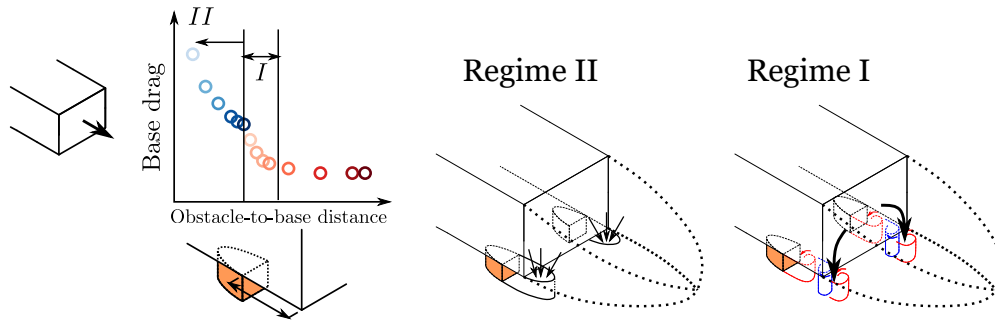


Figure A.12: Sensibilité de la traînée de base et du sillage à une paire d'obstacles en forme de D dans l'écoulement de soubassement. La dynamique de l'écoulement dans les différents régimes est mise en évidence dans la partie droite de la figure.

de la traînée de pression du corps en faisant varier la distance relative  $l$  entre la paire d'obstacles et la base.

Deux régimes successifs sont identifiés pour des distances obstacle-base  $l/d < 2,5$ , où la traînée de pression du corps est augmentée jusqu'à 22 %. Dans les différents régimes, la dynamique de l'écoulement mesurée en aval des obstacles est très différente. Ceci est confirmé par les mesures de vitesse et de pression. Lorsque les obstacles sont les plus proches de la base  $l/d < 1,5$  (Régime II, voir figure A.12), les changements de traînée de pression du corps principal sont dus à la fusion moyenne entre les sillages des obstacles et du corps principal, et varient linéairement avec  $d$ . En revanche, lorsque les obstacles sont situés plus loin de la base  $1.5 < l/d < 2.5$  (Régime I, voir figure A.12), les sillages des obstacles sont isolés du sillage du corps principal. Dans ce cas, la dynamique du sillage de l'obstacle détermine les changements de traînée de pression du corps principal, qui varient comme  $d^2$ .

Lorsque l'on réduit la distance à la base et malgré ces différences importantes entre les deux régimes d'augmentation de la traînée, les effets globaux sur le sillage principal sont très similaires aux effets d'une aspiration continue située à la base pour un cylindre en forme de D étudié par Bearman (1967) et pour un corps tridimensionnel étudié par Hsu *et al.* (2021). Un transfert de masse moyen entre le sillage du corps principal et les sillages des obstacles est en effet mis en évidence dans le présent chapitre. Par conséquent, nous supposons que ce mécanisme de transfert de masse du sillage du corps principal aux sillages des obstacles régit les interactions près du sillage et les changements de traînée de pression pour le corps principal. En utilisant nos résultats et les études de référence décrivant l'effet de la succion à partir du culot sur la traînée de pression des corps épais, un modèle physique basé sur un bilan de quantité de mouvement est proposé pour expliquer l'augmentation de la traînée de pression dans les différents régimes observés. Pour le premier régime, l'échelle  $d^2$  peut être simplement comprise en affirmant que la largeur et la longueur de la surface de l'échange de masse sont déterminées par la taille de l'obstacle  $d$ . En revanche, l'échelle linéaire observée dans le second régime implique que la taille de la surface d'échange de masse est gouvernée à la fois par l'échelle de l'obstacle et par l'échelle du corps. Nos données expérimentales sont toutes en accord avec ce modèle.

Les régimes d'augmentation de la traînée entraînés par l'échange de masse local mis en évidence dans ce chapitre sont considérés comme une caractéristique générale des interactions de sillage pour les corps épais tridimensionnels qui complètent notre compréhension physique de la réaction globale d'une bulle de recirculation tridimensionnelle à des perturbations en amont (Barros *et al.*, 2017). En outre, les obstacles perturbent également l'écoulement de soubassement, ce qui entraîne une variation globale de l'équilibre vertical du sillage. Ces effets locaux et globaux sont étudiés plus en détail dans le chapitre suivant en utilisant : des roues en rotation, afin d'éclairer davantage le problème de l'interaction roue-véhicule.

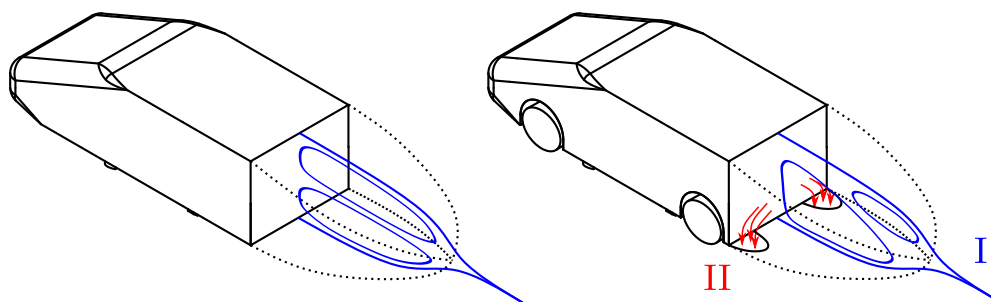


Figure A.13: Esquisse conceptuelle des deux mécanismes d'écoulement des interactions roue-véhicule responsables des variations de la traînée de base. I : variation globale de l'équilibre vertical du sillage du véhicule. II : échange de masse moyen entre le sillage du véhicule et les sillages des roues.

## Chapitre 5. Caractéristiques principales des interactions roue-véhicule : conséquences sur la traînée du véhicule

Les principales caractéristiques des interactions roue-véhicule et leurs conséquences sur la traînée sont étudiées dans ce chapitre sur la base du corps de Windsor à culot droit avec différentes distances  $l$  entre les roues arrière et la base du véhicule.

Dans un premier temps, nous avons montré que l'on pouvait distinguer deux mécanismes différents, schématisés sur la figure A.13. A l'échelle du véhicule, quelle que soit la distance  $l$ , les roues perturbent l'écoulement et induisent une variation globale de l'équilibre vertical du sillage du véhicule (I dans la figure A.13). Deux états initiaux du sillage sont considérés. Le premier se caractérise par une faible asymétrie verticale et une dynamique horizontale bistable. D'autre part, en plaçant un cylindre horizontal couvrant toute la largeur du véhicule sur la surface supérieure, le deuxième état de sillage est une asymétrie permanente dans la direction verticale sans aucune dynamique bi-stable dans la direction horizontale. Pour le premier état, les roues augmentent l'asymétrie verticale moyenne du sillage, entraînant une augmentation modérée de la traînée de base de  $\sim 5\%$ . Pour le deuxième état, les roues réduisent l'asymétrie moyenne du sillage, ce qui entraîne une diminution importante de la traînée de base de  $9\%$ .

Compte tenu de l'échelle des roues, si la distance roue-base  $l/w$  ( $w$  étant la largeur des roues) est inférieure à un seuil d'environ 3 dans la configuration actuelle, la traînée de base augmente et est très sensible à  $l/w$ . Dans cette situation, on observe un transfert de masse moyen du sillage du véhicule vers le sillage des roues arrière (II dans la figure A.13). Ce phénomène d'échange de masse et le changement de traînée qui en découle ne varient pas en fonction de l'état initial du sillage du véhicule. Un flux de masse moyen constant extrait de la région de recirculation signifie que ce flux de masse doit continuellement entrer dans la région de recirculation du sillage du véhicule et que les particules de fluide correspondantes ont perdu une partie de leur quantité de mouvement longitudinale moyenne. Le modèle physique proposé au chapitre 4 est utilisé pour relier l'échange de masse et l'augmentation de la traînée de base et pour vérifier la cohérence des mesures.

En outre, l'influence de l'état de la roue (en rotation ou stationnaire) est examinée. On constate que, dans le cadre du dispositif expérimental actuel, l'état de la roue n'a pratiquement aucune influence sur la traînée de base, mais une influence modérée sur la traînée totale. Cette différence est due au changement de pression à l'intérieur des passages de roue et à la surface avant du modèle de véhicule. Un examen plus approfondi des mesures de vitesse confirme que les caractéristiques principales des interactions roue-véhicule dérivées des cas en rotation peuvent être obtenues de la même manière en utilisant les cas stationnaires. Les principaux aspects des interactions roue-véhicule pour ce corps culot droit, à savoir le forçage global du sillage du véhicule et les interactions locales près du sillage, ne sont donc pas liés à l'état des roues.

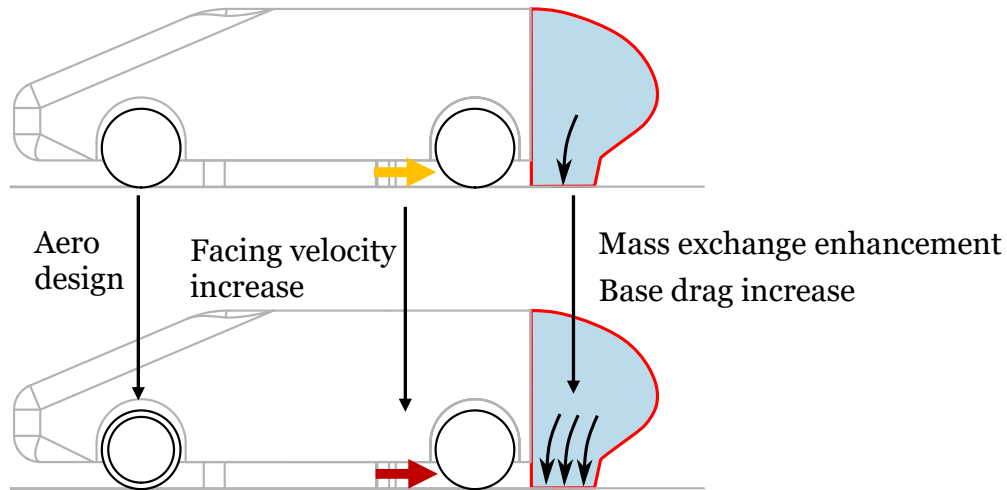


Figure A.14: Esquisse conceptuelle du mécanisme d'interaction entre la roue avant et la roue arrière.

## Chapitre 6. Influence de la géométrie des roues : importance des roues avant

Dans ce chapitre, on étudie l'influence de la géométrie des roues sur le sillage et la traînée d'un véhicule à culot droit.

Une étude préliminaire est d'abord menée pour explorer un espace paramétrique composé de plusieurs variables (l'équilibre initial du sillage et les rayons d'épaulement des roues aux essieux avant et arrière). On constate que des roues avant plus "aérodynamiques" (Rayon d'épaulement plus importants) augmentent la traînée de base et que le niveau d'augmentation dépend de l'équilibre initial du sillage. En revanche, au niveau de l'essieu arrière, la variation de la géométrie des roues arrière n'a pratiquement aucune influence sur la traînée de base, quelle que soit l'asymétrie du sillage du véhicule.

Sur la base de l'étude préliminaire, l'influence de la géométrie des roues avant est étudiée en détail en faisant varier l'épaulement des roues avant et la distance entre les roues arrière et la base  $l$ . Comme le montre schématiquement la figure A.14, nous mettons en évidence des interactions complexes entre trois acteurs : les roues avant, les roues arrière et le sillage du véhicule. Ces interactions entraînent une augmentation de la traînée de base pouvant aller jusqu'à 21 % par rapport au cas de base sans roues. La vitesse amont  $u_f$  des roues arrière est augmentée pour des roues avant ayant un épaulement arrondi, ce qui réduit le niveau de pression à l'intérieur des sillages des roues arrière. Dans la situation actuelle, lorsque la distance roue-base  $l/w$  ( $w$  est la largeur des roues) est inférieure à un seuil de 2,5, la diminution de la pression s'accompagne d'une augmentation du transfert de masse moyen mis en évidence au chapitre 5 du sillage du véhicule vers les sillages des roues arrière. Ces interactions se traduisent par une loi d'échelle où la traînée de base est linéairement proportionnelle à  $u_f$ .

Enfin, en proposant une relation entre le niveau de pression global établi par le sillage du véhicule, la vitesse d'écoulement impactant les roues arrière  $u_f$ , et le développement du sillage des roues arrière, un modèle physique est développé. Notre hypothèse est que la différence de pression entre les deux côtés de l'interface d'interaction (où se produit l'échange de masse moyen) gouverne la vitesse du transfert de masse moyen. Ce modèle est en accord avec les données expérimentales mesurées dans le présent chapitre. En outre, l'application du modèle d'échange de quantité de mouvement proposé dans le chapitre 4 explique la variation linéaire de la traînée de base avec la vitesse d'affrontement  $u_f$ .

Les résultats du présent chapitre affinent notre compréhension physique des interactions entre les roues et le sillage du véhicule dans l'industrie automobile et entre des zones décollées dans une situation plus générale avec un écoulement complexe de corps épais. Le modèle physique proposé permet d'illustrer l'insensibilité du transfert de masse moyen et des changements de traînée à l'asymétrie verticale du sillage du véhicule constatée dans le chapitre 5. On s'attend à ce que cela reste vrai lorsque la forme de l'arrière du véhicule est modifiée, ce qui est étudié dans le chapitre

suivant.

## Chapitre 7. Extension des résultats à une autre géométrie de culot

Dans ce chapitre, on étudie la dépendance des interactions roue-véhicule par rapport à la forme du culot du véhicule. Des mesures supplémentaires répétant les investigations des chapitres précédents utilisant un véhicule à culot droit sont effectuées sur la base d'un véhicule à culot incliné de  $20^\circ$ . Ce véhicule présente une topologie de sillage très tridimensionnelle avec une interaction complexe entre plusieurs structures d'écoulement. En plaçant une paire d'obstacles en forme de D sous le véhicule ou en installant des roues sur le véhicule, des différences et des similitudes dans les interactions roue-véhicule sont trouvées en comparant les résultats obtenus sur les deux formes de véhicule. Des différences sont constatées lorsque l'on examine globalement le sillage du corps principal du véhicule, qui réagit très différemment à la présence des roues ou des obstacles. Les études sur les propriétés moyennes et fluctuantes du sillage l'ont confirmé. Plus important encore, la forte sensibilité de l'équilibre vertical du sillage du véhicule à culot droit aux roues (ou aux obstacles) n'est pas observée pour la géométrie à culot incliné. On pense que c'est la clé pour mieux comprendre la sensibilité différente à la forme des roues de différentes formes de véhicules (Wittmeier *et al.*, 2013).

D'autre part, lorsque l'on examine localement l'écoulement près des roues arrière ou des obstacles, nous montrons qu'il est à peine modifié par la variation du sillage du véhicule. Parallèlement, le transfert de masse moyen du sillage du véhicule vers les sillages des roues arrière (ou des obstacles) s'avère quantitativement peu sensible à la forme du véhicule. Selon le modèle proposé au chapitre 4, la perte de quantité de mouvement dans le sens de l'écoulement des particules de fluide entrant dans le sillage est compensée par une chute de pression sur la base. Par conséquent, le même niveau de perte de masse moyenne correspond au même niveau de changement de pression à la base. Ce phénomène est mesuré avec succès en faisant varier systématiquement la distance relative entre les obstacles et la base verticale du véhicule. En effet, on a mesuré les mêmes régimes d'écoulement et la même sensibilité à la traînée de pression qu'au chapitre 4 en utilisant un modèle à culot droit. Ici, les variations de la traînée de pression sont toujours régies par les propriétés de mise à l'échelle trouvées pour le véhicule à culot droit. D'un autre point de vue, les présents travaux confirment également que le modèle physique proposé au chapitre 4 est robuste, même pour un sillage tridimensionnel complexe.

En outre, le rôle des roues avant reste le même que pour le modèle à culot droit étudié au chapitre 6. Pour des roues avant d'épaules plus arrondies, le transfert de masse moyen est amélioré et la traînée de base est augmentée.

Ces similitudes entre les deux véhicules montrent que les interactions entre les roues avant et arrière et les interactions locales entre les roues arrière et le sillage du véhicule sont insensibles au type de géométrie de culot. Ce dernier point est partiellement confirmé dans le chapitre 5 par l'étude de deux états de sillage initiaux différents du modèle à culot droit.

## Chapitre 8. Synthèse générale et perspectives

Ce dernier chapitre résume les principaux résultats du présent travail axé sur les interactions entre les roues et le corps principal du véhicule. Notre objectif était tout d'abord de mettre en évidence les principaux mécanismes d'écoulement régissant les interactions et leur impact sur la traînée du véhicule. Le second objectif était de montrer, d'un point de vue plus général, comment ces mécanismes d'écoulement évoluent en fonction de la forme du véhicule ou des roues. Les principaux résultats de ce travail sont les suivants.

Localement à l'échelle des roues, nous avons mis en évidence un transfert de masse moyen du sillage du véhicule vers les sillages des roues arrière. L'augmentation de la traînée de base associée à ce phénomène a été estimée jusqu'à 12%, ce qui correspond à une pénalité de traînée de  $0.024 \overline{C_D}$ . Un scénario physique a été proposé pour répondre à deux questions principales : (i) quelle est la cause du transfert de masse moyen ? et (ii) quelles sont les conséquences de ce transfert ?

Sur la base d'analyses de sensibilité systématiques, le phénomène d'échange de masse a été étudié plus en détail. D'une part, il n'est pas sensible aux variations de la topologie du sillage du véhicule. Cela a été démontré par deux scénarios dans lesquels la forme du culot du véhicule a été modifiée ou l'asymétrie verticale à grande échelle du sillage du véhicule a été manipulée. D'autre part, il est sensible aux paramètres liés aux roues, tels que la largeur des roues, la distance entre les roues arrière et la base, et les conditions d'écoulement en amont des roues arrière.

Globalement à l'échelle du véhicule, nous avons constaté que les roues (ou les obstacles) induisent des changements dans l'écoulement de soubassement, ce qui conduit à une variation globale de l'équilibre vertical du sillage moyen du véhicule. Selon l'état du sillage initial, une augmentation significative de la traînée de base de  $\sim 5\%$  (correspondant à  $0.01\overline{C_D}$ ) ou une diminution de  $\sim 9\%$  ( $0.02\overline{C_D}$ ) a été observée. Cette augmentation (diminution) de la traînée correspond à une augmentation (réduction) de l'asymétrie du sillage vertical. En outre, il a été constaté que les différentes géométries de véhicules ont une sensibilité très différente à la présence de roues dans le sillage.

Les principales perspectives de ce travail sont les suivantes :

- Le phénomène de transfert de masse moyen pourrait être étendu à d'autres configurations du point de vue des interactions de zones décollées ayant des échelles différentes.
- Pour une application plus poussée des présents résultats, des essais en soufflerie à grande échelle et la prise en compte des conditions réelles sur route sont jugés essentiels.
- La compréhension du problème de l'interaction roue-véhicule nous permet également de proposer des idées pour réduire davantage la traînée. Une ligne directrice pour l'optimisation aérodynamique est proposée. Les techniques de réduction de la traînée permettant de supprimer les interactions sont également discutées.

---

## Wheel-vehicle aerodynamic interactions: consequences for drag

For a road vehicle, the wheels and their interactions with the main vehicle body account for more than 25 % of the total aerodynamic drag. These interactions pose challenges to the aerodynamic development process as drag reduction is concerned. In this experimental study, we aim to identify the salient features of these interactions and their impact on drag using a simplified vehicle geometry. We find that the vehicle wake, the front wheels and the rear wheels are the main players in the interactions. There are two mechanisms that originate from these interactions and contribute to a pressure drag increase of up to 21 %. Between the four wheels and the vehicle wake, interactions exist which induce a global variation of the vertical balance of the vehicle wake. According to the state of the initial wake, this global variation can result in significant pressure drag increase or decrease. Furthermore, strong local near-wake interactions between the rear wheels and the vehicle wake lead to a mean mass transfer from the vehicle wake to the wakes of the rear wheels, resulting in a pressure drag increase. In the present situation, this occurs when the relative distance between the vehicle base and the rear wheels is less than 2.5 times the wheel width. In addition, the front wheels have influence on the interactions between the rear wheels and the vehicle wake, as the facing flow condition they provide for the rear wheels governs the strength of the mean mass transfer and thus the pressure drag change. Based on these findings, we propose a physical model that links the mean mass transfer to the pressure drag increase. This model is consistent with all the parametric measurements, including a situation where a pair of 2-D D-shaped obstacles of varying width and relative distance from the base is used to model the wheels. These local and global interactions are closely coupled to each other. This helps to explain why the ranking by aerodynamic drag of different tires varies with vehicle geometry. As such, the interactions are important to be considered in the aerodynamic development process of road vehicles.

**Keywords** : Automobiles – Aerodynamics, Wakes, Drag, Motor vehicle –Tires, Turbulence

## Interactions aérodynamiques roue-véhicule : conséquences sur la traînée

Pour un véhicule routier, les roues et leurs interactions avec le véhicule représentent plus de 25 % de la traînée aérodynamique totale. C'est pourquoi ces interactions doivent être mieux comprises afin d'aider à la réduction de la traînée dans le processus de développement aérodynamique. Dans cette étude expérimentale, nous cherchons à identifier les principales caractéristiques de ces interactions et leur impact sur la traînée à l'aide d'une géométrie de véhicule simplifiée. Nous avons mis en évidence que le sillage du véhicule, les roues avant et les roues arrière sont les principaux acteurs des interactions. Deux mécanismes physiques sont principalement responsables de ces interactions et contribuent à une augmentation de la traînée de pression pouvant atteindre 21 %. En premier lieu, entre les roues et le sillage du véhicule, il existe des interactions qui induisent une variation globale de l'équilibre vertical du sillage du véhicule. Selon l'état du sillage initial, cette variation globale peut entraîner une augmentation ou une diminution significative de la traînée de pression. Deuxièmement, de fortes interactions locales entre les sillages des roues arrière et le sillage du véhicule conduisent à un transfert moyen de masse du sillage du véhicule vers le sillage des roues arrière, entraînant une augmentation de la traînée de pression. Dans la situation étudiée, cela se produit lorsque la distance relative entre la base du véhicule et les roues arrière est inférieure à 2,5 fois la largeur des roues. De plus, les roues avant ont une influence sur les interactions entre les roues arrière et le sillage du véhicule, car elles modifient l'écoulement attaquant les roues arrière, qui régit l'intensité du transfert de masse moyen et donc le changement de traînée de pression. Sur la base de ces résultats, nous proposons un modèle physique qui relie le transfert de masse moyen à l'augmentation de la traînée de pression. Ce modèle est cohérent avec toutes les mesures paramétriques réalisées, y compris une situation où une paire d'obstacles bidimensionnels de largeur et de distance relative de la base variables est utilisée pour modéliser les roues. Ces interactions locales et globales sont étroitement liées les unes aux autres. Cela aide à expliquer pourquoi le classement par traînée aérodynamique des différents pneus varie avec la géométrie du véhicule. En tant que telles, les interactions sont importantes à prendre en compte dans le processus de développement aérodynamique des véhicules routiers.

**Mots clés** : Automobiles—Aérodynamique, Sillage, Traînée, Véhicules automobiles—Pneus, Turbulence

---